Diss. ETH No. 18673

Low temperature thermochronology of the northern Aegean Rhodope Massif

A dissertation submitted to the

SWISS FEDERAL INSTITUTE OF TECHNOLOGY ZURICH

for the degree of
Doctor of Sciences

presented by
Eliane Denise Wüthrich
Dipl. Natw. ETH Zürich
born 07.06.1978
from Eggiwil BE

accepted on the recommendation of:

Prof. Dr. Jean-Pierre Burg, examiner
Dr. Diane Seward, co-examiner
Dr. Alexandre Kounov, co-examiner
Prof. Dr. Jean-Pierre Brun, co-examiner

2009

Contents

Abstract

The Rhodope Massif, situated mainly in southern Bulgaria and northern Greece, evolved from Cretaceous shortening and thrusting to Cenozoic extension and the development of metamorphic core complexes. This work uses the fission-track method on apatite, zircon and titanite and the (U-Th)/He method on apatite to document the low-temperature evolution of three Rhodope core complexes: (i) the South Rhodope Core Complex (SRCC) of northern Greece, (ii) the Central Rhodope Metamorphic Complex (CRMC) of southern Bulgaria and (iii) the Kesebir–Kardamos Dome (KKD) straddling the Bulgarian–Greek border. Combining the new data with published, higher-temperature chronometer ages and structural and sedimentary information, has allowed constraints to be made on the timing of activity of the main detachments and shear zones.

The Rhodope Massif underwent extension since the Maastrichtian/Palaeocene. Early cooling and related extension was, however, moderate and restricted to the north-eastern part of the massif, i.e. the KKD and the CRMC. Cooling/exhumation reached a climax at about 40 Ma. This is indicated by (i) rapid cooling/exhumation controlled by the Tokachka Detachment of the KKD between at least 42 Ma and ∼35 Ma, (ii) very rapid cooling/exhumation in the CRMC between about 40 and 33 Ma, presumably mostly caused by movement along the Kardzhali shear zone and secondarily along the Smilian and Middle Rhodope shear zones, and (iii) the onset of cooling/extension in the SRCC at ∼40 Ma, controlled by the Kerdilion Detachment.

Each region studied underwent a change in the thermo-mechanical conditions leading to a second phase of cooling/exhumation. In the KKD, movements on the Tokachka Detachment possibly ceased after 35 Ma, certainly after 33 Ma, and further minor extension was accommodated only by high-angle normal faults. In the CRMC cooling/extension along the Kardzhali, Smilian and Middle Rhodope shear zones ceased at 33 Ma, and further cooling/extension after ∼30 Ma was localised in the south-central part of the metamorphic complex, controlled by the Madan shear zone. In the SRCC, the thermo-mechanical change was slightly later; the Kerdilion Detachment stopped functioning at about 26 Ma and by at least 20 Ma cooling/exhumation was localised in the central part of the core complex and controlled by the Strymon Valley Detachment. Detachment-controlled cooling/extension lasted in the CRMC until about 15 Ma while in the SRCC it continued until about 8 Ma.

The two extension phases may be related to a switch from syn-orogenic/thickening collapse to post-orogenic, slab-roll-back driven extension. The two extensional phases may also indicate two successive "push-pull" cycles caused by the accretion/subduction of continental and oceanic lithosphere fragments within the Aegean subduction zone.

In any case, peak-cooling/exhumation after around 40 Ma is related to magmatic activity in the Rhodope Massif. Convective removal of the lithopheric mantle and subsequent upwelling of the asthenosphere may have provided the necessary heat to cause, on the one hand, melt generation and volcanism and, on the other hand, weakening of the thickened crust and core complex formation.

Since about 8 Ma, detachment faulting in the Rhodope Massif has probably stopped with the cessation of the Strymon Valley Detachment and only high-angle normal faults such as the Xanthi Fault or the faults bounding the offshore Orfanos Basin continued to be active.

Zusammenfassung

Die Rhodopen sind ein Gebirge, welches sich hauptsächlich über Südbulgarien und Nordgriechenland erstreckt. Es wurde während der Kreide durch Kollision eines kontinentalen Fragmentes mit dem europäischen Kontinent gebildet. Auf diese, durch Kompression und Aufschiebungen geprägte Phase, folgte im Kenozoikum eine langgezogene Extensionsphase, während welcher mehrere metamorphe Kernkomplexe gebildet wurden.

Im Rahmen dieser Dissertation sind Gesteine aus drei metamorphen Kernkomplexen der Rhodopen mit der Spaltspurmethode an Apatiten, Zirkonen und Titaniten sowie mit der (U-Th)/He-Methode an Apatiten datiert worden. Anhand der erhobenen Daten wird die Abkühlungsgeschichte im Temperaturebereicht von etwa 300 bis 60°C rekonstruiert.

Die drei untersuchten Kernkomplexe sind der Kernkomplex der Südrhodopen (SRCC, Southern Rhodope Core Complex), welcher sich in Griechenland befindet, der Kernkomplex der Zentralrhodopen (CRMC, Central Rhodope Metamorphic Complex) im südlichen Bulgarien und der Kesebir–Kardamos Dome (KKD), welcher sich je zur Hälfte über Bulgarien und Griechenland erstreckt.

Die neu erhobenen Daten werden unter Einbezug von bereits publizierten geochronologischen Altern sowie strukturellen und sedimentologischen Erkenntnissen interpretiert und geben Aufschluss darüber, wann die wichtigsten flachen Abschiebungen (detachments) der verschiedenen Kernkomplexe aktive gewesen sein müssten.

Erste Anzeichen für Extension in den Rhodopen gibt es im Maastrichtium/Paläozän. Die frühe Extension, welche zur Exhumierung und somit Abkühlung der Gesteine führte, ist allerdings relative moderat und örtlich beschränkt auf die nord-östlichen Rhodopen, d.h. den KKD und den CRMC. Erst etwa vor 40 Ma ist ein Höhepunk in der Abkühlungs-/Exhumierungsgeschichte der Rhodopen zu beobachten. Dies ist ersichtlich aus (i) der schnellen Abkühlung der Gesteine des KKD zwischen mindestens 42 Ma und etwa 35 Ma, ausgelöst durch Exhumierung des Liegenden entlang der Tokachka Abschiebung, (ii) sehr schneller Abkühlung der Gesteine des CRMC zwischen etwa 40 und 33 Ma, verursacht hauptsächlich durch Exhumierung entlang der Kardzhali Abschiebung, aber daneben auch entlang der Smilian und Mittelrhodopen Abschiebungen, und (iii) der Aktivierung der Kerdilion Abschiebung, welche Abkühlung/Exhumierung im SRCC bedingt. Nach dieser ersten Phase der Abkühlung, welche in allen drei Kernkomplexen auftritt, führt eine Än-

derung in den thermischen und mechanischen Bedingungen der Kernkomplexe zu einer zweiten Abkühlungs-/Exhumierungsphase. Im KKD hört die Tokatchka Abschiebung wahrscheinlich vor 35 Ma auf aktiv zu sein; die darauf folgende, schwächer ausgeprägte Extensionsphase verursacht nur noch die Bildung von lokalen steilen Abschiebungen. Die Kardzhali, Smilian und Mittelrhodopen Abschiebungen im CRMC werden etwa vor 33 Ma inaktiv. Darauf folgend, etwa vor 30 Ma, wird die flache Madan Abschiebung aktiv, welche Abkühlung/Exhumierung von Gesteinen im südlich-zentralen Teil des CRMC verursacht. Im SRCC findet der Wechsel von einer Abkühlungsphase zur zweiten etwas später statt. Dort hört die Kerdilion Abschiebung etwa vor 26 Ma auf, Gesteinsmaterial an die Oberfläche zu befördern und abzukühlen. Spätestens seit 20 Ma ist eine zweite flache Abschiebung, die Strymon Valley Abschiebung im Zentrum des SRCC aktiv, welche dort weiterhin Gesteine exhumiert.

Abkühlung/Exhumierung welche durch flache Abschiebungen kontrolliert wird, ist im CRMC bis etwa vor 15 Ma beobachtbar und endet mit der Deaktivierung der Madan Abschiebung. Im SRCC ist schnelle Abkühlung bis etwa vor 8 Ma beobachtbar und endet damit, dass die Stymon Valley Abschiebung inaktiv wird.

Die zwei beobachteten Abkühlungsphasen könnten durch aufeinander folgende syn- und post-orogene Extensionphasen erklärt werden. Dabei ist syn-orogene Extension stark mit gravitativem Kollaps des Gebirges verknüpft, während post-orogene Extension durch das zurückrollen der subduzierten Lithosphärenplatte verursacht wird. Anderseits könnten die zwei Abkühlungsphasen auch mit so genannten “push-pull”-Zyklen zusammenhängen, welche durch alternierendes Anlagern von kontinentalen Fragmenten und Subduzieren von ozeanischen Fragmenten in der ägäischen Subduktionszone enstehen.

Der Höhepunkt in Abkühlung/Exhumierung vor etwa 40 Ma ist in jedem Fall eng verbunden mit vulkanischer Aktivität in den Rhodopen. Konvektive Strömungen sind wahrscheinlich verantwortlich für die Trennung des lithosphärischen Mantels von der Kruste, wobei der lithosphärische Mantel durch Asthenospärenmaterial ersetzt wird. Die heisse Asthenosphäre verursacht einerseits die Bildung von Schmelze und damit Vulkanismus, und andererseits schwächt sie die Kruste was zu erleichterter Kernkomplexbildung führen kann.

Seit etwa 8 Ma, als die Strymon Valley Abscheibung aufhört aktiv zu sein, findet man vermutlich keine flachen Abschiebungen mehr im Gebiet der Rhodopen. Nur steile Abschiebungen, wie die Xanthi Abschiebung oder die Brüche, welche das submarine Orfanos Becken begrenzen, sind länger aktiv.

Chapter 1

Introduction

1.1 Regional and Geological Background

1.1.1 Overview

The Rhodope Massif is a mountain range located to the north of the Aegean Sea and straddling southern Bulgaria and northern Greece (Fig. 1.1). It was first interpreted as a stable Precambrian to Variscan continental fragment (e.g. Kober, 1928) composed of high-grade metamorphic and igneous rocks (e.g. Burg et al., 1995; Dinter et al., 1995; Burg et al., 1996a; Ricou et al., 1998; Peytcheva et al., 1999; Ovtcharova et al., 2003b) and surrounded by two branches of the Alpine–Himalayan collisional system; the Balkan belt to the north and the Dinarides–Hellenides belt to the south-west. Alternative interpretations that linked the Rhodope Massif with the Alpine–Himalayan orogen (Ivanov et al., 1979; Ricou et al., 1985; Dercourt and Ricou, 1987) gave rise to remapping of thrust contacts (Ivanov, 1988) and investigating syn-metamorphic structures (Burg et al., 1990, 1996a,b). This led to a renewed interpretation, whereby the Rhodope Massif is regarded as a complex of Mesozoic syn-metamorphic nappes stacked in an Alpine active margin that later underwent extension and associated exhumation of high-grade rocks (Ivanov, 1988; Burg et al., 1990, 1996b).

1.1.2 Geological limits of the Rhodope Massif

The Rhodope Massif is separated to the north from the Sredna Gora volcanic arc and the Balkan by the Maritsa fault zone and recent deposits of the Maritsa basin (Fig. 1.1). Sredna Gora, a late Cretaceous (Turonian–Maastrichtian) volcanic arc and back-arc basin, and the Balkan together with the Kraishte are part of the European continental margin. The south-western border of the Rhodope Massif is, depending on the author, either the Vardar suture zone or the Serbo–Macedonian Massif (Fig. 1.1). The geological divide between the Rhodope and the Serbo–Macedonian is the Strymon Valley Detachment (Dinter and Royden, 1993; Sokoutis et al., 1993) which follows the valley called Struma River Valley

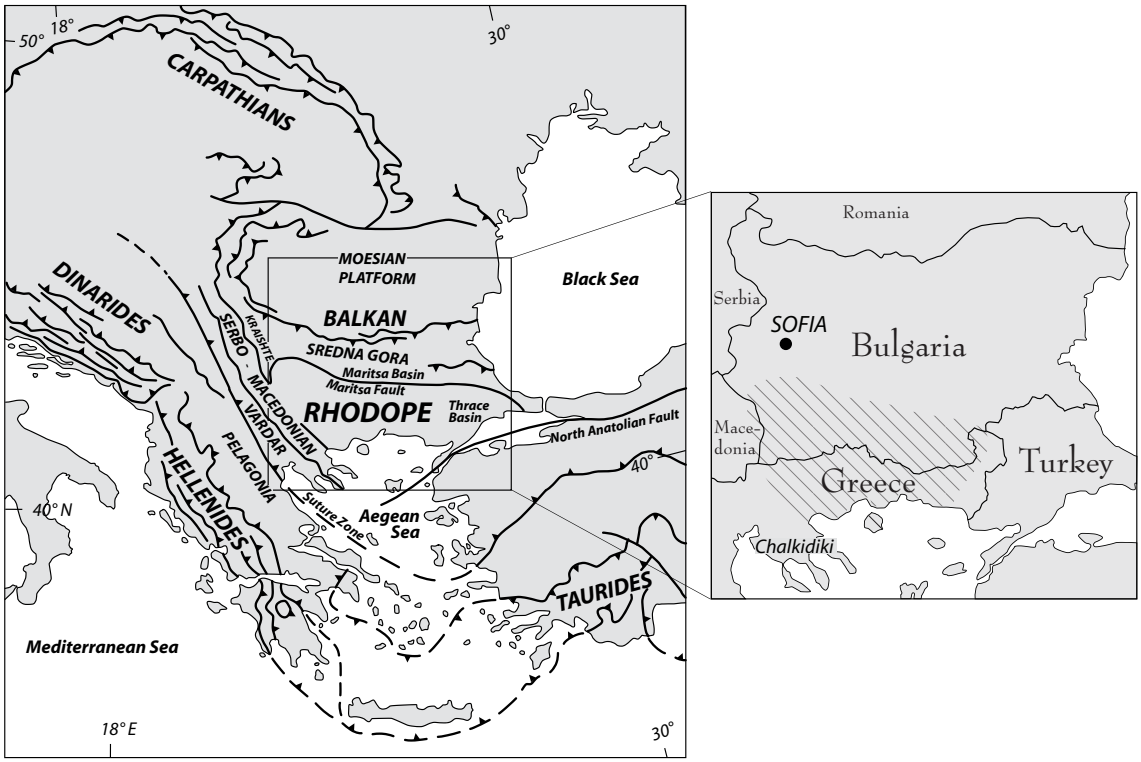

Figure 1.1: Location of the Rhodope Massif within the the Balkan Peninsula (left). Country boundaries are indicated on the right, where the Rhodope Massif corresponds to the shaded area.

in Bulgaria and Strymon Valley in Greece. Some years ago, the Rhodope and the Serbo–Macedonian have been unified on the basis of similarities in metamorphic type, age and ductile strain field (Burg et al., 1995; Ricou et al., 1998; Kilias et al., 1999; Lips et al., 2000). Accordingly, several units west of the Struma/Strymon Valley were assigned to the Rhodope Massif including the Vertiskos and the Kerdilion Units that crop out on the Chalkidiki Peninsula (Fig. 1.1). However, since the Serbo–Macedonian Massif of Serbia and Macedonia has not experienced a severe Alpine metamorphic overprint (Schmid et al., 2008, and references therein), the integration of the two massifs is still debated. The Aegean Sea, a Miocene to recent back-arc basin, forms the southern limit of the Rhodope Massif, while to the east it disappears below the Eocene–Oligocene sedimentary cover of the Thrace basin (Gorur and Okay, 1996) (Fig. 1.1).

1.1.3 Brief evolutionary history of the Rhodope Massif

The Rhodope Massif lies tectonically within the hanging wall of the Aegean subduction zone (Fig. 1.2f–g) and its formation is linked to the opening of the Central Atlantic Ocean which caused convergence between the European continental margin and Africa (Ricou, 1994; Ricou et al., 1998). Convergence was initiated in the Mid Jurassic and caused closure of a basin located between the Moesian platform (Fig. 1.1 and Fig. 1.2a) to the north and

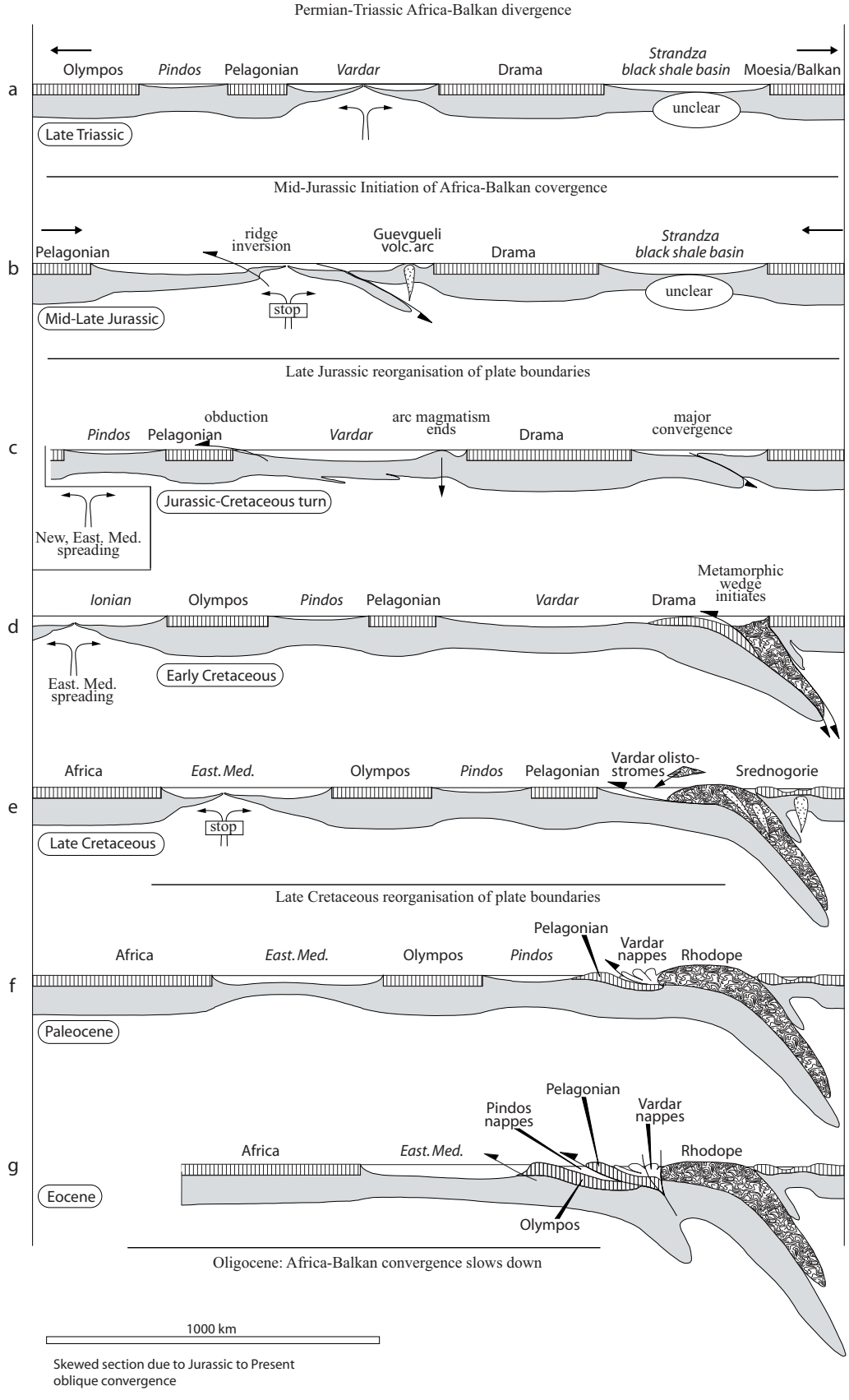

Figure 1.2: The Rhodope Mesozoic–Cenozoic history after Ricou et al. (1998).

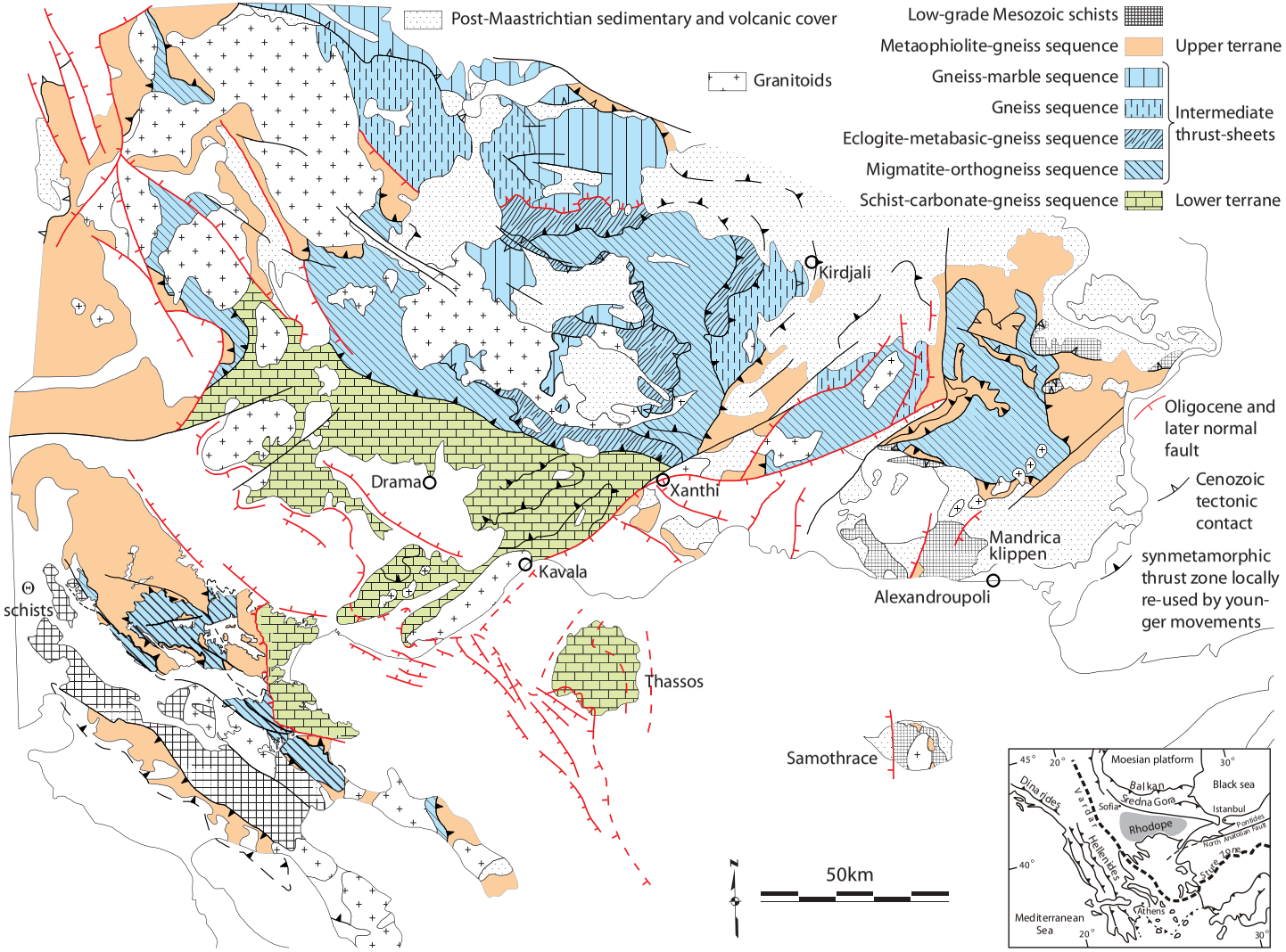

Figure 1.3: Sketch map of the Rhodope Massif after Burg et al. (1996a,b). Θ–schists represent the Thessaloniki–schists and carbonates.

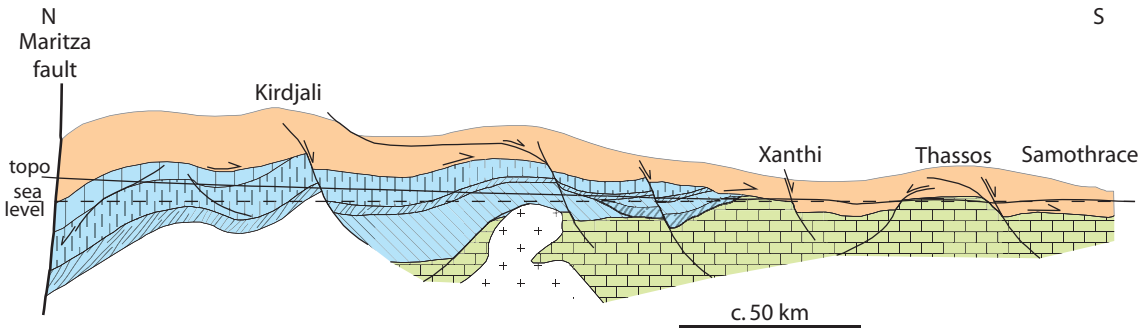

Figure 1.4: Unscaled simplified cross-section of the Rhodope massif to illustrate the crustal duplex defined by the upper and lower terranes (Burg et al., 1996a,b). Town names are indicative for the position of the profile in Fig. 1.3. Ornaments as in Fig. 1.3.

the Drama continental fragment to the south (Fig. 1.2a–c). This basin is of probably Triassic age and is possibly the source of the meta-ophiolites found between the Drama Window (equivalent to the lower terrane in Fig. 1.3) and the Balkan. Deep sea sediments originating from this basin include the Jurassic Strandza black schists (Fig. 1.2a,b), which were thrust northward over the Balkan units during the Senonian (∼93–65 Ma), and presumably also the Mandrica klippen on the high-grade metamorphic rocks of eastern Rhodope at Mandrica and near Alexandropolis (Fig. 1.3), which show southward shear criteria at the base (Ricou et al., 1998). In the Early Cretaceous, ongoing convergence/subduction caused collision of the Drama continental fragment with the Moesian platform (Fig. 1.2d). Consequently a stack of nappes with large-scale south-southwest-vergent thrusts was formed in the Rhodope region, building a crustal-scale duplex structure (Fig. 1.2d–e and Fig. 1.4). Subduction-/collision-related shortening and crustal thickening caused high-pressure (HP) regional metamorphism (e.g. Burg et al., 1996a; Liati et al., 2004) and locally even ultra-high-pressure metamorphism (e.g. Mposkos and Kostopoulos, 2001; Perraki et al., 2006).

After collision, the Rhodope Massif underwent extension during the Cenozoic accompanied by high temperature amphibolite facies metamorphism, migmatisation and magmatism (e.g. Dinter et al., 1995; Burg et al., 1996a; Ovtcharova et al., 2003b; Peytcheva et al., 2004). Extensional movements are indicated by low-angle detachment faults (Dinter and Royden, 1993; Sokoutis et al., 1993) and syntectonic, asymmetric graben depressions filled with Maastrichtian to Oligocene continental and marine sediments and locally abundant rhyolitic volcanic rocks (Dimov et al., 2000; Burchfiel et al., 2003; Marchev et al., 2005; Burchfiel et al., 2008). Extension might be the product of two discrete events – syn-orogenic or syn-thickening extension and post-orogenic, slab-rollback driven extension (e.g. Brun and Faccenna, 2008).

1.1.4 Internal structure of the Rhodope Massif

Cretaceous nappe stacking caused the formation of three regionally distinguishable terranes: the "lower terrane", the "intermediate thrust sheets" (or "intermediate terrane") and the "upper terrane" (Burg et al., 1996a,b) (Fig. 1.3 and Fig. 1.4).

The lower terrane (also Drama Window, Pangeon or Boz Dag unit) is composed from bottom to top of schists, carbonates, leucocratic ortho- and paragneisses and micaschists, amphibolites and thin intercalations of marbles. Intermediate-pressure metamorphism evolves from amphibolite to upper greenschist facies from south-west to north-east (Liati, 2005). The intermediate terrane is composed of several sequences, which are from bottom to top a migmatite-orthogneiss sequence, an eclogite-metabasic-gneiss sequence, a gneiss sequence exhibiting signs of partial melting and containing very minor marble and amphibolites and a gneiss-marble sequence. All thrust sheets of this terrane are predominately amphibolite facies metamorphosed, but relict eclogites can be found.

The upper terrane (including Parvenets, Northern Rhodope Unit, Krumovitsa, parts of the Vertiskos Unit and parts of the Kesebir–Kardamos and Biala–Reka–Kechros domes) is described as a mafic-ultramafic-gneiss sequence containing meta-ophiolites. The protolithic composition of these basic rocks corresponds to mid-ocean-ridge basalts (e.g. Liati et al., 1990) providing evidence for a suture within the thrust complex of the Rhodope Massif (Burg et al., 1996b). The metamorphic grade of the upper terrane is generally greenschist to lower amphibolite facies (Burg et al., 1996b; Krohe and Mposkos, 2002; Gerdjikov, 2004; Sarov et al., 2004).

1.1.5 Aegean extension

The Rhodope Massif is situated in the north of the Aegean region (Fig. 1.5) and strongly linked to its protracted extensional history (e.g. Jolivet et al., 2004; Brun and Faccenna, 2008). Extension in the Aegean region was initiated in the Rhodope Massif and "migrated" southward (Brun and Faccenna, 2008). The Aegean has been affected by syn- to post-orogenic extension that caused exhumation of high-grade metamorphic rocks and core complex formation (Lister et al., 1984; Gautier and Brun, 1994; Jolivet and Patriat, 1999). Syn-orogenic exhumation is assumed to have involved little or no overall horizontal stretching of the crust or lithosphere, and is ascribed to the effect of extrusion wedges or the influence of a subduction channel (e.g. Schmädicke and Will, 2003; Ring et al., 2007b,a). Post-orogenic extension, on the other hand, is ascribed to "whole lithosphere" stretching which involves large detachments (Lister et al., 1984; Gautier et al., 1993; Jolivet et al., 1994; Avigad et al., 1997; Zeffren et al., 2005; Brichau et al., 2007). The migration of the extensional regime is attributed to the successive accretion of several continental and oceanic blocks in the subduction zone and the related retreat of the trench (Fig. 1.2).

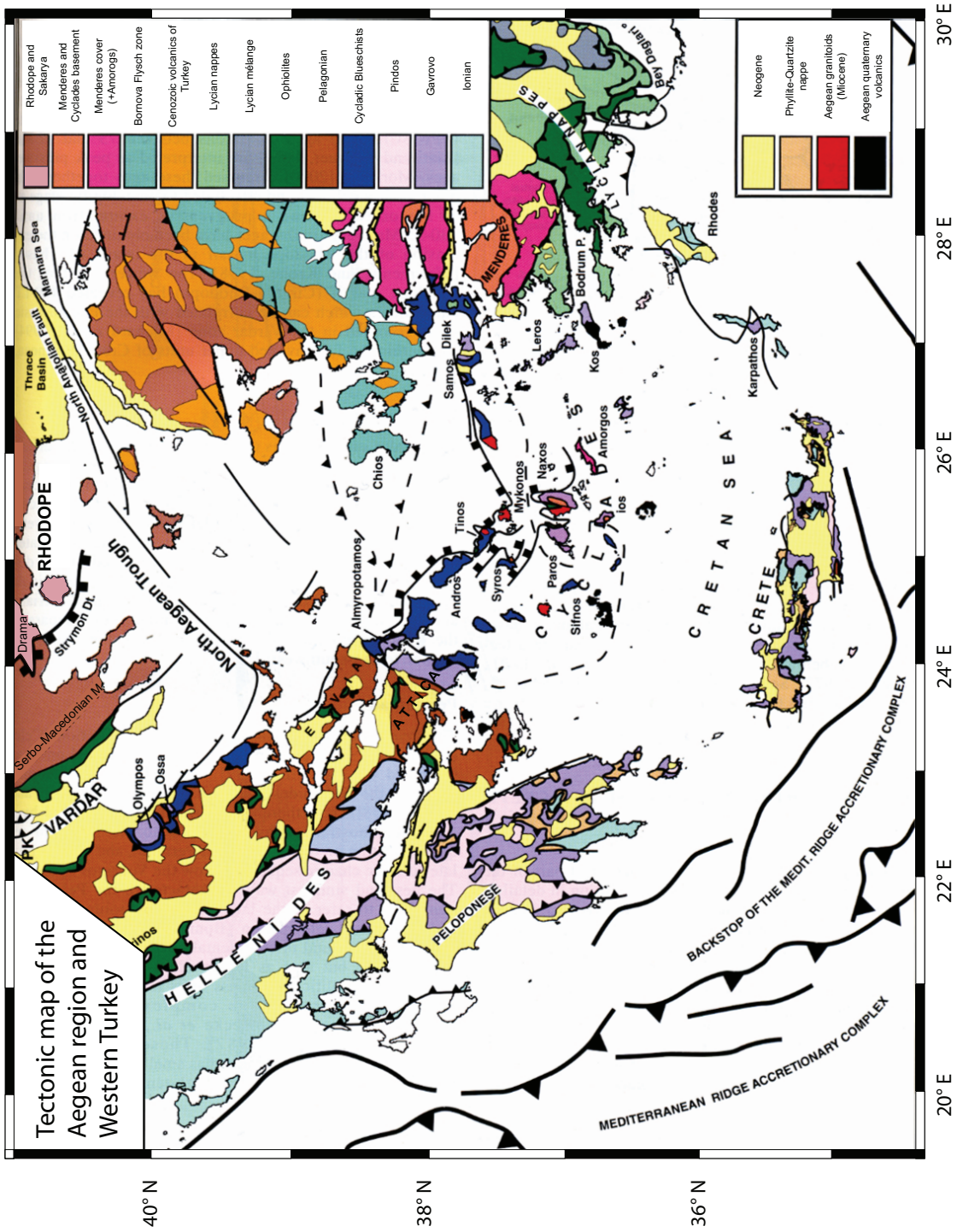

Figure 1.5: Tectonic map of the Aegean Region and Western Turkey (Jolivet et al., 2004).

Brun and Faccenna (2008) assume that (syn-orogenic) extension is triggered by the switch from subduction/accretion of a continental block to the subduction of an oceanic fragment. Easy subduction of dense oceanic crust might cause slab-rollback that creates the necessary space for the exhumation of the buoyant continental crust that was just previously deeply buried. The buoyancy force of the subducted continental crust is assumed to increase until the crust detaches from the down-going slab and then is exhumed at a rate that depends directly on the velocity of the trench retreat. The exhumed crust, weakened by the heat from asthenosphere material that flows into the opening mantle wedge, undergoes a second (post-orogenic) stage of exhumation at a lower rate and by formation of core complexes (Brun and Faccenna, 2008). Forster and Lister (2009) hold a similar view of the processes triggering extension, however, they decline the term "syn-orogenic" exhumation, because they assume only "whole lithosphere" stretching takes place during periods thought to be "syn-orogenic". They state that the Aegean lithosphere was subject to a sequence of "push-pull" cycles associated with individual accretion events; accretion of a continental fragment causes overall shortening and subsequent subduction of a oceanic basin overall extension in the overriding plate.

The Rhodope Massif underwent initial extension in the Palaeocene which is coeval with the accretion of the Pelagonian continental block, after the subduction of the Vardar Ocean (Ricou et al., 1998; van Hinsbergen et al., 2005; Bonev et al., 2006a) (Fig. 1.2f and Fig. 1.6). From Late Lutetian (∼42 Ma) until approximately the Eocene–Oligocene transition (35–33 Ma), subduction of the Pindos Ocean occurred (Ferrière et al., 2004). Accretion of the Pelagonian and Pindos blocks (Fig. 1.2f,g) caused the formation of the Cycladic Blueschists (CB) unit (Fig. 1.6), which today outcrops in the Cyclades along a belt that reaches from the southern parts of Evia Island and Attica to the Turkish mainland near Samos (Fig. 1.5) and denotes the area where finite extension is largest (Avigad and Garfunkel, 1989). Consistently, the crustal thickness has been decreased to 26 km in this belt while areas with less extension show a thickness of up to ∼45 km (Tirel et al., 2004). The lithostratigraphy of the CB is difficult to reconstruct as they are highly deformed and metamorphosed. The metamorphic event has been dated at ∼70 to 35 Ma where most ages cluster around 45 to 50 Ma (Jolivet et al., 2004, and references therein), hence approximately coeval with the transition from Pelagonian to Pindos subduction (Fig. 1.6). Consequently, the CB are attributed either to the basement of the Pindos basin or to the Pelagonian domain (Jolivet et al., 2004, and references therein). Core-complex-related (post-orogenic) exhumation in the Cyclades is now considered to have started at ∼35 Ma (Forster and Lister, 2009) with the formation of the low angle, top-to-the-south South Cyclades Shear Zone (SCSZ, Fig. 1.6) on the Island of Ios (Forster and Lister, 2009) (Fig. 1.5), and is coeval with the final subduction of the Pindos Ocean and core-complex-related extension in the Rhodope Massif (e.g. Brun and Sokoutis, 2007)

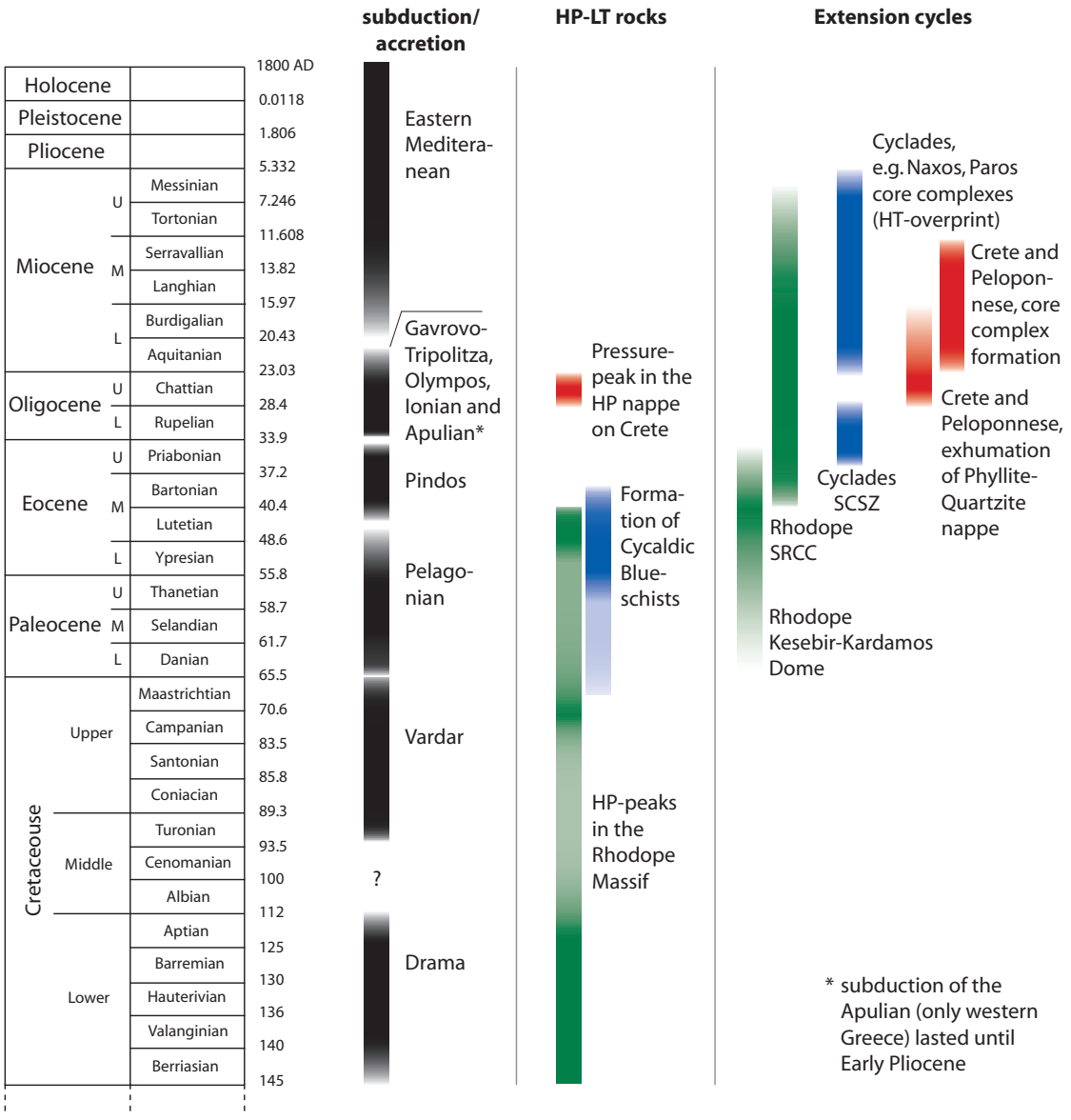

Figure 1.6: Summary of events in the Aegean region (Ricou et al., 1998; Liati and Gebauer, 1999; Jolivet et al., 2003, 2004; Ferrière et al., 2004; Liati, 2005; van Hinsbergen et al., 2005; Bonev et al., 2006a; Bauer et al., 2007; Brun and Faccenna, 2008; Forster and Lister, 2009).

(Fig 1.6). As already mentioned, during the Miocene (from 24 to 10 Ma) a second phase of extension caused the formation of core complexes in the Cyclades (e.g. Naxos, Paros) which show rather uniform top-to-the-north to top-to-the-northeast sense of shear (e.g. Lister et al., 1984; Wijbrans and McDougall, 1988; Gautier and Brun, 1994; Brichau et al., 2006). Deformation was simultaneous with a high-temperature amphibolite facies metamorphism which, e.g. on Naxos and Paros, overprinted the high-pressure rocks completely (Jansen and Schuiling, 1976; Buick and Holland, 1989; Buick, 1991). This second phase of core-complex-related extension in the Cyclades is coeval with subduction/accretion of a continental block composed of several entities called Gavrovo–Tripolitza, Olympos (Fig. 1.2), Ionian and Apulian (only western Greece). Its subduction started at the Eocene–Oligocene transition (∼33.9 Ma, Ferrière et al., 2004) and lasted until the Early Pliocene in western Greece where the Apulian platform underthrusted the Ionian unit, and until Early Miocene in eastern Greece where this platform did not exist (Underhill, 1989; Le Pichon et al., 2002) (Fig. 1.6). Subduction of these continental blocks caused the formation of HP rocks on Crete and the Peloponnese (Phyllite–Quartzite nappe, Fig. 1.5) (Bonneau, 1984). The pressure peak is dated at 25 Ma in Crete (Jolivet et al., 1996) (Fig. 1.6), which is in good agreement with the stratigraphic constraints on the age of thrusting (Jolivet et al., 2003). Exhumation of the Phyllite–Quartzite nappe occurred in the Middle Oligocene to Early Miocene, while thrusting was active deeper in the accretionary complex (Jolivet et al., 2003). On Crete and the Peloponese, metamorphic core complexes bounded by detachment faults (e.g. Crete Detachment and Khelmos Detachment) outcrop as well. These formed in the Early to Middle Miocene, 23–11 Ma (Fassoulas et al., 1994; Jolivet et al., 1994, 1996) (Fig. 1.6).

1.2 Aim of this study

The Rhodope Massif experienced, after a major period of Cretaceous compression and crustal thickening, a protracted extensional history and can be today divided into several subareas, each representing an extensional complex in itself with associated detachment faults (e.g. Dinter and Royden, 1993; Sokoutis et al., 1993; Burg et al., 1996b; Wawrzenitz and Krohe, 1998; Krohe and Mposkos, 2002; Sarov and Gerdjikov, 2002; Burchfiel et al., 2003; Kaiser Rohrmeier, 2005; Bonev et al., 2006a). The relative age and significance of the different detachments, along which extension was accommodated and high-grade metamorphic rocks were exhumed, is still not fully understood, despite an increasing number of studies. The timing of these events is also important as they are a link to the better understanding of the extensional history of the whole Aegean region; extension in the Aegean initiated in the Rhodope Massif (or even the Srenda Gnora) before migrating southward.

Abundant data are available regarding the tectonothermal events that have shaped the

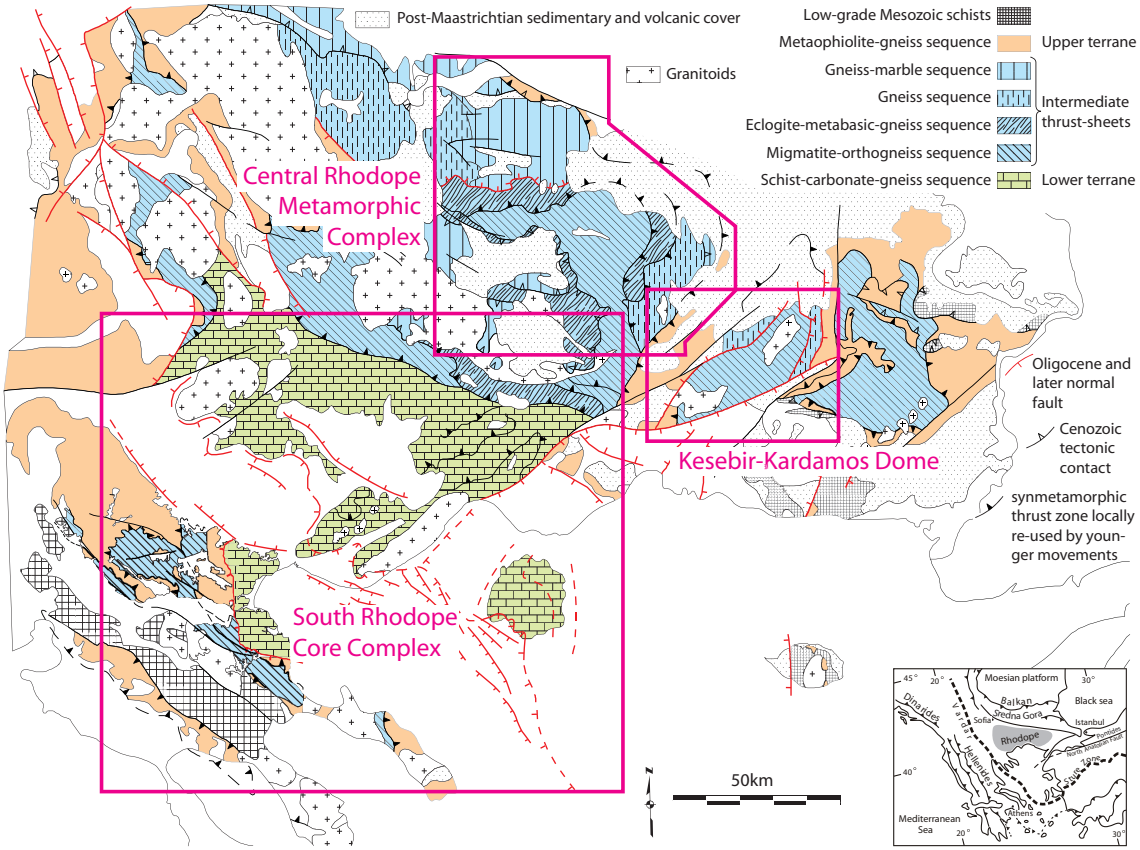

Figure 1.7: Sketch map of the Rhodope Massif after Burg et al. (1996a,b). The red rectangles indicate the three subareas that will be discussed separately in the following chapters 2 to 4.

Rhodope Massif at temperatures above 300°C, i.e. to within 10–15 km depth, but lower temperature thermochronological data are almost non-existent (Harre et al., 1968; Liati, 1986; Arnaudov et al., 1989, 1990a,b; Del Moro et al., 1990; Dinter et al., 1995; Kyriakopoulos et al., 1996; Hejl et al., 1998; Wawrzenitz and Krohe, 1998; Liati and Gebauer, 1999; Arkadakskiy et al., 2000; Krohe and Mposkos, 2002; Ovtcharova et al., 2002, 2003b, 2004; Peytcheva et al., 2004; Kaiser Rohrmeier, 2005; Liati, 2005). Accordingly, the chronometers employed in this thesis are fission-track analyses on apatite, zircon and titanite, as well as the (U-Th)/He method on apatite. With published higher chronometer ages as a working basis and structural as well as sedimentary literature data it is possible to reconstruct the Cenozoic evolution of important parts of the Rhodope Massif.

Three subareas of the Rhodope Massif have been analysed and will be discussed in this thesis: the South Rhodope Core Complex in northern Greece, the Central Rhodope Metamorphic Complex in southern Bulgaria and the Kesebir–Kardamos Dome which straddles the Greek–Bulgarian border (Fig. 1.7).

1.3 Outline of the thesis

Following this introduction, chapter 2 focuses on the South Rhodope Core Complex, which is one of the best studied core complexes within the Rhodope Massif. The combination and interpretation of fission-track and (U-Th)/He data obtained during this research work with previously published high temperature geochronological ages leads to a model for the Cenozoic evolution of the South Rhodope Core Complex.

Chapter 3 is dedicated to the Central Rhodope Metamorphic Complex. Fission-track and (U-Th)/He data obtained across several important shear zones are discussed and interpreted together with published high temperature geochronological data and structural and sedimentary findings. This integrated information results in a model for the Cenozoic evolution of the Central Rhodope Metamorphic Complex.

Chapter 4 discusses the Kesebir–Kardamos Dome. A review of important metamorphic events in this area and of previously published high temperature geochronometer ages is presented. The discussion and interpretation of the new fission-track and (U-Th)/He ages focuses on the Tokatcha Detachment, on the northern flank of the dome.

Chapter 5 combines the results presented in chapters 2 – 4 and gives a general conclusion in the broader context of the Aegean subduction zones. This is followed by a brief outlook describing open questions for future research in the study area.

The methods employed in this thesis are described in the appendices. Appendix I introduces the fission-track method whilst appendix II deals with the (U-Th)/He method. Brief technical introductions are also given as appendices to chapter 2 and 3. Appendix III contains all fission-track grain-age data and appendix IV the confined track length data.

Chapter 2

Low-temperature thermal evolution of the Southern Rhodope Core Complex (Northern Greece) during the Cenozoic

[1]

Abstract

The South Rhodope Core Complex (SRCC) of northern Greece is probably the most studied metamorphic core complex of the Rhodope Massif. We applied the fission-track method on apatite and zircon and the (U-Th)/He method on apatite in order to unravel its low temperature thermal history. Cooling/exhumation of high-grade metamorphic rocks occurred along two major detachments. The Kerdilion Detachment, in the SE of the core complex, was active from the Early Eocene (about 40 Ma) until about 26 Ma. After a possibly short period of quiescence, cooling and exhumation became focused along the Strymon Valley Detachment, in the center of the SRCC, from at least 20 Ma until about 8 Ma. After this protracted history of detachment faulting, the SRCC underwent minor extension along high-angle normal faults such as Strymon 2, a range of faults bounding the offshore Orfanos Basin, and the Xanthi Fault.

The apparent period of quiescence bridging the activity of the Kerdillion and Strymon Valley Detachments suggests a change in the thermo-mechanical conditions of extension in

[1]To be submitted to an international journal as: Wüthrich E., Seward D., Kounov A., Stockli D. and Burg J-P., Cenozoic thermal evolution of the Central Rhodope Metamorphic Complex, Southern Bulgaria

the SRCC, perhaps a switch from syn-orogenic extension of the Rhodope continental crust to post-orogenic, slab-rollback generated extension as in the Aegean.

2.1 Introduction

Cenozoic extension, in the southern region of the Balkan Peninsula and particularly in the Rhodope Massif (Fig. 2.1, inset), has been the focus of interest during the last two decades (e.g. Dinter and Royden, 1993; Sokoutis et al., 1993; Burg et al., 1995, 1996b; Dinter, 1998; Ricou et al., 1998; Krohe and Mposkos, 2002; Kounov et al., 2004; Brun and Sokoutis, 2007). Both structural and geochronological studies have confirmed that the Rhodope crystalline terrain includes deeply denuded Cenozoic metamorphic core complexes (e.g. Krohe and Mposkos, 2002; Bonev et al., 2006a; Brun and Sokoutis, 2007). These complexes were formed during a period of substantial crustal extension that followed Cretaceous subduction/collision with associated crustal thickening. Recent studies, based on geochronological data and detailed structural analysis, have shown that the extension in the Rhodope started during middle Eocene times (Burchfiel et al., 2003; Kounov et al., 2004; Brun and Sokoutis, 2007) some 5 to 10 Ma earlier than in the Cyclades (Forster and Lister, 2009).

The Southern Rhodope Core Complex (SRCC, Brun and Sokoutis, 2007) (Fig. 2.1) is one of the most extensively studied Rhodope core complexes. Structural and geochronological data show that the rocks of this complex have experienced large-scale syn-metamorphic extension since the Middle Eocene. However, the relative age and significance of the different low-angle normal faults along which extension was accommodated is still controversial. In particular, the south-western boundary of the SRCC has been variously placed either along the Strymon Valley Detachment (Dinter and Royden, 1993; Sokoutis et al., 1993) or the Kerdilion Detachment (Brun and Sokoutis, 2007) (Fig. 2.1).

In order to understand the relevance of each of the faults over time and the associated unroofing of the metamorphic core, we have applied fission-track analyses on zircon and apatite as well as (U-Th)/He analyses on apatite. These methods are suitable for revealing the timing of tectonothermal events that have shaped the SRCC at temperatures between ∼300 and ∼60°C, approximately corresponding to the field of brittle deformation. The results have allowed us to reconstruct the differential movements of individual blocks bounded by normal faults and to propose a new model for the Cenozoic evolution of the SRCC.

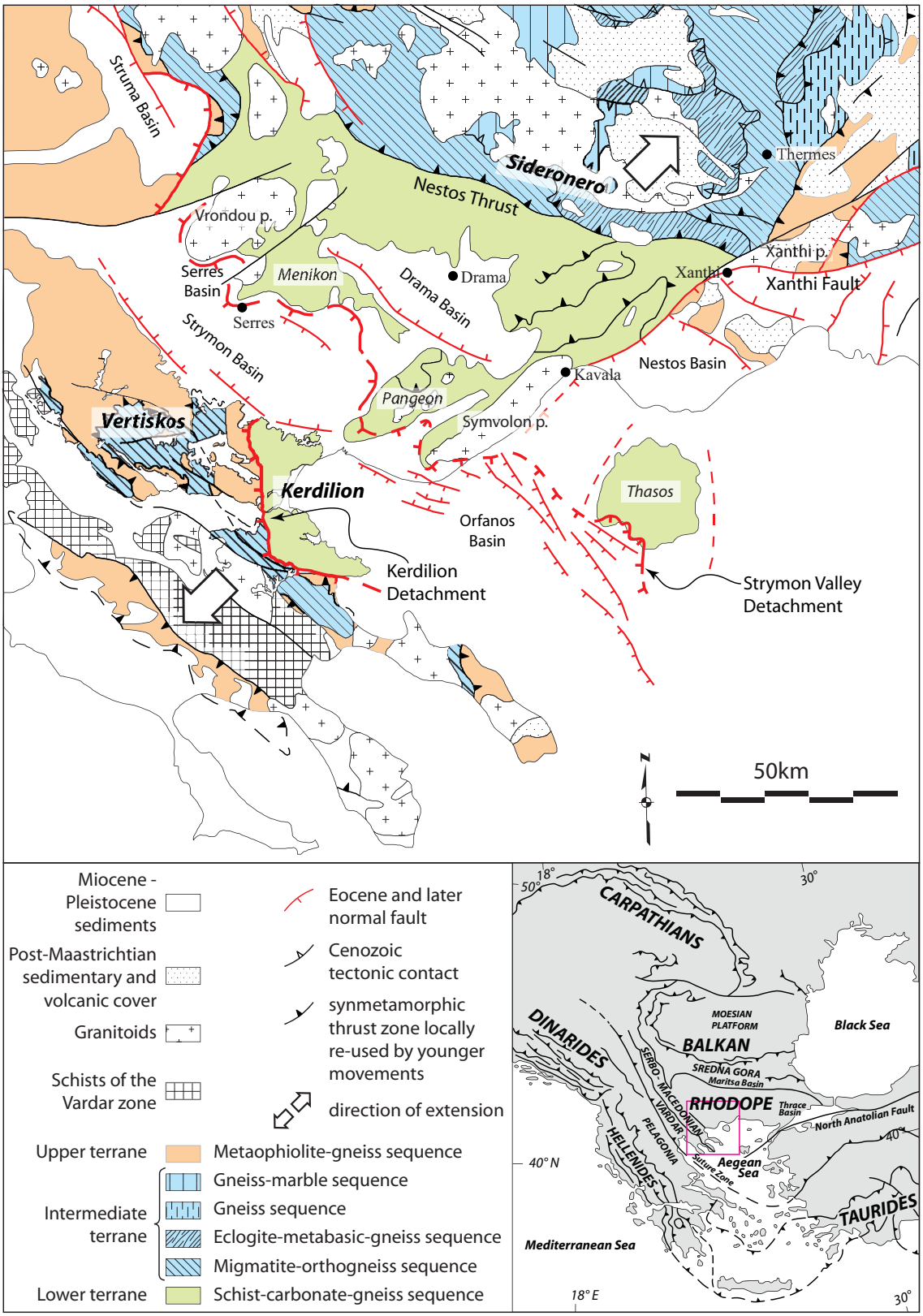

Figure 2.1: Geological map of the South Rhodope Core Complex (SRCC) after Burg et al. (1996b), Dinter and Royden (1993), Wawrzenitz and Krohe (1998) and Sokoutis et al. (1993). Vertiskos, Kerdilion and Sideronero are names of tectonic units; Menikon, Pangeon and Thasos are geographic notations; abbreviation p. stands for pluton. Inset: Location of the SRCC within the Balkan Peninsula.

2.2 Geological setting

2.2.1 The Rhodope Massif

The Rhodope Massif is located in southern Bulgaria and northern Greece. It is separated towards the north from the Sredna Gora volcanic arc by the Maritsa fault zone which is largely covered by the Neogene deposits of the Maritsa Basin (Fig. 2.1, inset). The south-western border of the Rhodope Massif is, depending on the author, the Vardar suture zone or the Serbo–Macedonian Massif (SMM). Based on similarities in metamorphic grade and structural style, the Rhodope and the SMM are often viewed as a single tectonic element (e.g. Burg et al., 1995; Ricou et al., 1998). To the east, the Rhodope Massif disappears below the Neogene sedimentary cover of the Thrace Basin (Gorur and Okay, 1996) and to the south below the Miocene to recent sediments of Aegean Sea (Fig. 2.1, inset).

The Rhodope Massif is composed of high-grade metamorphic and igneous rocks (e.g. Burg et al., 1990; Mposkos and Krohe, 2000; Ovtcharova et al., 2003b; Liati, 2005) forming a stack of large scale, south-vergent nappes (Burg et al., 1990, 1996b). These were formed during Mid Jurassic to Cretaceous convergence in the hanging wall of the subduction zone between Africa and Europe and underwent subsequent extension in Palaeogene and Neogene times (Dinter and Royden, 1993; Sokoutis et al., 1993; Krohe and Mposkos, 2002).

2.2.2 The Southern Rhodope Core Complex

The SRCC is located in the south-western part of the Rhodope Massif. It is composed of three main units, the upper, intermediate and the lower Rhodopean terranes (Burg et al., 1996b,a) (Fig. 2.1). The core itself, also called the Drama Window (Burg et al., 1996b), consists of rocks of the lower terrane overlain in the north by units of the intermediate terrane, termed in this region the Sideronero or West Thracian gneiss complex (e.g. Dinter et al., 1995; Krohe and Mposkos, 2002). The Drama Window and the Sideronero complex are separated by the Nestos Thrust (Fig. 2.1). In the southwest, the Drama Window is overlain along the Kerdilion Detachment by rocks of the intermediate and upper terrane, also known as Vertiskos Unit (Kockel et al., 1971). The rocks of the Drama Window, which outcrop between the Kerdilion Detachment and the ductile-to-brittle Strymon Valley Detachment (Dinter and Royden, 1993; Sokoutis et al., 1993) (Fig. 2.1), are additionally called the Kerdilion Unit (Kockel et al., 1971). The Vertiskos and the Kerdilion Units together constitute the southern extension of the SMM (Kockel et al., 1971).

The Drama Window consists mostly of massive marbles intercalated with amphibolite and metapelite layers bearing upper greenschist facies mineral assemblages (e.g. Dinter et al., 1995). The time of the greenschist facies metamorphic event has not been reported. In the Kerdilion Unit and on Thasos (Fig. 2.1), also rocks bearing amphibolite facies are outcropping (Brun and Sokoutis, 2007).

The Sideronero complex comprises various gneisses reaching in general amphibolite and locally granulite facies metamorphic grade. Some basic lithologies have preserved relics of a previous eclogite facies (Liati, 1986; Mposkos, 1989; Liati and Seidel, 1996) which is variably dated on zircon minerals (U-Pb SHRIMP) at ∼145 Ma in the area to the north of Xanthi (Liati and Gebauer, 2001; Liati, 2005), 51 Ma to the north of Drama (Liati, 2005) and ∼42 Ma near Thermes (Liati and Gebauer, 1999; Liati et al., 2004) (Fig. 2.2).

The Vertiskos Unit is composed of schists, gneisses, amphibolites and subordinate ultrabasites (Burg et al., 1995). The rocks reached upper greenschist to lower amphibolite facies, dated generally between ∼140 and 80 Ma (Papadopoulos and Kilias, 1985).

Parts of the SRCC have suffered a high temperature stage leading to partial melting. Migmatites have been found on Thasos, in the Kerdilion Unit and in the Sideronero complex (e.g. Liati, 2005; Brun and Sokoutis, 2007). In the Sideronero complex, north of Drama and near Thermes, dated zircons from leucosomes yielded partial melting ages of 39 Ma and 40 Ma (Liati and Gebauer, 1999; Liati, 2005) (Fig. 2.2).

Several plutons have intruded the SRCC, the main of which are the Vrondou, Xanthi and Symvolon (or Kavala) granitoids (Fig. 2.1). The Xanthi pluton was emplaced between 34 and 30 Ma (Liati, 1986) and seals the Nestos thrust to its east (Liati, 1986; Dinter, 1998). The Vrondou pluton, generally undeformed but showing mylonitic deformation in its western part, may have been emplaced in earliest Miocene (Kaufman, 1995) whereas the eastern undeformed section is assumed to have intruded contemporaneously with the Xanthi pluton (Dinter et al., 1995). K-Ar hornblende ages indicate minimum values for the emplacement of the eastern Vrondou between 33 ± 2 and 29 ± 1 Ma (Marakis, 1969) while dated deformational structures in the surrounding rocks constrain the maximum emplacement age to 36 Ma (Dinter, 1994). The Symvolon pluton is strongly mylonitic (e.g. Kokkinakis, 1979). Its intrusion age, based on U-Pb in titanite, is 21–22 Ma (Dinter et al., 1995) (Fig. 2.2). This age is very similar to the Rb-Sr muscovite ages of the host rock of 18–23 Ma (Del Moro et al., 1990) (Fig. 2.2) implying rapid cooling following intrusion.

Generally, extension in the SRCC is thought to have occurred from Early Miocene until Late Pliocene (Dinter and Royden, 1993; Sokoutis et al., 1993; Wawrzenitz and Krohe, 1998). However, some early geochronological data (e.g. Harre et al., 1968) point to an initiation of the extension possibly already in the Middle Eocene (Fig. 2.2, see the ages in the Kerdilion Unit).

The major detachment fault responsible for the exhumation of the SRCC is still not well identified. Earlier suggestions (Dinter and Royden, 1993; Sokoutis et al., 1993; Wawrzenitz and Krohe, 1998) assigned the Strymon Valley Detachment as the main structure. More recently, Brun and Sokoutis (2007) suggested that the Kerdilion Detachment was responsible for the major exhumation in the SRCC.

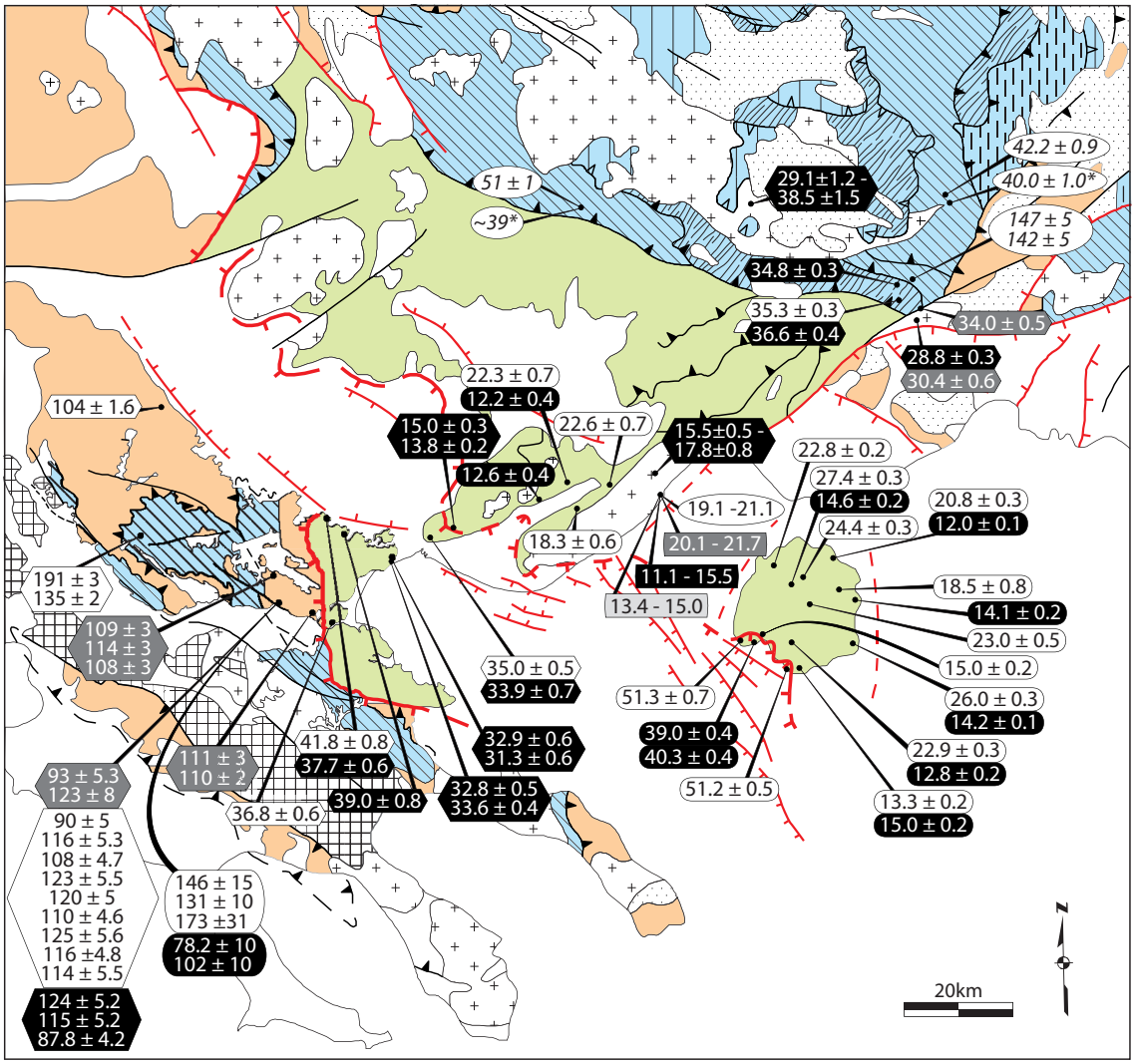

K-Ar ages (Ma)		*^{40}Ar/^{39}Ar ages (Ma)*		*Rb-Sr ages (Ma)*		*U-Pb ages (Ma)*	
78 ± 2	hornblende	20.1 - 21.7	hornblende	51.2 ± 0.5	muscovite	19.1 -21.1	titanite
104 ± 1.6	muscovite	11.1 - 15.5	biotite	14.1 ± 0.2	biotite	*42.2 ± 0.9*	zircon SHRIMP
39.0 ± 0.8	biotite	13.4 - 15.0	K-feldspar			*	partial melting
Papadopoulos and Kilias 1985 Harre et al. 1968 Liati 1986		Dinter et al. 1995		Papadopoulos and Kilias 1985 Del Moro et al. 1990 Wawrzenitz and Krohe 1998		Dinter et al. 1995 Liati and Gebauer 1999 Liati 2005	

Figure 2.2: Geological map of the SRCC (map key see Fig. 2.1) with published geochronological data. Closure temperatures for the listed chronometers are: 500 ± 50°C for K-Ar and ^{40}Ar/^{39}Ar on hornblende (Harrison, 1981), 350 ± 50°C for K-Ar and ^{40}Ar/^{39}Ar on muscovite (Hames and Bowring, 1994), 300 ± 50°C for K-Ar and ^{40}Ar/^{39}Ar on biotite (Harrison et al., 1985), 150 − 350°C for K-Ar and ^{40}Ar/^{39}Ar on K–feldspar, 500 ± 50°C and 300 ± 50°C for Rb-Sr on muscovite and biotite respectively (Dickin, 1995, and references therein), 550 − 600°C for U-Pb on titanite and > 700°C for U-Pb on zircon.

2.3 Results

The fission-track (FT) method on apatite and zircon and the (U-Th)/He method on apatite were applied to various rocks sampled from both the hanging and the footwall units of the SRCC. The analytical procedures are described in the appendix to this chapter. FT ages are reported as central ages with a 2σ error (Galbraith and Laslett, 1993). (U-Th)/He ages are reported as average values calculated from single grain ages ± 2 standard errors of the mean (SEM).

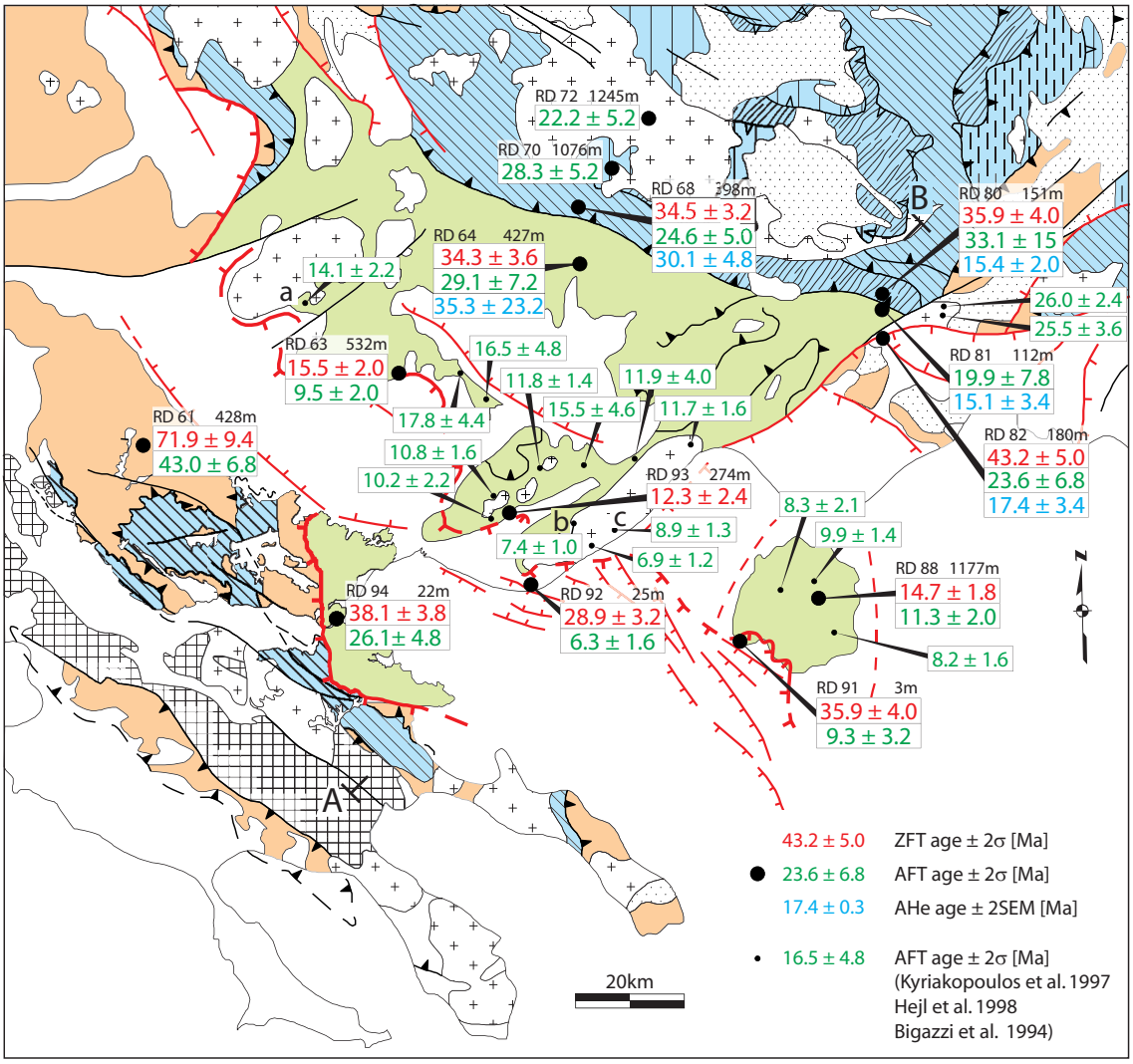

Figure 2.3: Geological map of the SRCC (map key see Fig. 2.1) with results of apatite and zircon fission-track (AFT and ZFT) and apatite (U-Th)/He (AHe) analyses. FT ages are reported as central ages (Galbraith and Laslett, 1993) $\pm$ 2σ error. For the AHe ages a mean value over the single grain ages ± 2 standard error of the mean (SEM) is given. For calculation of SEM see table 2.2. Letters a, b and c indicate the sample locations of the track-length models by Hejl et al. (1998), which are shown in Fig. 2.7.

2.3.1 Zircon fission-track ages

Eleven samples yielded zircon fission-track (ZFT) ages ranging from 12.3 ± 2.4 Ma to 71.9 ± 9.4 Ma (Tab. 2.1, Fig. 2.3). The youngest ages occur in the footwall of the Strymon Valley Detachment close to its trace, 15.5 ± 2.0, 14.7 ± 1.8 and 12.3 ± 2.4 Ma (RD63, 88, 93). In the Kerdilion Unit (hanging wall of the Strymon Valley Detachment) and in the footwall of the Strymon Valley Detachment far from its trace (close to the Nestos Thrust) ages are similar ranging between 34 and 38 Ma. The oldest samples were obtained from the Vertiskos Unit in the hanging wall of the Kerdilion Detachment (71.9 ± 9.4, RD61) and from the upper terrane in the hanging wall of the Xanthi Fault (43.2 ± 5.0, RD82) (Fig. 2.1).

2.3.2 Apatite fission track ages and track length modelling

Thirteen apatite fission-track (AFT) ages range from 6.3 ± 1.6 Ma to 43.0 ± 6.8 Ma (Tab. 2.1, Fig. 2.3). As with the ZFT ages, the youngest AFT ages of 9.5 ± 2.0 Ma (RD63) and 11.3 ± 2.0 (RD88) occur in the footwall of the Strymon Valley Detachment close to its trace. However, in addition, two exceptionally young ages of 9.3 ± 3.2 Ma (RD91) and 6.3 ± 1.6 Ma (RD92) also occur in the hanging wall of the Strymon Valley Detachment. Samples with intermediate ages of 20 to 30 Ma are obtained from the Kerdilion Unit, close to the Nestos Thrust and from the hanging wall of the Xanthi Fault. The oldest AFT age, like its zircon equivalent, is found in the Vertiskos Unit (43.0 ± 6.8, RD61). The regional FT age pattern is emphasised by the cross section A–B (Fig. 2.4) whereby regardless of altitude, the youngest ages occur in the centre of the SRCC.

For one sample (RD64) track-lengths have been measured allowing for AFT modelling (Fig. 2.5). Time(t)–temperature(T) paths were derived using the HeFTy program of Ketcham (2005). The model paths were forced to pass through certain constraints (t–T boxes), where a large box was chosen, in order to give the path as much freedom as possible to move through the partial annealing zone, and a small box corresponding to the ZFT age and the zircon closure temperature. The modelling reveals two distinct cooling events, a first one between ∼40 and ∼30 Ma from 300 to 100°C and a second between ∼25 and ∼20 Ma from 80 to <60°C. The two events are separated by a period of relative quiescence during which the sample was at temperatures between 110° to 80°C.

Table 2.1: Apatite (A) and zircon (Z) fission-track results. All ages are central ages (Galbraith and Laslett, 1993). ρd, ρs and ρi represent the standard, spontaneous and induced tracks densities, respectively. P(χ^2) is the probability of failing the χ^2 test. U represents the approximate uranium content. Dpar denotes the mean track pit diameter of a sample and MTL the c-axis corrected mean track length.

Sample number	**Grid reference**	**Alti. [m]**	**Min.**	**Age [Ma]**	**$\pm 2\sigma$ [Ma]**	**No. of grains**	**ρd [$10^5 cm^{-2}$] (counted)**	**ρs [$10^5 cm^{-2}$] (counted)**	**ρi [$10^5 cm^{-2}$] (counted)**	**P(χ^2) [%]**	**U [ppm]**	**Dpar [μm]**	**MTL [μm]**
RD 61	N 40° 58' 42.9"	428	Z	**71.9**	**9.4**	20	4.6	60.7	25.6	80.9	186		
	E 23° 11' 09.7"						(2947)	(940)	(397)				
			A	**43.0**	**6.8**	20	13.1	4.3	27.1	23.2	25	1.46	
							(4631)	(233)	(1470)				
RD 63	N 41° 05' 11.3"	532	Z	**15.5**	**2.0**	20	4.5	17.7	34.9	10.9	271		
	E 23° 49' 08.1"						(2947)	(612)	(1206)				
			A	**9.5**	**2.0**	21	12.9	1.6	44.7	84.6	45	1.54	
							(4631)	(111)	(3114)				
RD 64	N 41° 15' 50.2"	427	Z	**34.3**	**3.6**	20	4.4	75.4	65.0	4.0	467		
	E 24° 12' 05.2"						(3627)	(1675)	(1443)				
			A	**29.1**	**7.2**	20	13.7	2.2	21.6	83.0	18	1.57	14.73 ± 1.23
							(5073)	(79)	(770)				
RD 68	N 41° 21' 12.1"	398	Z	**34.5**	**3.2**	20	5.2	70.7	70.4	21.0	447		
	E 24° 12' 14.4"						(3627)	(1528)	(1523)				
			A	**24.6**	**5.0**	20	12.8	3.5	39.0	0.9	37	1.45	
							(7878)	(206)	(2306)				
RD 70	N 41° 25' 23.3"	1076	A	**28.3**	**5.2**	20	12.8	2.4	22.3	85.1	19	1.84	
	E 24° 16' 53.1"						(7878)	(154)	(1448)				
RD 72	N 41° 30' 09.4"	1245	A	**22.2**	**5.2**	20	10.4	1.6	15.7	42.4	19	1.26	
	E 24° 22' 36.4"						(4019)	(88)	(856)				
RD 80	N 41° 12' 27.0"	151	A	**33.1**	**15.2**	20	10.6	0.5	3.2	44.4	3	1.42	
	E 24° 51' 44.8"						(4019)	(23)	(154)				

Table 2.1: (continued)

Sample number	**Grid reference**	**Alti. [m]**	**Min.**	**Age [Ma]**	**$\pm 2\sigma$ [Ma]**	**No. of grains**	**ρd [$10^5 cm^{-2}$] (counted)**	**ρs [$10^5 cm^{-2}$] (counted)**	**ρi [$10^5 cm^{-2}$] (counted)**	**P(χ^2) [%]**	**U [ppm]**	**Dpar [μm]**	**MTL [μm]**
RD 81	N 41° 11' 11.0"	112	Z	**35.9**	**4.0**	20	4.9	23.6	21.4	61.5	137		
	E 24° 51' 42.0"						(3627)	(932)	(845)				
			A	**19.9**	**7.8**	20	10.9	0.5	6.2	98.1	8	1.65	
							(4019)	(30)	(340)				
RD 82	N 41° 08' 06.7"	180	Z	**43.2**	**5.0**	9	4.9	58.0	43.3	78.7	275		
	E 24° 51' 47.7"						(3627)	(851)	(636)				
			A	**23.6**	**6.8**	20	11.0	0.9	8.4	97.2	10	1.71	
							(4019)	(58)	(559)				
RD 88	N 40° 42' 13.1"	1177	Z	**14.7**	**1.8**	20	4.2	11.4	22.0	34.0	203		
	E 24° 42' 15.7"						(2947)	(550)	(1061)				
			A	**11.3**	**2.0**	20	11.4	2.6	54.4	60.6	53	1.52	
							(4631)	(150)	(3143)				
RD 91	N 40° 38' 11.0"	3	Z	**35.9**	**4.0**	21	4.8	37.6	33.4	0.4	243		
	E 24° 31' 25.0"						(3627)	(1858)	(1651)				
			A	**9.3**	**3.2**	20	11.1	0.8	19.0	91.5	20	2.12	
							(4019)	(38)	(937)				
RD 92	N 40° 44' 02.4"	25	Z	**28.9**	**3.2**	20	4.7	39.9	43.1	0.1	318		
	E 24° 05' 30.6"						(3627)	(1895)	(2048)				
			A	**6.3**	**1.6**	20	13.4	1.1	48.2	70.8	44	1.55	
							(5073)	(62)	(2737)				
RD 93	N 40° 50' 58.0"	274	Z	**12.3**	**2.4**	10	4.6	11.5	29.0	68.7	206		
	E 24° 03' 31.7"						(3627)	(166)	(418)				
RD 94	N 40° 40' 22.8"	22	Z	**38.1**	**3.8**	20	4.6	55.1	44.1	62.7	309		
	E 23° 39' 49.1"						(3627)	(1266)	(1014)				
			A	**26.1**	**4.8**	20	13.5	2.6	27.8	71.5	22	1.44	
							(5073)	(149)	(1603)				

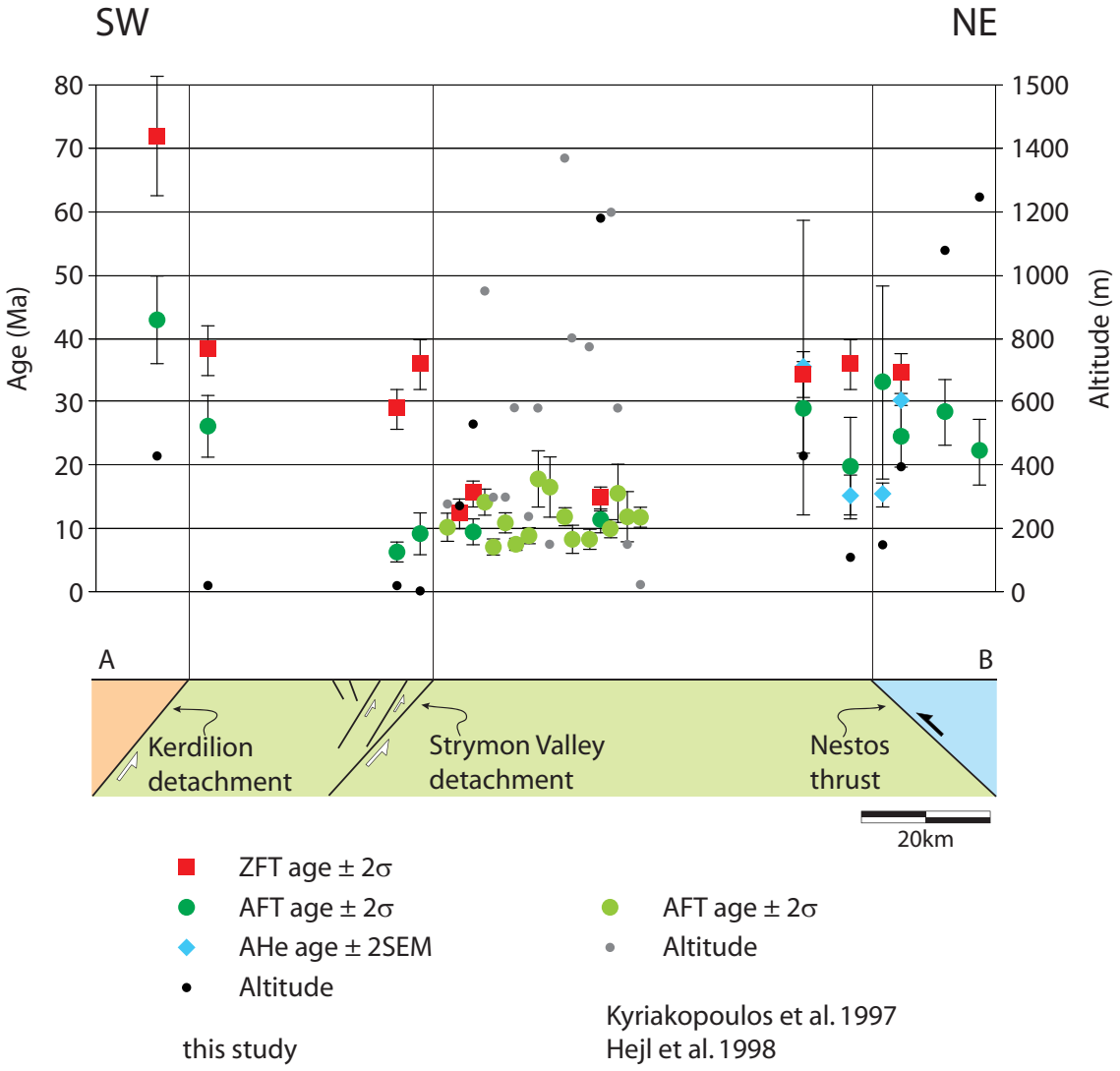

Figure 2.4: Zircon and apatite fission-track (ZFT and AFT) and apatite (U-Th)/He (AHe) ages projected onto a NW–SE oriented, schematic profile. Profile line A–B is indicated in Fig. 2.3.

2.3.3 Apatite (U-Th)/He ages

(U-Th)/He ages were determined on apatite grains from five sites along the Nestos Thrust (Tab. 2.2, Fig. 2.3). The two sample sites in the northwest of the Nestos Thrust (RD64, RD68) yield (U-Th)/He ages of 35.3 ± 23.2 and 30.1 ± 4.8 Ma that are identical within error to their fission-track ages. The three sample sites at the south-eastern edge of the Nestos Thrust and close to the Xanthi Fault yield much younger ages of ∼16 Ma. Sample RD82 (17.4 ± 3.4 Ma) collected from the hanging wall of the Xanthi Fault has a slightly older age than the two footwall samples RD80 and RD81 (15.4 ± 2.0 and 15.1 ± 3.4 Ma).

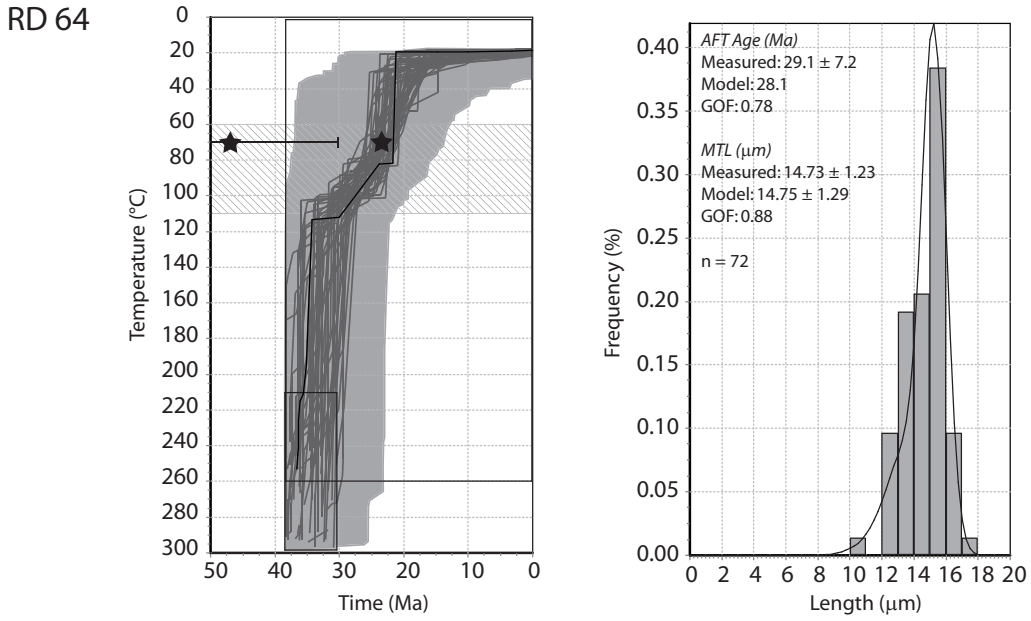

Figure 2.5: Inverse temperature–time model for sample RD64 and its track length histogram of corrected length for confined tracks. In the model: Back boxes show the given constraints to the model. The light gray field shows the envelop of possible acceptable fit-paths, while the dark gray lines are possible good fits and the black line the best fit. In order to determine the goodness of fit (GOF) the Kolmogorov–Smirnov statistical test was used. The apatite partial annealing zone is denoted as striated area. (110–60°C, Gleadow and Duddy, 1981). Black stars indicate the (U-Th)/He single grain ages. In the histogram: AFT Age – apatite fission track age, MLT – mean track length, n – number of measured confined track lengths. Indications about modelled parameters correspond to the best fitting path, and its track track-length distribution is shown by the black line.

Table 2.2: Apatite (U-Th)/He results. Ages are reported as single grain ages and their mean value. The error of the mean is given as 2SEM. SEM is calculated from the age data of the single analysis and the number of analysis (N) per sample (SEM = $\sigma/\sqrt{N}$). F_t is the alpha ejection correction factor (Farley et al., 1996; Farley, 2002). For grid references and sample elevations see Tab. 2.1.

Sample	**Grain**	**Age [Ma]**	**± [Ma]**	**U [ppm]**	**Th [ppm]**	**Sm [ppm]**	**Th/U**	**He [nmol/g]**	**mass [mg]**	F_t
RD64	RD64-2	46.9	16.6	0.16	1.91	0.41	12.16	0.11	3.20	0.69
	RD64-3	23.7	1.4	7.58	9.49	7.46	1.25	0.79	1.40	0.62
Mean Age ± 2SEM		**35.3**	**23.2**							
RD68	RD68-1	27.9	1.7	31.65	2.41	98.89	0.08	3.86	14.30	0.78
	RD68-2	27.6	1.7	30.71	3.20	112.62	0.10	3.39	5.00	0.70
	RD68-3	34.8	2.1	26.85	3.32	145.78	0.12	4.26	7.10	0.79
Mean Age ± 2SEM		**30.1**	**4.8**							
RD80	RD80-1	14.0	0.6	2.84	0.66	6.70	0.23	0.16	5.60	0.70
	RD80-2	14.9	0.9	2.26	0.31	8.19	0.14	0.15	5.40	0.76
	RD80-3	17.3	2.9	1.38	0.57	7.93	0.41	0.09	2.70	0.63
Mean Age ± 2SEM		**15.4**	**2.0**							
RD81	RD81-1	17.0	0.4	6.95	0.78	13.70	0.11	0.46	5.00	0.70
	RD81-2	16.7	0.2	8.51	1.05	11.75	0.12	0.61	10.90	0.76
	RD81-3	11.8	0.3	5.60	6.17	20.55	1.10	0.35	6.10	0.76
Mean Age ± 2SEM		**15.1**	**3.4**							
RD82	RD82-1	17.4	0.3	8.25	0.45	10.34	0.05	0.63	7.80	0.79
	RD82-2	14.4	0.3	5.11	0.47	8.96	0.09	0.33	9.60	0.80
	RD82-3	20.2	0.4	4.63	1.16	2.99	0.25	0.42	7.60	0.79
Mean Age ± 2SEM		**17.4**	**3.4**							

2.4 Interpretation and discussion

The new FT data combined with the previous analyses reveal a quite distinct pattern with respect to the Strymon Valley and Kerdilion Detachments (Fig. 2.3 and Fig. 2.4). The data are generally consistent with that expected from a core complex – older ages in the proposed hanging walls and younger in the footwalls.

In detail, the youngest zircon FT ages occur in the central part of the SRCC, mainly in the proximal footwall (within about 20 km) of the Strymon Valley Detachment (Fig. 2.3 and Fig. 2.4). Older ages were obtained for the lower and intermediate terranes outcropping in the northeast near the Nestos Thrust as well as for the Kerdilion Unit in the southwest, which forms the hanging wall of the Strymon Valley Detachment and the footwall of the Kerdilion Detachment. The oldest age of 72 Ma is in the Vertiskos Unit, the hanging wall of the Kerdilion Detachment. This age, however, is also at a higher altitude than other ages in its vicinity and may perhaps be partly a consequence of this position. However, the possible "jump" in zircon age is geographically consistent with the distribution of higher temperature chronometers (Fig. 2.2) and is thus considered real even if it may be exaggerated by its altitude. Thus, the "jump" in ages over the Kerdilion Detachment for the range of closure temperatures from about 450 to 300°C is clear, supporting the idea of this fault acting as a detachment from at least ∼40 Ma (muscovite K-Ar ages in the Kerdilion Unit, Harre et al., 1968) as proposed by Brun and Sokoutis (2007).

A very marked change in the zircon ages is evident across the Strymon Valley Detachment. Ages in the footwall are between 15 and 17 Ma while those in the hanging wall are 36 and 29 Ma. Across the Nestos Fault there is no change in ages and one concludes that the fault was closed by about 35 Ma. This suggestion is in agreement with the fact that the 34–30 Ma Xanthi pluton (Liati, 1986) seals the fault at its south-eastern tip.

AFT ages reveal a somewhat similar regional distribution with generally younger ages in the central core region. However, the ages from the immediate hanging wall of the Strymon Valley Detachment are similar to those in the proximal footwall (Fig. 2.3 and Fig. 2.4). The difference between the ages across the Kerdilion Detachment is less pronounced than that for the zircons and could be an effect of the altitude difference. Across the Strymon Valley Detachment, the AFT ages imply closure of this fault by about 9 to 6 Ma. The AFT ages confirm the closure of the Nestos Fault as already discussed above.

The apatite (U-Th)/He ages across the Nestos Fault confirm the closure already noted through the ZFT ages.

From a regional perspective, the data are consistent with that expected from a core complex but there is strong evidence that both faults, the Kerdilion and the Strymon Valley, were operating as detachments. With these new ages, in combination with previous published data, a new model for the Cenozoic thermotectonic evolution of the SRCC is

proposed (section 2.4.1, Fig. 2.6). In section 2.4.2 the (U-Th)/He ages, which are related to the final cooling, will be discussed separately.

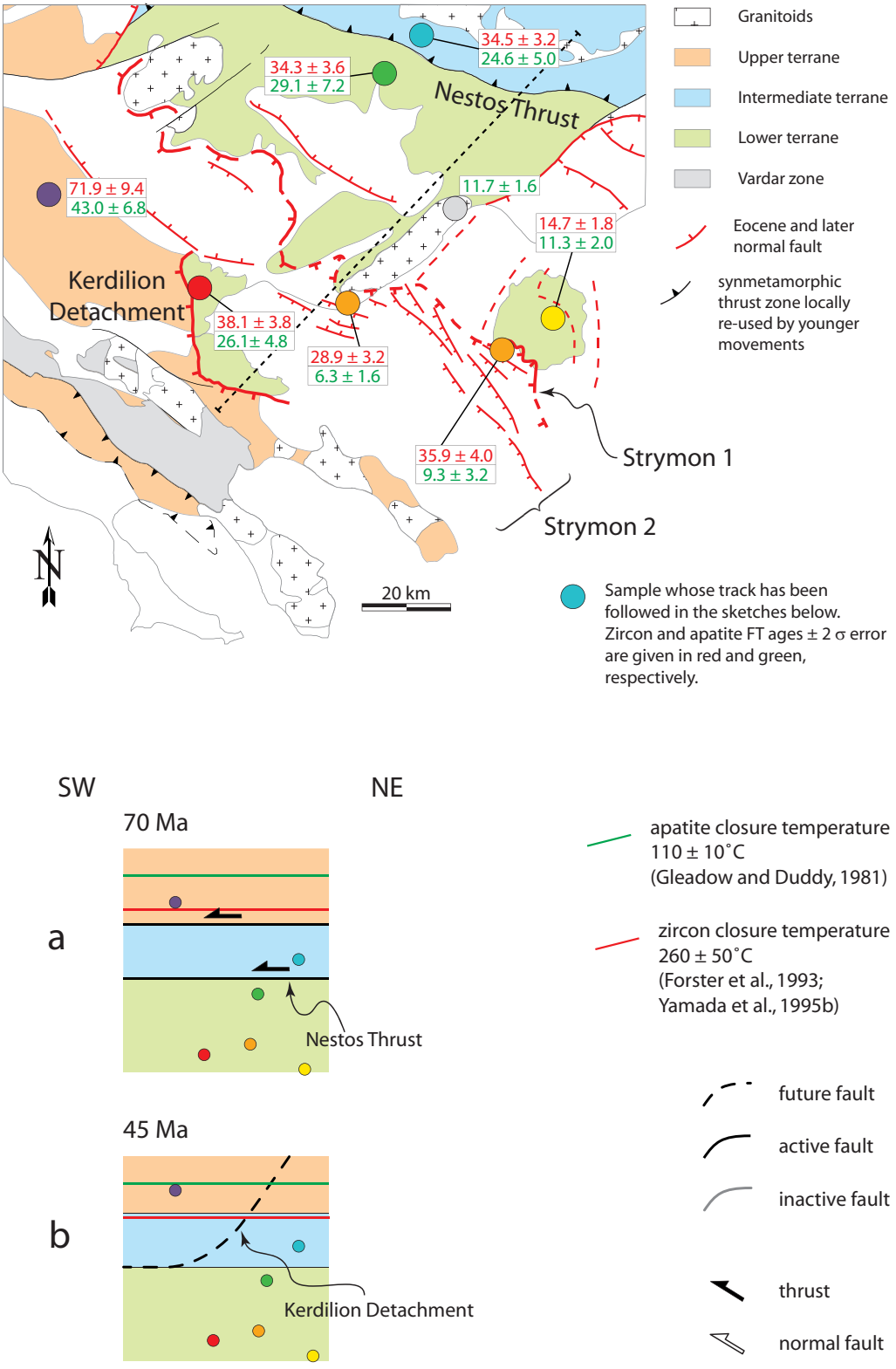

Figure 2.6: (continued on next page) Proposed sketch model for the evolution of the SRCC. For discussion see text.

Figure 2.6: (continued)

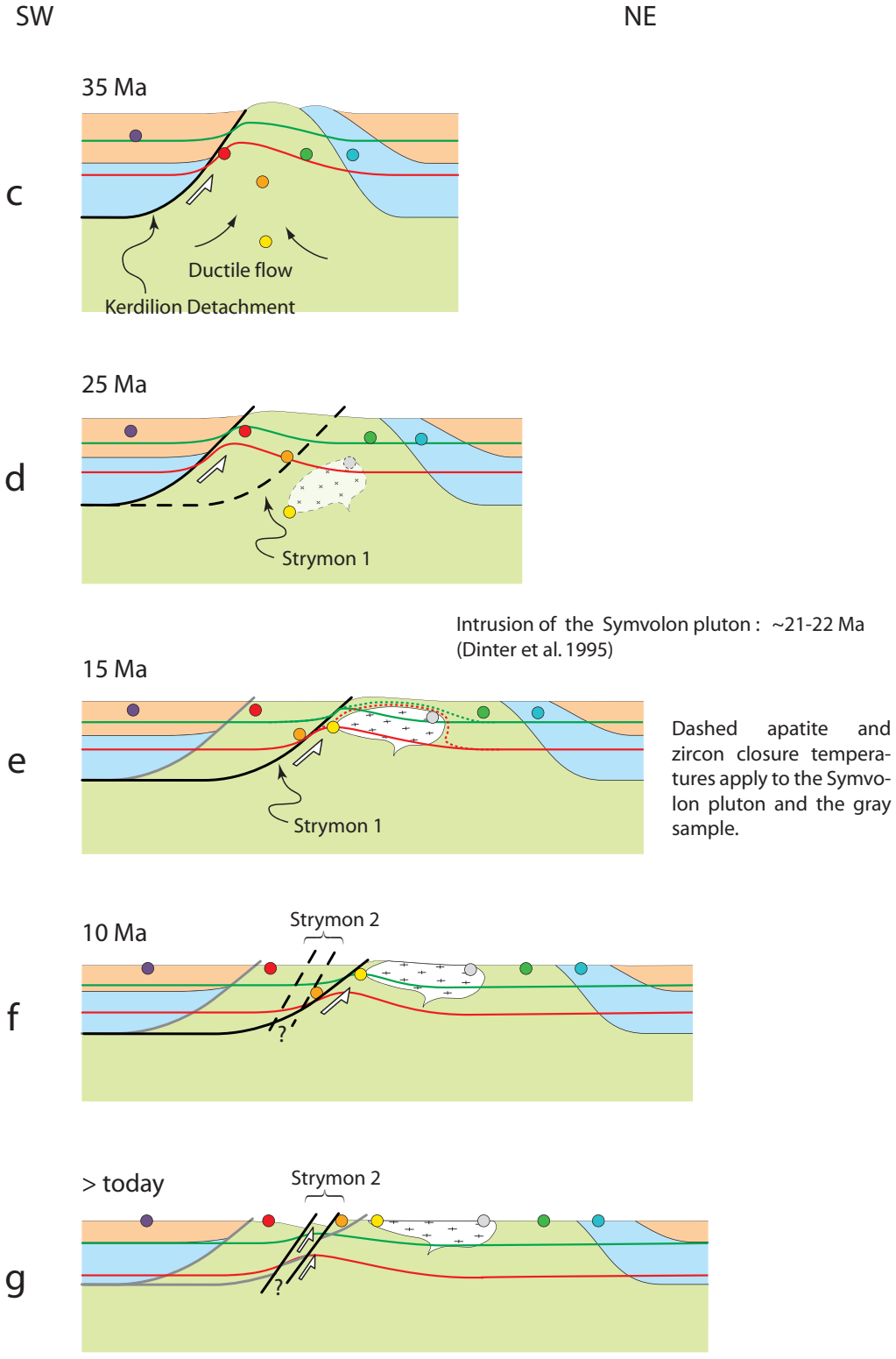

2.4.1 An evolutionary model of the Southern Rhodope Core Complex

Cretaceous collision and thrusting along the European margin led to crustal thickening in the Rhodope area (e.g. Burg et al., 1996b; Gautier et al., 1999). Extension in the SRCC most probably started in the Middle Eocene and was controlled by the Kerdilion Detachment (Fig. 2.6b) (Brun and Sokoutis, 2007). The exact onset of extension is difficult to determine, but the difference in thermochronological ages across this detachment, with ages between 30 and 42 Ma in the footwall (K-Ar on muscovite and biotite, Harre et al., 1968) and ∼80–190 Ma in the hanging wall (K-Ar on muscovite and biotite, Harre et al., 1968; Papadopoulos and Kilias, 1985) (Fig. 2.2), argues for an onset around 40 Ma (Brun and Sokoutis, 2007).

The track length model of sample RD64, north of Drama, shows two cooling events (Fig. 2.5), an earlier one between ∼40 and ∼30 Ma and a later one between ∼25 and ∼20 Ma. The first rapid cooling event coincides with the onset of extension and the development of the Kerdilion Detachment at around 40 Ma. The minimum duration of the extension along this detachment is constrained by the AFT ages in the Kerdilion Unit and in the area of the Nestos Thrust. Those samples most likely were cooled through the AFT closure temperature due to exhumation along the Kerdilion Detachment whose activity therefore continued until about 26 Ma (Fig. 2.6c,d).

According to Dinter and Royden (1993), Dinter et al. (1995) and Wawrzenitz and Krohe (1998) the Strymon Valley Detachment started to control exhumation at around 20 Ma, resulting in renewed rapid cooling inside the dome (Fig. 2.6e,f). Even though sample RD64 was in the first instance exhumed by the Kerdilion Detachment, its track-length model records the onset of this second cooling event and suggests that its timing might be closer to 25 Ma (Fig. 2.5). In the footwall close to the Strymon Valley Detachment, rapid cooling from about 300 to 110°C at about 17 to 7 Ma is seen from the zircon and apatite FT ages (Fig. 2.3 and Fig. 2.4), indicating that fault activity continued until the Late Tortonian. The timing of sedimentation in the area is compatible with these findings. Biostratigraphic ages on syn-detachment deposits on the hanging wall of the Strymon Valley Detachment are ∼9.8 Ma (rodent remains in non-marine clastic sequences north of Serres, Armour-Brown et al., 1977); deeper in the sequence, syn-detachment sediments also crop out in that area, but provide no fossils suitable for dating (Dinter and Royden, 1993). Probably correlative, early syn-detachment sediments in the Bulgarian branch of the Strymon Basin, the Struma Basin (Fig. 2.1), contain mammal fauna yielding a Middle Miocene age (Kojumdgieva et al., 1982), which would imply that syn-detachment sedimentation had commenced at least by ∼15 Ma (Dinter and Royden, 1993).

The apatite and zircon FT ages presented here suggest that the trace of the Strymon Valley Detachment (called Strymon 1 in Fig. 2.6) can be followed along the western contact of the Symvolon pluton and along the southern tip of Thasos Island as was already proposed

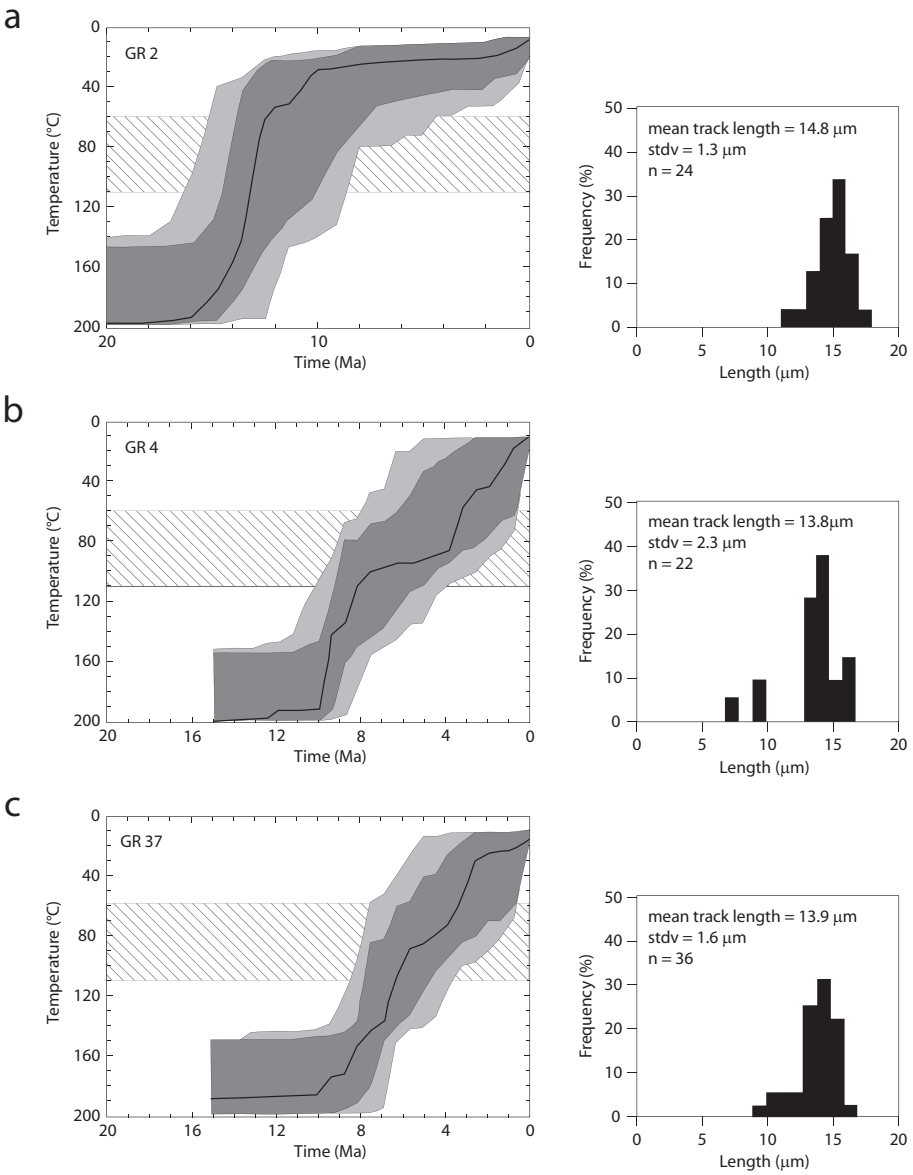

Figure 2.7: Monte Carlo inverse temperature-time models and the corresponding frequency distributions of confined spontaneous track lengths by Hejl et al. (1998). Sample locations are indicated on Fig. 2.3 with the corresponding letters a, b and c. In the model: The light and dark grey fields show the envelops of "acceptable fit" and "good fit" paths, respectively. The black line is the best fit. Goodness of fit is evaluated by a Kolmogorov–Smirnov test. The apatite partial annealing zone is denoted as a striated area. In the histogram: n corresponds to the number of measured confined track lengths.

by Dinter and Royden (1993) and Wawrzenitz and Krohe (1993). The pattern of the AFT ages to the south of the Strymon Valley Detachment, however, is consistent with a zone of steep brittle normal faults responsible for the formation of the offshore Orfanos Basin (Fig. 2.1) whose maximum subsidence (>3 km, Sokoutis et al., 1993) is probably related to exhumation along its shoulders. This zone of brittle faults is termed Strymon 2 in Fig. 2.6. The AFT and ZFT ages further allow constraints on the timing of fault activity. Strymon 1 must have been active at 15 Ma which is the time when the footwall samples (RD88, 93) cooled through the zircon closure temperature (Fig. 2.6f). Rapid cooling in the footwall continued until about 7 Ma, as indicated by the AFT ages, and therefore Strymon 1 might have been active until this time. On the other hand, the apatite FT ages close to and on either side of Strymon 1 are very similar, indicating cessation of faulting between 9 and 6 Ma (Fig. 2.6g). The cessation of Strymon 1 is also recorded in track-length models from Hejl et al. (1998) (Fig. 2.7), which originate from the footwall of the detachment (Fig. 2.3). The first model (Fig. 2.7a) shows fast cooling from 110 to 60°C at ∼15–11 Ma to ∼14–8 Ma, while their other models (Fig. 2.7b,c) show slightly slower cooling rates from 110 to 60°C at ∼9–5 Ma to ∼6–2 Ma. This indicates that fault activity might have slowed down or stopped at ∼8 Ma.

The oldest syn-tectonic sediments deposited in the Orfanos Basin are Tortonian (11.6 to 7.2 Ma) (Büttner and Kowalczyk, 1978; Kousparis, 1979; Lalechos, 1986), constraining the onset of faulting on the Strymon 2 fault zone. Strymon 2 was active until at least 6 Ma, the time when footwall samples RD91 and 92 cooled through the apatite closure temperature (Fig. 2.6f,g). All constraints combined suggest that both the Strymon 1 and Strymon 2 fault zones have been active during the Tortonian. Strymon 2 might still be active today, as indicated by seismicity maps published by the European–Mediterranean Seismological Centre (www.emsc-csem.org).

2.4.2 Final cooling below ∼70°C

(U-Th)/He analyses on samples from the northern part of the SRCC (Fig. 2.3) provide some constraints on cooling below ∼70°C. A plot of ages against their altitude (Fig. 2.8) shows a positive linear trend. This indicates that the rocks might have cooled as a single block through the He closure temperature (corresponding to 75 ± 5°C, Wolf et al., 1998; Farley, 2000).

(U-Th)/He ages from sites on either side of the Nestos Fault (RD64 and RD68) overlap within error with both the AFT and ZFT data implying that cooling through the temperature range 300 to 75°C was very fast and, as previously argued, that there was no differential movement along the Nestos Fault since about 30 Ma.

Younger (U-Th)/He apatite ages occur at the eastern limit of the Nestos Fault. The three ages in this region are 15–17 Ma, (Fig. 2.3). The Xanthi Fault displays normal and strike-slip movements (Burchfiel et al., 2000), but it is unclear at what time the fault was initiated. Koukouvelas and Pe-Piper (1991) state that the Xanthi Fault controlled the emplacement of the Xanthi pluton, and is therefore older than 34 to 30 Ma. On the other hand, sediment studies suggest that the fault only dates back to ∼14 Ma, as the oldest syn-tectonic sediments in the Nestos Basin (Fig. 2.1) are Serravallian (13.8–11.6 Ma) (Kousparis, 1979; Gautier et al., 1999). (U-Th)/He ages of footwall samples yield values of ∼15 Ma (RD80, 81), compared to the hanging wall sample RD82 of ∼17 Ma, perhaps indicating normal faulting at this time. Although the errors are large on these ages, they are consistent with the sedimentary evidence for ages of initiation of the Nestos Basin. As strike slip faulting is not recorded in the thermochronological data, we are thus unable to assess such activity.

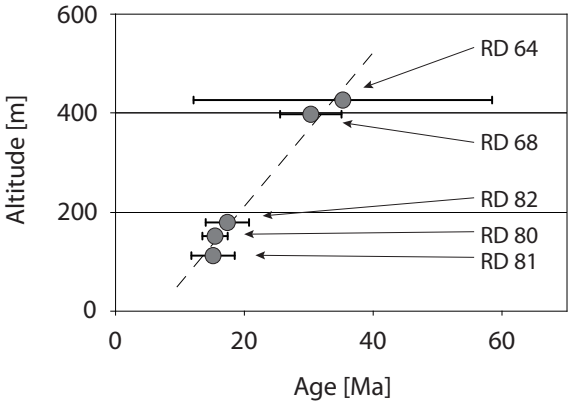

Figure 2.8: (U-Th)/He mean ages ± 2SEM (standard error of the mean) plotted against their altitude. SEM was calculated according to the formula given in table 2.2.

2.5 Conclusions

Extension causing cooling and exhumation of the South Rhodope Core Complex began in the Middle Eocene. Two detachments (Kerdilion and Strymon Valley) and a more localised fault zone (Strymon 2) controlled a protracted exhumation:

1. Exhumation along the Kerdilion Detachment initiated at around 40 Ma and lasted until about 26 Ma. Cooling/exhumation may have halted for the next ∼5 Ma, but this is not firmly constrained by our data. If this 5 Ma quiecent period is confirmed by future work, it implies a change in the thermo-mechanical conditions of extension in the SRCC, perhaps involving a switch from syn-thickening extension of the Rhodope continental crust to the well-documented Aegean slab-rollback-generated-extension (Jolivet et al., 2004; Brun and Faccenna, 2008).

2. Cooling/exhumation along the Strymon Valley Detachment started by at least 20 Ma and ceased at around 8 Ma.

3. During the Tortonian (11.6 to 7.2 Ma), when the Strymon Valley Detachment was still active, a zone of brittle faults, Strymon 2, started to form the offshore Orfanos

Basin and to control the cooling/exhumation of the surrounding area. Activity on Strymon 2 possibly remains until today.

Appendix: Analytical methods

Whole rock samples were crushed and apatite and zircon grains were recovered by conventional heavy liquid and magnetic methods. Apatite grains for FT analysis were mounted in epoxy resin, polished and etched with $5.5N\ HNO_3$ for 20s at 21°C. Zircon grains were mounted in teflon, polished and etched in a eutectic mixture of KOH and $NaOH$ at 220°C for 10 to 20 hours. Irradiation was carried out at the OSU facility, Oregon State University Radiation Center, USA. Microscopic analysis was completed using an optical microscope with a Kinetek computer driven stage (Dumitru, 1995). The magnifications used were ×1250 (dry) for apatite and ×1600 (oil) for zircon. All ages were determined using the zeta approach (Hurford and Green, 1983) with a zeta value of 416 ± 13 (1σ) for apatite and CN5 standard glass, and 133 ± 2.5 (1σ) for zircon and CN1 standard glass (Tab. 2.1). Ages are reported as central ages (Galbraith and Laslett, 1993) with a 2σ error.

Horizontal confined track lengths in apatite were measured at a magnification of ×1250 (dry), as well as etch pit diameters (Dpar) which are used as a proxy for chemistry and which in turn has an influence on FT annealing (Carlson et al., 1999). Time(t)–temperature(T) paths were derived using the HeFTy program of Ketcham (2005). Input parameters are FT age, track-length distribution and Dpars. The model paths are forced to move through certain constraints (t–T boxes). One large box was chosen, in order to give the path as much freedom as possible to move through the partial annealing zone, and a small box corresponding to the ZFT age and the zircon closure temperature (Fig. 2.5). An inverse Monte Carlo algorithm with a multikinetic annealing model Ketcham et al. (2007) was used to generate a large number of t–T paths which are compared to the input data. The Kolmogorov–Smirnov statistical test was used to test the goodness of fit (GOF) between modelled and measured track length distributions, with merit values of 0.5 and 0.05 for "good" and "acceptable" fits respectively. The best fitting thermal history obtained by the model is not the only possible. Other thermal histories match the data similarly well and it is thus important to consider all geological constraints to determine the most acceptable path.

Apatite (U-Th)/He analysis were performed at the University of Kansas following procedures similar to those reported in House et al. (2000) and Farley and Stockli (2002). Measurements were carried out on 2 to 3 single grains per sample. Helium was degassed using a Nd–YAG laser and subsequently measured on a quadrupole mass spectrometer. Uranium, thorium and samarium were measured on a VG Plasmaquad–2 ICP–MS. Ages were corrected for α–ejection using the F_t ejection correction (Farley et al., 1996; Farley,

2002). Ages are reported as the average values of the two to three single grains ±2SEM (Tab. 2.2).

Chapter 3

Cenozoic thermal evolution of the Central Rhodope Metamorphic Complex, Southern Bulgaria

[1]

Abstract

The Central Rhodope Metamorphic Complex (CRMC) of southern Bulgaria is one of several core complexes within the north Aegean Rhodope Massif, where high-grade metamorphic rocks were exhumed during a protracted Cenozoic extensional history.

New apatite, zircon and titanite fission-track and apatite (U-Th)/He ages combined with published higher temperature chronometer data and structural and sedimentary studies, have allowed us to develop and propose an evolutionary model for the CRMC. In contrast to previous studies we believe that most of the shear zones within the CRMC played only a minor role in the cooling and exhumation of the high grade metamorphic rocks. The Kardzhali shear zone, which can be traced along the eastern edge of the core complex, appears to be the main detachment causing the cooling and associated exhumation, starting in the Maastrichtian–Palaeocene. However, initial cooling is assumed to be slow as it only reached a peak at about 40 Ma. The entire CRMC cooled rapidly between 40 and 33 Ma. Subsequent cooling, from about 30 until no later than 15 Ma, only affected the south-central part of the metamorphic complex, where metamorphic rocks were exhumed along the Madan shear zone.

[1]To be submitted to an international journal as: Wüthrich E., Seward D., Kounov A., Stockli D., Latkoczy C. and Burg, J-P. Cenozoic thermal evolution of the Central Rhodope Metamorphic Complex, Southern Bulgaria

The two observed cooling/exhumation phases (Maastrichtian/Palaeocene to ∼33 Ma and ∼30 to ∼15 Ma) might represent the extensional stages of two subsequent "push-pull" cycles as proposed for the central Aegean (Forster and Lister, 2009).

3.1 Introduction

In the Rhodope Massif of southern Bulgaria/northern Greece, after a period of Mesozoic compression (e.g. Burg et al., 1990, 1996b; Ricou et al., 1998), extension generated several metamorphic core complexes bounded by low-angle shear zones (e.g. Dinter and Royden, 1993; Sokoutis et al., 1993; Wawrzenitz and Krohe, 1998; Bonev et al., 2006a; Brun and Sokoutis, 2007) . The Central Rhodope Metamorphic Complex (CRMC) in Bulgaria (Fig. 3.1) is a complex Cenozoic structure including several low-angle ductile to brittle shear zones that were active during exhumation of the high-grade metamorphic rocks (e.g. Georgieva et al., 2002; Sarov and Gerdjikov, 2002; Kaiser Rohrmeier, 2005). Although these shear zones have been well mapped, their respective role in the tectonic evolution of the CRMC remains only partially resolved. Ovtcharova et al. (2001) commented on the lack of sizeable change in $^{40}Ar/^{39}Ar$ and Rb-Sr ages across these shear zones, questioning their actual role in exhuming the metamorphic complex at temperatures >300°C.

This study aims to reconstruct the Cenozoic evolution of the CRMC within the temperature range of ∼300 to 60°C using fission-track analyses on titanite, zircon and apatite and (U-Th)/He on apatite. Higher temperature data from earlier studies are incorporated to propose a more complete model of the thermotectonic evolution of the CRMC. We conclude that the CRMC experienced exhumation driven cooling since the Maastrichtian until 15 Ma, while peak- cooling/exhumation took place between ∼40 and ∼33 Ma.

3.2 Geological setting

3.2.1 The Rhodope Massif

The Rhodope Massif, in south Bulgaria and northern Greece, is part of the Alpine–Himalayan orogenic belt (Burg et al., 1990). It comprises high-grade metamorphic rocks intruded by several Cretaceous and Cenozoic igneous bodies (e.g. Dinter et al., 1995; Ovtcharova et al., 2003b). To the north, the Maritsa fault zone separates the Rhodope Massif from the Cretaceous Sredna Gora volcanic arc and its Variscan basement (Fig. 3.1, inset). In the south and east, the Rhodope Massif is overlain by Miocene to recent sediments of the Aegean Sea and Palaeogene to Neogene sediments of the Thrace basin, respectively (Gorur and Okay, 1996; Ricou et al., 1998). To the west it is separated from the Dinarides/Hellenides by the Vardar suture zone (Fig. 3.1, inset). This description considers the Serbo–Macedonian Massif to be part of the Rhodope on the basis of sim-

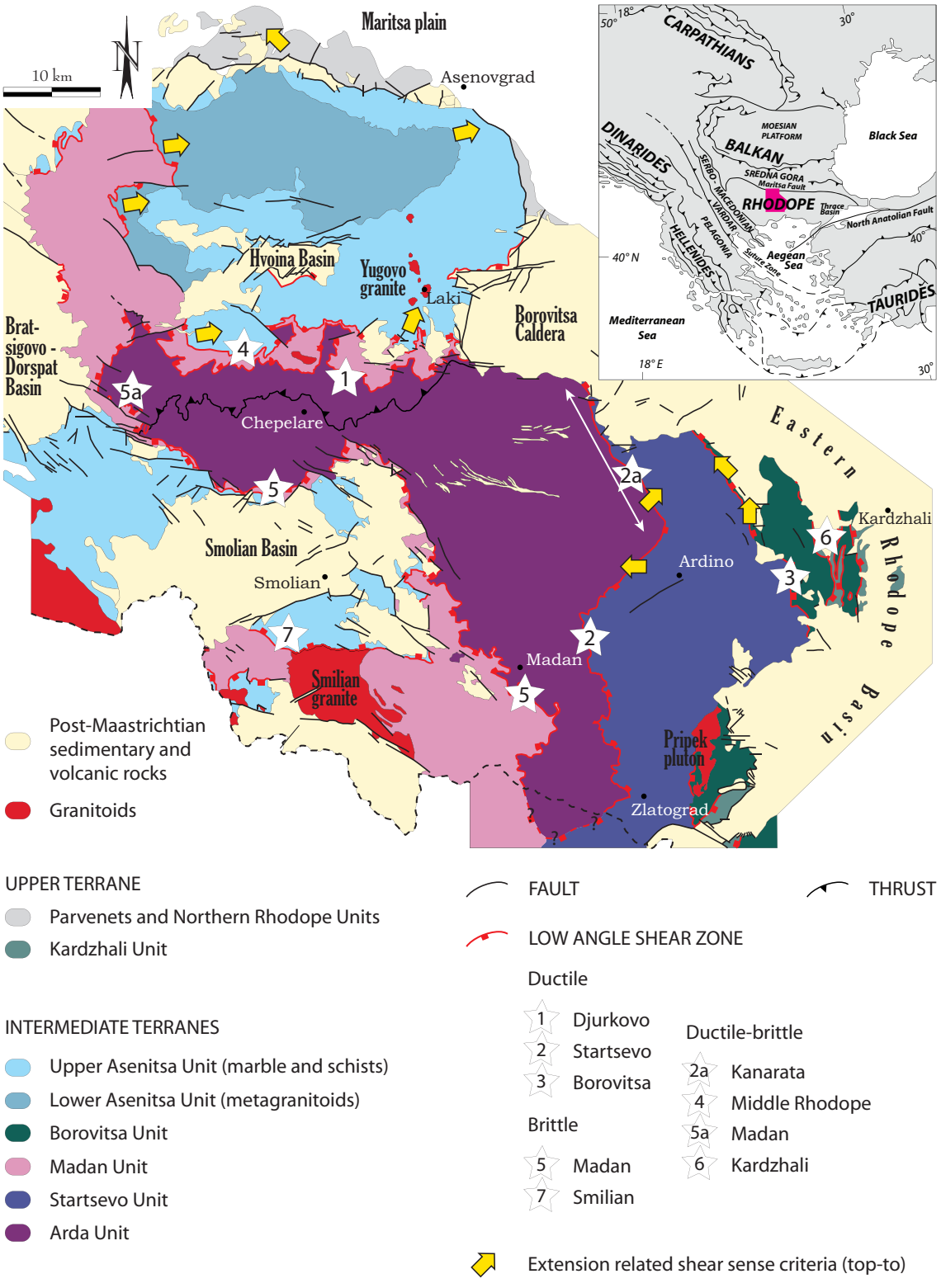

Figure 3.1: Tectonic map of the CRMC after the Geological Map of the Republic of Bulgaria, Burg et al. (1996b) and Gerdjikov (2005b). Burg et al. (1996b) introduced the differentiation of the metamorphic basement into three terranes, the upper, intermediate and lower terranes, of which only the upper two units are exposed in the CRMC. Shear sense criteria after Burg et al. (1996b), Gerdjikov (2004) and Pleuger et al. (2009).

ilarities in metamorphism, age and ductile strain field in both the Greek and Bulgarian areas (e.g. Burg et al., 1995; Ricou et al., 1998; Kilias et al., 1999). However, since the Serbo–Macedonian Massif of Serbia and Macedonia has not experienced severe Alpine metamorphic overprinting (Schmid et al., 2008, and references therein), the integration of the two massifs is still debated. Field descriptions identified two major deformational stages (e.g. Burg et al., 1996b; Ricou et al., 1998; Dimov et al., 2000). Intensive shortening during the Cretaceous led to southwest-directed thrusting and nappe-stacking causing crustal thickening and high-grade regional metamorphism. Within this nappe-imbrication, Burg et al. (1990, 1996b) distinguished three major units termed lower, intermediate and upper terranes according to their present-day structural position (Fig. 3.1). Subsequent extension, attributed to Cenozoic gravitational collapse of the thickened crust, resulted in the formation of core complexes bounded by gently dipping detachment faults (e.g. Dinter and Royden, 1993; Sokoutis et al., 1993), accompanied by migmatisation (40 to 37 Ma, e.g. Liati and Gebauer, 1999; Ovtcharova et al., 2003b) and followed by volcanism (∼35 to 25 Ma, e.g. Marchev et al., 2004a; Dhont et al., 2008). Several Rhodope detachments are interpreted as reactivated thrusts (e.g. Burg et al., 1996b). The extensional deformation also resulted in the formation of asymmetric grabens filled with mainly Eocene to Oligocene continental and marine sediments (e.g Smolian Basin, Fig. 3.1) (Cernjavska, 1977; Dimov et al., 2000).

3.2.2 The Central Rhodope Metamorphic Complex

The CRMC occupies the central part of the Bulgarian Rhodope Massif (Fig. 3.2, inset). It incorporates the Central Rhodope Dome (e.g. Ovtcharova et al., 2003b; Kaiser-Rohrmeier et al., 2004) and higher units of the intermediate and upper terranes (Burg et al., 1996b), and exposes gneisses, micaschists, amphibolites, marbles and ultrabasites (Fig. 3.1). Migmatisation is pervasive in the structurally deeper lithological units, locally called Arda, Madan and Startsevo (Fig. 3.1). All units have been predominantly metamorphosed to amphibolite facies, with the exception of the uppermost Kardzhali and Parvenets/Northern Rhodope Units, which were metamorphosed to greenschist facies (Gerdjikov, 2004; Sarov et al., 2004).

The metamorphic event, contemporaneous with regional thrusting and nappe-stacking, has been dated to between 128 and 82 Ma in a structurally higher unit (U-Pb zircon and Rb-Sr whole rock of the so-called Lower Asenitsa Unit, Zagorcev and Moorbath, 1986; Arnaudov et al., 1989) and 42 Ma in a structurally deeper unit (U-Pb SHRIMP zircon from Arda Unit, Liati and Gebauer, 1999; Liati, 2005) (Fig. 3.2).

Crustal extension is denoted by the occurrence of sedimentary basins filled with predominantly Upper Eocene to Oligocene deposits (Fig. 3.1). Extension reactivated thrust contacts as low angle detachment faults (Burg et al., 1990; Dimov et al., 2000; Ovtcharova

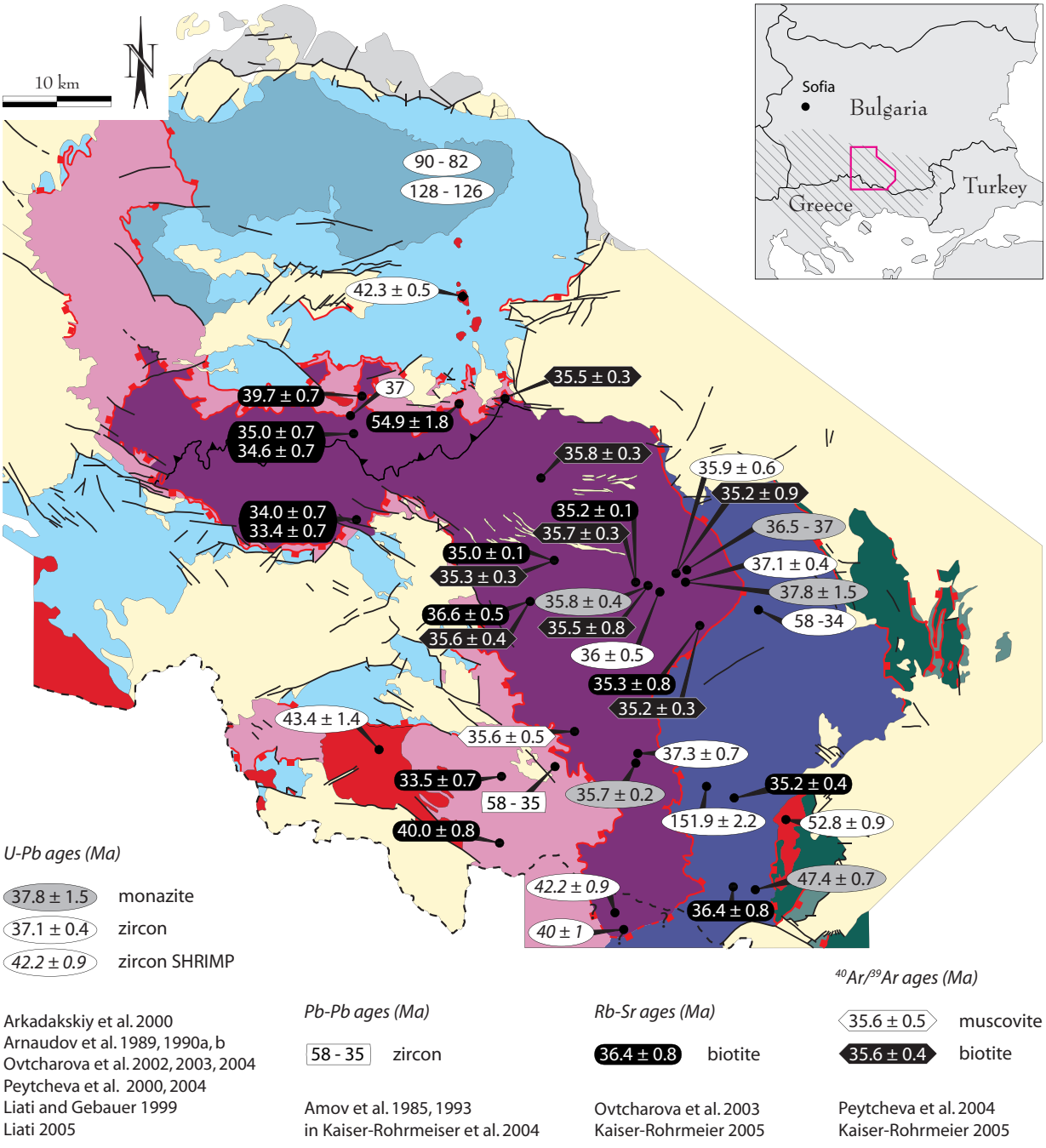

Figure 3.2: Tectonic map of the CRMC with location and ages of previously published high temperature cooling data. Map key see Fig. 3.1.

et al., 2003a; Kaiser Rohrmeier, 2005) and was accompanied by migmatisation of the deep Arda, Startsevo and Madan Units and intrusion of several granitic plutons. Migmatisation has been dated between 40 and 37 Ma (leucosome U-Pb zircon and monazite, Arnaudov et al., 1989, 1990a,b; Liati and Gebauer, 1999; Arkadakskiy et al., 2000; Ovtcharova et al., 2002, 2003b, 2004; Liati, 2005). The most prominent, non-pervasively deformed plutons are (1) Pripek, in the south-east of the CRMC, dated at 52.8 ± 0.89 Ma (U-Pb zircon, Ovtcharova et al., 2003b), (2) Smilian, in the south-west, with an age of 43.4 ± 1.41 Ma (U-Pb zircon, Ovtcharova et al., 2003b) and (3) Yugovo, which intruded in the north as several small bodies at 42.3 ± 0.54 Ma (U-Pb zircon, Ovtcharova et al., 2003b) (Fig. 3.1 and Fig. 3.2).

The kinematics of the thrust-reactivated detachment zones is often poorly constrained, therefore to avoid controversial interpretation, these structures are here termed shear zones. The most relevant of these in the CRMC are (1) the Startsevo (northern section also called Kanarata) shear zone that separates the Arda and Startsevo Units along the eastern flank of the dome, (2) the Madan shear zone, between the Arda and Madan Units in the south-west of the dome, (3) the Middle Rhodope and Smilian shear zones that separate the Asenitsa from the Madan Unit, (4) the Borovitsa shear zone between the Startsevo and the Borovitsa Unit in the eastern part of the dome and (5) the Kardzhali shear zone, further to the east, between the Borovitsa and Kardzhali Units (Fig. 3.1). The similarity of Rb-Sr and $^{40}Ar/^{39}Ar$ cooling ages (∼35 Ma, Ovtcharova et al., 2003b; Peytcheva et al., 2004; Kaiser Rohrmeier, 2005) with migmatisation ages of the core units of the CRMC (∼40 to 37 Ma, Liati and Gebauer, 1999; Arkadakskiy et al., 2000; Ovtcharova et al., 2002, 2003b; Peytcheva et al., 2004; Liati, 2005) indicates rapid cooling between >700 and ∼300°C, probably related to rapid exhumation during the Middle to Late Eocene. Extension lasted until the Miocene as indicated by the overlying Late Eocene to Oligocene sedimentary basins (Cernjavska, 1977) and widespread Late Eocene to Early Miocene magmatism (35 to 25 Ma, Marchev et al., 2005, and references therein).

3.3 Methods and Results

Thirty-one rock samples, collected from different units of the CRMC, were analysed using the fission-track method on titanite, zircon and apatite (TFT, ZFT and AFT) and the (U-Th)/He method on apatite. The analytical procedures are described in the appendix to this chapter. FT ages are reported as central ages with a 2σ error (Galbraith and Laslett, 1993). Most of the FT ages passed the χ^2–test ($P(\chi^2)$ >5%), except for the titanite age, four zircon and one apatite age (Tab. 3.1). The test failure of these samples is presumably related to the variable chemical compositions of the individual dated grains which, in turn, relate to different annealing kinetics (e.g. Green et al., 1986; Yamada et al., 1995). (U-

Th)/He ages are reported as average values calculated from single grain ages ±2 standard errors of the mean (SEM) (Tab. 3.2).

3.3.1 Titanite fission-track ages

One sample (RD16) was dated with the TFT method yielding an age of 55.9 ± 6.2 Ma (Tab. 3.1, Fig. 3.3).

3.3.2 Zircon fission-track ages

The ZFT ages (14) are relatively similar within their errors, ranging from 26.0 ± 3.2 to 37.2 ± 3.6 Ma (Tab. 3.1, Fig. 3.3).

3.3.3 Apatite fission-track ages and track length modelling

The AFT ages (24) range between 18.4 ± 5.2 and 48.2 ± 14 Ma (Tab. 3.1, Fig. 3.3). Generally these ages do not show any particular change across the major shear zones. The younger ages, between 18.4 ± 5.2 and 23.7 ± 3.0 Ma, are from the southern part of the Arda and Startsevo Units (Fig. 3.3).

For three samples (RD2, RD26 and RD34) apatite track lengths (n >90), as well as etch pit diameters (Dpar), were measured and subsequently modelled with the HeFTy program (Ketcham, 2005) to reveal time–temperature histories (Fig. 3.4). Sample RD2 (northern Asenitsa Unit, Fig. 3.3), shows rapid cooling between 40 and 30 Ma through the zircon closure temperature and the apatite partial annealing zone (from 300 to 60°C, Gleadow and Duddy, 1981; Foster et al., 1993; Tagami et al., 1998). Sample RD34 (Startsevo Unit, Fig. 3.3), passes very rapidly through the same temperature range as RD2 at 30 Ma. The model for sample RD26 (Arda Unit, Fig. 3.3) shows two phases of cooling, both of which are less distinct than for the previous samples. The first phase is related to cooling from ∼280 to ∼100°C between ∼38 to ∼23 Ma and the second is from ∼100 to ∼60°C between ∼20 and ∼13 Ma.

3.3.4 Apatite (U-Th)/He ages

Apatite (U-Th)/He ages (10) range from 13.6 ± 1.4 Ma to 32.4 ± 1.9 Ma (Tab. 3.2, Fig. 3.3). The oldest ages, ∼30 Ma, were found in the Startsevo and Borovitsa Units (RD34 and 35, Fig. 3.3).

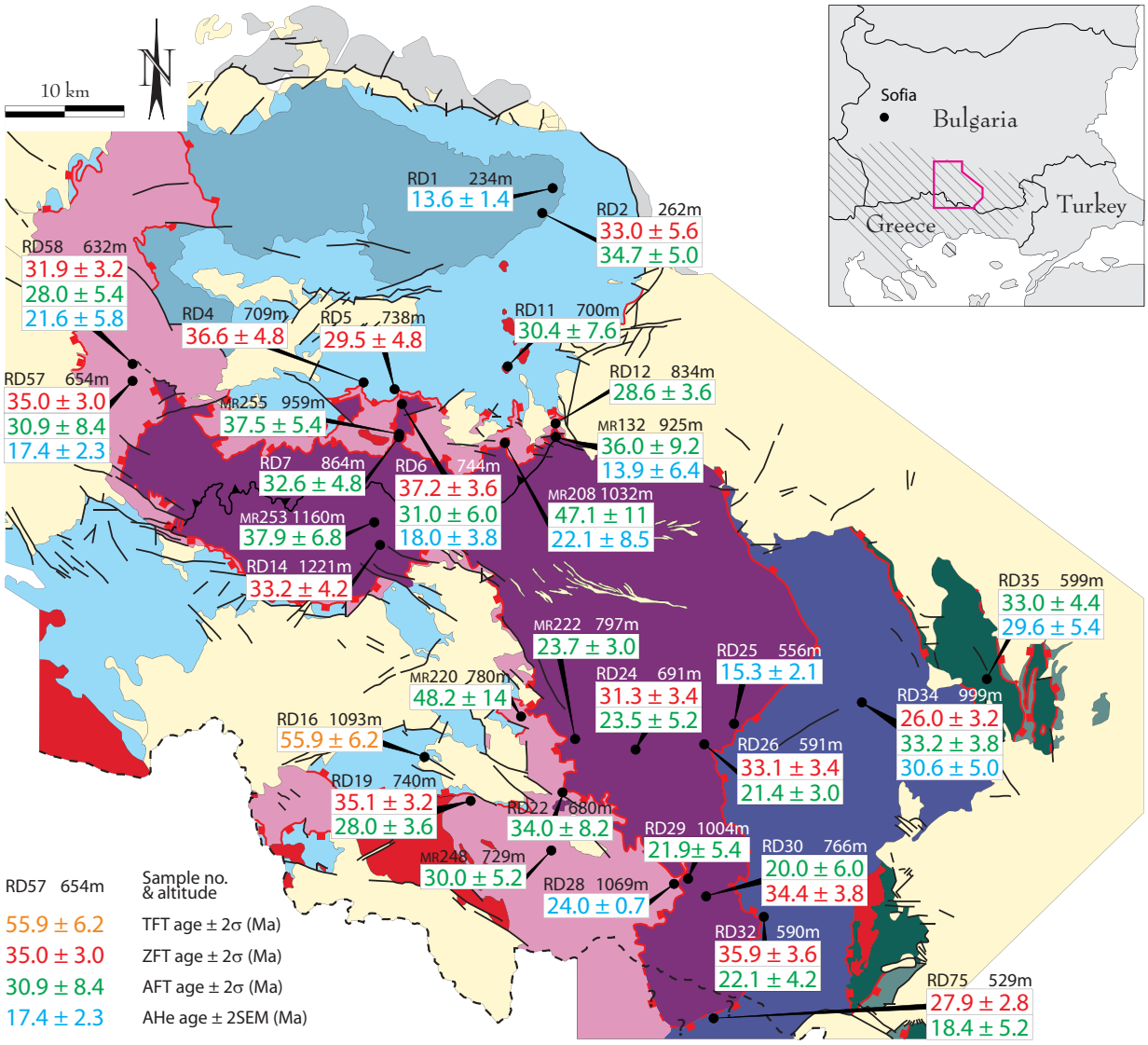

Figure 3.3: Tectonic map of the CRMC with new fission-track and (U-Th)/He ages. Map key see Fig. 3.1.

Table 3.1: Apatite (A), zircon (Z) and titanite (T) fission track results. All ages are reported as central ages (Galbraith and Laslett, 1993). ρd is the induced track density, ρs and ρi are the densities of spontaneous and induced tracks, respectively. P(χ^2) is the probability of failing the χ^2–test. Dpar denotes the mean track pit diameter of a sample. MTL is the c-axis corrected mean track length while n is the number of lengths measured.

Sample number	**Grid reference**	**Alti. [m]**	**Min.**	**Age [Ma]**	**$\pm 2\sigma$ [Ma]**	**No. of grains**	**ρd [$10^5 cm^{-2}$] (counted)**	**ρs [$10^5 cm^{-2}$] (counted)**	**ρi [$10^5 cm^{-2}$] (counted)**	**P(χ^2) [%]**	**U [ppm]**	**Dpar [μm]**	**MTL [μm] (n)**
RD 2	N 41° 56' 23.2"	262	Z	**33.0**	**5.6**	10	3.5	111.0	78.2	2.2	709		
	E 24° 50' 50.6"						(2185)	(811)	(571)				
			A	**34.7**	**5.0**	20	13.2	5.0	39.2	63.3	32	1.5	14.34 ± 0.87
							(4611)	(289)	(2279)				(91)
RD 4	N 41° 48' 58.8"	709	Z	**36.6**	**4.8**	20	4.2	39.5	29.8	25.7	284		
	E 24° 40' 20.4"						(2376)	(809)	(611)				
RD 5	N 41° 48' 36.0"	738	Z	**29.5**	**4.8**	20	4.0	39.8	33.7	0.2	277		
	E 24° 42' 25.2"						(2376)	(961)	(814)				
RD 6	N 41° 48' 09.2"	744	Z	**37.2**†	**3.6**	20	3.9	92.9	57.9	6.9	405		
	E 24° 42' 35.1"						(2091)	(2473)	(1540)				
			A	**31.0**	**6.0**	20	10.9	1.9	13.7	68.3	16	1.7	
							(4611)	(138)	(1005)				
RD 7	N 41° 46' 32.1"	864	A	**32.6**	**4.8**	20	12.5	4.5	36.1	37.2	33	1.6	
	E 24° 42' 28.3"						(4450)	(280)	(2230)				
RD 11	N 41° 49' 33.0"	700	A	**30.4**	**7.6**	20	10.2	1.5	10.2	97.5	14	1.6	
	E 24° 48' 55.7"						(4450)	(80)	(558)				
RD 12	N 41° 47' 07.7"	834	A	**28.6**	**3.6**	20	14.2	5.1	52.7	38.4	45	1.9	
	E 24° 51' 44.5"						(3733)	(415)	(4279)				
RD 14	N 41° 41' 45.6"	1221	Z	**33.2**	**4.2**	20	3.2	81.3	50.8	0.0	530		
	E 24° 41' 30.8"						(2376)	(2038)	(1274)				
RD 16	N 41° 32' 17.7"	1093	T	**55.9**†	**5.6**	13	9.8	42.7	15.2	0.1			
	E 24° 43' 54.4"						(2641)	(1931)	(6886)				

† *Age counted by D. Seward*

Table 3.1: (continued)

Sample number	Grid reference	Alti. [m]	Min.	Age [Ma]	$\pm 2\sigma$ [Ma]	No. of grains	ρd [$10^5 cm^{-2}$] (counted)	ρs [$10^5 cm^{-2}$] (counted)	ρi [$10^5 cm^{-2}$] (counted)	P(χ^2) [%]	U [ppm]	Dpar [μm]	MTL [μm] (n)
RD 19	N 41° 30' 31.1"	740	Z	**35.1**	**3.2**	27	3.9	44.6	32.5	10.3	273		
	E 24° 46' 31.0"						(2251)	(2902)	(2116)				
			A	**28.0**	**3.6**	20	13.7	4.3	43.7	53.1	37	1.8	
							(6179)	(358)	(3651)				
RD 22	N 41° 30' 58.0"	680	A	**34.0**	**8.2**	20	13.5	1.1	8.7	91.9	9	1.5	
	E 24° 52' 12.9"						(6179)	(85)	(698)				
RD 24	N 41° 32' 40.9"	691	Z	**31.3**	**3.4**	20	3.2	66.0	44.4	9.7	517		
	E 24° 56' 38.3"						(2251)	(1570)	(1056)				
			A	**23.5**	**5.2**	20	12.1	1.4	15.2	79.0	14	1.4	
							(6179)	(102)	(1092)				
RD 26	N 41° 32' 50.8"	591	Z	**33.1**	**3.4**	21	4.2	41.6	34.3	13.7	287		
	E 25° 00' 27.2"						(2409)	(1572)	(1297)				
			A	**21.4**	**3.0**	20	11.0	2.7	28.6	31.5	30	1.7	14.47 ± 1.37
							(6179)	(286)	(3055)				(91)
RD 29	N 41° 27' 08.7"	1004	A	**21.9**	**5.4**	20	13.5	2.2	28.6	88.1	24	1.3	
	E 24° 59' 15.0"						(4917)	(78)	(1006)				
RD 30	N 41° 26' 21.2"	766	Z	**34.2**	**3.8**	20	3.8	30.7	22.4	92.4	196		
	E 25° 00' 32.8"						(2409)	(1096)	(800)				
			A	**20.0**	**6.0**	20	12.0	0.7	9.1	63.2	10	1.5	
							(2946)	(53)	(660)				
RD 32	N 41° 25' 23.5"	590	Z	**35.7**	**3.6**	20	3.6	51.6	33.7	17.0	287		
	E 25° 03' 44.3"						(2409)	(2048)	(1340)				
			A	**22.1**	**4.2**	20	11.6	1.6	16.8	87.9	18	1.7	
							(2946)	(144)	(1560)				
RD 34	N 41° 34' 20.1"	999	Z	**26.0**	**3.2**	20	5.2	66.3	89.4	0.2	568		
	E 25° 10' 06.4"						(3627)	(1280)	(1726)				
			A	**33.2**	**3.8**	21	12.5	7.3	51.2	24.1	50	1.8	15.17 ± 0.55
							(7878)	(532)	(4153)				(104)

Table 3.1: (continued)

Sample number	Grid reference	Alti. [m]	Min.	Age [Ma]	$\pm 2\sigma$ [Ma]	No. of grains	ρd [$10^5 cm^{-2}$] (counted)	ρs [$10^5 cm^{-2}$] (counted)	ρi [$10^5 cm^{-2}$] (counted)	P(χ^2) [%]	U [ppm]	Dpar [μm]	MTL [μm] (n)
RD 35	N 41° 36' 01.9"	599	A	**33.0**	**4.4**	20	12.6	5.4	43.2	40.2	38	1.5	
	E 25° 16' 49.0"						(7878)	(335)	(2659)				
RD 57	N 41° 49' 12.1"	654	Z	**31.9**	**3.2**	25	4.8	31.0	31.0	20.1	230		
	E 24° 26' 24.3"						(2947)	(1386)	(1383)				
			A	**28.0**	**5.4**	20	14.2	1.5	16.2	89.8	13	2.0	
							(5595)	(135)	(1420)				
RD 58	N 41° 50' 06.4"	632	Z	**35.0**	**3.0**	20	4.7	58.2	52.1	38.6	402		
	E 24° 26' 22.9"						(2947)	(1734)	(1553)				
			A	**30.9**	**8.4**	20	13.8	0.7	6.8	96.0	6	1.5	
							(5595)	(64)	(594)				
RD 75	N 41° 21' 15.5"	529	Z	**27.9**	**2.8**	20	4.5	54.6	58.5	17.8	437		
	E 25° 00' 47.6"						(3627)	(1388)	(1488)				
			A	**18.4**	**5.2**	19	12.5	0.9	13.4	48.3	12	1.3	
							(4631)	(58)	(829)				
MR 132	N 41° 46' 29.4"	925	A	**36.0**	**9.2**	20	11.1	1.9	12.1	59.2	14	-	
	E 24° 51' 40.2						(3794)	(81)	(517)				
MR 208	N 41° 46' 20.9"	1032	A	**47.1**	**10.8**	21	11.5	2.2	11.3	17.8	13	-	
	E 24° 48' 55.2"						(4075)	(138)	(711)				
MR 220	N 41° 34' 2.1"	780	A	**48.2**	**14.2**	19	9.7	0.9	3.9	69.1	5	1.9	
	E 24° 49' 39.6"						(4075)	(60)	(251)				
MR 222	N 41° 33' 8.2"	797	A	**23.7**	**3.0**	20	12.3	5.4	58.1	32.9	53	-	
	E 24° 52' 43.1"						(4075)	(441)	(4771)				
MR 248	N 41° 28' 30.7"	729	A	**30.0**	**5.2**	20	9.5	4.0	26.8	4.9	32	-	
	E 24° 51' 27.1						(4075)	(321)	(2128)				
MR 253	N 41° 42' 43.0"	1160	A	**37.9**	**6.8**	20	11.8	2.8	18.2	23.1	19	-	
	E 24° 41' 21.3"						(4075)	(200)	(1304)				
MR 255	N 41° 46' 42.8"	959	A	**37.5**	**5.4**	20	9.8	3.2	17.5	52.2	21	-	
	E 24° 42' 28.7"						(3794)	(301)	(1635)				

Table 3.2: Apatite (U-Th)/He results: Ages are reported as single grain ages and their mean value. The error of the mean is given as 2SEM. SEM is calculated from the age data of the single analysis and the number of analysis (N) per sample (SEM = $\sigma/\sqrt{N}$). F_t is the alpha ejection correction factor (Farley et al., 1996; Farley, 2002).

Sample	Grid reference	Alti. [m]	Grain	Age [Ma]	± [Ma]	U [ppm]	Th [ppm]	Sm [ppm]	Th/U	He [nmol/g]	mass [mg]	F_t
RD 1	N 41° 57' 20.5"	234	RD 1-2	12.9	0.3	5.70	6.09		1.07	0.39	4.77	0.78
	E 24° 51' 22.4"		RD 1-3	14.3	0.4	4.46	4.55		1.02	0.34	5.57	0.80
		Mean Age ± 2SEM		**13.6**	**1.4**							
RD 6	N 41° 48' 09.2"	744	RD 6-1	14.4	0.9	8.89	1.09	9.90	0.12	0.51	5.90	0.72
	E 24° 42' 35.1"		RD 6-2	20.9	1.3	8.70	4.89	14.28	0.56	0.81	6.90	0.72
			RD 6-3	18.8	1.1	12.28	2.45	12.97	0.20	0.90	4.30	0.69
		Mean Age ± 2SEM		**18.0**	**3.8**							
RD 25	N 41° 34' 01.6"	556	RD 25-1	13.9	0.8	9.15	1.84	74.91	0.20	0.57	3.80	0.74
	E 25° 02' 25.4"		RD 25-2	17.3	1.0	10.00	1.60	67.98	0.16	0.74	3.10	0.72
			RD 25-3	14.6	0.9	15.11	1.92	70.41	0.13	0.84	3.40	0.66
		Mean Age ± 2SEM		**15.3**	**2.1**							
RD 28	N 41° 27' 00.5"	1069	RD 28-1	24.7	3.1	6.30	1.41		0.22	0.71	56.87	0.80
	E 24° 58' 41.0"		RD 28-3	23.5	3.0	2.53	0.21		0.08	0.26	65.81	0.80
			RD 28-4	23.9	2.7	2.48	0.30		0.12	0.25	38.19	0.77
		Mean Age ± 2SEM		**24.0**	**0.7**							
RD 34	N 41° 34' 20.1"	999	RD 34-1	33.6	2.0	58.55	8.77	44.99	0.15	7.40	4.20	0.67
	E 25° 10' 06.4"		RD 34-2	25.6	1.5	30.80	6.17	45.79	0.20	3.15	4.90	0.70
			RD 34-3	32.4	1.9	32.29	6.94	66.90	0.22	4.25	5.60	0.71
		Mean Age ± 2SEM		**30.5**	**5.0**							
RD 35	N 41° 36' 01.9"	599	RD 35-1	24.9	1.5	7.76	16.79	0.88	2.16	1.09	3.00	0.69
	E 25° 16' 49.0"		RD 35-2	29.8	1.8	19.44	21.19	14.21	1.09	2.73	2.80	0.69
			RD 35-3	34.2	3.5	2.95	3.33	1.02	1.13	0.48	2.60	0.69
		Mean Age ± 2SEM		**29.6**	**5.4**							

Table 3.2: (continued)

Sample	Grid reference	Alti. [m]	Grain	Age [Ma]	± [Ma]	U [ppm]	Th [ppm]	Sm [ppm]	Th/U	He [nmol/g]	mass [mg]	F_t
RD 57	N 41° 49' 12.1"	654	RD 57-1	16.7	1.0	4.55	0.74	42.14	0.16	0.37	14.00	0.81
	E 24° 26' 24.3"		RD 57-2	19.7	1.2	5.89	0.76	35.58	0.13	0.51	4.60	0.75
			RD 57-3	15.9	1.0	8.84	0.53	48.29	0.06	0.53	3.50	0.66
		Mean Age ± 2SEM		**17.4**	**2.3**							
RD 58	N 41° 50' 06.4"	632	RD 58-1	27.2	1.6	4.06	0.49	6.92	0.12	0.48	11.00	0.77
	E 24° 26' 22.9"		RD 58-2	19.7	1.2	4.36	1.02	6.75	0.23	0.39	14.60	0.78
			RD 58-3	17.8	1.1	2.45	0.41	16.04	0.17	0.19	7.30	0.73
		Mean Age ± 2SEM		**21.6**	**5.8**							
MR 132	N 41° 46' 29.4"	925	MR 132-1	20.2	0.5	6.99	6.85		0.98	0.74	4.57	0.79
	E 24° 51' 40.2		MR 132-2	11.1	0.5	5.41	0.54		0.10	0.26	3.46	0.77
			MR 132-3	10.2	0.3	7.38	4.98		0.67	0.36	3.46	0.77
		Mean Age ± 2SEM		**13.8**	**6.4**							
MR 208	N 41° 46' 20.9"	1032	MR 208-2	19.9	0.6	14.55	1.12		0.08	1.14	1.82	0.72
	E 24° 48' 55.2"		MR 208-3	16.0	0.3	13.70	2.03		0.15	0.93	4.15	0.76
			MR 208-4	30.3	1.3	4.55	1.33		0.29	0.61	3.92	0.77
		Mean Age ± 2SEM		**22.1**	**8.5**							

3.4 Interpretation and Discussion

The core of the CRMC, the CRD, has been interpreted as a Cenozoic extensional metamorphic core complex in which several low-angle shear zones, regarded as major detachments, were responsible for the exhumation of the dome (Dimov et al., 2000; Georgieva et al., 2002; Sarov and Gerdjikov, 2002; Kaiser Rohrmeier, 2005). Nevertheless, the relative importance and the time over which these shear zones were active is only loosely constrained.

The deep units of the CRMC (Arda, Madan and Startsevo Units) experienced very fast cooling from >700 to ∼300°C between 40 and 35 Ma, i.e. after migmatite generation at 40–37 Ma (Arnaudov et al., 1990b; Liati and Gebauer, 1999; Arkadakskiy et al., 2000; Ovtcharova et al., 2002, 2003b, 2004; Peytcheva et al., 2004; Liati, 2005) until closure temperatures of the Rb-Sr- and $^{40}Ar/^{39}Ar$-system at ∼35 Ma (Ovtcharova et al., 2003b; Peytcheva et al., 2004; Kaiser Rohrmeier, 2005). This very fast cooling (up to 200°C/Ma) is also recorded in structurally higher units. The track-length models of RD2, RD26 and RD34 yield rapid cooling from about 300°C to at least 110°C (Fig. 3.4) at approximately the same time: between 40 and 38 Ma for the Asenitsa Unit (RD2), at about 30 Ma for the Startsevo Unit (RD34) and between 37 and 23 Ma for the Arda unit (RD26). Additionally, the ZFT ages show no variation with altitude, implying nearly "instantaneous" cooling through the zircon closure temperature (260 ± 50°C, Foster et al., 1993; Tagami et al., 1998), regardless of the tectonic position. Generally, in core complexes, cooling is faster and younger in the footwall than in the hanging wall (e.g. Gessner et al., 2001; Shirvell et al., 2009). Since none of the studied shear zones yield distinct differential cooling of the adjacent units, we conclude that they played a minor role in the unroofing of the CRMC. If exhumation was detachment controlled, the major shear zones may occur further away from the central region and we provide a hypothesis on their location.

The AFT data is slightly more variable than the ZFT data, for example across the southern part of the Madan shear zone (Fig. 3.3), and a plausible explanation refers to variable cooling rates. A fast cooling rate close to the zircon closure temperature will result in similar ZFT ages for samples of variable depth while a later, slower cooling rate during

---

Figure 3.4 ***(following page)*:** Monte Carlo inverse temperature–time model of samples RD2, RD34 and RD26 and the corresponding track length histogram of corrected length for confined tracks. In the model: Black lined boxes show the given constrains to the model. The light grey field shows the envelop of possible acceptable fit-paths, while the dark grey lines are possible good fits and the black line the best fit. In order to determine the goodness of fit the Kolmogorov–Smirnov statistical test was used. The apatite partial annealing zone is denoted as striated area (110–60°C, Gleadow and Duddy, 1981). Black stars indicate the apatite (U-Th)/He single grain ages. Abbreviations: GOF – goodness of fit, MTL – c-axis corrected mean track length, n – number of measured confined track lengths.

RD 2

Asenitsa Unit

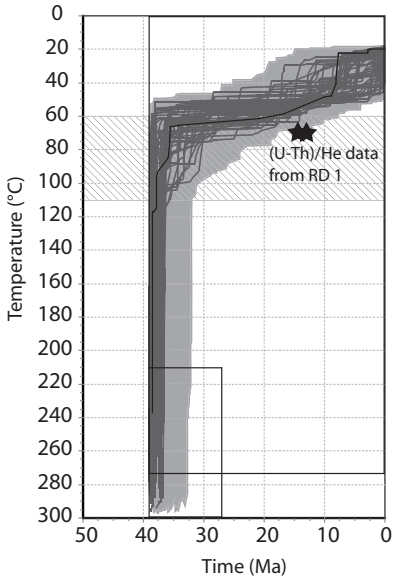

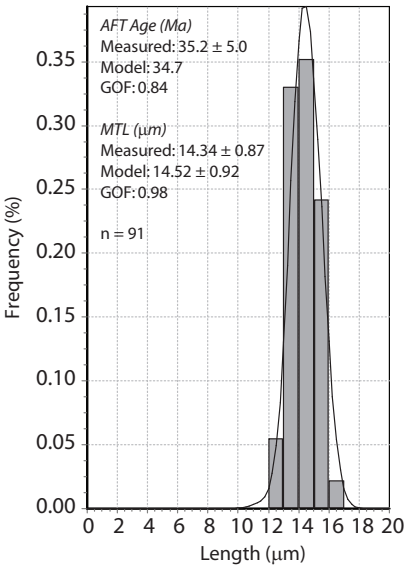

RD 34

Startsevo Unit

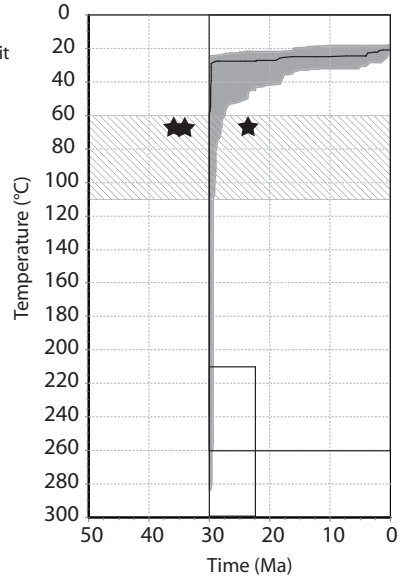

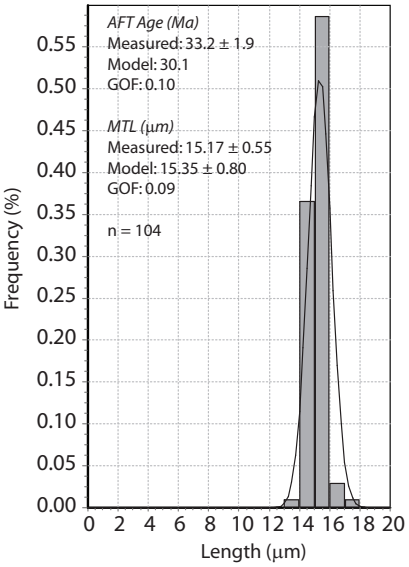

RD 26

Arda Unit

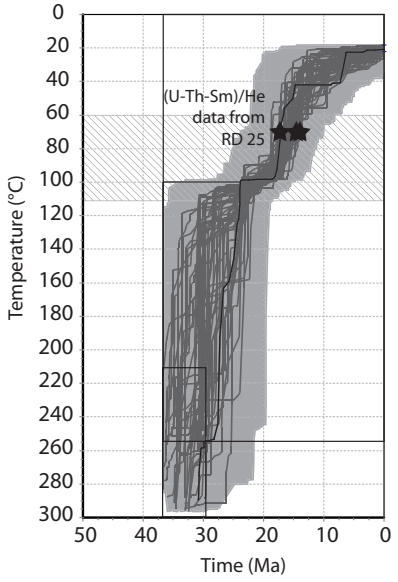

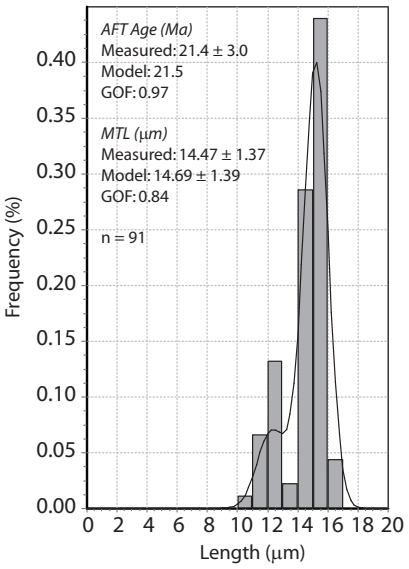

the passage through the apatite closure temperature will be reflected in larger AFT age differences between the same samples.

The overall picture for FT and (U-Th)/He ages is summarised in Fig. 3.5, whereby ZFT ages are uniform, AFT ages show significantly younger ages in the south-central part of the CRMC and the apatite (U-Th)/He ages only reveal a "jump" across the Startsevo shear zone. In the following sections, shear zones will be discussed individually from north to south, taking into account previously published, higher temperature chronometric ages (Fig. 3.6).

Middle Rhodope shear zone

The Middle Rhodope shear zone separates the Asenitsa Unit from the northern Madan Unit (Fig. 3.1). The U-Pb zircon ages from gneisses of the Lower Asenitsa Unit are between 128 and 90 Ma (Arnaudov et al., 1989) and were interpreted to date syn-thrusting metamorphism in this upper unit (Burg et al., 1990). A much younger U-Pb zircon age, 37 Ma, was obtained from leucosomes of the migmatites in the underlying Arda Unit (Arkadakskiy et al., 2000) (Fig. 3.6a). This large age difference might reflect the structural position of the two units, with the higher Asenitsa Unit cooling earlier than the structurally lower Arda Unit. Normal faulting along the North Rhodope shear zone (Burg et al., 1990) may also contribute to this large age difference. The existing high-temperature ages across the Middle Rhodope shear zone suggest that normal faulting was active at 37 Ma but its onset cannot be constrained. This activity, however, did not last longer than ∼33 Ma: the average FT ages for zircon and apatite both correspond to 34 Ma in the hanging wall (RD2, 4, 5, 11) and to 33 Ma in the footwall (RD6, 7, 12, 14, 57, 58, MR132, 208, 253 and 255). This is consistent with a 32.8 ± 0.41 Ma, undeformed rhyolitic dyke that cuts the Middle Rhodope shear zone (Ovtcharova et al., 2003b). (U-Th)/He ages (RD1, 6, 57, 58, MR132, 208) do not change across the fault (Fig. 3.5c) but reflect their altitude (younger ages are of lower altitude than older ages), which further confirms the lack of extensional activity on the fault after ∼35 Ma.

Smilian shear zone

The Smilian shear zone separates the Madan from the Asenitsa Unit in the southern part of the study area (Fig. 3.1). The TFT age of 55.9 ± 5.6 Ma (RD16) was obtained in its hanging wall. This age can be compared to Rb-Sr biotite ages of the footwall with an average of ∼37 Ma (Kaiser Rohrmeier, 2005) (Fig. 3.6b), since the fission-track closure temperature for titanite is 265–310°C (Coyle and Wagner, 1998), almost the same as for the Rb-Sr system in biotite (300 ± 50°C, Dickin, 1995, and references therein). The clear difference between the titanite and the Rb-Sr ages provides evidence that the Smilian shear zone was active at about ∼37 Ma. This is consistent with the fact that the shear zone

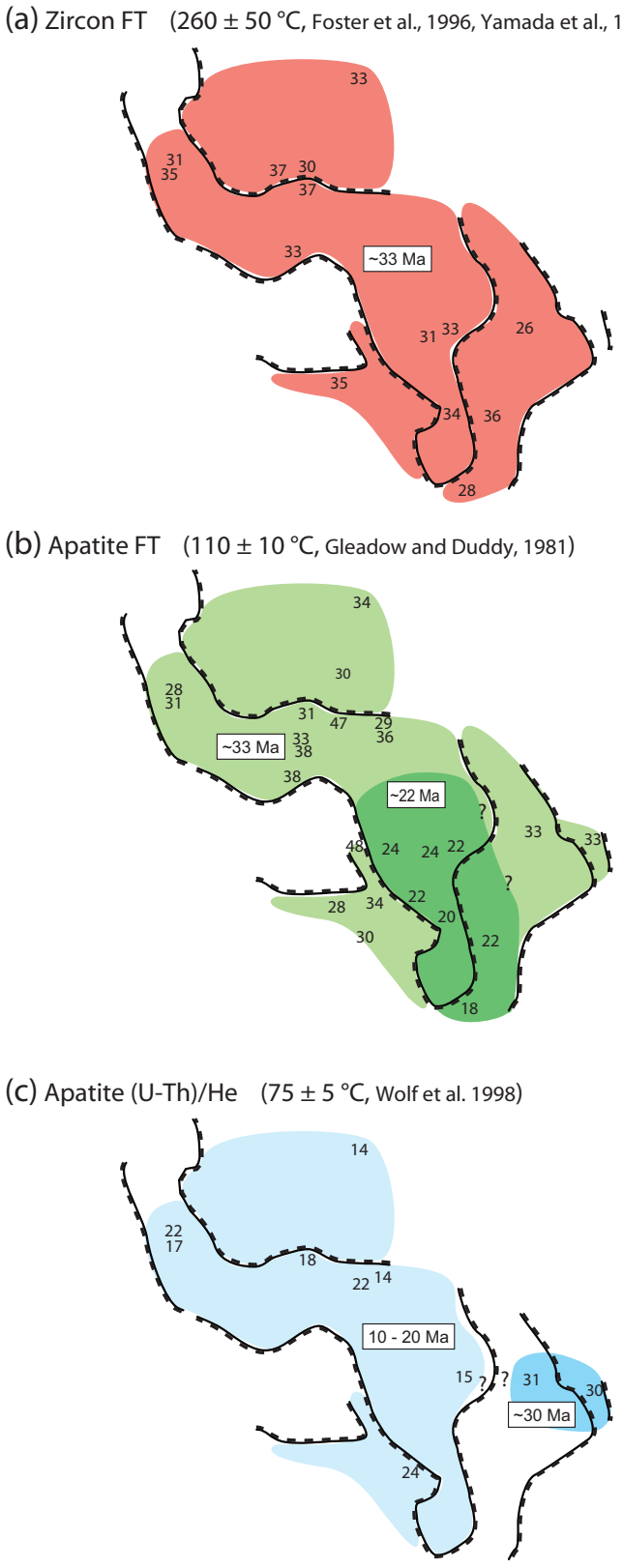

Figure 3.5: Simplified maps of the CRMC showing only the main shear zones with (a) zircon FT ages, (b) apatite FT ages and (c) apatite (U-Th)/He ages. Closure temperatures are given in brackets. Colours are used to emphasise zones of similar ages.

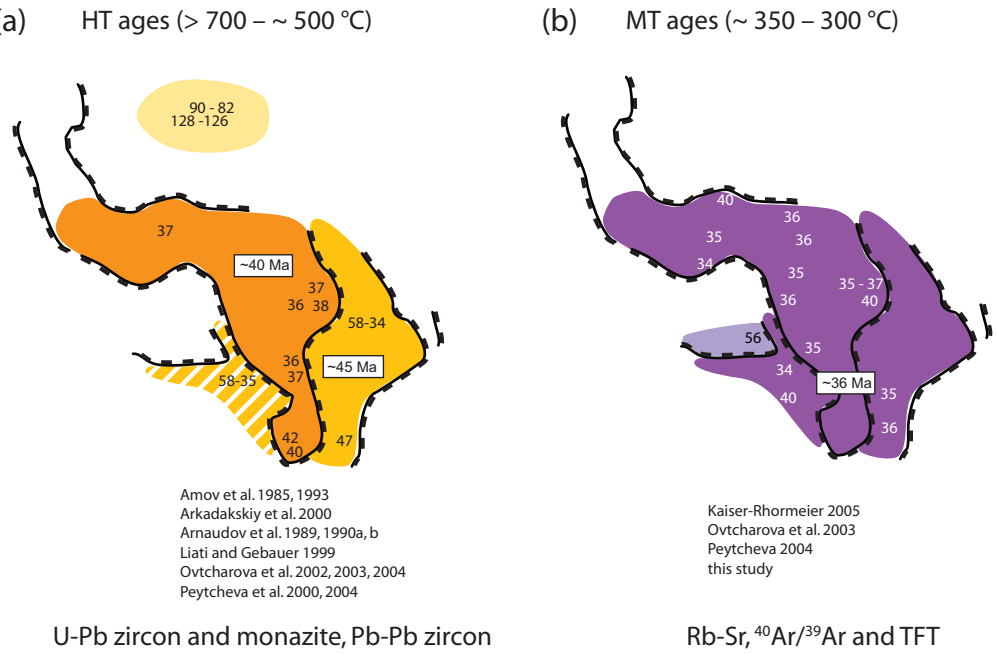

Figure 3.6: Simplified map of the CRMC showing only the main shear zones with cooling ages in the range of (a) $> 700- \sim 500°C$ and in the range of (b) $\sim 300°C$. Colours are used to emphasise zones of similar ages.

cuts the 43 Ma Smilian granite (Ovtcharova et al., 2003b) (Fig. 3.1 and Fig. 3.2). No data allows an unambiguous determination of the onset and the end of the shear zone activity. The TFT age, from a structurally high position, could however suggest that extension in the CRMC had started in the Eocene.

Madan shear zone

The Madan shear zone separates the Arda and Madan Units, in the south of the study area (Fig. 3.1). The AFT ages in the hanging wall are around 32 Ma and those from the footwall are approximately 22 Ma (Fig. 3.5b). This suggests that the shear zone was probably an active detachment at ~22 Ma. Only a minor difference exists in the ZFT ages while the Rb-Sr data are the same (Kaiser Rohrmeier, 2005). The U-Pb and Pb-Pb data do not allow firm conclusions at temperatures >700°C as the age uncertainty in the hanging wall is very large (Amov et al., 1985, 1993; Ovtcharova et al., 2002; Peytcheva et al., 2004; Liati, 2005). The lack of change in the ZFT and higher temperature chronometer ages across the shear zone reflects very fast cooling within the temperature range of ~700 to ~250°C. Interestingly, samples from the southern Startsevo Unit (RD32, 75) seem to have been exhumed along the Madan shear zone as well, as indicated by similar AFT ages for the Arda and the southern Startsevo Units (Fig. 3.5b). This implies that the Madan shear zone does not merge with the Startsevo shear zone at the southern boundary of the Arda Unit (e.g. Gerdjikov, 2005a). Instead, it is likely that it continues southward, maybe even

cutting off the Startsevo shear zone.

Cooling related to normal faulting along the Madan shear zone is indicated by the track-length model of sample RD26, which suggests activity along the fault until ∼15 Ma (Fig. 3.4). (U-Th)/He ages of samples taken across the Madan shear zone are difficult to interpret because there is only one sample on each side of the shear zone and they come from markedly different altitudes. The younger age (15.3 ± 2.1 Ma, RD25) is likely to reflect its lower altitude rather than fault activity, which had thus ceased prior to 15 Ma.

Startsevo shear zone

To the east, the Arda Unit is separated from the Startsevo Unit by the Startsevo–Kanarata shear zone. Field observations show that this shear zone is mainly ductile and only its northern part, the Kanarata shear zone, displays brittle features (Sarov and Gerdjikov, 2002; Sarov et al., 2007b; Pleuger et al., 2009).

The U-Pb and Pb-Pb ages (corresponding to temperatures >700°C) do not vary unambiguously across this zone because the age uncertainty is very large in the hanging wall (Arnaudov et al., 1990b; Ovtcharova et al., 2002, 2003b, 2004; Peytcheva et al., 2004). Nevertheless, the difference between average U-Pb and Pb-Pb ages of ∼37 Ma in the footwall and ∼46 Ma in the hanging wall may indicate extensional shearing at about 37 Ma (Fig. 3.6a). This is in agreement with field observations where top-to-the-east shear senses are coeval with migmatisation (Pleuger et al., 2009) dated with zircon at ∼37 Ma (e.g. Ovtcharova et al., 2004; Peytcheva et al., 2004). Effectively constant ZFT ages across the zone could be related to the previously proposed rapid cooling through the zircon closure temperature, which is recognised throughout the whole region (Fig. 3.5a). Hence, no specific timing of fault activity in this temperature range can be deduced.

The AFT ages should not show any difference across the shear zone as apatite has a low closure temperature (110 ± 10°C, Gleadow and Duddy, 1981; Corrigan, 1993) and the samples are to the south of the brittle Kanarata shear zone next to the ductile Startsevo shear zone. Additionally, to the southwest of Ardino, the shear zone is cut by an undeformed 30.5 ± 1.23 Ma rhyolitic dyke (U-Pb zircon, Ovtcharova et al., 2003b) demonstrating locking of the Startsevo shear zone at that time. This is also confirmed by a Rupelian (33.9–28.4 Ma) rhyolitic flow covering the Startsevo shear zone west of Ardino (Sarov et al., 2007b). The observed contrast in AFT ages across the northern part of the shear zone, therefore, appears to be in conflict with field observations. A possible interpretation is that these ages denote displacement along the Madan shear zone: samples RD24 and RD26 experienced final exhumation and cooling related to this displacement (indicated by the track-length model of RD26, Fig. 3.4), while samples RD34 and 35 were apparently not affected due to their larger distance from the Madan shear zone.

Field evidence suggest that it is unlikely that younger brittle faults are responsible for the age difference between RD24/26 and RD34/35 (Sarov et al., 2007b,c). (U-Th)/He apatite ages vary across the northern segment of the Startsevo shear zone (Fig. 3.5c), with significantly older ages in the northern Startsevo Unit and the Borovitsa Unit (∼30 Ma) than in the Arda Unit (∼15 Ma). Rupelian (33.9–28.4 Ma) rhyolitic flows cover both the Startsevo shear zone, to the west of Ardino, and parts of the northern Startsevo Unit, but are absent further to the south and west (Sarov et al., 2007b,c). The presence of rhyolites covering the metamorphic basement indicates that the latter was already exposed at ∼30 Ma and that erosion has been inconsequential in this area since then. A decreasing proportion of acidic igneous rocks to the east of the 25°E meridian (passing approximately through sample RD26) compared to the west, suggests that the crust below the Startsevo and Borovitsa Units and the Eastern Rhodope Basin was, in Oligocene times, thinner than below the western part of the CRMC (Marchev et al., 2005). The thin crust in the east, presumably indicative of lower relief, and the occurrence of rhyolites both support the concept that the eastern CRMC was characterised by sedimentation and minor erosion since the Oligocene. This may explain older (U-Th)/He ages in the northern Startsevo Unit and the Borovitsa Unit than in other parts of the CRMC. On the other hand, the volcano-sedimentary cover on the Startsevo and Borovitsa Units did not reach more than ∼3 km in thickness, as this would have reset the (U-Th)/He system.

Borovitsa shear zone

The ductile Borovitsa shear zone separates the Startsevo and Borovitsa Units (Sarov et al., 2007a,b). There is no change in the FT and (U-Th)/He ages across the shear zone (Fig. 3.5) and higher temperature chronometer ages are not reported. Therefore, this zone has not been active since at least 33 Ma.

3.4.1 Evolutionary model of the CRMC

Based on the new results and available literature data, a model for the thermal and associated tectonic evolution of the CRMC is presented along W–E "profile 1" and N–S "profile 2" (Fig. 3.7 and Fig. 3.8). Five representative samples have been chosen along each profile to follow their probable positions over time from ∼70 Ma to the present. In profile 1 the Madan and Startsevo Units and the Asenitsa and Borovitsa Units are considered to be equivalents because they occupy comparable structural positions with respect to the Arda Unit. As previously mentioned, homogeneous cooling/exhumation in the CRMC shows that tectonic unroofing has only occurred to a subordinate extent along the studied shear zones. The onset of extension is assumed to be Eocene as suggested by the TFT age of 55.9 Ma. This conclusion agrees with the oldest sediments in the overlying basins: breccias of the Krumovgrad Group, in the extreme east of the CRMC lie on the Kardzhali Unit

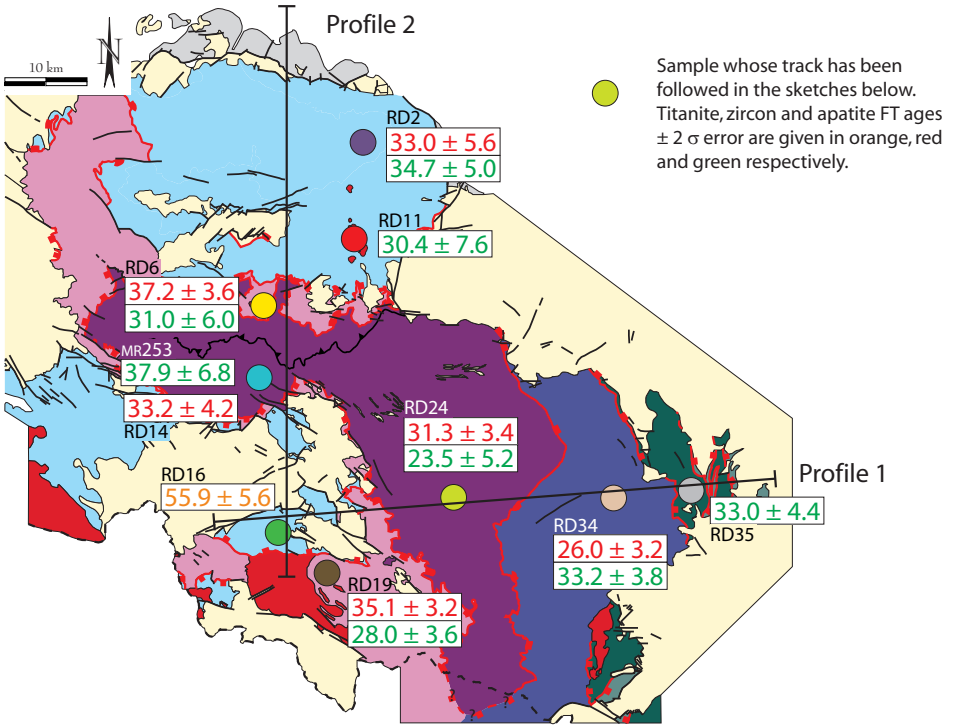

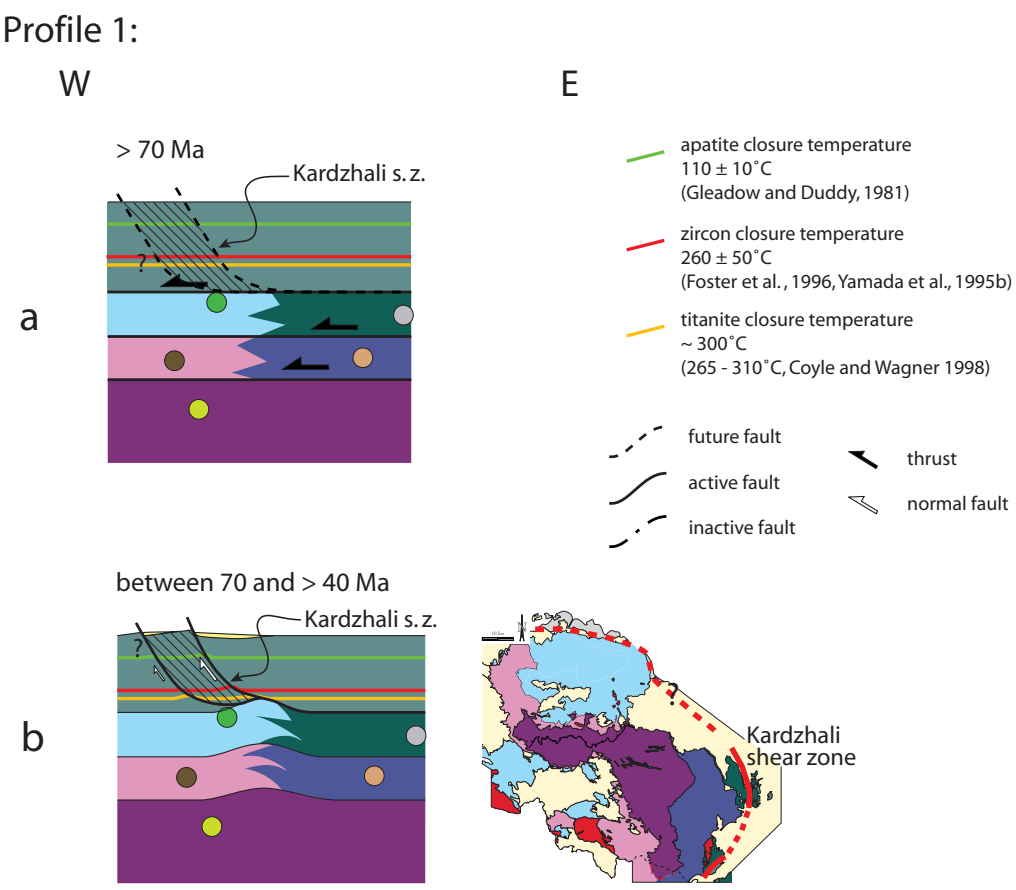

Figure 3.7: (continued on next page) Proposed sketch model for the evolution of the CRMC along the W–E profile 1. For discussion see text. Map key see Fig. 3.1.

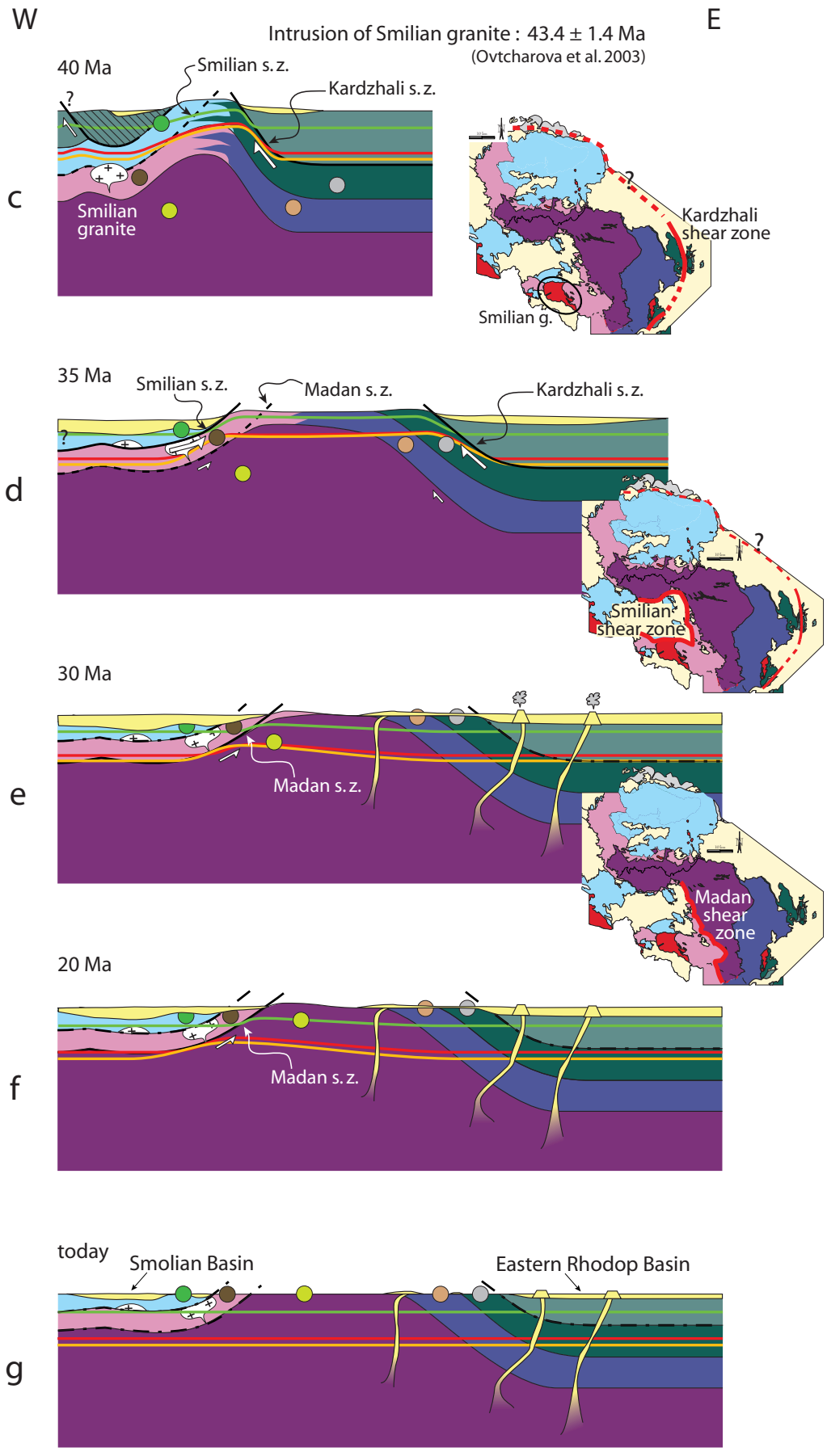

Figure 3.7: (continued)

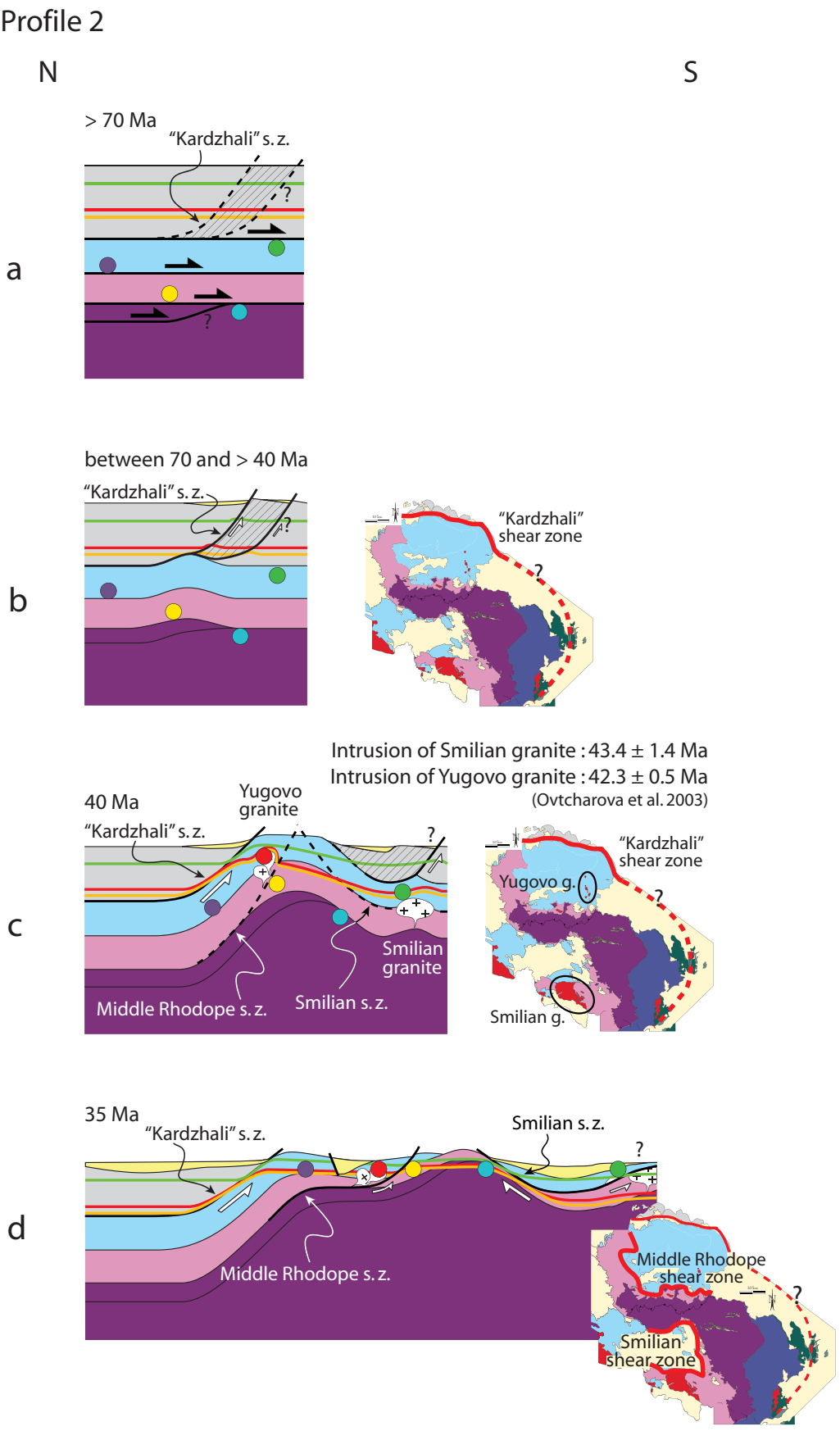

Figure 3.8: (continued on next page) Proposed sketch model for the evolution of the CRMC along the N–S profile 2. The position of profile 2 is indicated on the map in Fig. 3.7. For discussion see text.

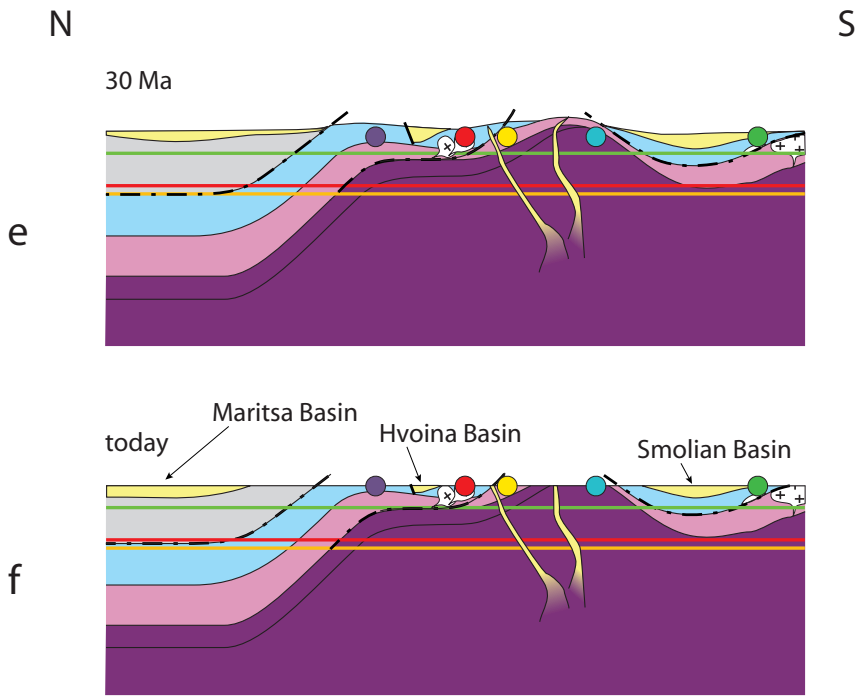

Figure 3.8: (continued)

(Sarov et al., 2007c) and are Maastrichtian to Palaeocene (Goranov and Atanasov, 1992). Major unroofing may therefore have taken place along the Kardzhali shear zone along which greenschist facies rocks of the Kardzhali Unit were juxtaposed against amphibolite facies rocks (Fig. 3.7b).

Early extensional movements accelerated dramatically at ∼40 Ma, with the intrusion of the Smilian and Yougovo granites as indicted by the rapid cooling. The Smilian shear zone was a normal fault at about 37 Ma. We assume that its activity started shortly after 40 Ma (Fig. 3.7c). Migmatisation at ∼37 Ma possibly resulted from the simultaneous normal faulting along the Kardzhali and the Smilian shear zones (Fig. 3.7d). Indeed, the resulting very rapid exhumation may have caused a dramatic rise in the geothermal gradient and decompressional partial melting (Rey et al., 2009). This is consistently coeval with the onset of sedimentation in the Smilian and Hvoina Basins (Fig. 3.1) (Cernjavska, 1977). Faulting along the Kardzhali shear zone ceased at about 30 Ma, shortly after samples RD34 and RD35 cooled below 60°C (Fig. 3.7d,e). The eastern CRMC became dominated by volcanic activity and rhyolitic flows and dykes covered and cut the now inactive Startsevo shear zone (Fig. 3.7e). The Smilian shear zone presumably ceased at about the same time as the Kardzhali shear zone and further faulting concentrated on the Madan shear zone (Fig. 3.7e,f), where normal faulting started around 30 Ma and lasted until ∼15 Ma (Fig. 3.7f). After ∼15 Ma, none of the studied shear zones accommodated discernable vertical displacement between the CRMC units (Fig. 3.7g).

The uppermost Parvenets/Northern Rhodope Unit at the northern end of profile 2, is seen as equivalent to the Kardzhali Unit (Gerdjikov, 2004). Therefore, the major shear zone, which would be the continuation of the Kardzhali shear zone in this section, runs between the Asenitsa and the Parvenets/Northern Rhodope Units (Fig. 3.8a,b). The contact is, however, not evident in the field because it has been obliterated by the Late Cretaceous/Tertiary Maritsa strike-slip fault (Fig. 3.1). Similar evolution along profiles 1 and 2 is consistent with the new data until 40 Ma (Fig. 3.8a–c). Normal faulting along the Middle Rhodope shear zone started at the same time as the Smilian shear zone, shortly after 40 Ma, ceasing by 33 Ma (Fig. 3.8c–e). Temporally focused activity along this shear zone may represent a vital component for fast exhumation and associated migmatisation in the core. We assume that faulting on all shear zones of this N–S profile stopped at 33 Ma (Fig. 3.8e–f) before intrusion of rhyolitic dykes.

3.5 Conclusions

The CRMC is a core complex that cooled and exhumed between the Maastrichtian (70.6–65.5 Ma) and ∼15 Ma. Two stages of cooling are observed. The first was initiated in the Maastrichtian and lasted until ∼33 Ma; very rapid cooling (up to 200°C/Ma) was, however, limited to a phase between ∼40 and ∼33 Ma. The associated exhumation was mainly accommodated along the Kardzahli shear zone, supported by the Smilian and Northern Rhodope shear zones. The second cooling stage occurred after ∼30 Ma and was restricted to the south-central part of the CRMC. It lasted until 15 Ma and was associated with exhumation along the Madan shear zone.

The two cooling/exhumation events may record the extensional phases of two successive "push-pull" cycles as proposed for the central Aegean (Forster and Lister, 2009). One such cycle is caused by the accretion of a continental fragment and the subsequent subduction of an oceanic basin within the Aegean subduction zone; accretion of a continental fragment causes overall compression ("push" phase), and subduction of an oceanic basin causes overall extension ("pull" phase) in the overriding plate (Forster and Lister, 2009).

Peak cooling/exhumation between ∼40 and ∼33 Ma, which is related to the first "push-pull" cycle, could have been triggered by magmatic activity. Volcanism in the CRMC has been reported for the Late Eocene–Oligocene (∼35 – ∼25, references in Marchev et al., 2005) and it is assumed to have been caused by convective removal of the lithospheric mantle and subsequent upwelling of the asthenosphere (Marchev et al., 2004a). The upwelling asthenosphere provided the necessary heat for melt generation, and the consequential weakening of the crust may have provoked the accelerated formation of the CRMC.

Appendix: Analytical methods

Apatite, zircon and titanite grains were separated and concentrated from the rock samples using conventional mineral separation techniques. Grain separates for fission track analysis were mounted in epoxy resin (apatite, titanite) and Teflon (zircon), polished and etched. The apatites were etched in $5.5N$ HNO_3 for 20s at 21°C, zircons in a eutectic melt of $NaOH$ and KOH at 220°C for 10 to 20 hours and titanite in a mixture of HF, HNO_3, HCl and water (volumetric ratios 1:2:3:6, Naeser and McKee, 1970). Irradiation of the samples was carried out at the OSU facility, Oregon State University Radiation Center, USA and the ANSTO facility, Lucas Heights, Australia. Microscopic analysis were completed at ETH Zurich using an optical microscope with a Kinetek computer driven stage (Dumitru, 1995) and magnifications of ×1250 (dry) for apatite and titanite, and ×1600 (oil) for zircon. All ages were determined using the zeta approach (Hurford and Green, 1983), with a zeta value of 416 ± 13 (1σ) for apatite and CN5 standard glass (analyst E. Wüthrich), with zeta values of 133 ± 2.5 (1σ, E.W.) and 120 ± 5 (1σ, D. Seward) for zircon and CN1, and a zeta of 410 ± 10 (1σ, D.S.) for titanite and CN5.

Horizontal confined track lengths in apatite as well as etch pit diameters (Dpar) were measured at a magnification of ×1250 (dry). Dpars are used as a proxy for the apatite chemistry which has an influence on the FT annealing (e.g. Carlson et al., 1999).

Temperature(T)–time(t) paths for the measured track lengths were modelled with the HeFTy program (Ketcham, 2005) using AFT age, c axis corrected track-length distribution and Dpars as input parameters. The model was constrained with two T–t boxes. As a boundary condition one box corresponded to the ZFT age and the zircon closure temperature (260 ± 50°C, Foster et al., 1996), combined with a large box that allowed the path as much freedom as possible through the partial annealing zone. An inverse Monte Carlo algorithm with a multikinetic annealing model (Ketcham et al., 2007) was used to generate the T–t paths. The algorithm generates a large number of paths, which are tested with respect to the input data. The Kolmogorov–Smirnov statistical test was used to test the goodness of fit (GOF) between modelled t–T paths and input data, with merit values of 0.5 and 0.05 for good and acceptable fits respectively. It is important to remember that the best thermal history obtained during this process is not necessarily the only possible. Other thermal histories may match the observed data similarly well and it is therefore imperative to consider as many other geological constraints as possible to determine the most likely path.

Apatite (U-Th)/He analysis were carried out at the University of Kansas and at ETH Zurich following procedures similar to those outlined in House et al. (2000) and Farley and Stockli (2002). Measurements were carried out on 2 to 3 single grains per sample. Helium was degassed using an Nd–YAG laser and subsequently measured on a quadrupole

mass spectrometer (Kansas), respectively on the "Albatros" noble gas mass spectrometer designed and built at ETH Zurich. Uranium, Th and Sm were measured on a VG Plasmaquad–2 ICP–MS in Kansas. At ETH Zurich U and Th (not including Sm) were measured on a Thermo Finnigan, Element II ICP–MS. Ages were corrected for σ–ejection using the F_t ejection correction (Farley et al., 1996; Farley, 2002) and are reported as average values calculated from single grain ages ±2SEM.

Chapter 4

The Kesebir–Kardamos Dome

4.1 Introduction

The Kesebir–Kardamos Dome (KKD), one of the extensional complexes within the Rhodope Massif, is situated in the eastern Rhodope, straddling the border of Greece and Bulgaria (Fig. 4.1, inset). It is divided into an Upper and a Lower Unit (Bonev et al. 2006a) (Fig. 4.1). In the Greek region the nomenclature is slightly different where the KKD is subdivided into the Kimi and Kardamos Complexes (Mposkos, 1989; Mposkos and Krohe, 2000). The Upper Unit is equivalent to the Kimi Complex and the uppermost unit of the Kardamos Complex, which is lithologically indistinguishable from the latter (Bonev et al., 2006a), while the Lower Unit is equivalent to the intermediate and lower units of the Kardamos Complex (Bonev et al., 2006a). The Upper Unit is composed of amphibolites, marbles, various schists and gneisses enclosing eclogite lenses and meta-ophiolites. The Lower Unit is composed of para- and predominantly orthogneisses and migmatitic gneisses intercalated with schists and amphibolites (Bonev et al., 2006b). Both, Upper and Lower Units, have suffered high-pressure eclogite facies metamorphism retrogressed into medium-pressure amphibolite and greenschist facies (e.g. Mposkos and Liati, 1993). Following the terminology of Burg et al. (1996b), the KKD is composed of the intermediate and upper terrane (compare Fig. 4.1 to Fig. 1.3).

4.2 Geological setting

4.2.1 P–T history

The Cretaceous metamorphic evolution of the Upper Unit is characterised by a decreased in the pressure–temperature (P–T) conditions from >26 kbar and 900°C (ultra-high-pressure event with coesite and diamond) to eclogite/granulite facies at 12–17.5 kbar and 730–820°C, and subsequently to greenschist facies conditions (Kozhoukharova, 1998; Mposkos and Krohe, 2000; Mposkos and Kostopoulos, 2001; Bauer et al., 2007) (Tab. 4.1). The

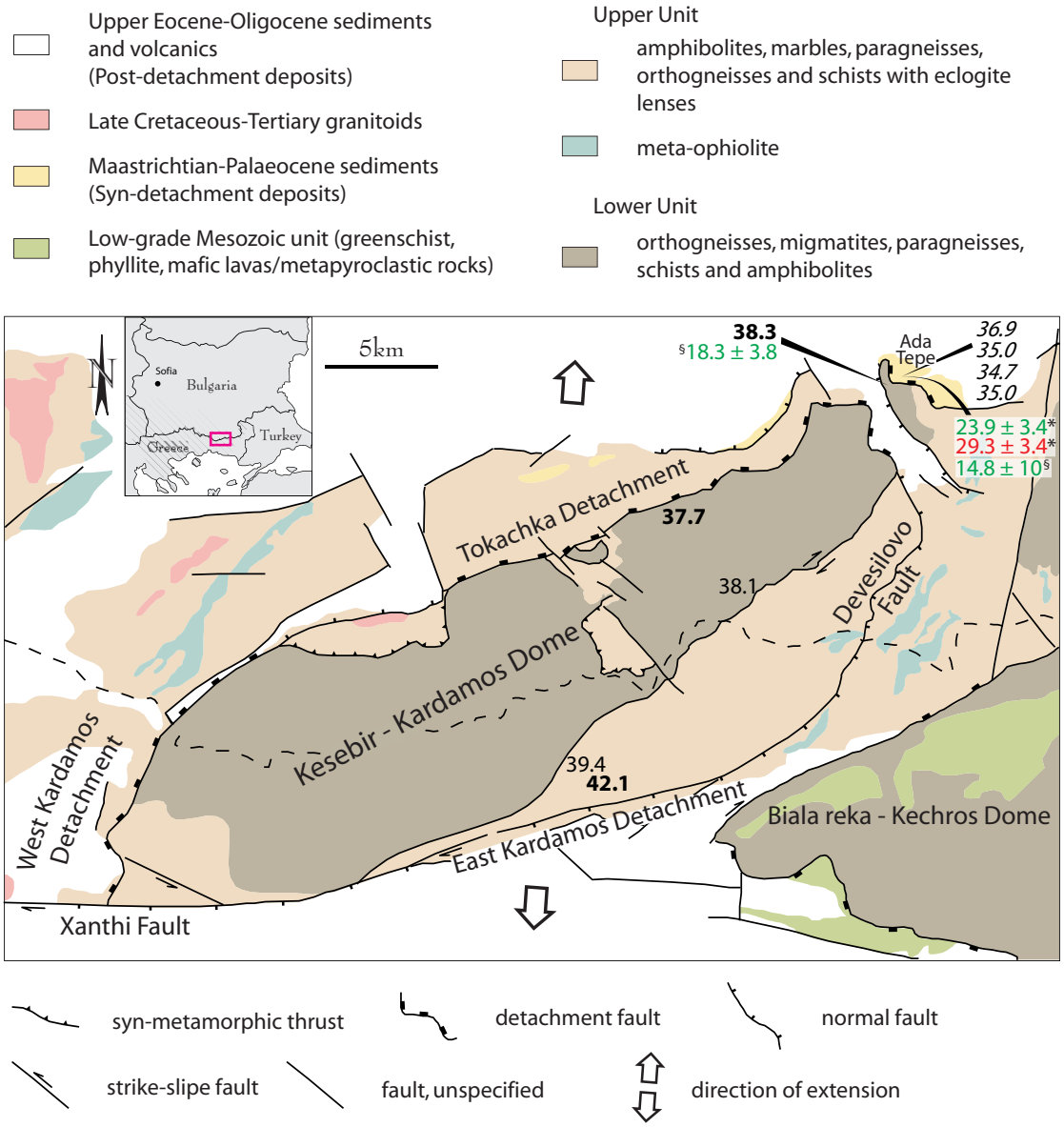

Figure 4.1: Tectonic sketch map of the Kesebir–Kardamos dome (Bonev and Beccaletto, 2007) with published apatite and zircon fission-track (AFT and ZFT) and $^{40}Ar/^{39}Ar$ ages.

Lower Unit retrogressed from eclogite facies conditions of 13–15 kbar and 450–600°C to amphibolite facies conditions with P–T conditions of 3–9 kbar and 550–620°C, and finally to greenschist facies conditions of 2–3 kbar and 400°C (Mposkos, 1989; Mposkos and Liati, 1993; Wawrzenitz and Mposkos, 1997; Marcheva, 1998) (Tab. 4.1). Several authors report different ages for the main metamorphic events in Upper Unit. Wawrzenitz and Mposkos (1997) interpreted a Sm-Nd whole-rock, garnet and clinopyroxene isochron age of 119.9 ± 3.5 Ma as the time of eclogite/granulite facies metamorphism, while Liati et al. (2002) have dated zircons (U-Pb SHRIMP method), attributed to the eclogite/granulite facies paragenesis, at 73.5 ± 3.57 Ma. Bauer et al. (2007) on the other hand, recorded two high-grade metamorphic events; one between 170 and 160 Ma and one at around 115 Ma (U-Pb SHRIMP zircon). Hence, they concluded that the UHP metamorphism must have taken place before 171 Ma. They interpreted a protolith age of 117 Ma (U-Pb SHRIMP zircon) reported by Liati et al. (2002) as dating the partial melting caused by their second high-grade metamorphic event. Medium pressure amphibolite facies metamorphism is related to ages of 65.4 ± 0.7 Ma (Rb-Sr muscovite, Mposkos and Wawrzenitz, 1995), 61.9 ± 1.9 Ma (U-Pb SHRIMP zircon, Liati et al., 2002) and 79 ± 3 Ma (U-Pb SHRIMP zircon, Bauer et al., 2007) (Tab. 4.1). The cooling of the rocks of the Upper and Lower Unit is constrained by thermochronological data: $^{40}Ar/^{39}Ar$ and K-Ar data from various authors on hornblende, biotite and muscovite yield ages of ∼42 to 34 Ma (Krohe and Mposkos, 2002; Marchev et al., 2003; Bonev et al., 2006b; Márton et al., sub) (Fig. 4.1, Tab. 4.1).

4.2.2 Detachments

Eocene cooling is assumed to be due to detachment faulting on either side of the dome (Krohe and Mposkos, 2002; Bonev et al., 2006a). The north-western to northern flank of the dome is bounded by the Tokachka Detachment, called the West–Kardamos Detachment in Greece (Krohe and Mposkos, 2002; Bonev et al., 2006a) (Fig. 4.1). It separates rocks of the Upper Unit from those of the Lower Unit. The detachment on the south-eastern flank is called East–Kardamos Detachment in Greece and Devisilovo Fault in Bulgaria (Krohe and Mposkos, 2002; Bonev et al., 2006a). It cuts through the rocks of the Upper Unit. An un-named fault between the Upper and Lower Units in the south-eastern part of the dome (Fig. 4.1) records a dextral strike-slip component (Bonev et al., 2006a). The Tokachka Detachment exhibits successive overprinting of ductile fabrics by brittle-ductile and then brittle structures. Ductile and brittle lineations are parallel, both indicating top-to-the-NNE shearing (Bonev et al., 2006a). The equivalent West–Kardamos Detachment, on the other hand is a discrete surface underlain by a 0.5–2 m thick cataclastic zone that dips at a low angle and truncates the mylonitic foliation of the footwall (Krohe and Mposkos, 2002). The Devesilovo Fault/East–Kardamos Detachment is a brittle fault contact, which

Table 4.1: Summary of metamorphic events and geochronological data

	Upper Unit Kimi complex and upper part of Kardamos complex						
	P [kbar]	T [°C]	Reference	Age [Ma]	Methode	Rock	Reference
protolith				117 *	U-Pb SHRIMP zircon	garnet pyroxenite	Liati et al. 2002
				288 ± 6	U-Pb SHRIMP zircon	eclogite	Bauer et al. 2007
UHP conditons	> 26	> 900	Mposkos and Kostopoulos 2001	before 171			Bauer et al.2007
(diamond and coesite)			Perraki et al. 2006				
high-pressure	12 – 17	750 – 811	Kozhoukharova 1998	119	Sm-Nd isochron	garnet pyroxenite	Wawrzenitz and Mposkos 1997
eclogite facies	13.5 – 16	750 – 775	Mposkos and Krohe 2000	73	U-Pb SHRIMP zircon		Liati et al. 2002
	> 9	750	Bauer et al. 2007	170	U-Pb SHRIMP zircon	metapelite	Bauer et al. 2007
	15.5 – 17.5	730 – 820	Bauer et al. 2007	160	U-Pb SHRIMP zircon	eclogite	Bauer et al. 2007
				115	U-Pb SHRIMP zircon	eclogite	Bauer et al. 2007
medium-pressure	8 – 10	560 – 623	Kozhoukharova 1998	62	U-Pb SHRIMP zircon		Liati et al. 2002
amphibolite facies	10	600 – 650	Mposkos and Krohe 2000	65	Rb-Sr muscovite	pegmatite	Mposkos and Wawrzenitz 1995
		670 – 680	Bauer et al. 2007	79 ± 3	U-Pb SHRIMP zircon	eclogite	Bauer et al. 2007
cooling				35.0 ± 0.23	$^{40}Ar/^{39}Ar$ adularia	qtz-adularia alteration	Marchev et al. 2003
				35.0 ± 0.15	$^{40}Ar/^{39}Ar$ adularia	qtz-ca-adularia vein	Marton et al. submitted
				34.7 ± 0.1.6	$^{40}Ar/^{39}Ar$ adularia	qtz-ca-adularia vein	Marton et al. submitted
				36.4 ± 0.27	$^{40}Ar/^{39}Ar$ adularia	qtz-ca-adularia vein	Marton et al. submitted

* interpreted by Bauer et al. 2007 as partial melting of garnet-rich mafic rocks during metamorphism

	Lower Unit intermediate and lower part of Kardamos complex						
	P [kbar]	T [°C]	Reference	Age [Ma]	Methode	Rock	Reference
protolith				319 – 305	U-Pb zircon		Peytcheva and von Quadt 1995
				334	Rb-Sr isochron	metapegmatite	Mposkos and Wawrzenitz 1995
				328	Rb-Sr w.r.	orthogneiss	Peytcheva et al. 1998
high-pressure	13 – 16	600	Mposkos and Liati 1993				
eclogite facies	13	450	Macheva 1998				
medium-pressure	< 8	560 – 620	Mposkos 1998				
amphibolite facies	9 – 3	550	Macheva 1998				
greenschist facies	3 – 2	400	Macheva 1998				
cooling				42.1 ± 1	K-Ar muscovite	orthogneiss	Krohe and Mposkos 2002
				39.4 ± 1	K-Ar biotite	orthogneiss	Krohe and Mposkos 2002
				38.13 ± 0.36	$^{40}Ar/^{39}Ar$ muscovite	musc. gneiss	Marchev et al. 2003
				37.73 ± 0.25	$^{40}Ar/^{39}Ar$ biotite	augen gneiss	Marchev et al. 2003

is underlain by a greenschist facies shear zone that developed on the amphibolite facies metamorphics (Krohe and Mposkos, 2002; Bonev et al., 2006a). It dips moderately (∼50°) to the SE with down-slip or dextral oblique south-westward movement that led Bonev et al. (2006a) to consider it as a high angle normal fault. The un-named fault between Upper and Lower Units is interpreted as a bowed-up and abandoned segment of the Tokachka Detachment with ductile top-to-the S to SSW sense of shear. According to Bonev et al. (2006a), it has been reactivated as a dextral strike-slip zone during final doming.

4.2.3 Timing of fault activity

The onset of extension by detachment faulting is inferred to be Palaeocene–Eocene (Bonev et al., 2006a) from the oldest unmetamorphosed sediments in the supra-detachment sedimentary basins (Maastrichtian–Palaeocene Krumovgrad Group deposits, Goranov and Atanasov, 1992). Fault activity continued until the Upper Eocene (Bonev et al., 2006a) which is indicated by a flat-lying Priabonian (37.2–33.9 Ma) breccia-conglomerate suite that unconformably covers the tilted and strongly fractured syn-detachment sediments (Goranov and Atanasov, 1992; Boyanov and Goranov, 1994). $^{40}Ar/^{39}Ar$ muscovite and biotite ages of 38–37 Ma from the Lower Unit in Bulgaria (Marchev et al., 2003) are attributed to the cessation of ductile displacement on the Tokachka Detachment (Bonev et al., 2006b). Brittle deformation is assumed to have begun at 35 Ma, which is constrained by $^{40}Ar/^{39}Ar$ ages on hydrothermal adularia crystallised in open spaces provided by high-angle faults in the hanging wall of the Tokachka Detachment near Ada Tepe (Marchev et al., 2003, 2004b; Márton et al., sub) (Fig. 4.1). Post-detachment extension was accommodated by high-angle normal faults (forming horst-graben structures) which for example caused the exhumation of the northern termination of the KKD (Márton et al., sub). Reset zircon and apatite FT ages from sedimentary rocks of the northern supra-detachment basin and adjacent basement rocks (Fig. 4.1) indicate the onset of high-angle normal faulting between 33 and 24 Ma (Márton et al., sub).

4.3 Methods and Results

The analytical methods are presented in Appendix I and II. Fission-track ages are reported as central ages (Galbraith and Laslett, 1993) with a 2σ error (Fig. 4.2, Tab. 4.2), and (U-Th)/He ages are reported as the average values of three single grain ages ±2 standard errors of the mean (SEM) (Fig. 4.2, Tab. 4.3).

Six samples from the Bulgarian part of the dome yielded very homogeneous zircon fission-track (ZFT) ages ranging from 39.2 ± 4.2 to 35.6 ± 5.2 Ma. The nine apatite fission-track (AFT) ages that include the Greek section are also very homogeneous, overlapping within the error margins. They range from 35.8 ± 8.6 to 28.1 ± 6.2 Ma (Fig. 4.2).

Table 4.2: Apatite (A) and zircon (Z) fission track results. All ages are reported as central ages (Galbraith and Laslett, 1993). ρd is the induced track density, ρs and ρi are the densities of spontaneous and induced tracks, respectively. Numbers in brackets are the numbers of measurements. P(χ^2) is the probability of failing the χ^2–test. U denotes the approximate uranium content. Dpar represents the mean track pit diameter of a sample.

Sample number	**Grid reference**	**Alti. [m]**	**Min.**	**Age [Ma]**	**2σ error**	**No. of grains**	**ρd [$10^5 cm^{-2}$] (counted)**	**ρs [$10^5 cm^{-2}$] (counted)**	**ρi [$10^5 cm^{-2}$] (counted)**	**P(χ^2) [%]**	**U [ppm]**	**Dpar [μm]**
RD 36	N 41° 20' 43.3"	412	Z	**39.2**	**4.2**	20	5.3	29.4	25.8	14.3	175	
	E 25° 33' 15.2"						(2947)	(1529)	(1346)			
			A	**28.1**	**6.2**	20	16.2	3.1	38.2	23.7	28	1.6
							(5595)	(128)	(1594)			
RD 37	N 41° 21' 48.2"	653	Z	**36.4**	**4.2**	20	5.2	31.4	29.2	1.6	197	
	E 25° 31' 53.2"						(2947)	(1642)	(1530)			
			A	**33.4**	**7.6**	20	16.0	2.2	22.1	99.9	19	1.5
							(5595)	(92)	(911)			
RD 38	N 41° 22' 35.2"	595	A	**35.3**	**10.8**	20	15.5	1.7	16.5	44.3	15	2.0
	E 25° 31' 15.1"						(5595)	(60)	(587)			
RD 39	N 41° 23' 36.7"	533	Z	**36.5**	**3.8**	20	5.1	33.3	30.7	6.3	196	
	E 25° 33' 44.6"						(2947)	(1647)	(1521)			
			A	**30.7**	**8.2**	20	15.4	1.6	16.6	97.0	14	1.8
							(5595)	(65)	(678)			
RD 40	N 41° 21' 41.2"	474	Z	**35.6**	**5.2**	17	5.0	38.3	35.0	31.6	247	
	E 25° 37' 28.4"						(2947)	(641)	(585)			
			A	**32.5**	**5.6**	20	15.0	3.0	28.4	99.8	22	1.8
							(5595)	(171)	(1641)			
RD 41	N 41° 21' 21.7"	447	Z	**36.4**	**4.6**	20	5.0	35.5	32.1	82.3	222	
	E 25° 38' 35.1"						(2947)	(621)	(562)			
			A	**31.6**	**4.8**	20	14.7	5.4	52.5	87.3	42	1.8
							(5595)	(234)	(2267)			
RD 43	N 41° 24' 18.1"	541	Z	**37.5**	**4.6**	20	4.9	42.0	36.2	22.8	248	
	E 25° 45' 50.9"						(2947)	(900)	(775)			
			A	**35.8**	**8.6**	20	14.5	1.9	15.9	93.9	14	1.5
							(5595)	(85)	(713)			
RD 85	N 41° 10' 09.2"	137	A	**29.6**	**9.2**	20	12.1	1.0	8.7	76.9	8	1.2
	E 25° 22' 08.1"						(4631)	(48)	(406)			
RD 87	N 41° 11' 33.5"	414	A	**29.1**	**6.6**	20	11.7	2.5	20.8	98.1	20	1.6
	E 25° 25' 42.7"						(4631)	(96)	(798)			

Table 4.3: Apatite (U-Th)/He results: Ages are reported as single grain ages and their mean value. The error of the mean is given as 2SEM (standard error of the mean). SEM is calculated from the age data of the single analysis and the number of analysis (N) per sample (SEM = $\sigma/\sqrt{N}$). F_t is the alpha ejection correction factor (Farley et al., 1996; Farley, 2002).

Sample	Alti. [m]	Grid reference	Grain	Age [Ma]	± [Ma]	U [ppm]	Th [ppm]	Sm [ppm]	Th/U	He [nmol/g]	mass [mg]	Ft
RD37	653	N 41° 21' 48.2"	RD37-1	25.7	1.5	5.6	2.0	20.0	0.3	0.62	6.0	0.71
		E 25° 31' 53.2"	RD37-2	38.8	2.3	11.8	1.1	39.1	0.1	1.81	6.2	0.70
			RD37-3	45.7	2.7	31.5	5.0	48.9	0.2	6.30	5.9	0.77
		Mean Age ± 2SEM		**36.8**	**11.7**							
RD38	595	N 41° 22' 35.2"	RD38-1	28.7	1.7	4.4	0.2	1.7	0.1	0.45	1.5	0.65
		E 25° 31' 15.1"	RD38-2	24.9	1.5	4.0	1.0	2.2	0.2	0.35	1.2	0.62
			RD38-3	21.8	1.3	5.0	1.2	1.7	0.3	0.39	1.5	0.63
		Mean Age ± 2SEM		**25.1**	**4.0**							
RD86	184	N 41° 10' 40.0"	RD86-1	13.0	4.0	1.0	7.5	3.3	7.6	0.11	0.8	0.55
		E 25° 23' 48.0"	RD86-2	12.8	2.5	0.8	4.5	1.4	5.7	0.08	1.9	0.64
			RD86-3	11.8	3.6	0.5	2.5	1.3	5.5	0.04	2.1	0.66
		Mean Age ± 2SEM		**12.6**	**0.8**							

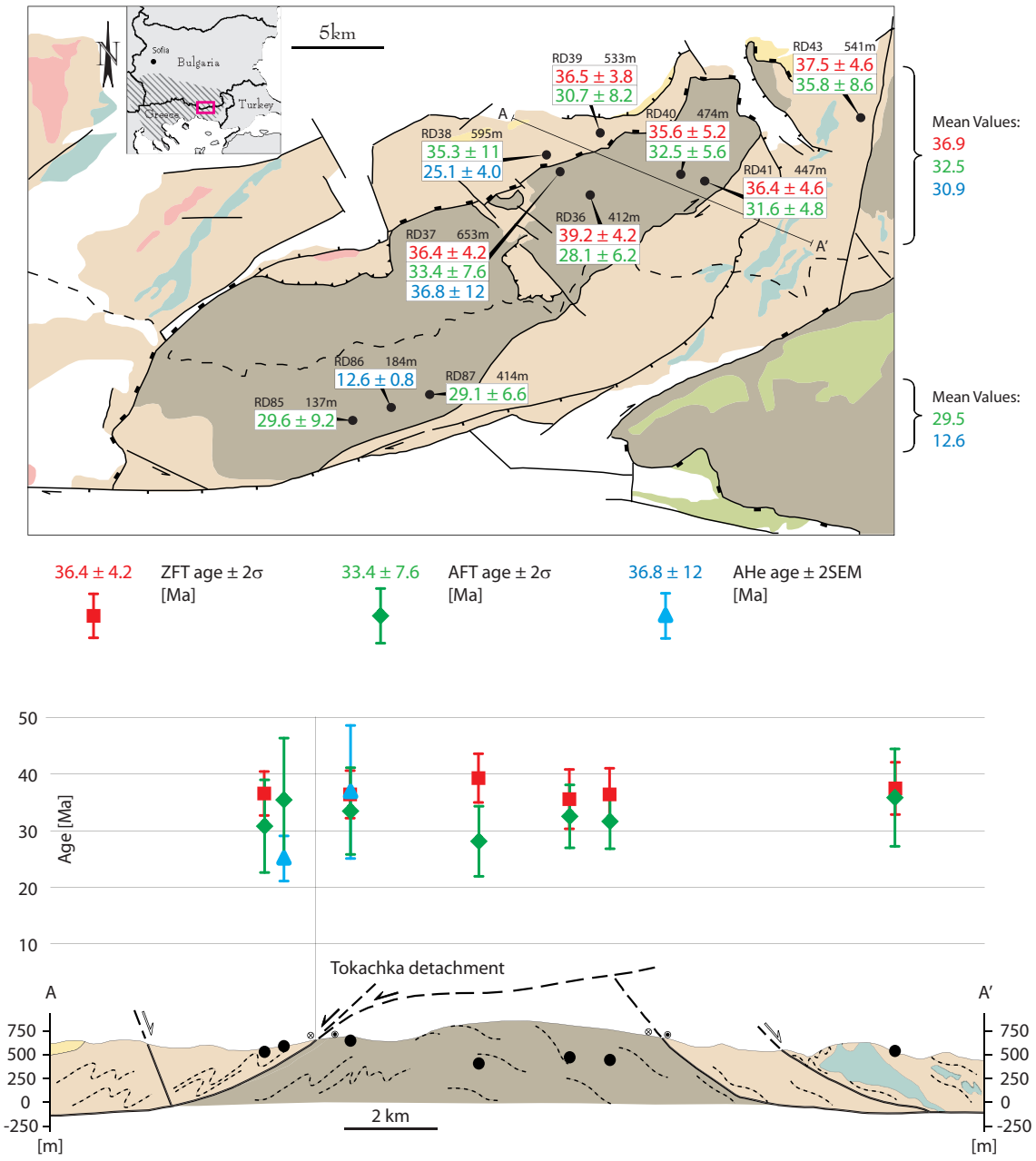

Figure 4.2: Upper: Tectonic sketch map of the Kesebir–Kardamos Dome (Bonev and Beccaletto, 2007) with fission-track and (U-Th)/He data. For key see Fig. 4.1. Lower: Fisson-track and (U-Th)/He data from the northern part of the dome projected onto a NW–SE profile (Bonev et al., 2006a). Profile line is indicated on the map.

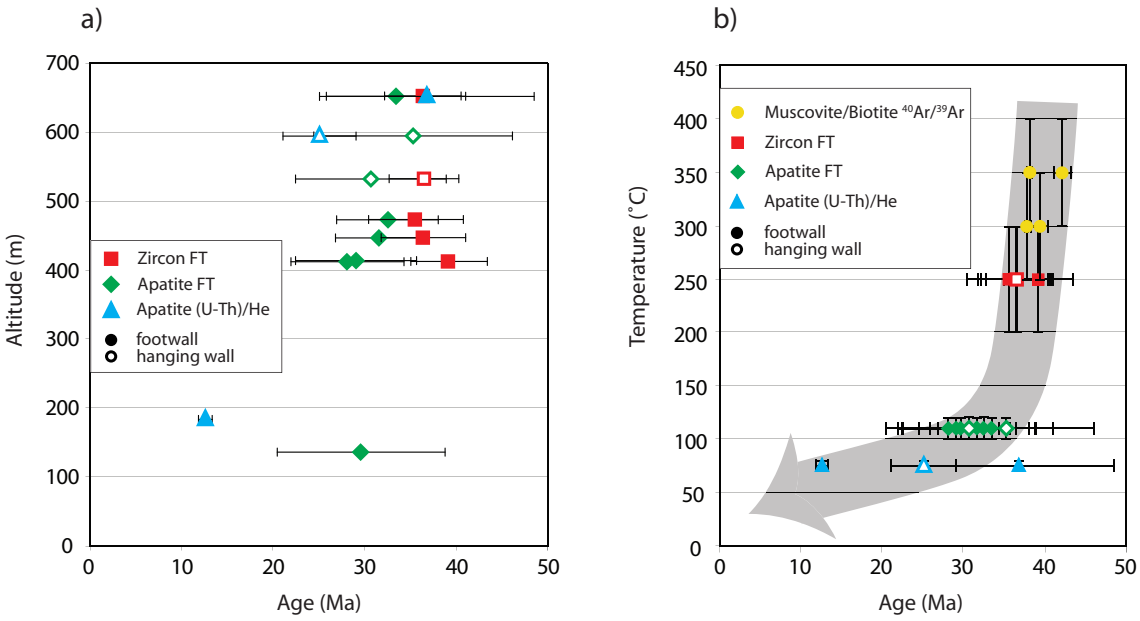

Figure 4.3: a) Age–altitude plot with ages from the hanging and footwall of the Tokachka Detachment; ages with 2σ error. b) Age–closure temperature (T_c) plot of the same data; FT ages with 2σ error; $^{40}Ar/^{39}Ar$ data from Marchev et al. (2003, 2004b) and Bonev et al. (2006b). $^{40}Ar/^{39}Ar$ muscovite $T_c = 350 \pm 50$°C (Hames and Bowring, 1994), $^{40}Ar/^{39}Ar$ biotite $T_c = 300 \pm 50$°C (Harrison et al., 1985), zircon fission-track $T_c = 260 \pm 50$°C (Foster et al., 1996; Yamada et al., 1995), apatite fission-track $T_c = 110 \pm 10$°C (Gleadow and Duddy, 1981), apatite (U-Th)/He $T_c = 75 \pm 5$°C (Wolf et al., 1998).

(U-Th)/He ages were determined on apatite grains for three samples. Two samples in the north, on either side of the Tokachka Detachment, yield 36.8 ± 11.7 and 25.1 ± 4.0 Ma (RD37 and RD38), while the topographically lower sample, close to the East–Kardamos Detachment, gives 12.6 ± 0.8 Ma (RD86).

4.4 Discussion

In the following we will discuss only the Tokachka Detachment as a debate on other structures would require supplementary data.

Although there are only two samples in the hanging wall of the Tokachka Detachment, none of the three thermochronometers used in this work changes across this fault contact (Fig. 4.2). The age–altitude plots (Fig. 4.3a) yield for all three thermochronometers a rather linear trend indicating that the hanging and the footwall of the Tokachka Detachment cooled coevally from ∼300 to 60°C without significant displacement. However, as the ZFT ages are equal within error, regardless of their structural position and sample elevation (Fig. 4.3a), displacement along the Tokachka Detachment within the temperature range bracketed by the zircon and apatite closure temperatures would not be detectable.

In conclusion, the Tokachka Detachment may have ceased functioning by ∼37 Ma, but at least by ∼33 Ma as constrained by the AFT ages. This is in agreement with the post-detachment Priabonian sediments (between ∼37 and ∼34 Ma, Goranov and Atanasov, 1992; Boyanov and Goranov, 1994; Bonev et al., 2006b) that cover the detachment. Late brittle faulting at 35 Ma (Marchev et al., 2003, 2004b; Bonev et al., 2006b; Márton et al., sub) could have generated only small displacements, below the detection limit of the data. The age–altitude plot (Fig. 4.3a) and the age–closure temperature plot, combining previous $^{40}Ar/^{39}Ar$ data with FT and He ages of this study (Fig. 4.3b), further suggest that cooling of the footwall down to ∼200°C at >35 Ma was rapid (at least 30°C/Ma). At 37 to 35 Ma cooling decelerated, as indicated by the increase in age discrepancies between the ZFT data to AFT and AHe data (Fig. 4.3a), and by the decreasing gradient in the cooling path (Fig. 4.3b). The decrease in cooling rate is likely to coincide with the cessation of detachment faulting, hence the Tokachka Detachment would have ceased at ∼37 to 35 Ma. Age data for the hanging wall are sparse and cooling rates can not be easily assessed but clearly after 33 Ma, when the detachment was definitely inactive, they were the same as for the footwall (about 3°C/Ma).

4.5 Conclusions

The Tokachka Detachment, that is inferred to have been initiated in Palaeocene–Eocene (Bonev et al., 2006a), caused rapid cooling (at least 30°C/Ma) of the Kesebir–Kardamos Dome from at least 42 Ma until 37–35 Ma. Detachment faulting ceased by probably ∼37–35 Ma with the associated rapid cooling of the core. From 33 Ma, cooling of the whole region was uniform at about 3°C/Ma.

Chapter 5

Overall conclusions and outlook

5.1 Conclusions

A summary of the timing of extension-driven cooling/exhumation in the three studied subareas of the Rhodope Massif is given in Fig. 5.1.

Cooling/exhumation in the Rhodope was initiated in Maastrichtian to Early Palaeocene times in the northern and eastern parts of the massif (CRMC and KKD, respectively). Early cooling was, however, slow as it only reached a climax at approximately 40 Ma, in all parts of the Rhodope. This widespread climax is indicated by (i) rapid cooling/exhumation between at least 42 and ∼35 Ma in the KKD, controlled by the Tokatcha Detachment, (ii) very rapid cooling/exhumation in the CRMC between 40 and ∼33 Ma, presumably associated with faulting along the Kardzhali shear zone and supported by the Smilian and Northern Rhodope shear zones, and (iii) the onset of cooling/exhumation in the SRCC at ∼40 Ma, controlled by the Kerdilion Detachment and lasting until about 26 Ma.

In the three subareas, a change in the thermo-mechanical evolution is observed between 37 and 20 Ma. In the KKD, detachment faulting stopped between 37 and 33 Ma; further minor extension was accommodated by high-angle normal faults (e.g. Márton et al., sub). In the CRMC, major cooling/exhumation along the Kardzhali shear zone ceased at 33 Ma and slower cooling, between ∼30 and 15 Ma, was localised in the south-central part of the core complex, along the Madan shear zone. In the SRCC, activity along the Kerdilion Detachment ceased at ∼26 Ma and the Strymon Valley Detachment was initiated not later than 20 Ma, causing rapid cooling until approximately 8 Ma. Hence, the timing of these thermo-mechanical changes varies geographically from 37–33 Ma in the east of the Rhodope Massif, through 33–30 Ma in the north to 26–20 Ma in the southwest.

These changes can possibly be attributed to the transition from syn-orogenic extension to post-orogenic, slab-rollback driven extension as previously reported for the Aegean (Jolivet et al., 2004; Brun and Faccenna, 2008). However, this is in contradiction with the assumption that syn-orogenic extension involves little or no overall horizontal stretching

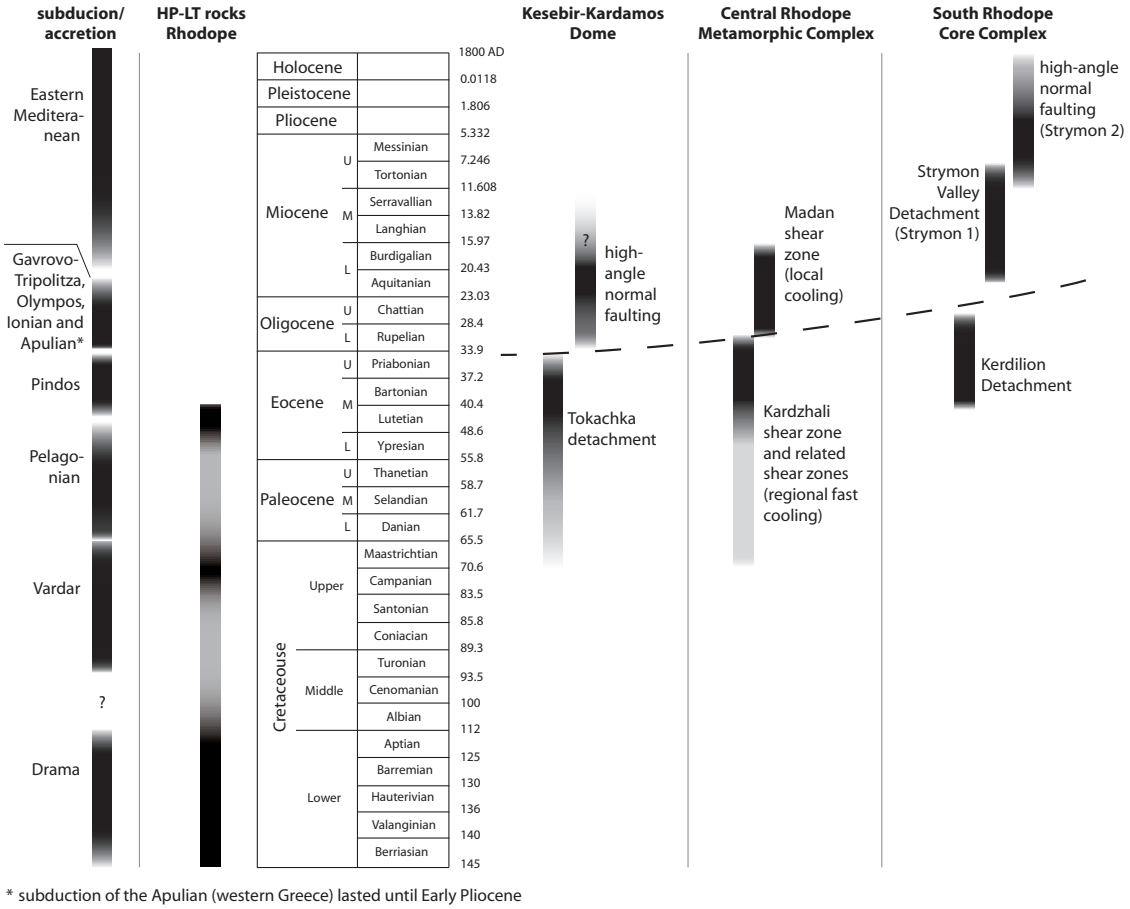

Figure 5.1: Left: Summary of accretion/subduction events in the Aegean region and high-pressure events in the Rhodope Massif (Ricou et al., 1998; Liati and Gebauer, 1999; Jolivet et al., 2003, 2004; Ferrière et al., 2004; Liati, 2005; van Hinsbergen et al., 2005; Bonev et al., 2006a; Bauer et al., 2007; Brun and Faccenna, 2008; Forster and Lister, 2009). Right: Summary of the cooling events in the Rhodope Massif.

of the crust or lithosphere and does not involve core complex formation but channel flow or extrusion wedges (e.g. Brun and Faccenna, 2008; Forster and Lister, 2009). Another possibility is that we record the extensional phases of two successive "push-pull" cycles as proposed for the central Aegean by Forster and Lister (2009). They state that the Aegean lithosphere was subject to a sequence of "push-pull" cycles associated with individual accretion events (Ricou, 1994; Ricou et al., 1998; Stampfli and Borel, 2004): on the one hand, accretion of a continental fragment causes overall shortening and, on the other hand, subduction of an oceanic basin causes overall extension in the overriding plate (Lister and Forster, 2009). In the central Aegean two distinct phases of core complex formation are assumed to represent general extension after a period of general compression (Forster and Lister, 2009). The first extension phase initiated at ∼35 Ma and lasted for about ∼5 Ma (Forster and Lister, 2009); the second phase started at 24 Ma and lasted until 10 Ma (e.g. Lister et al., 1984; Wijbrans and McDougall, 1988; Gautier and Brun, 1994; Brichau et al., 2006). These two phases are almost coeval with the two cooling stages identified in the Rhodope Massif, confirming that large horizontal stretching was involved (Forster and Lister, 2009). Peak cooling/exhumation in the Rhodope between 40 and 33 Ma, the first phase of core complex formation in the Aegean, and subduction of the Pindos Ocean (from ∼42 until 35–33 Ma, Ferrière et al., 2004) following accretion of the Pelagonian continental block to the Moesian platform and previously accreted units such as the Drama continental fragment and the Vardar Ocean (Fig. 5.1, left) coincide. The second phase of core complex related extension in the Rhodope Massif and the central Aegean is coeval with the accretion/subduction of a continental block composed of several entities (Gavrovo–Tripolitza, Olympos, Ionian and Apulian), and the subsequent subduction of the Mediterranean Ocean (Fig. 5.1). Such "push-pull" cycles were possibly also responsible for the different high-pressure events in the Rhodope Massif (between ∼180 and ∼110 Ma, at about 70 Ma, and between 50 and 40 Ma, Wawrzenitz and Mposkos, 1997; Liati et al., 2002; Liati, 2005; Bauer et al., 2007) (Fig. 5.1). They may also relate to the Maastrichtian/Palaeocene onset of extension in the KKD and the CRMC as a weak "pull" after the 70 Ma "push" phase.

The fact that cooling/exhumation in the Rhodope Massif reached a peak at around 40 Ma may also be related to magmatic activity. Volcanism in the Rhodope Massif has been reported for the Late Eocene–Oligocene (39–26 Ma, references in Marchev et al., 2005) and it is thought that convective removal of the lithospheric mantle and subsequent upwelling of asthenosphere material provided the necessary heat to cause melt generation (Marchev et al., 2004a). Other models, such as slab-rollback or mantle delamination also cause asthenosphere upwelling and heating (Marchev et al., 2004a; Brun and Faccenna, 2008) and seem to be more appropriate for the development of the Aegean subduction zone, where magmatic activity migrated from north to south. However, these latter models

have been declared to be inconsistent with the chemical composition of igneous rocks in the Rhodope Massif (Marchev et al., 2004a). Nevertheless, heating and the consequent weakening of the crust below the Rhodope Massif, either previous to or coeval with the onset of volcanic activity on the surface, might have triggered accelerated core complex formation at around 40 Ma.

At around 7 Ma, detachment faulting in the Rhodope Massif probably stopped with the cessation of the Strymon Valley Detachment. However, high-angle normal faults such as the Xanthi Fault or the faults of Strymon 2 remained active until recently (Goldsworthy et al., 2002, European–Mediterranean Seismological Centre, www.emsc-csem.org).

5.2 Outlook

Despite the fact that this thesis presents a set of insightful and comprehensive data, the evolution of the Rhodope Massif still has a variety of open questions to be addressed in future projects.

Only a small part of the evolution of the KKD can be interpreted with the data obtained during this work, and the timing of major events is still relatively poorly constrained. It is therefore necessary to obtain a better spatial coverage of FT ages, and also higher closure temperature chronometer ages (such as $^{40}Ar/^{39}Ar$ or Rb-Sr), as unroofing of the whole dome was probably completed when samples now at the surface cooled through the apatite closure temperature.

In the CRMC, thermochronological dating of the Kardzhali and the Parvenets/Northern Rhodope Units is crucial in order to fully understand its unroofing history. Such data is currently missing. Furthermore it is important to have a better spatial coverage of higher closure temperature chronometer ages in the structurally high Asenitsa and Borovits Units to clarify the early cooling history of the CRMC.

Bibliography

Amov, B., Baldjieva, T., Breskovska, V., Dimitrov, R. B. K., Stoikov, C., and Todosov, T. (1985). Isotopic composition of lead, origin and age of deposits in south Bulgaria. *Geolgija Rudnyich Mjestororozhdenij*, 3:3–17.

Amov, B., Kolkovski, B., and Dimitrov, R. (1993). Genesis and age of hydrothermal ore mineralization in the Rhodope metallogenic zone on the basis of the isotopic composition of lead in galena. *Annuaire de l'université de Sofia "St.Kliment Ohridski" Faculté de Géologie et Géographie*, 85:73–98.

Arkadakskiy, S., Böhm, S. C., Heaman, L., Cherneva, Z., and Stancheva, E. (2000). New U-Pb results from the central Rhodope Mts., Bulgaria. In Bogdanov, K., editor, *Geodynamics and Ore Deposit Evolution of the Alpine–Balkan–Carpathian–Dinaride–Province. Abstracts, ABCD–GEODE 2000 Workshop, Borovets, Sofia University, Bulgaria*, page 5.

Armour-Brown, A., de Brujin, H., Maniati, C., Siatos, G., and Neisen, P. (1977). The geology of the Neogene sediments north of Serrai and the use of rodent faunas for biostratigraphic control. *Proceedings of the Sixth Colloquium on the Geology of the Aegean region, Athens, Institute of Geological and Mining Research*, 2:615–622.

Arnaudov, V., Amov, B., Baldjieva, T., and Pavlova, M. (1990a). Tertiary migmatic pegmatites in the central Rhodope crystalline complex; uranium-lead zircon dating. *Geologica Balcanica*, 20(6):25–32.

Arnaudov, V., Amov, B., Bratnitzkii, B., and Pavlova, M. (1989). Isotopic geochronology of magmatic and metamorphic rocks from Balkanides and Rhodope Massif. *XIV – The Congres CBGA, Sofia*, pages 1145–1157.

Arnaudov, V., Amov, B., Cherneva, Z., Arnaudova, R., Pavlova, M., and Bartnistsky, E. (1990b). Petrological-geochemical and lead-isotope evidence of Alpine metamorphism in the Rhodope crystalline complex. *Geologica Balcanica*, 20(5):29–44.

Avigad, D. and Garfunkel, Z. (1989). Low-angle faults above and below a blueschist belt – Tinos Island, Cyclades, Greece. *Terra Nova*, 1(2):182–187.

Avigad, D., Garfunkel, Z., Jolivet, L., and Azanon, J. M. (1997). Back arc extension and denudation of Mediterranean eclogites. *Tectonics*, 16(6):924–941.

Bauer, C., Rubatto, D., Krenn, K., Proyer, A., and Hoinkes, G. (2007). A zircon study from the Rhodope metamorphic complex, N–Greece: Time record of a multistage evolution. *Lithos*, 99(3–4):207–228.

Bonev, N. and Beccaletto, L. (2007). From syn- to post-orogenic Tertiary extension in the north Aegean region: constraints on the kinematics in the eastern Rhodope–Thrace, Bulgaria–Greece and the Biga Peninsula, NW Turkey. In Taymaz, T., Yilmaz, Y., and Dilek, Y., editors, *The Geodynamics of the Aegean and Anatolia*, volume 291, pages 113–142. Geological Society, London, Special Publications.

Bonev, N., Burg, J.-P., and Ivanov, Z. (2006a). Mesozoic-Tertiary structural evolution of an extensional gneiss dome – the Kesebir–Kardamos dome, eastern Rhodope (Bulgaria–Greece). *International Journal of Earth Sciences*, 95(2):318–340.

Bonev, N., Marchev, P., and Singer, B. (2006b). $^{40}Ar/^{39}Ar$ geochronology constraints on the Middle Tertiary basement extensional exhumation, and its relation to ore-forming and magmatic processes in the eastern Rhodope (Bulgaria). *Geodinamica Acta*, 19(5):267–282.

Bonneau, M. (1984). Correlation of the Hellenic nappes in the southeast Aegean and their tectonic reconstruction. In Dixon, J. and Robertson, A., editors, *Geological Evolution of the eastern Mediterranean*, volume 17, pages 517–527. Geological Society London Special Publications.

Boyanov, I. and Goranov, A. (1994). Late Alpine (Palaeogene) superimposed depressions in parts of southeast Bulgaria. *Geologica Balcanica*, 31:3–36.

Brichau, S., Ring, U., Carter, A., Monie, P., Bolhar, R., Stockli, D., and Brunel, M. (2007). Extensional faulting on Tinos island, Aegean sea, Greece: How many detachments? *Tectonics*, 26(4):19.

Brichau, S., Ring, U., Ketcham, R. A., Carter, A., Stockli, D., and Brunel, M. (2006). Constraining the long-term evolution of the slip rate for a major extensional fault system in the central Aegean, Greece, using thermochronology. *Earth and Planetary Science Letters*, 241(1–2):293–306.

Brun, J.-P. and Faccenna, C. (2008). Exhumation of high-pressure rocks driven by slab rollback. *Earth and Planetary Science Letters*, 272(1–2):1–7.

Brun, J.-P. and Sokoutis, D. (2007). Kinematics of the southern rhodope core complex (north Greece). *International Journal of Earth Sciences*, 96(6):1079–1099.

Buick, I. and Holland, T. (1989). The P-T-t path associated with crustal extension, Naxos, Cyclades, Greece. In Daly, J. S., Cliff, R. A., and Yardley, B. W. D., editors, *Evolution of Metamorphic Belts*, volume 43, pages 365–369. Geological Society, London, Special Publications.

Buick, I. S. (1991). The late Alpine evolution of an extensional shear zone, Naxos, Greece. *Journal of the Geological Society*, 148:93–103.

Burchfiel, B. C., Nakov, R., Dumurdzanov, N., Papanikolaou, D., Tzankov, T., Serafimovski, T., King, R., Kotzev, V., Todosov, A., and Nurce, B. (2008). Evolution and dynamics of the Cenozoic tectonics of the south Balkan extensional system. *Geosphere*, 4:919–938.

Burchfiel, B. C., Nakov, R., and Tzankov, T. (2003). Evidence from the Mesta half-graben, SW Bulgaria, for the Late Eocene beginning of Aegean extension in the Central Balkan Peninsula. *Tectonophysics*, 375(1–4):61–76.

Burchfiel, C. B., Nakov, R., Tzankov, T., and Royden, L. H. (2000). Cenozoic extension in Bulgaria and northern Greece: the northern part of the Aegean extensional regime. In Bozkurt, E., Winchester, J. A., and Piper, J. D. A., editors, *Tectonics and Magmatism in Turkey and the Surrounding Area*, volume 173, pages 325–352. Geological Society, London, Special Publications.

Burg, J.-P., Godfriaux, I., and Ricou, L. E. (1995). Extension of the Mesozoic Rhodope thrust units in the Vertiskos–Kerdilion Massifs (northern Greece). *Comptes Rendus De L'Academie Des Sciences Paris*, 320(9):889–896.

Burg, J.-P., Ivanov, Z., Ricou, L. E., Dimor, D., and Klain, L. (1990). Implications of shear-sense criteria for the tectonic evolution of the Central Rhodope massif, southern Bulgaria. *Geology*, 18(5):451–454.

Burg, J.-P., Klain, L., Ivanov, Z., Ricou, L. E., and Dimov, D. (1996a). Crustal-scale, thrust complex in the rhodope massif. evidence from structures and fabrics. In *The ocean basins and margins, Vol. 8 The Tethys Ocean*, pages 125–149.

Burg, J.-P., Ricou, L. E., Ivanov, Z., Godfriaux, I., Dimov, D., and Klain, L. (1996b). Synmetamorphic nappe complex in the Rhodope Massif. Structure and kinematics. *Terra Nova*, 8(1):6–15.

Büttner, D. and Kowalczyk, G. (1978). Late Cenozoic stratigraphy and paleogeography of Greece – A review. In Closs, H., Roeder, D., and Schmidt, K., editors, *Alps–Apennines–Hellenides*. Stuttgart, E. Schweizerbart.

Carlson, W. D., Donelick, R. A., and Ketcham, R. A. (1999). Variability of apatite fission-track annealing kinetics: I. Experimental results. *American Mineralogist*, 84(9):1213–1223.

Cernjavska, S. (1977). Palynological studies on Paleogene deposits in south Bulgaria. *Geologica Balcanica*, 7(4):3–26.

Corrigan, J. D. (1993). Apatite fission-track analysis of Oligocene strata in South Texas, USA – Testing annealing models. *Chemical Geology*, 104(1–4):227–249.

Coyle, D. A. and Wagner, G. A. (1998). Positioning the titanite fission-track partial annealing zone. *Chemical Geology*, 149(1–2):117–125.

Del Moro, A., Kyriakopoulos, K., Pezzino, A., Atzori, P., and Lo Giudice, A. (1990). The metamorphic complex associated to the Kavala plutonites: An Rb-Sr geochronological, petrological and structural study. *Geologica Rhodopica*, 2:143–152.

Dercourt, J. and Ricou, L. E. (1987). Discussion sur la place de la Bulgarie au sein du système alpin. *Rev. Bulg. Geol. Soc.*, 48(3):1–14.

Dhont, D., Yanev, Y., Bardintzeff, J. M., and ChorowiCz, J. (2008). Evolution and relationships between volcanism and tectonics in the central-eastern part of the Oligocene Borovitsa caldera (eastern Rhodopes, Bulgaria). *Journal of Volcanology and Geothermal Research*, 171(3–4):269–286.

Dickin, A. (1995). *Radiogenic Isotope Geology*. Cambridge University Press, Cambridge, 2nd edition.

Dimov, D., Dobrev, S., Ivanov, Z., Kolkovski, B., and Sarov, S. (2000). Structure, alpine evolution and mineralizations of the Central Rhodopes area (south Bulgaria). In Ivanov, Z., editor, *Geodynamics and ore deposits evolution of the Alpine–Balkan–Carpathian–Dinaride province, Guide to Excursion B, ABCD–GEODE, Borovets, University Press "St. Kliment Ohridski", Bulgaria*.

Dinter, D. A. (1994). *Tectonic evolution of the Rhodope metamorphic core complex, northeastern Greece*. PhD thesis, Massachusetts Institute of Technology, Cambridge.

Dinter, D. A. (1998). Late Cenozoic extension of the Alpine collisional orogen, northeastern Greece: Origin of the north Aegean basin. *Geological Society of America Bulletin*, 110(9):1208–1226.

Dinter, D. A., Macfarlane, A., Hames, W., Isachsen, C., Bowring, S., and Royden, L. (1995). U-Pb and $^{40}Ar/^{39}Ar$ geochronology of the Symvolon granodiorite – Implications

for the thermal and structural evolution of the Rhodope Metamorphic Core Complex, northeastern Greece. *Tectonics*, 14(4):886–908.

Dinter, D. A. and Royden, L. (1993). Late Cenozoic extension in northeastern Greece – Strymon Valley detachment system and Rhodope Metamorphic Core Complex. *Geology*, 21(1):45–48.

Dumitru, T. A. (1995). A new computer automated microscope stage system for fission-track analysis. *Nuclear Tracks and Radiation Measurements*, 21:575–580.

Farley, K. A. (2000). Helium diffusion from apatite: General behavior as illustrated by Durango fluorapatite. *Journal of Geophysical Research–Solid Earth*, 105(B2):2903–2914.

Farley, K. A. (2002). (U-Th)/He dating: Techniques, calibrations, and applications. In Porcelli, D. B. C. J. W. R., editor, *Nobel Gases in Geochemistry and Cosmochemistry*, volume 47, pages 819–844. Mineralogical Society of America.

Farley, K. A. and Stockli, D. F. (2002). (U-Th)/He dating of phosphates: Apatite, monazite, and xenotime. In Kohn, M. J., Rakovan, J., and Hughes, J. M., editors, *Conference on Phosphates – Geochemical, Geobiological and Materials Importance, Golden, Colorado*, pages 559–577. Mineralogical Soc America.

Farley, K. A., Wolf, R. A., and Silver, L. T. (1996). The effects of long alpha-stopping distances on (U-Th)/ He ages. *Geochimica Et Cosmochimica Acta*, 60(21):4223–4229.

Fassoulas, C., Kilias, A., and Mountrakis, D. (1994). Postnappe stacking extension and exhumation of high-pressure low-temperature rocks in the Island of Crete, Greece. *Tectonics*, 13(1):127–138.

Ferrière, J., Reynaud, J. Y., Pavlopoulos, A., Bonneau, M., Migiros, G., Chanier, F., Proust, J. N., and Gardin, S. (2004). Geologic evolution and geodynamic controls of the Tertiary intramontane piggyback Meso-Hellenic basin, Greece. *Bulletin De La Societe Geologique De France*, 175(4):361–381.

Forster, M. and Lister, G. (2009). Core-complex-related extension of the Aegean lithosphere initiated at the Eocene–Oligocene transition. *Journal of Geophysical Research–Solid Earth*, 114:36.

Foster, D. A., Gleadow, A. J. W., Reynolds, S. J., and Fitzgerald, P. G. (1993). Denudation of metamorphic core complexes and the reconstruction of the transition zone, West Central Arizona – Constraints from apatite fission-track thermochronology. *Journal of Geophysical Research–Solid Earth*, 98(B2):2167–2185.

Foster, D. A., Kohn, B. P., and Gleadow, A. J. W. (1996). Sphene and zircon fission track closure temperatures revisited: empirical calibration from $^{40}Ar/^{39}Ar$ diffusion studies of K-feldspar and biotite. *International Workshop on Fission Track Dating Abstracts, August 26–30, University of Gent, Gent*, page 37.

Galbraith, R. F. and Laslett, G. M. (1993). Statistical-models for mixed fission-track ages. *Nuclear Tracks and Radiation Measurements*, 21(4):459–470.

Gautier, P. and Brun, J.-P. (1994). Ductile crust exhumation and extensional detachments in the central Aegean (Cyclades and Evvia Islands). *Geodinamica Acta*, 7(2):57–85.

Gautier, P., Brun, J.-P., and Jolivet, L. (1993). Structure and kinematics of Upper Cenozoic extensional detachment on Naxos and Paros (Cyclades Islands, Greece). *Tectonics*, 12(5):1180–1194.

Gautier, P., Brun, J.-P., Moriceau, R., Sokoutis, D., Martinod, J., and Jolivet, L. (1999). Timing, kinematics and cause of Aegean extension; a scenario based on a comparison with simple analogue experiments.; Basin dynamics and basin fill; models and constraints; Part I. *Tectonophysics*, 315(1–4):31–72.

Georgieva, M., Cherneva, Z., Kolcheva, K., Sarov, S., Gerdjikov, I., and Voinova, E. (2002). P-T metamorphic path of sillimanite-bearing schists in an extensional shear zone, central Rhodopes, Bulgaria. *Geokhimiya, Mineralogiya i Petrologiya*, 39:95–106.

Gerdjikov, I. (2004). Hight-strain greenshist belt along the margins of the Central Rhodopes. In *Bulgarian Geological Society, Annual Scientific Conference*, pages 24–26.

Gerdjikov, I. (2005a). Low-angle fault zones in the Central Rhodopes. pages 25–29.

Gerdjikov, I. (2005b). Tectonic position, fabric and significance of Aleksandrovo and Pripek granites (south Bulgaria). *Review of the Bulgarian Geological Society*, 66(1–3):75–86.

Gessner, K., Ring, U., Johnson, C., Hetzel, R., Passchier, C. W., and Gungor, T. (2001). An active bivergent rolling-hinge detachment system: Central Menderes metamorphic core complex in western Turkey. *Geology*, 29(7):611–614.

Gleadow, A. J. W. and Duddy, I. R. (1981). A natural long-term Track annealing experiment for apatite. *Nuclear Tracks and Radiation Measurements*, 5(1–2):169–174.

Goldsworthy, M., Jackson, J., and Haines, J. (2002). The continuity of active fault systems in Greece. *Geophysical Journal International*, 148(3):596–618.

Goranov, A. and Atanasov, G. (1992). Lithostratigraphy and formation conditions of Maastrichtian–Paleocene deposit in Krumovgrad District. *Geologica Balcanica*, 22:71–82.

Gorur, N. and Okay, A. I. (1996). A fore-arc origin for the Thrace Basin, NW Turkey. *Geologische Rundschau*, 85(4):662–668.

Green, P. F., Duddy, I. R., Gleadow, A. J. W., Tingate, P. R., and Laslett, G. M. (1986). Thermal Annealing of Fission Tracks in Apatite. 1. A Qualitative Description. *Chemical Geology*, 59(4):237–253.

Hames, W. E. and Bowring, S. A. (1994). An empirical evaluation of the argon diffusion geometry in muscovite. *Earth and Planetary Science Letters*, 124(1–2):161–167.

Harre, W., Kockel, F., Kreuzer, H., Lenz, H., Mueller, P., and Walther, H. W. (1968). Über Rejuvenationen im Serbo–Mazedonischen Massiv (Deutung radiometrischer Altersbestimmungen). *Report of the International Geological Congress*, 6:223–236.

Harrison, M. T. (1981). Diffusion of ^{40}ar in hornblende. *Contributions to Mineralogy and Petrology*, 78.

Harrison, M. T., Duncan, I., and McDougall, I. (1985). Diffusion of ^{40}ar in biotite: Temperature, pressure and compositional effects. *Geochimica Et Cosmochimica Acta*, 49.

Hejl, E., Weingartner, H., Vavliakis, E., and Psilovikos, A. (1998). Macrorelief features and fission-track thermochronology of the Rila–Rhodope massif (eastern Macedonia, Greece). *Zeitschrift fuer Geomorphologie*, 42(4):517–530.

House, M. A., Farley, K. A., and Stockli, D. (2000). Helium chronometry of apatite and titanite using Nd–YAG laser heating. *Earth and Planetary Science Letters*, 183(3–4):365–368.

Hurford, A. J. and Green, P. F. (1983). The zeta age calibration of fission-track dating. *Chemical Geology*, 41(4):285–317.

Ivanov, Z. (1988). General framework of the Rhodope Massif geological and structural development, in the Balkanides setting. *Bulletin de la Societe Geologique de France*, 4(2):227–240.

Ivanov, Z., Moskovski, S., and Kolceva, K. (1979). Basic features on the structure of the central parts of the Rhodope massif. *Geologica Balcanica*, 9(1):3–50.

Jansen, J. B. H. and Schuiling, R. D. (1976). Metamorphism on Naxos – Petrology and geothermal gradients. *American Journal of Science*, 276(10):1225–1253.

Jolivet, L., Daniel, J. M., Truffert, C., and Goffe, B. (1994). Exhumation of deep-crustal metamorphic rocks and crustal extension in arc and back-arc regions. *Lithos*, 33(1–3):3–30.

Jolivet, L., Faccenna, C., Goffe, B., Burov, E., and Agard, P. (2003). Subduction tectonics and exhumation of high-pressure metamorphic rocks in the Mediterranean orogens. *American Journal of Science*, 303(5):353–409.

Jolivet, L., Goffe, B., Monie, P., TruffertLuxey, C., Patriat, M., and Bonneau, M. (1996). Miocene detachment in Crete and exhumation P-T-t paths of high-pressure metamorphic rocks. *Tectonics*, 15(6):1129–1153.

Jolivet, L. and Patriat, M. (1999). Ductile extension and the formation of the Aegean Sea. In Durand, B., Jolivet, L., Horvath, F., and Séranne, M., editors, *The Mediterranean basins: Tertiary exhumation within the Alpine orogen*, volume 156, pages 427–456. Geological Society Special Publications.

Jolivet, L., Rimmele, G., Oberhansli, R., Goffe, B., and Candan, O. (2004). Correlation of syn-orogenic tectonic and metamorphic events in the Cyclades, the Lycian nappes and the Menderes massif. Geodynamic implications. *Bulletin de la Societe Geologique de France*, 175(3):217–238.

Kaiser Rohrmeier, M. (2005). *Age and geodynamic evolution of hydrothermal vein deposits in the Madan extensional complex (Bulgaria)*. PhD thesis, Swiss Federal Institute of Technology Zurich.

Kaiser-Rohrmeier, M., Handler, R., von Quadt, A., and Heinrich, C. (2004). Hydrothermal Pb-Zn ore formation in the Central Rhodopian Dome, south Bulgaria: Review and new time constraints from Ar-Ar geochronology. *Schweizerische Mineralogische und Petrographische Mitteilungen*, 84(1–2):37–58.

Kaufman, P. S. (1995). *Extensional tectonic history of the Rhodope metamorphic core complex, Greece and geophysical modeling of the Halloran Hills, California*. PhD thesis, Massachusetts Institute of Technology, Cambridge.

Ketcham, R. A. (2005). Forward and inverse modeling of low-temperature thermochronometry data. In *Low-temperature thermochronology: techniques, interpretations, and applications*, volume 58 of *Reviews in Mineralogy and Geochemistry*, pages 275–314. Mineralogical Soc America, Chantilly.

Ketcham, R. A., Carter, A., Donelick, R. A., Barbarand, J., and Hurford, A. J. (2007). Improved modeling of fission-track annealing in apatite. *American Mineralogist*, 92(5–6):799–810.

Kilias, A., Falalakis, G., and Mountrakis, D. (1999). Cretaceous–Tertiary structures and kinematics of the Serbomacedonian metamorphic rocks and their relation to the exhuma-

tion of the Hellenic hinterland (Macedonia, Greece). *International Journal of Earth Sciences*, 88(3):513–531.

Kober, L. (1928). *Der Bau der Erde: Eine Einführung in die Geotektonik*. Berlin: Borntreager, Zweite neubearbeitete und vermehrte Auflage.

Kockel, F., Mollat, H., and Walther, H. W. (1971). Geologie des Serbo–Mazedonischen Massivs und seines mesozoischen Rahmens (Nordgriechenland). *Geologisches Jahrbuch*, 89:529–551.

Kojumdgieva, E., Nikolov, I., Nedjalkov, P., and Busev, A. (1982). Stratigraphy of the Neogene in Sandanski graben. *Geologica Balcanica*, 12:69–81.

Kokkinakis, A. (1979). Zum Faltenbau des Symvolongebirges und des Gebietes von Kavala (Griechisch–Ostmakedonien). *Annales Geologiques des Pays Helleniques*, 30(1):398–420.

Koukouvelas, I. and Pe-Piper, G. (1991). The Oligocene Xanthi pluton, northern Greece: a granodiorite emplaced during regional extension. *Journal of the Geological Society*, 148(4):749–758.

Kounov, A., Seward, D., Bernoulli, D., Burg, J.-P., and Ivanov, Z. (2004). Thermotectonic evolution of an extensional dome: the Cenozoic Osogovo–Lisets core complex (Kraishte zone, western Bulgaria). *International Journal of Earth Sciences*, 93(6):1008–1024.

Kousparis, D. (1979). *Seismic stratigraphy and basin development – Nestos Delta area, northeastern Greece*. PhD thesis, University of Tulsa, USA.

Kozhoukharova, E. (1998). Eclogitization of serpentinites into narrow shear zones from the avren syncline, eastern Rhodopes. *Geokhimiya, Mineralogiya i Petrologiya*, 35:29–46.

Krohe, A. and Mposkos, E. (2002). Multiple generations of extensional detachments in the Rhodope Mountains (northern Greece): evidence of episodic exhumation of high-pressure rocks. In Blundell, D., Neubauer, F., and von Quadt, A., editors, *The Timing and Location of Major Ore Deposits in an Evolving Orogen*, volume 204, pages 151–178. Geological Society, London, Special Publications.

Kyriakopoulos, K. G., Magganas, A. C., Norelli, P., Bigazzi, G., Del Moro, A., and Kokkinakis, A. (1996). Thermochronological evolution of Symvolon and Pangeon Plutons and their country rocks, Kavala area, N. Greece; an apatite fission track analysis. *Neues Jahrbuch fuer Mineralogie*, 1996(11):519–529.

Lalechos, N. (1986). Correlations and observations in molassic sediments in onshore and offshore areas of northern Greece. *Mineral Wealth*, 42.

Le Pichon, X., Lallemant, S. J., Chamotrooke, N., Lemeur, D., and Pascal, G. (2002). The Mediterranean Ridge backstop and the Hellenic nappes. *Marine Geology*, 186(1–2):111–125.

Liati, A. (1986). *Regional metamorphism and overprinting contact metamorphism of the Rhodope zone, near Xanthi (N. Greece).* PhD thesis, Technische Universität Carolo–Wilhelmina.

Liati, A. (2005). Identification of repeated Alpine (ultra) high-pressure metamorphic events by U-Pb SHRIMP geochronology and REE geochemistry of zircon: the Rhodope zone of northern Greece. *Contributions to Mineralogy and Petrology*, 150(6):608–630.

Liati, A. and Gebauer, D. (1999). Constraining the prograde and retrograde P-T-t path of Eocene HP rocks by SHRIMP dating of different zircon domains: inferred rates of heating, burial, cooling and exhumation for central Rhodope, northern Greece. *Contributions to Mineralogy and Petrology*, 135(4):340–354.

Liati, A. and Gebauer, D. (2001). Palaeoyoic as well as Mesozoic sedimentation and polymetamorphism in Central Rhodope (N Greece) as inferred from U-Pb SHRIMP-dating of detrital zircons. *EUG, Journal of Conference Abstracts*, 6:315.

Liati, A., Gebauer, D., and Fanning, C. M. (2004). The druration of exhumation processes in (U)HP terranes – a geochronological approach applied to the Rhodope terrane, N Greece. *'Geoscience Africa 2004', The Birth and Growth of Continents, Abstract volume*, 1:384–385.

Liati, A., Gebauer, D., and Wysoczanski, R. (2002). U-Pb SHRIMP-dating of zircon domains from UHP garnet-rich mafic rocks and late pegmatoids in the Rhodope zone (N Greece); evidence for Early Cretaceous crystallization and Late Cretaceous metamorphism. *Chemical Geology*, 184(3–4):281–299.

Liati, A., Mposkos, E., and Perdikatsis, V. (1990). Geochemical constraints on the nature and tectonic setting of the metabasite protoliths from the Rhodope zone, N Greece. *Ber. Deutsch. Mineral. Gesellschaft*, 1:162.

Liati, A. and Seidel, E. (1996). Metamorphic evolution and geochemistry of kyanite eclogites in central Rhodope, northern Greece. *Contributions to Mineralogy and Petrology*, 123(3):293–307.

Lips, A. L. W., White, S. H., and Wijbrans, J. R. (2000). Middle-Late Alpine thermotectonic evolution of the southern Rhodope Massif, Greece. *Geodinamica Acta*, 13(5):281–292.

Lister, G. and Forster, M. (2009). Tectonic mode switches and the nature of orogenesis. *Lithos*.

Lister, G. S., Banga, G., and Feenstra, A. (1984). Metamorphic core complexes of Cordilleran type in the Cyclades, Aegean Sea, Greece. *Geology*, 12(4):221–225.

Marakis, G. I. (1969). Geochronologic studies of some granites from Macedonia. *Annales Geologiques des Pays Helleniques*, 21:121–152.

Marchev, P., Kaiser Rohrmeier, M., Heinrich, C., Ovtcharova, M., von Quadt, A., and Raicheva, R. (2005). Hydrothermal ore deposits related to post-orogenic extensional magmatism and core complex formation; the Rhodope Massif of Bulgaria and Greece.; Geodynamics and ore deposit evolution in Europe. *Ore Geology Reviews*, 27(1–4):53–89.

Marchev, P., Raicheva, R., Downes, H., Vaselli, O., Chiaradia, M., and Moritz, R. (2004a). Compositional diversity of Eocene–Oligocene basaltic magmatism in the eastern Rhodopes, SE Bulgaria: implications for genesis and tectonic setting. *Tectonophysics*, 393(1–4):301–328.

Marchev, P., Singer, B., Andrew, C., Hasson, S., Moritz, R., and Bonev, N. (2003). Characteristics and preliminary $^{40}Ar/^{39}Ar$ and $^{87}Sr/^{86}Sr$ data of the Upper Eocene sedimentary-hosted low-sulfidation gold deposits Ada Tepe and Rosino, SE Bulgaria: possible relation with core complex formation. In Eliopoulous, D. G., editor, *Mineral exploration and sustainable development, Proceedings of the 7th Biennial SGA Meeting Athens, Greece*, volume 2, pages 1193–1196. Millpress Science Publishers.

Marchev, P., Singer, B., Jelev, D., Hasson, S., Moritz, R., and Bonev, N. (2004b). The Ada Tepe deposit: a sediment-hosted, detachment faultcontrolled, low-sulfidation gold deposit in the eastern Rhodopes, SE Bulgaria. *Schweizerische Mineralogische Und Petrographische Mitteilungen*, 84:59–78.

Marcheva, L. A. (1998). 3T-phengites in the rocks of biala reka metamorphic group: an indicator for high-pressure metamorphism. *Geokhimiya, Mineralogiya i Petrologiya*, 35:17–28.

Márton, I., Moritz, R., and Spikings, R. (sub.). Application of low-temperature thermochronology to hydrothermal ore deposits: formation, preservation and exhumation of epithermal gold systems from the eastern Rhodopes, Bulgaria. *Tectonophysics*.

Mposkos, E. (1989). High-pressure metamorphism in gneisses and pelitic schists in the east Rhodope Zone (N Greece). *Mineralogy and Petrology*, 41(1):25–39.

Mposkos, E. and Krohe, A. (2000). Petrological and structural evolution of continental high pressure (HP) metamorphic rocks in the Alpine Rhodope Domain (N. Greece). .

In Panayides, J., Xenophontos, C., and Malpas, J., editors, *Proceedings of the Third international conference on the Geology of the Eastern Mediterranean. Ministry of Agriculture, Natural Resources and Environment, Geological Survey Department. Nicosia, Cyprus.*, volume 3, pages 221–232.

Mposkos, E. and Liati, A. (1993). Metamorphic evolution of metapelites in the high-pressure terrane of the Rhodope Zone, northern Greece. *The Canadian Mineralogist*, 31(Part 2):401–424.

Mposkos, E. and Wawrzenitz, N. (1995). Metapegmatites and pegmatites bracketing the time of HP-metamorphism in polymetamorphic rocks of the E-Rhodope, N. Greece; petrological and geochronological constraints. In *Proceedings of the XV congress of the Carpatho–Balkan Geological Association*, volume 4, pages 602–608. Special Publications of the Geological Society of Greece.

Mposkos, E. D. and Kostopoulos, D. K. (2001). Diamond, former coesite and supersilicic garnet in metasedimentary rocks from the Greek Rhodope: a new ultrahigh-pressure metamorphic province established. *Earth and Planetary Science Letters*, 192(4):497–506.

Naeser, C. W. and McKee, E. H. (1970). Fission-track and K-Ar Ages of Tertiary ash-flow tuffs, north-central Nevada. *Geological Society of America Bulletin*, 81(11):3375–3384.

Ovtcharova, M., Cherneva, Z., Quadt, A. V., Peytcheva, I., and Anonymous (2002). Migmatitic geochronology and geochemistry; a key to understanding the exhumation of the Madan Dome (Bulgaria).; Abstracts of the 12th annual V. M. Goldschmidt conference. *Geochimica Et Cosmochimica Acta*, 66(15A):573.

Ovtcharova, M., Quadt, A. V., Cherneva, Z., Sarov, S., Heinrich, C., and Peytcheva, I. (2004). U-Pb dating of zircon and monazite from granitoids and migmatites in the core and eastern periphery of the Central Rhodopean Dome, Bulgaria. *Geochimica Et Cosmochimica Acta*, 68(11):A664–A664.

Ovtcharova, M., Von Quadt, A., Cherneva, Z., Peytcheva, I., Heinrich Christoph, A., Kaiser Rohrmeier, M., Neubauer, F., and Frank, M. (2003a). Isotope and geochronological study on magmatism and migmatization in the central Rhodopean core complex, Bulgaria. In F., N. and R., H., editors, *Geodynamics and ore deposit evolution of the Alpine–Balkan–Carpathian–Dinaride province*, page 42. Seggauberg, Austria.

Ovtcharova, M., von Quadt, A., Heinrich, C., Frank, M., Kaiser-Rohrmeier, M., Peytcheva, I., and Cherneva, Z. (2003b). Triggering of hydrothermal ore mineralization in the central rhodopean core complex (bulgaria) – insight from isotope and geochronological

studies on tertiary magmatism and mineralisation. In Eliopoulous, D. G., editor, *Mineral exploration and sustainable development, Proceedings of the 7th Biennial SGA Meeting Athens, Greece*, pages 367–370. Millpress Science Publishers.

Ovtcharova, M., Von Quadt, A., Heinrich Christoph, A., Frank, M., Rohrmeier, M., Peycheva, I., and Neubauer, F. (2001). Late Alpine extensional stage of the Central Rhodopian Core Complex and related acid magmatism (Madan Dome, Bulgaria) – Isotope and geochronological data. In Piestrzynski, A., Speczik, S., Pasava, J., Gize, A., Sass-Gustkiewicz, M., Leach, D., P., M., Oszczepalski, S., Brown, A., Blundell, D. J., Kotlinski, R., Herzig, P., Plimer, I., A., K., Mikulski, A., Seltmann, R., Heinrich, C. A., and Kucha, H., editors, *Mineral Deposits at the Beginning of the 21st Century*, pages 551–553. Balkema Rotterdam.

Papadopoulos, C. and Kilias, A. (1985). Altersbeziehungen zwischen Metamorphose und Deformation im zentralen Teil des Serbomezedonischen Massivs (Vertiskos Gebirge, Nord–Griechenland). *Geologische Rundschau*, 74(1):77–85.

Perraki, M., Proyer, A., Mposkos, E., Kaindl, R., and Hoinkes, G. (2006). Raman microspectroscopy on diamond, graphite and other carbon polymorphs from the ultrahigh-pressure metamorphic Kimi Complex of the Rhodope Metamorphic Province, NE Greece. *Earth and Planetary Science Letters*, 241(3–4):672–685.

Peytcheva, I., Kostitsin, Y., Salnikova, E., von Quadt, A., Kamenov, B., Klain, L., and Anonymous (1999). Alpine evolution of the magmatism in the West–Rhodopes; Rb-Sr and U-Pb isotope data. *European Union of Geosciences, Journal of Conference Abstracts*, 4(1):470.

Peytcheva, I., von Quadt, A., Ovtcharova, M., Handler, R., Neubauer, F., Salnikova, E., Kostitsyn, Y., Sarov, S., and Kolcheva, K. (2004). Metagranitoids from the eastern part of the Central Rhodopean dome (Bulgaria): U-Pb, Rb-Sr and $^{40}Ar/^{39}Ar$ timing of emplacement and exhumation and isotope-geochemical features. *Mineralogy and Petrology*, 82(1–2):1–31.

Pleuger, J., Georgiev, N., and Jahn-Awe, S. (2009). Kinematics of the Kyuse–Hasanlartepesi Fault at the boundary between the eastern Rhodope volcano-sedimentary basin and the Rhodopean basement. *Abstracts of the Conference Tectonics and Sedimentation, Bonn*, page 57.

Rey, P., Teyssier, C., and Whitney, D. (2009). Extension rates, crustal melting, and core complex dynamics. *Geology*, 37(5):391–394.

Ricou, L. E. (1994). Tethys reconstructed – Plates, continental fragments and their boundaries since 260 Ma from Central–America to south–eastern Asia. *Geodinamica Acta*, 7(4):169–218.

Ricou, L. E., Burg, J.-P., Godfriaux, I., and Ivanov, Z. (1998). Rhodope and vardar: the metamorphic and the olistostromic paired belts related to the Cretaceous subduction under Europe. *Geodinamica Acta*, 11(6):285–309.

Ricou, L. E., Zonenshain, L. P., Dercourt, J., Kazmin, V. G., Le Pichon, X., Knipper, A. L., Grandjacquet, C., Sborshchikov, I. M., Geyssant, J., Lepvrier, C., Pechersky, D. M., Boulin, J., Sibuet, J. C., Savostin, L. A., Sorotkin, O., Westphal, M., Bazenov, M. L., Lauer, J. P., and Biju-Duval, B. (1985). Methodes pour l'établissement de neuf cartes paléogéogaphiques de l'Atlantique au Pamir depuis le Lias. *Bulletin de la Societe Geologique de France*, 8(5):625–635.

Ring, U., Glodny, J., Will, T., and Thomson, S. (2007a). An Oligocene extrusion wedge of blueschist-facies nappes on Evia, Aegean Sea, Greece: implications for the early exhumation of high-pressure rocks. *Journal of the Geological Society*, 164(3):637–652.

Ring, U., Will, T., Glodny, J., Kumerics, C., Gessner, K., Thomson, S., Gungor, T., Monie, P., Okrusch, M., and Druppel, K. (2007b). Early exhumation of high-pressure rocks in extrusion wedges: Cycladic blueschist unit in the eastern Aegean, Greece, and Turkey. *Tectonics*, 26(2).

Sarov, S., Cherneva, Z., Kolcheva, K., Voinova, E., and Gerdjikov, I. (2004). Lithotectonic subdivision of the metamorphic rocks from the eastern parts of the Central Rhodope extension structure. *Review of the Bulgarian Geological Society*, 65(1–3):101–106.

Sarov, S. and Gerdjikov, I. (2002). Unroofing the Central Rhodopian Dome from the East–Kanarata enxtensional shear zone. *Comptes rendus de l' Academie bulgare des Sciences*, 55(2):71–74.

Sarov, S., Yordanov, B., Valkov, V., Georgiev, S., Kamburov, D., Raeva, E., Balkanska, E., Grozdev, V., Moskovska, L., and Dobrev, G. (2007a). Geological Map of the Republic of Bulgaria 1:50000, K-35-87-V (Zlatograd) and K-35-99 (Drangovo).

Sarov, S., Yordanov, B., Valkov, V., Georgiev, S., Kamburov, D., Raeva, E., Grosdev, V., Balkanska, E., Moskovska, L., Dobrev, G., and Kalinova, I. (2007b). Geological Map of the Republic of Bulgaria 1:50000, K-35-87-A (Ardino).

Sarov, S., Yordanov, B., Valkov, V., Georgiev, S., Kamburov, D., Raeva, E., Grozdev, V., Balkanska, E., Moskovska, L., and Dobrev, G. (2007c). Geological Map of the Republic of Bulgaria 1:50000, K-35-87-B (Kardzhali).

Schmädicke, E. and Will, T. M. (2003). Pressure-temperature evolution of blueschist facies rocks from Sifnos, Greece, and implications for the exhumation of high-pressure rocks in the Central Aegean. *Journal of Metamorphic Geology*, 21(8):799–811.

Schmid, S. M., Bernoulli, D., Fugenschuh, B., Matenco, L., Schefer, S., Schuster, R., Tischler, M., and Ustaszewski, K. (2008). The Alpine–Carpathian–Dinaridic orogenic system: correlation and evolution of tectonic units. *Swiss Journal of Geosciences*, 101(1):139–183.

Shirvell, C. R., Stockli, D. F., Axen, G. J., and Grove, M. (2009). Miocene–Pliocene exhumation along the west Salton detachment fault, southern California, from (U-Th)/He thermochronometry of apatite and zircon. *Tectonics*, 28:doi:10.1029/2007TC002172.

Sokoutis, D., Brun, J.-P., van den Driessche, J., and Pavlides, S. (1993). A major Oligo–Miocene detachment in southern Rhodope controlling north Aegean extension. *Journal of the Geological Society of London*, 150(Part 2):243–246.

Stampfli, G. M. and Borel, G. (2004). *The TRANSMED Atlas: The Mediterranean Region from Crust to Mantle*, chapter "The TRANSMED transects in space and time: constraints on the paleotectonic evolution of the Mediterranean domain", pages 53–80. Springer, Berlin and Heidelberg.

Tagami, T., Galbraith, R. F., Yamada, R., and Laslett, G. M. (1998). Revised annealing kinetics of fission tracks in zircon and geological implications. In VandenHaute, P. and DeCorte, F., editors, *Advances in Fission-Track Geochronology*.

Tirel, C., Gueydan, F., Tiberi, C., and Brun, J.-P. (2004). Aegean crustal thickness inferred from gravity inversion. Geodynamical implications. *Earth and Planetary Science Letters*, 228(3–4):267–280.

Underhill, J. R. (1989). Late Cenozoic deformation of the Hellenide foreland, western Greece. *Geological Society of America Bulletin*, 101(5):613–634.

van Hinsbergen, D. J. J., Hafkenscheid, E., Spakman, W., Meulenkamp, J. E., and Wortel, R. (2005). Nappe stacking resulting from subduction of oceanic and continental lithosphere below Greece. *Geology*, 33(4):325–328.

Wawrzenitz, N. and Krohe, A. (1998). Exhumation and doming of the Thasos metamorphic core complex (S Rhodope, Greece): structural and geochronological constraints. *Tectonophysics*, 285(3–4):301–332.

Wawrzenitz, N. and Mposkos, E. (1997). First evidence for Lower Cretaceous HP/HT-metamorphism in the eastern Rhodope, north Aegean Region, North–East Greece. *European Journal of Mineralogy*, 9(3):659–664.

Wijbrans, J. R. and McDougall, I. (1988). Metamorphic evolution of the Attic Cycladic Metamorphic Belt on Naxos (Cyclades, Greece) utilizing $^{40}Ar/^{39}Ar$ age spectrum measurements. *Journal of Metamorphic Geology*, 6(5):571–594.

Wolf, R. A., Farley, K. A., and Kass, D. M. (1998). Modeling of the temperature sensitivity of the apatite (U-Th)/He thermochronometer. *Chemical Geology*, 148(1–2):105–114.

Yamada, R., Tagami, T., Nishimura, S., and Ito, H. (1995). Annealing Kinetics of Fission Tracks in Zircon – an Experimental-Study. *Chemical Geology*, 122(1–4):249–258.

Zagorcev, I. S. and Moorbath, S. (1986). Problems of metamorphism in Central Rhodope mountains in the light of Rb-Sr isotopic data. *Geologica Balcanica*, 16(6):61–67.

Zeffren, S., Avigad, D., Heimann, A., and Gvirtzman, Z. (2005). Age resetting of hanging wall rocks above a low-angle detachment fault: Tinos Island (Aegean Sea). *Tectonophysics*, 400(1–4):1–25.

Appendices

Appendix I: The fission-track method

1. Definition and formation of fission tracks

The fission-track dating method is based on the spontaneous fission of the unstable uranium isotope ^{238}U (Price and Walker, 1963; Fleischer et al., 1975). During the fission reaction unlike the usual radioactive decay the nucleus splits into two daughter fragments that are unequal in mass and atomic number. Usually they are unstable and disintegrate further by β–emission. Fission occurs with heavy nuclides (atomic number $Z \geq 90$ and atomic mass $A \geq 230$), e.g. ^{232}Th and the three U isotopes ^{234}U, ^{235}U and ^{238}U. But for fission-track analysis nuclides other than ^{238}U are insignificant because of their low natural abundance or their long half-life. Fission can occur spontaneously due to existing instability within the nucleus itself, or it can be induced when the nucleus is irradiated. After fission both daughter fragments carry a strong positive charge and the resulting repulsive force catapults the two fragments in opposite directions (Fleischer et al., 1975). When a fissioning nuclide such as ^{238}U is embedded in a solid, for example as a trace element in a crystal lattice, the fission fragments create a narrow trail of damage along their trajectories. The mechanism causing this damage trails is still debated, but the most widely accepted theory is the "ion explosion spike" model (Fleischer et al., 1975). As the fission fragments rapidly travel through the lattice, they rip off electrons from lattice atoms they pass by. This leaves a zone of positively charged ions in the lattice that repel each other and force themselves into the crystal lattice, causing interstitials and vacancies. Consequently the stressed region relaxes elastically by straining the surrounding undamaged lattice (Fig. 5.2). The evolved trail of lattice damage is called the fission track (FT). An alternative model is the "thermal spike" model (Seitz, 1949; Bonfiglioli et al., 1961; Chadderton and Montagupollock, 1963). The passage of the fission fragments is assumed to produce instantaneous, intense heating of the lattice along their trajectories. This rapidly heated zone is subsequently quenched by thermal conduction into the surrounding lattice, leaving a trail of disordered lattice, the fission track. Chadderton (2003) argued that both ion explosion and thermal spikes could be present to different degrees for track formation and registration in a variety of solids.

Latent (unetched) tracks can only be viewed by transmission electron microscopy (TEM) and other high-resolution microscopic techniques. In general, latent tracks have a cylindrical shape of amorphous material in a crystalline matrix, with a sharp amorphous-crystalline transition (e.g. Paul and Fitzgerald, 1992). A latent FT is up to 20 μm long, depending on the energy of the fission fragments and the stability of the surrounding crystal. The cross section of the track has a nearly circular shape with widths of a few nm.

There is no reason why any particular direction of the track may be preferred, nor is there any empirical evidence for this, so it is assumed that the orientations are random.

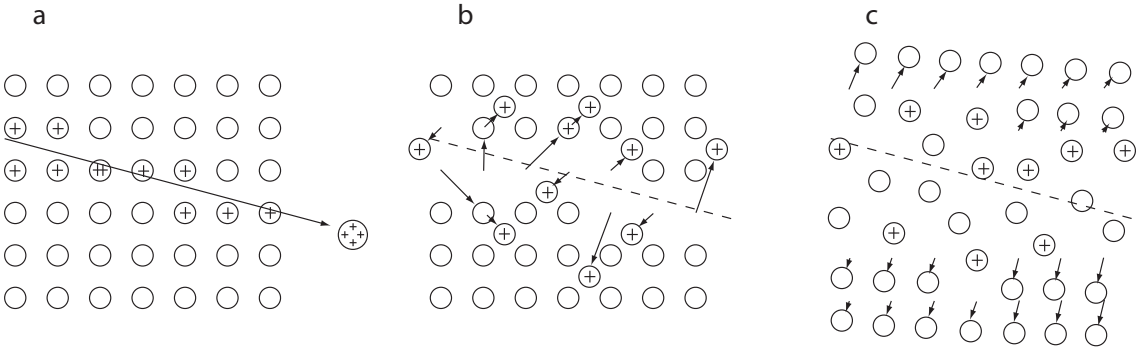

Figure 5.2: Track formation after the "ion explosion spike" model of Fleischer et al. (1975). (a) The strongly charged fission fragment of ^{238}U ionises the lattice atoms. (b) Due to Coulomb repulsion, the ions are displaced from their lattice sites into interstitial positions; at the same time, a number of vacant lattice sites are created. (c) The stressed region of the track relaxes, elastically straining the surrounding undamaged lattice.

2. Fission-track revelation

Latent FTs (and other lattice defects) are vulnerable to chemical etching because the disordered region of the track core is more rapidly dissolved than the surrounding undamaged crystal lattice. After etching a latent track for an appropriate time span, with an appropriate chemical and at an appropriate temperature, it can be viewed with an optical microscope. This is the most widely used revelation method in FT dating. The reagent and etching conditions are selected on an empirical basis and have been established for a variety of minerals (Fleischer et al., 1975; Durrani and Bull, 1987; Wagner and Van den Haute, 1992).

Etched FTs in crystals have characteristic shapes due to lattice symmetry dependent anisotropy in the etch rates v_e. Minerals such as apatite and zircon show the highest v_e parallel to the crystal c-axis (Fig. 5.3). Considering the shape of the FT-pit, that is created when the track meets the etched surface, the crystallographic orientation of this surface can be identified.

For reliable track density determination, the observed track density ρ_{etch} needs to be as close as possible to the latent track density ρ_{latent}. As tracks inclined at relatively low angle to the surface will be removed during etching, it is necessary to use mineral surfaces having the lowest possible v_e in order to minimise this track loss. For apatite and zircon this is the case parallel to the crystal c-axis.

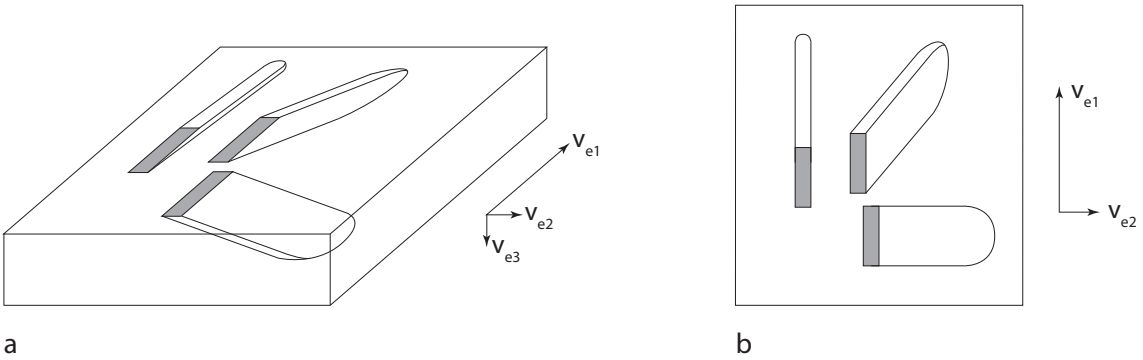

Figure 5.3: (a) 3D view and (b) surface view of etched tracks in a mineral (e.g. zircon) with anisotropic etch rates v_e. After Gleadow (1981).

3. Age determination

3.1 Age equation and zeta factor

As any other radiometric dating method, fission-track analysis is based on the following age equation:

$$N_D = N_P(e^{\lambda t} - 1) \tag{5.1}$$

where N_D is the number of daughter isotopes at time t, N_P the number of parent isotopes at time t and λ the decay constant (in a^{-1}). Each fission reaction creates one fission track, so the number of fission tracks corresponds to the number of daughter isotopes as in usual radioactive decay.

Apart from the spontaneous fission, ^{238}U decays to ^{206}Pb by successive α– and β–decays. The total decay constant λ_{tot} of ^{238}U is composed of the fission decay constant $\lambda_f = (7.03 \pm 0.11) \times 10^{-17}\ a^{-1}$ (Fleischer and Price, 1964; Roberts et al., 1968) and the α-decay constant $\lambda_\alpha = 1.55125 \times 10^{-10}\ a^{-1}$ (Jaffey et al., 1971) .

$$\lambda_{tot} = \lambda_f + \lambda_\alpha \tag{5.2}$$

If ^{238}N represents the present-day concentration of ^{238}U then the number of present-day spontaneous fission tracks N_S per unit volume is:

$$N_s = \frac{\lambda_f}{\lambda_{tot}} {}^{238}N(e^{\lambda_{tot} t} - 1) \tag{5.3}$$

λ_α is several orders of magnitude greater than λ_f so such that: $\lambda_{tot} \approx \lambda_\alpha$. Equation 5.3 becomes

$$N_s = \frac{\lambda_f}{\lambda_\alpha} {}^{238}N(e^{\lambda_\alpha t} - 1) \tag{5.4}$$

and solved for t it can be written as

$$t = \frac{1}{\lambda_\alpha} ln(\frac{\lambda_\alpha}{\lambda_f} \frac{N_s}{{}^{238}N} + 1) \tag{5.5}$$

The method of measuring the present ^{238}U concentration (^{238}N) in the FT system is based on counting etched FTs of specially prepared samples under a high powered microscope. When a sample is irradiated with a known flux φ of thermal neutrons over a time t_{irr}, a number of nuclei of ^{235}U are induced to fission ($\varphi \times t_{irr} = \phi$ the thermal fluence (in neutrons per cm^2)). These induced fission reactions produce *induced FTs*, that can be viewed and counted. The number of induced FTs per unit of volume is given by $N_i = {}^{235}N\sigma\phi$. The parameter σ is the cross section for induced nuclear fission of ^{235}U by thermal neutrons and can be considered a constant for a specific nuclear reaction (here $\sigma = 580.2 \times 10^{-24} cm^2$). As the present isotopic ratio $I = {}^{235}U/{}^{238}U$ is constant (7.2527×10^{-3}, Cowan and Adler, 1976), the number of induced fission tracks per unit volume is $N_i = {}^{238}NI\sigma\phi$ and equation 5.5 becomes

$$t = \frac{1}{\lambda_\alpha} ln(\frac{\lambda_\alpha}{\lambda_f}\frac{N_s}{N_i} I\sigma\phi + 1) \tag{5.6}$$

The FTs are counted using a microscope and an *areal density* is determined, thus the equation 5.6 has to be rewritten with areal densities (ρ_s and ρ_i) instead of volume densities (N_s and N_i). To do this, two factors are needed, the geometry ratio G and the procedure factor Q. G is the ratio of the geometry factors for the registration geometries of the spontaneous and the induced FT. Q is personal to the researcher and dependent on the optics of the microscope and the etching (efficiency and time).

$$t = \frac{1}{\lambda_\alpha} ln(\frac{\lambda_\alpha}{\lambda_f}\frac{\rho_s}{\rho_i} QGI\sigma\phi + 1) \tag{5.7}$$

The thermal neutron fluence ϕ is conventionally measured by determining the induced fission-track density ρ_d produced in a uranium-doped standard glass (dosimeter glass) irradiated along with the samples to be studied. The value of ρ_d commonly is an interpolated value, calculated from two standard glasses in an irradiation package. The induced track density ρ_d of the glass is proportional to ϕ. The proportionality factor is called B and depends on the U content of the standard glass, etching and observation conditions of the individual researcher. The age equation can now be written as:

$$t = \frac{1}{\lambda_\alpha} ln(\frac{\lambda_\alpha}{\lambda_f}\frac{\rho_s}{\rho_i} QGI\sigma B\rho_d + 1) \tag{5.8}$$

Even though λ_f is not well determined and other factors are difficult to measure it is possible to determine them individually and calculate t (Wagner and Van den Haute, 1992). However a more elegant solution was introduced by Hurford and Green (1983) with the zeta age calibration factor (ζ–factor). The ζ–factor (in $a\ cm^2$) depends on the individual etching and counting habits of the FT researcher and varies with the U concentration of the standard glass and, because of the Q–factor, with the mineral that is observed.

$$\zeta = \frac{1}{\lambda_f} QI\sigma B \tag{5.9}$$

To calculate the personal ζ–factor the observer counts the spontaneous and the induced tracks of an age standard, with well determined age t_{std}, and evaluates the corresponding induced track density ρ_{dstd}. As the α–decay constant for ^{238}U ($\lambda_\alpha = 1.55125 \times 10^{-10} a^{-1}$) and the geometry factor G are known ($G = 0.5$ for external detector method, $G = 1.0$ for population method, Gleadow and Lovering, 1977; Green and Durrani, 1979), the ζ–value can be calculated as follows

$$\zeta = \frac{e^{\lambda_\alpha t_{std}} - 1}{\lambda_\alpha (\frac{\rho_s}{\rho_i})_{std} G \rho_{dstd}} \tag{5.10}$$

and the age equation can be solved:

$$t = \frac{1}{\lambda_\alpha} ln(\lambda_\alpha \frac{\rho_s}{\rho_i} G \zeta \rho_d + 1) \tag{5.11}$$

3.2 Application range

It is possible to date geological samples from hundreds of millions of years down to archeological ages. In general for apatite FT systems the suitable age ranges from 1 to 400 Ma. The application range is only limited by the uranium content. If the uranium content (U) and the age of the sample (t) is low, then so is the track density. The counting becomes very time consuming and the calculated uncertainty of the FT age is very large. On the other hand, when the uranium content is high and the sample very old, tracks overlap and are not individually resolvable under the microscope.

4. Stability of fission tracks – Annealing

FTs are stable in insulating solids under certain mineral specific conditions while they are not stable in conducting and semi-conducting solids. This observation supports the "ion explosion spike" model as movements of electrons would rapidly neutralise the ions produced by the fission fragments.

The diffusion-based process that shortens and ultimately erases tracks in insulting minerals is referred to as annealing. Temperature is the dominant environmental factor controlling annealing and the length of exposure to those temperatures ("heating time") is a secondary factor (Fleischer et al., 1975; Naeser and Dodge, 1969; Green et al., 1989; Green and Duddy, 1989). Annealing temperatures vary greatly from mineral to mineral. To a smaller extent they vary for different chemical compositions of the same mineral (Green et al., 1986; Crowley et al., 1991; Carlson et al., 1999; Barbarand et al., 2003) or with the accumulation of radiation damage in a grain (Kasuya and Naeser, 1988; Carter, 1990; Yamada et al., 1998; Rahn et al., 2004). During early stages of annealing, fission tracks shrink progressively from both ends (Green et al., 1986; Donelick, 1991; Donelick et al., 1999; Yamada et al., 1995a). At later stages shrinking continues but they also become broken into segments (Green et al., 1986; Hejl, 1995; Yamada et al., 1995a).

Because shorter tracks are less likely to intersect the planar internal surface within the grain where the tracks are counted, annealing reduces the apparent number of tracks and thus the "apparent" fission-track age. Total annealing erases all tracks completely and resets the fission-track clock to zero.

The temperature range within partial annealing takes place is called partial annealing zone, PAZ. It is defined by a lower blocking temperatures T_b, where track annealing basically stops, and an upper total annealing temperature, T_o, where tracks anneal faster then new ones are formed.

Total annealing temperatures for titanite and zircon are poorly constrained but are on the order of 330°C, assuming heating times of a few million years (Yamada et al., 1995b; Foster et al., 1996; Tagami and Shimada, 1996; Coyle and Wagner, 1998). Much more is known about the annealing behavior of the mineral apatite, partly because its PAZ overlaps with the petroleum generation temperature window. This has lead to the development of sophisticated procedures for recognising and interpreting totally annealed and partially annealed apatite samples (e.g. Gleadow et al., 1986b,a; Green et al., 1989; Green and Duddy, 1989; Corrigan, 1993; Burtner and Nigrini, 1994). Studies of drill cores by Gleadow and Duddy (1981) have shown that the temperature of total annealing in apatite is 120 ± 10°C.

The term closure temperature, T_c, was introduced by Dodson (1973). It is defined as the temperature of a thermochronological system at the time corresponding to its "apparent" age (Fig. 5.4). Even though the statement of Dodson (1973) is based on diffusion of a single atomic species through a material, it is still applicable to FT annealing. Annealing, though it is a much more complicated process as FTs are made up of multiple defects, is still a temperature-dependent process and so diffusion laws are valid (e.g. Arrhenius law). Dodson (1973) showed mathematically that the closure temperature is dependent on the cooling rate. The cooling rate defines how much time a sample spends in the PAZ, thus influencing the amount of fission track annealing in this transition zone. Rapid cooling does not allow much time for track shortening, and the resulting age is close to that represented by the time when the sample passed through t_o. On the other hand, slow cooling allows for considerable track length shortening, and the "apparent" age will be younger than t_o, not specified completely by passage through a single temperature isotherm. As the closure temperature is directly defined with respect to the "apparent" age, T_c will be higher for the fast cooling sample than for the slow cooling sample. Table 5.1 shows closure temperatures and PAZs of minerals commonly used in fission track dating.

4.1 Track length modeling

The annealing of tracks has allowed FT analysis to become a powerful tool in the realm of low temperature thermochronology. It is possible to reconstruct the thermal history of a

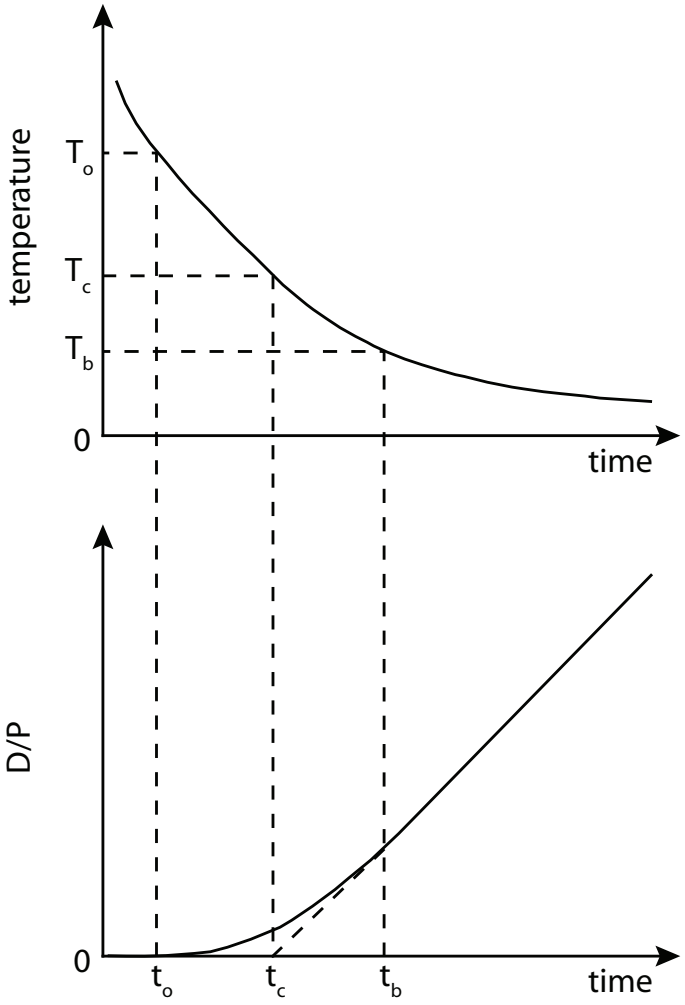

Figure 5.4: Graphical definition of closure temperature T_c, "open-system" temperature T_o and blocking temperature T_b by Braun et al. (2006) modified after Dodson (1973). The upper plot shows a cooling path and the lower plot the corresponding ratio of daughter products (D) and parent isotopes (P). t_c is the apparent thermochronological age, t_o is the time when the system changes from totally open to partially closed and t_b is the time when the system gets totally blocked.

Table 5.1: Closure temperature T_c and partial annealing zone PAZ of minerals commonly used for fission-track analyses.

Mineral	T_c [°C]	PAZ [°C]	Reference e.g.
Apatite	110 ± 10	$110 - -60$	Gleadow and Duddy (1981)
Zircon	240 ± 20	$390 - -170$	Brandon et al. (1998)
			Yamada et al. (1995a)
Titanite	$265 - -310$		Coyle and Wagner (1998)

sample by measuring track lengths. From the track-length distribution, together with the apparent age, estimates of the time–temperature path can be made.

Track length modeling is used very frequently for apatite as its annealing behavior has been calibrated in borehole studies (e.g. Naeser and Forbes, 1976; Wagner et al., 1994) and in extensive laboratory furnace annealing experiments at various temperatures and exposure times (e.g. Green et al., 1986; Green and Duddy, 1989; Crowley et al., 1991). These data have been used to develop computer programs for calculating the FT parameters expected with any postulated geologic time(t)–temperature(T) history (e.g. Green and Duddy, 1989; Corrigan, 1991, 1993; Gallagher, 1995). Research into zircon annealing is not so advanced and therefore such modelling is not in common practice.

Track length measurements are made on horizontal confined tracks. They do not pierce the polished surface of a studied grain but are revealed because they are hit by a surface-piercing track or because they penetrate cracks or cleavage. During this work, the program "HeFTy Beta version 2" (Ketcham, 2005) has been used for track-length modeling.

5. Sample preparation and dating procedure

The samples were crushed and ground to a grain size of less than 250 μm. To retrieve apatite and zircon from the sediment, several steps of mineral separation had to be carried out: (i) A rough separation with the Wilfley Table; (ii) heavy liquid separation using methylene iodide (MI) with a density of 3.1 g/cm^3 and 3.33 g/cm^3 respectively; (iii) magnetic separation using the Frantz® Electromagnetic Separator. Some pyrite contaminated zircon fractions were additionally treated with aqua regia.

Apatite and titanite grains were mounted on glasses using Epofix, while the zircons were mounted in FEP Teflon^{TM}. All mounts were cut with 800 grit wet sandpaper and then polished on 1 μm diamond paste. The apatites were etched in 5.5N HNO_3 at 21 °C for 20 seconds (Carlson et al., 1999). The zircon mounts were etched in a eutectic $NaOH$–KOH mixture at 210 °C for various times until full track revelation was reached (Gleadow et al., 1976). The titanite mounts were etched in a mixture of HF, HNO_3, HCl and water (Naeser and McKee, 1970).

After etching, the mounts were covered with a low-uranium mica detector as sample analyses were carried out using the external detector method (Fleischer et al., 1964; Naeser and Dodge, 1969; Hurford and Green, 1983). Samples were then irradiated with thermal neutrons at ANSTO facility, Lucas Heights, Australia, and later at the Radiation Center of the Oregon State University, Corvallis, USA. The requested integrated fluxes were 1×10^{16} n/cm^2 for apatite and 1×10^{15} n/cm^2 for zircon. All samples were irradiated along with an age standard and two standard glasses (dosimeter glasses). Table 5.2 shows age standards and reference glass dosimeters for apatite and zircon. After irradiation the mica detector was etched in 40% HF at room temperature for 50 minutes.

Table 5.2: Age standards and glass dosimeters used in this study.

Mineral	reference glass dosimeter	Age standards
Apatite / Titanite	$CN5$	Durango
		Fish Canyon Tuff
Zircon	$CN1$	Fish Canyon Tuff
		Tardree

Counting and track-length measurements were carried out on a Zeiss optical microscope equipped with a Kinetek computer driven stage (Dumitru, 1995). Tracks in apatite, titanite and mica were counted at a magnification of $10 \times 100 \times 1.25$ (dry) while tracks in zircon were counted at a magnification of $10 \times 100 \times 1.6$ (oil). Track length measurements in apatite were done with a magnification of $10 \times 100 \times 1.25$ (dry).

For each mineral several age standards were counted along with their standard glasses, and a ζ–factor was calculated. The weighted mean over all ζ–factors for one mineral was then used for age calculations of the corresponding samples (Hurford and Green, 1983). The ζ–values used in this thesis are 416 ± 13 (1σ, analyst E. Wüthrich) for apatite, 133 ± 2.5 (1σ, E.W.) and 120 ± 5 (1σ, D. Seward) for zircon and 410 ± 10 (1σ, D.S.) for titanite (Tab. 5.3, Fig. 5.5).

Table 5.3: Zeta values evaluated for apatite and zircon and their corresponding weighted mean (analyst E. Wüthrich).

Apatite		**Zircon**	
Age Standard	Zeta $\pm$ 1σ	Age Standard	Zeta $\pm$ 1σ
Durango	390 ± 35	Fish Canyon Tuff	148 ± 7
Durango	373 ± 35	Tardree Rhyolite	139 ± 8
Durango	366 ± 33	Fish Canyon Tuff	128 ± 6
Durango	481 ± 47	Tardree Rhyolite	144 ± 8
Durango	567 ± 58	Fish Canyon Tuff	123 ± 6
Fish Canyon Tuff	429 ± 76	Fish Canyon Tuff	129 ± 6
Durango	442 ± 41	Tardree Rhyolite	136 ± 8
Fish Canyon Tuff	380 ± 34	Fish Canyon Tuff	131 ± 6
Durango	676 ± 74		
Durango	404 ± 30		
weighted mean:		weighted mean:	
416 ± 13		**133 ± 2.5**	

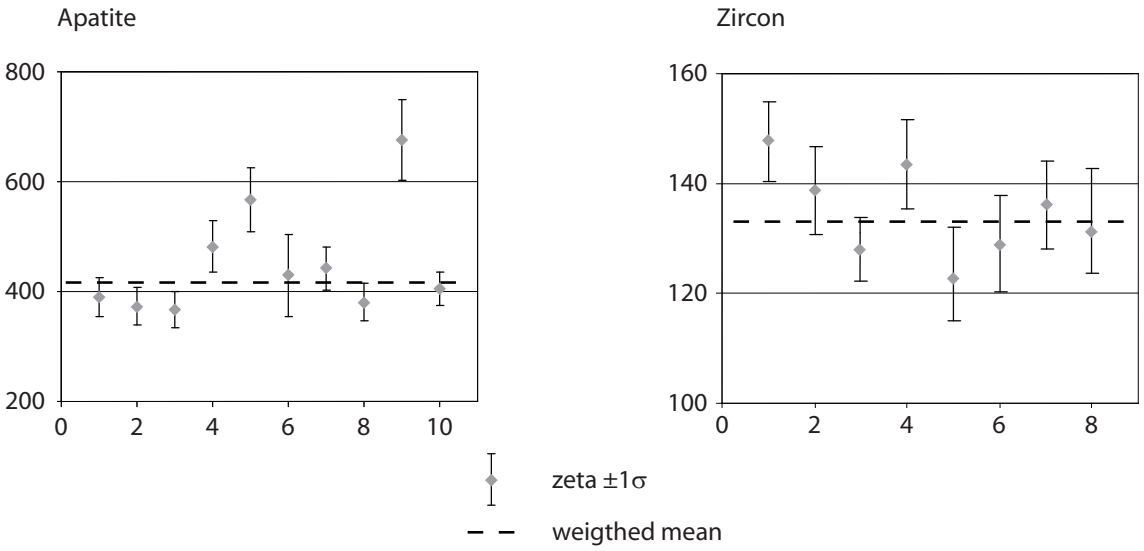

Figure 5.5: Plots for apatite and zircon showing the ζ–factors derived from single age standard sample and their corresponding weighted mean.

5.1 Closure temperatures

The closure temperatures generally accepted are displayed in table 5.1. However, it has been shown that for cooling rates > 30°C/Ma the zircon closure temperature might be well above this value (Yamada et al., 1995b; Foster et al., 1996). In addition, the closure temperature for titanite can be up to 350°C for very rapid cooling of 100°C/Ma (Foster et al., 1996). For this work a zircon closure temperature of 260 ± 50°C is assumed and a titanite closure temperature of 300 ± 40°C. For the apatite closure temperature the well established value of 110 ± 10°C is used.

Appendix II: The (U-Th)/He method

$(U\text{-}Th)/He$ dating (subsequently called He dating) is based on the series decay of ^{238}U, ^{235}U and ^{232}Th and the α–decay of ^{147}Sm leading to ^{4}He nuclei (α particles) production. The ingrowth equation is as follows (compare to the basic decay equation 5.1):

$$\begin{aligned} {}^{4}He = {} & 8^{238}U(e^{\lambda_{238}t} - 1) + 7^{235}U(e^{\lambda_{238}t} - 1) + 6^{232}Th(e^{\lambda_{232}t} - 1) \\ & + {}^{147}Sm(e^{\lambda_{147}t} - 1) \end{aligned} \tag{5.12}$$

Where ^{238}U, ^{235}U, ^{232}Th, ^{147}Sm and ^{4}He refer to present-day amounts of the according isotopes in a medium, t is the accumulation time or He age and the decay constants are represented by the different λ's. The Uranium isotope ^{235}U can also be expressed by $^{238}U/137.88$ as the present-day ratio of ^{238}U and ^{235}U in nature is constant (Cowan and Adler, 1976).

Generally the single α particle produced by the decay of ^{147}Sm to ^{143}Nd is neglected for age calculations, as it has a minor input compared to the eight, seven and six α particles produced by the decay of the actinoids. However, it has been noted that depending on the concentrations of the different α producers in a grain, ^{147}Sm may become important and by neglecting it one may introduce a systematic error to the calculated age (Kohn et al., 2006). In apatite this error normally lies between $0.1--10\%$ but can grow to 25% in grains showing total actinoid concentrations lower than $10ppm$. Equation 5.12 implies that no initial ^{4}He is present in the system. Inputs from the atmosphere can indeed be neglected as the concentration of ^{4}He is low ($\sim 5ppm$), but inclusions (fluids or other minerals) can contribute significant amounts of foreign helium and therefore must be avoided.

1. Diffusion of He

The first attempts to use $(U\text{-}Th)/He$ as a method to date rocks were undertaken by Strutt (1905) and Rutherford (1907). They were abandoned as these workers were trying to date the formation ages of a rock and did not understand the process of diffusion yet. He diffuses easily out of a mineral lattice and hence their ages were too young when compared with results from other methods.

Zeitler et al. (1987) were the first to point out the fact that He is lost from the system by diffusion at temperatures higher than the mineral-specific closure temperature and they recognised the great potential of this method as a low temperature thermochronometer.

To be able to date a mineral with the He method it is essential that this mineral retains He at earth surface conditions. Minerals known to fulfil this condition are olivine (Trull et al., 1991), pyroxene and amphibole (Lippolt and Weigel, 1988), garnet (Dunai

and Roselieb, 1996), non-metamict zircon (Hurley, 1952; Damon and Kulp, 1957), non-metamict titanite (Hurley, 1952; Reiners and Farley, 1999), apatite (Zeitler et al., 1987), allanite (Wolf, 1997), magnetite (Fanale and Kulp, 1962) and hematite (Wernicke and Lippolt, 1994b,a; Bähr et al., 1994). Furthermore also submarine basaltic glass has been shown to match this criteria (Graham et al., 1987). On the other hand one has to understand the temperature dependent diffusion behavior to be able to determine a closure temperature. A mineral is only suitable for dating if diffusion fulfils the Arrhenius relationship:

$$\frac{D(T)}{a^2} = \frac{D_0}{a^2} e^{-E_a/RT} \tag{5.13}$$

where $D(T)$ is the temperature dependent diffusivity, D_0 the diffusivity at infinite temperature (also known as diffusion constant), E_a the activation energy, R the gas constant, T the temperature in Kelvin and a the diffusion domain radius, which in simple systems can be equal to the size (radius) of the grain, but can also be some sub-grain structure with a corresponding smaller size. To test this relationship one can plot results from a diffusion experiment with $1/T$ as x-axis and $ln(D(T)/a^2)$ on the y-axis. The plot should be a linear line with an axis intercept at $ln(D_0/a^2)$ and a slope of $-E_a/R$.

Probably the most intensively studied mineral is apatite. Apatite obeys the Arrhenius diffusion law and a is equal to the grain size (radius). Hence diffusion processes and the closure temperature T_c, which is defined identical as in section (Dodson, 1973), are dependent on the size of an analysed grain. The other factor influencing T_c is again the cooling rate, as already discussed in section . The closure temperature of apatite is usually quoted as 75 $\pm$ 5°C for typical geological rates of cooling and mineral grain sizes (Farley, 2000). Wolf et al. (1998) demonstrated that over geological time scales He is retained in apatite at temperatures less than $\sim$ 40°C (= blocking temperature T_b) and totally lost from the crystal lattice at temperatures above $85 - 90$°C (= "open-system" temperature T_o). The temperature zone between T_b and T_o is called the partial retention zone, PRZ, and is the analogue of the fission-track PAZ.

Table 5.4 shows the He closure temperatures of apatite and other minerals used for He dating.

Table 5.4: The He closure temperatures T_c of variable minerals.

Mineral	T_c [°C]	Reference e.g.
Apatite	75 $\pm$ 5	Wolf et al. (1998); Farley (2000)
Zircon	$200 - 230$	Reiners et al. (2002)
Titanite	$150 - 200$	Reiners and Farley (1999)
Hematite	~ 120	Wernicke and Lippolt (1994a)
Garnet	~ 600	Dunai and Roselieb (1996)

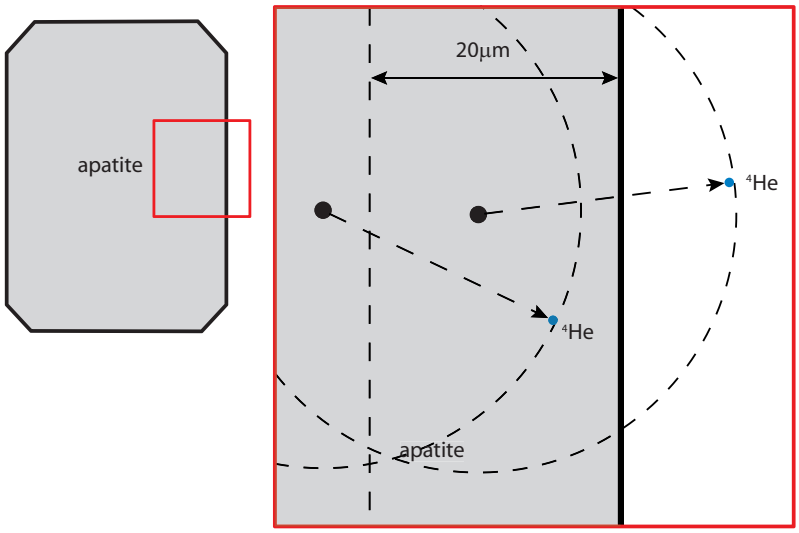

Figure 5.6: Schematic depiction of α ejection in apatite.

2. Alpha–emission correction

Alpha particles produced by radioactive decay carry a high kinetic energy that allows them to travel up to $20\mu m$ through a mineral lattice. This so-called stopping distance is dependent on the decaying isotope as well as on the density of the matrix hosting the isotope, hence of the mineral (Table 1 in Farley et al., 1996). The stopping distance has to be taken into account when calculating an age from a single grain. If a decaying atom sits within the stopping distance from the edge of a grain there is a chance that the α particle is ejected (Fig. 5.6). If the decaying atom is located right at the edge of a grain and this edge is considered a flat surface, the ejecting probability is 50%.

To overcome the α ejection problem in age calculation, Farley et al. (1996) developed a quantitative model for correcting He ages. Several assumptions were made and should be reflected in appropriate grain selection when applying He dating. 1. The correction is based on simplified grain geometry and thus the analysed crystals should fit this geometry as accurately as possible. 2. The concentration of the parent nuclei is assumed to be homogenous, although this will in general be unknown. 3. Implantation of He by neighboring minerals with higher actinoid concentrations than the studied grain, is assumed to be insignificant.

The model of Farley et al. (1996) showed that the important variables controlling the α ejection correction are the surface to volume ratio β of a crystal and the α stopping distance. The bigger a crystal the smaller is β and thus a smaller portion of the mineral is affected by α ejection and smaller corrections are needed. They showed that, while each decay in the U and Th chains has a characteristic stopping distance, the mean α correction obtained for one mineral by modeling each decay separately does not differ significant from simply using a mean stopping distance for each parent. The parameter by

which the measured age must be divided to obtain the "α–ejection-corrected" age is called FT factor.

3. Sample preparation, measuring procedures and age calculation

He dating has been carried out on single apatite grains. Mineral separation was done as described in section . Some samples were handpicked and analysed at the He laboratory at the University of Kansas, others were picked and analysed at ETH Zürich.

Handpicking was carried out under polarised and nonpolarised light with a binocular microscope in order to exclude broken grains or grains containing mineral/fluid inclusions. A digital picture was taken of the grains accepted for analysis and their length and width were measured. Based on these measurements the α ejection correction (FT factor) was calculated according to Farley et al. (1996). The single grains were wrapped in pure platinum tubes to prevent melting and ensure heterogenous outgassing during laser heating for He extraction. At Kansas Universtiy He was measured using an all-metal, ultra-high vacuum noble gas extraction and purification line with a quadrupole mass spectrometry system and a continuous-mode Nd–YAG laser. At ETH He extractions and measurements were done on the "Albatros" nobel gas mass spectrometer, a non-commercial mass spectrometer designed and built at the ETH Zurich by H. Bauer, using a continuous-mode Nd–YAG laser. To measure U, Th and if required Sm the previously degassed grains were dissolved in concentrated HNO_3 (4.25 molar) and spiked. As no Sm was measured at ETH, a ^{233}U–^{229}Th mixed spike was used. The Kansas Lab measures Sm as well as all other rare earth elements (REE) and thus a mixed ^{230}Th–^{235}U–^{149}Sm–REE spike was used. Their measurements were carried out by using a Fisons/VG PlasmaQuad II Inductively Coupled Plasma Mass Spectrometer (ICP–MS) while at ETH a Thermo Finnigan, Element 2 ICP–MS was used.

Age calculations were done by iteratively solving equation 5.12.

Appendix III: Fission-track grain-age data

Age and zeta calculations as well as graphical presentation of the fission track data was carried out with the program TrackKey Dunkl (2002).

Information to the data sets

Ns:	Number of spontaneous tracks counted
Ni:	Number of induced tracks counted
Area:	Number of microscope squares. One grid, equivalent to 100 squares, corresponds to an area of 62.44 μm.
RhoS:	Density of spontaneous tracks in 10^5 tracks/cm^2cm
RhoI:	Density of induced tracks in 10^5 tracks/cm^2
Pooled Age:	Pooled age $\pm$ 2σ in Ma. This age is calculated with a value of ρ_{ratio} of $\frac{\sum N_s}{\sum N_i}$
Mean Age:	Mean age $\pm$ 2σ in Ma. This age is calculated with a value of ρ_{ratio} of $\frac{\sum \frac{\rho_s}{\rho_i}}{n}$ where n is the number of dated grains
Central Age:	Central age $\pm$ 2σ in Ma after Galbraith and Laslett (1993)
Chi-sq.:	χ^2 value according to Green (1981)
P(%):	Probability of χ^2 for ν degrees of freedom where ν equals the number of grains -1
Dispersion:	
RhoD:	Standard track density in 10^5 tracks/cm^2
Nd:	Number of induced tracks counted on the U standards.
U standard:	Used standard glass
Zeta:	ζ factor $\pm$ 1σ

The table at the bottom of each page features the values corresponding to the single analysed grains. The radial plot Galbraith (1990) is shown in the top right corner.

Titanite fission track grain-age data

Sample number:	**RD 16**
Mineral:	Titanite
Irradiation code:	eth-333-10
Ns:	1931
Ni:	6886
Area:	725
RohS:	42.66
RohI:	152.11
Pooled Age:	56.1 ± 4.6
Mean Age:	56.5 ± 5.8
Central Age:	55.9 ± 6.2
Chi-sq.:	32.19
P(%)	0.13
Dispersion:	0.13
RohD:	9.80
Nd:	2641
U standard	CN 5
Zeta ±1σ	140 ± 5
counted by	DS

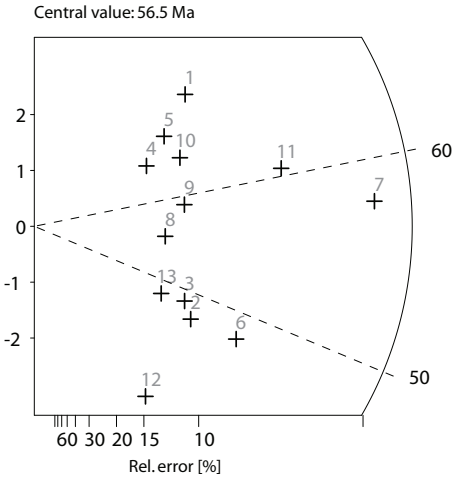

Crystal	Ns	Ni	Area	RhoS (e5)	RhoI (e5)	Age (Ma)	+- 1s	U (ppm)
1	115	314	25	73.67	201.15	73.12	8.29	233.68
2	112	472	100	17.94	75.59	47.47	5.20	87.82
3	104	426	50	33.31	136.45	48.84	5.55	158.52
4	62	187	25	39.72	119.80	66.23	9.92	139.17
5	84	242	100	13.45	38.76	69.32	9.04	45.02
6	187	780	100	29.95	124.92	47.96	4.18	145.12
7	552	1910	100	88.41	305.89	57.77	3.32	355.36
8	81	293	25	51.89	187.70	55.27	7.15	218.05
9	108	366	25	69.19	234.47	58.98	6.72	272.38
10	104	320	25	66.62	205.00	64.93	7.60	238.15
11	294	970	100	47.09	155.35	60.57	4.45	180.47
12	54	300	25	34.59	192.18	36.04	5.45	223.26
13	74	306	25	47.41	196.03	48.38	6.45	227.73

Zircon fission track grain-age data

Sample number:	**RD 2**
Mineral:	Zircon
Irradiation code:	eth-327-15/16
Ns:	811
Ni:	571
Area:	117
RohS:	111.0
RohI:	78.2
Pooled Age:	32.8 ± 4.0
Mean Age:	34.2 ± 5.4
Central Age:	33.0 ± 5.6
Chi-sq.:	19.43
P(%)	2.18
Dispersion:	0.18
RohD:	3.5
Nd:	2185
U standard	CN 1
Zeta ±1σ	133 ± 2.5
counted by	EW

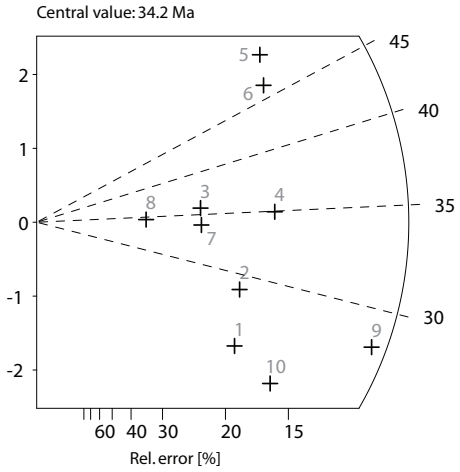

Crystal	Ns	Ni	Area	RhoS (e5)	RhoI (e5)	Age (Ma)	+- 1s	U (ppm)
1	57	53	10	91.29	84.88	24.83	4.79	774.04
2	65	52	12	86.75	69.40	28.85	5.43	632.86
3	48	31	9	85.42	55.16	35.72	8.29	503.05
4	100	66	12	133.46	88.09	34.95	5.63	803.25
5	111	51	9	197.52	90.75	50.15	8.60	827.59
6	109	54	9	193.96	96.09	46.52	7.85	876.27
7	47	32	6	125.45	85.42	33.89	7.83	778.91
8	21	14	4	84.08	56.05	34.60	11.98	511.16
9	175	143	30	93.42	76.34	28.25	3.28	696.15
10	78	75	16	78.08	75.07	24.01	3.94	684.59

Sample number:	**RD 4**
Mineral:	Zircon
Irradiation code:	eth-334-7
Ns:	809
Ni:	611
Area:	524
RohS:	24.73
RohI:	18.67
Pooled Age:	36.6 ± 4.4
Mean Age:	38.2 ± 4.4
Central Age:	36.6 ± 4.8
Chi-sq.:	22.57
P(%)	25.70
Dispersion:	0.10
RohD:	4.165
Nd:	2376
U standard	CN 1
Zeta ±1σ	133 ± 2.5
counted by	EW

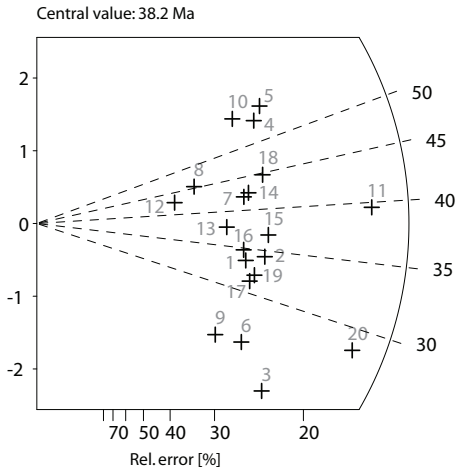

Crystal	Ns	Ni	Area	RhoS (e5)	RhoI (e5)	Age (Ma)	+- 1s	U (ppm)
1	34	28	15	36.30	29.90	33.55	8.61	227.67
2	41	33	28	23.45	18.88	34.32	8.08	143.75
3	32	40	36	14.24	17.80	22.12	5.28	135.52
4	49	25	45	17.44	8.90	54.06	13.37	67.76
5	53	26	24	35.37	17.35	56.22	13.55	132.13
6	28	31	24	18.69	20.69	24.97	6.55	157.54
7	38	25	8	76.07	50.05	41.97	10.87	381.15
8	23	14	16	23.02	14.01	45.35	15.42	106.72
9	21	24	18	18.69	21.35	24.19	7.26	162.62
10	41	20	32	20.52	10.01	56.53	15.50	76.23
11	96	67	100	15.38	10.73	39.57	6.39	81.72
12	17	11	15	18.15	11.75	42.67	16.55	89.44
13	30	22	18	26.69	19.57	37.66	10.62	149.07
14	40	26	14	45.76	29.74	42.47	10.76	226.51
15	44	33	12	58.72	44.04	36.83	8.54	335.41
16	34	27	40	13.61	10.81	34.79	9.02	82.33
17	34	30	15	36.30	32.03	31.32	7.89	243.93
18	47	29	20	37.64	23.22	44.74	10.64	176.85
19	36	31	24	24.02	20.69	32.09	7.91	157.54
20	71	69	20	56.86	55.25	28.44	4.87	420.79

Sample number:	**RD 5**
Mineral:	Zircon
Irradiation code:	eth-334-11
Ns:	961
Ni:	814
Area:	387
RohS:	39.77
RohI:	33.69
Pooled Age:	31.3 ± 3.4
Mean Age:	30.5 ± 4.6
Central Age:	29.8 ± 4.8
Chi-sq.:	41.72
P(%)	0.19
Dispersion:	0.22
RohD:	3.99
Nd:	2376
U standard	CN 1
Zeta ±1σ	133 ± 2.5
counted by	EW

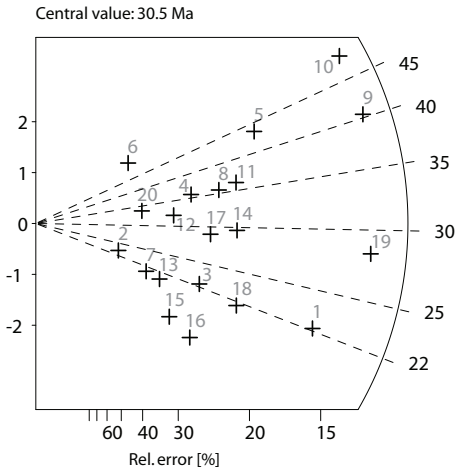

Crystal	Ns	Ni	Area	RhoS (e5)	RhoI (e5)	Age (Ma)	+- 1s	U (ppm)
1	77	92	24	51.38	61.39	22.18	3.48	487.93
2	7	8	15	7.47	8.54	23.18	12.01	67.89
3	27	32	21	20.59	24.40	22.36	5.87	193.96
4	31	23	21	23.64	17.54	35.67	9.87	139.41
5	69	42	14	78.93	48.05	43.46	8.59	381.86
6	14	7	12	18.69	9.34	52.86	24.52	74.25
7	12	15	4	48.05	60.06	21.20	8.23	477.32
8	43	32	24	28.69	21.35	35.57	8.36	169.72
9	148	97	48	49.38	32.36	40.37	5.39	257.22
10	143	78	40	57.26	31.23	48.48	6.96	248.21
11	52	38	12	69.40	50.72	36.22	7.79	403.07
12	23	19	20	18.42	15.22	32.05	9.98	120.92
13	15	19	10	24.02	30.43	20.92	7.25	241.84
14	47	42	15	50.18	44.84	29.63	6.35	356.40
15	16	25	28	9.15	14.30	16.96	5.45	113.65
16	21	34	10	33.63	54.45	16.37	4.57	432.77
17	35	32	12	46.71	42.71	28.96	7.13	339.43
18	40	49	18	35.59	43.60	21.63	4.65	346.50
19	127	119	27	75.33	70.59	28.26	3.69	561.00
20	14	11	12	18.69	14.68	33.69	13.61	116.68

Sample number:	**RD 6**
Mineral:	Zircon
Irradiation code:	eth-327-17
Ns:	2473
Ni:	1540
Area:	880
RohS:	71.87
RohI:	44.76
Pooled Age:	37.3 ± 3.4
Mean Age:	37.7 ± 3.0
Central Age:	37.2 ± 3.6
Chi-sq.:	28.81
P(%)	6.90
Dispersion:	0.08
RohD:	3.89
Nd:	2091
U standard	CN 1
Zeta $\pm 1\sigma$	120 ± 2.5
counted by	DS

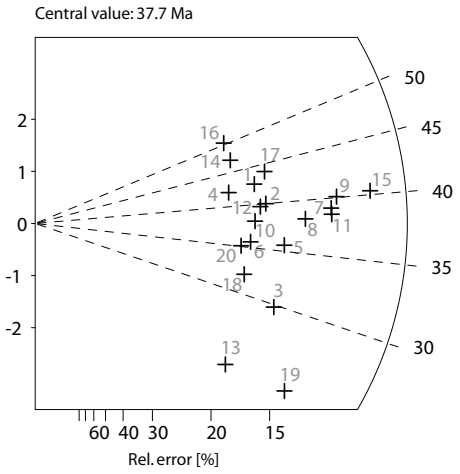

Crystal	Ns	Ni	Area	RhoS (e5)	RhoI (e5)	Age (Ma)	+- 1s	U (ppm)
1	110	60	50	56.27	30.69	42.62	6.96	250.46
2	117	68	25	119.69	69.57	40.00	6.22	567.70
3	105	82	25	107.42	83.89	29.79	4.48	684.58
4	85	47	48	45.29	25.04	42.04	7.75	204.37
5	127	83	32	101.50	66.34	35.59	5.14	541.35
6	95	62	40	60.74	39.64	35.64	5.92	323.51
7	190	113	40	121.48	72.25	39.10	4.79	589.62
8	156	95	50	79.80	48.59	38.18	5.10	396.56
9	200	116	40	127.88	74.17	40.09	4.83	605.27
10	103	63	25	105.37	64.45	38.02	6.19	525.96
11	189	114	100	48.34	29.16	38.55	4.72	237.93
12	111	65	40	70.97	41.56	39.70	6.32	339.16
13	58	59	40	37.08	37.72	22.89	4.29	307.85
14	93	46	50	47.57	23.53	46.98	8.59	192.02
15	248	143	100	63.43	36.57	40.32	4.41	298.46
16	91	42	25	93.10	42.97	50.33	9.51	350.64
17	123	65	25	125.83	66.50	43.98	6.87	542.65
18	84	61	50	42.97	31.20	32.04	5.48	254.63
19	102	99	50	52.17	50.64	23.98	3.46	413.25
20	86	57	25	87.98	58.31	35.09	6.09	475.87

Sample number:	**RD 14**
Mineral:	Zircon
Irradiation code:	eth-334-29
Ns:	2038
Ni:	1274
Area:	641
RohS:	81.3
RohI:	50.8
Pooled Age:	33.8 ± 3.0
Mean Age:	34.1 ± 4.2
Central Age:	33.2 ± 4.2
Chi-sq.:	48.7
P(%)	0.02
Dispersion:	0.19
RohD:	3.18
Nd:	2376
U standard	CN 1
Zeta $\pm 1\sigma$	133 ± 2.5
counted by	EW

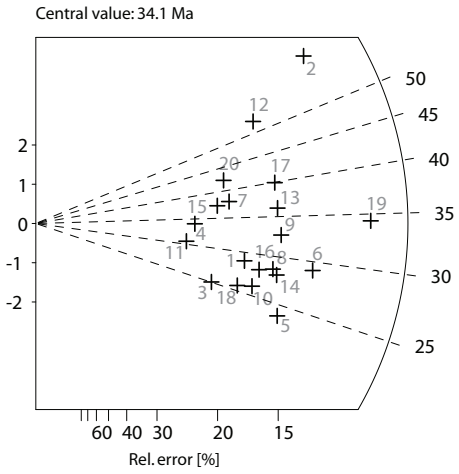

Crystal	Ns	Ni	Area	RhoS (e5)	RhoI (e5)	Age (Ma)	+- 1s	U (ppm)
1	78	57	20	99.74	72.89	28.88	5.10	726.83
2	211	73	25	215.86	74.68	60.86	8.44	744.68
3	51	43	40	32.61	27.49	25.04	5.23	274.15
4	50	31	20	63.94	39.64	34.03	7.84	395.29
5	94	83	50	48.08	42.46	23.91	3.66	423.34
6	138	100	50	70.59	51.15	29.13	3.91	510.05
7	79	44	30	67.35	37.51	37.87	7.20	374.04
8	100	74	30	85.25	63.09	28.52	4.45	629.07
9	116	75	40	74.17	47.95	32.64	4.92	478.18
10	79	64	24	84.19	68.20	26.06	4.44	680.07
11	42	29	12	89.51	61.81	30.56	7.43	616.31
12	125	50	30	106.56	42.63	52.67	8.93	425.04
13	120	70	32	95.91	55.95	36.16	5.53	557.87
14	102	77	40	65.22	49.23	27.96	4.29	490.93
15	69	39	18	98.04	55.41	37.32	7.55	552.56
16	88	66	24	93.78	70.33	28.14	4.65	701.32
17	125	66	36	88.80	46.89	39.94	6.18	467.55
18	68	56	20	86.96	71.61	25.64	4.68	714.08
19	223	137	70	81.48	50.06	34.34	3.85	499.12
20	80	40	30	68.20	34.10	42.17	8.25	340.04

Sample number:	**RD 19**
Mineral:	Zircon
Irradiation code:	eth-335-11
Ns:	2902
Ni:	2116
Area:	1664
RohS:	44.6
RohI:	32.5
Pooled Age:	35.2 ± 2.8
Mean Age:	35.6 ± 2.4
Central Age:	35.1 ± 3.2
Chi-sq.:	35.43
P(%)	10.27
Dispersion:	0.10
RohD:	3.87
Nd:	2251
U standard	CN 1
Zeta $\pm 1\sigma$	133 ± 2.5
counted by	EW

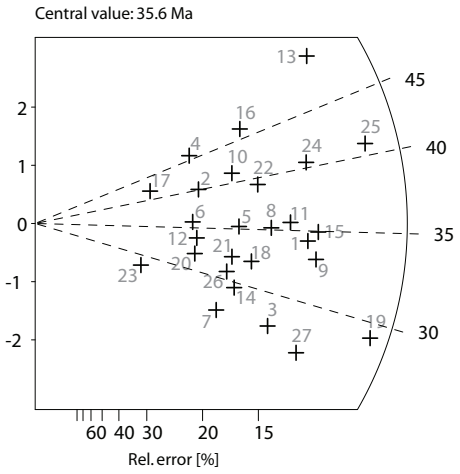

Table with grain data see next page.

Continuation of RD19–data set.

Crystal	Ns	Ni	Area	RhoS (e5)	RhoI (e5)	Age (Ma)	+- 1s	U (ppm)
1	155	116	70	56.63	42.38	34.26	4.32	347.73
2	61	39	27	57.78	36.94	40.09	8.30	303.10
3	100	93	50	51.15	47.57	27.59	4.05	390.30
4	59	33	18	83.83	46.89	45.80	10.04	384.70
5	88	64	50	45.01	32.74	35.25	5.88	268.59
6	53	38	40	33.89	24.30	35.76	7.67	199.35
7	60	57	50	30.69	29.16	27.01	5.05	239.22
8	118	86	100	30.18	22.00	35.18	5.09	180.46
9	161	125	100	41.18	31.97	33.03	4.05	262.30
10	90	56	50	46.04	28.65	41.19	7.11	235.02
11	139	100	50	71.10	51.15	35.64	4.78	419.68
12	54	41	30	46.04	34.95	33.77	7.06	286.78
13	196	99	100	50.13	25.32	50.70	6.41	207.74
14	76	66	30	64.79	56.27	29.54	5.04	461.64
15	169	124	100	43.22	31.71	34.95	4.25	260.20
16	105	58	80	33.57	18.54	46.38	7.70	152.13
17	31	19	50	15.86	9.72	41.81	12.24	79.74
18	94	75	50	48.08	38.36	32.14	5.06	314.76
19	214	188	100	54.73	48.08	29.20	3.03	394.50
20	51	41	60	21.74	17.48	31.90	6.75	143.39
21	78	62	49	40.71	32.36	32.26	5.56	265.51
22	112	73	60	47.74	31.12	39.33	6.02	255.30
23	21	19	20	26.85	24.30	28.35	9.01	199.35
24	169	107	100	43.22	27.37	40.48	5.13	224.53
25	252	158	100	64.45	40.41	40.88	4.31	331.54
26	72	60	60	30.69	25.58	30.78	5.45	209.84
27	124	119	70	45.31	43.48	26.73	3.51	356.73

Sample number:	**RD 24**
Mineral:	Zircon
Irradiation code:	eth-335-22
Ns:	1570
Ni:	1056
Area:	608
RohS:	66.0
RohI:	44.4
Pooled Age:	31.1 ± 3.0
Mean Age:	32.2 ± 3.4
Central Age:	31.3 ± 3.4
Chi-sq.:	27.36
P(%)	9.65
Dispersion:	0.11
RohD:	3.15
Nd:	2251
U standard	CN 1
Zeta $\pm 1\sigma$	133 ± 2.5
counted by	EW

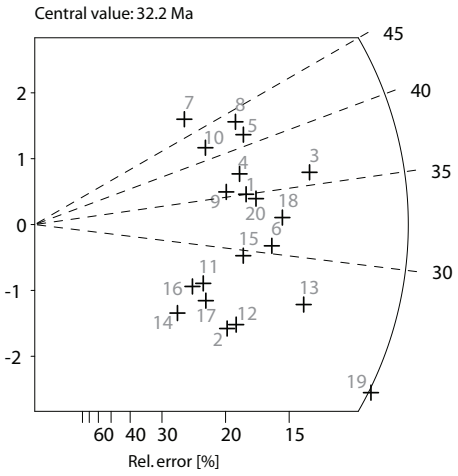

Crystal	Ns	Ni	Area	RhoS (e5)	RhoI (e5)	Age (Ma)	+- 1s	U (ppm)
1	82	49	18	116.51	69.622	35.01	6.4	700.05
2	54	48	40	34.527	30.691	23.56	4.72	308.59
3	141	82	35	103.033	59.92	35.97	5.1	602.49
4	80	45	36	56.834	31.969	37.19	7.01	321.45
5	89	45	24	94.842	47.954	41.36	7.65	482.18
6	95	65	28	86.774	59.372	30.59	5	596.98
7	51	22	30	43.478	18.755	48.45	12.43	188.58
8	85	41	20	108.696	52.43	43.35	8.33	527.18
9	68	40	20	86.957	51.151	35.57	7.16	514.32
10	60	30	12	127.877	63.939	41.82	9.43	642.9
11	44	35	21	53.587	42.626	26.32	6.01	428.6
12	60	52	24	63.939	55.413	24.16	4.63	557.18
13	114	88	30	97.187	75.021	27.12	3.92	754.34
14	29	27	100	7.417	6.905	22.49	6.05	69.43
15	72	51	20	92.072	65.217	29.55	5.47	655.76
16	38	31	20	48.593	39.642	25.66	6.25	398.6
17	44	37	32	35.166	29.572	24.9	5.6	297.34
18	108	69	18	153.453	98.039	32.75	5.13	985.78
19	167	145	60	71.185	61.807	24.12	2.82	621.47
20	89	54	20	113.811	69.054	34.48	6.03	694.33

Sample number:	**RD 26**
Mineral:	Zircon
Irradiation code:	eth-336-4
Ns:	1572
Ni:	1297
Area:	967
RohS:	41.6
RohI:	34.3
Pooled Age:	33.4 ± 3.2
Mean Age:	33.6 ± 3.6
Central Age:	33.1 ± 3.4
Chi-sq.:	26.94
P(%)	13.71
Dispersion:	0.09
RohD:	4.15
Nd:	2409
U standard	CN 1
Zeta ±1σ	133 ± 2.5
counted by	EW

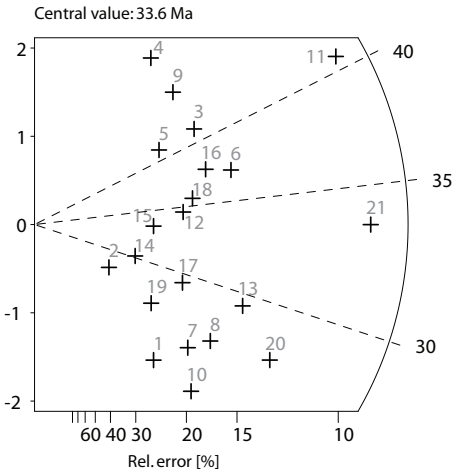

Crystal	Ns	Ni	Area	RhoS (e5)	RhoI (e5)	Age (Ma)	+- 1s	U (ppm)
1	28	34	21	34.10	41.41	22.71	5.83	316.20
2	12	12	30	10.23	10.23	27.56	11.28	78.12
3	69	46	18	98.04	65.36	41.30	7.94	499.10
4	44	22	12	93.78	46.89	55.01	14.45	358.05
5	42	28	24	44.76	29.84	41.30	10.14	227.85
6	98	73	40	62.66	46.68	36.98	5.81	356.42
7	49	53	100	12.53	13.56	25.49	5.10	103.51
8	66	68	18	93.78	96.62	26.76	4.68	737.80
9	56	33	20	71.61	42.20	46.71	10.33	322.25
10	49	58	30	41.77	49.45	23.30	4.57	377.58
11	244	165	100	62.40	42.20	40.72	4.26	322.25
12	54	43	24	57.55	45.82	34.60	7.14	349.91
13	97	91	50	49.62	46.55	29.38	4.36	355.45
14	23	21	40	14.71	13.43	30.18	9.15	102.53
15	34	28	30	28.99	23.87	33.46	8.59	182.28
16	75	55	50	38.36	28.13	37.56	6.75	214.83
17	49	46	50	25.06	23.53	29.36	6.08	179.68
18	62	48	60	26.43	20.46	35.58	6.91	156.24
19	29	30	50	14.83	15.35	26.65	6.98	117.18
20	120	120	100	30.69	30.69	27.56	3.64	234.36
21	272	223	100	69.57	57.03	33.61	3.18	435.52

Sample number:	**RD 30**
Mineral:	Zircon
Irradiation code:	eth-336-10
Ns:	1096
Ni:	800
Area:	913
RohS:	30.7
RohI:	22.4
Pooled Age:	34.2 ± 3.8
Mean Age:	34.2 ± 2.8
Central Age:	34.2 ± 3.8
Chi-sq.:	10.99
P(%)	92.42
Dispersion:	0.00
RohD:	3.76
Nd:	2409
U standard	CN 1
Zeta ±1σ	133 ± 2.5
counted by	EW

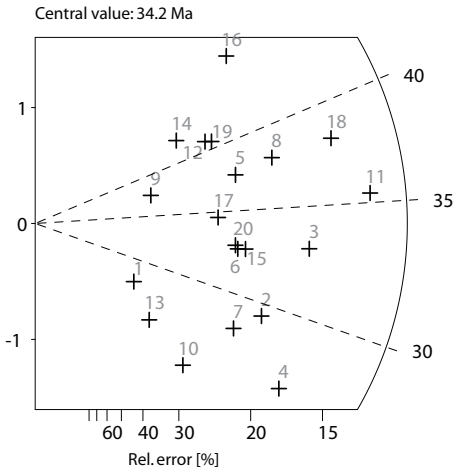

Crystal	Ns	Ni	Area	RhoS (e5)	RhoI (e5)	Age (Ma)	+- 1s	U (ppm)
1	11	10	16	17.58	15.99	27.47	12.03	134.75
2	60	51	42	36.54	31.06	29.37	5.65	261.80
3	94	71	40	60.10	45.40	33.04	5.28	382.68
4	66	62	40	42.20	39.64	26.58	4.76	334.17
5	54	36	36	38.36	25.58	37.43	8.12	215.60
6	51	39	50	26.09	19.95	32.64	7.00	168.17
7	45	40	30	38.36	34.10	28.09	6.15	287.46
8	76	50	50	38.88	25.58	37.92	6.99	215.60
9	18	12	30	15.35	10.23	37.43	13.99	86.24
10	23	24	50	11.77	12.28	23.94	7.02	103.49
11	146	103	60	62.23	43.91	35.37	4.66	370.11
12	41	25	24	43.69	26.64	40.91	10.44	224.58
13	14	14	30	11.94	11.94	24.97	9.46	100.61
14	29	17	50	14.83	8.70	42.55	13.05	73.30
15	55	42	100	14.07	10.74	32.69	6.76	90.55
16	57	30	80	18.22	9.59	47.37	10.77	80.85
17	43	31	40	27.49	19.82	34.62	8.21	167.09
18	119	78	70	43.48	28.50	38.06	5.64	240.24
19	44	27	40	28.13	17.26	40.65	10.00	145.53
20	50	38	35	36.54	27.77	32.84	7.13	234.08

Sample number:	**RD 32**
Mineral:	Zircon
Irradiation code:	eth-336-13
Ns:	2048
Ni:	1340
Area:	1016
RohS:	51.6
RohI:	33.7
Pooled Age:	36.2 ± 3.2
Mean Age:	36.0 ± 3.4
Central Age:	35.7 ± 3.6
Chi-sq.:	24.73
P(%)	16.97
Dispersion:	0.08
RohD:	3.57
Nd:	2409
U standard	CN 1
Zeta ±1σ	133 ± 2.5
counted by	EW

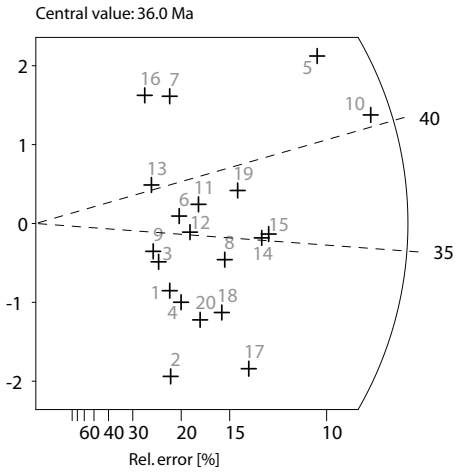

Crystal	Ns	Ni	Area	RhoS (e5)	RhoI (e5)	Age (Ma)	+- 1s	U (ppm)
1	48	38	36	34.10	27.00	29.90	6.54	240.05
2	43	43	15	73.32	73.32	23.68	5.15	651.92
3	42	31	42	25.58	18.88	32.06	7.64	167.85
4	56	45	10	143.22	115.09	29.45	5.95	1023.36
5	271	143	200	34.66	18.29	44.80	4.79	162.60
6	62	40	25	63.43	40.92	36.67	7.51	363.86
7	67	31	28	61.20	28.32	51.07	11.18	251.78
8	102	72	60	43.48	30.69	33.52	5.24	272.89
9	39	28	12	83.12	59.68	32.96	8.21	530.63
10	360	210	70	131.53	76.73	40.54	3.70	682.24
11	81	51	20	103.58	65.22	37.57	6.80	579.90
12	70	47	16	111.89	75.13	35.24	6.72	668.02
13	43	25	60	18.33	10.66	40.68	10.29	94.76
14	150	101	42	91.34	61.50	35.14	4.63	546.87
15	160	107	70	58.46	39.09	35.38	4.53	347.62
16	47	20	100	12.02	5.12	55.51	14.90	45.48
17	117	99	30	99.74	84.40	27.98	3.90	750.46
18	93	73	50	47.57	37.34	30.15	4.79	332.02
19	126	78	100	32.23	19.95	38.21	5.61	177.38
20	71	58	30	60.53	49.45	28.98	5.19	439.66

Sample number:	**RD 34**
Mineral:	Zircon
Irradiation code:	eth-355-6
Ns:	1280
Ni:	1726
Area:	494
RohS:	66.3
RohI:	89.4
Pooled Age:	25.8 ± 2.4
Mean Age:	26.7 ± 2.8
Central Age:	26.0 ± 3.2
Chi-sq.:	42.44
P(%)	0.15
Dispersion:	0.18
RohD:	5.24
Nd:	3627
U standard	CN 1
Zeta $\pm 1\sigma$	133 ± 2.5
counted by	EW

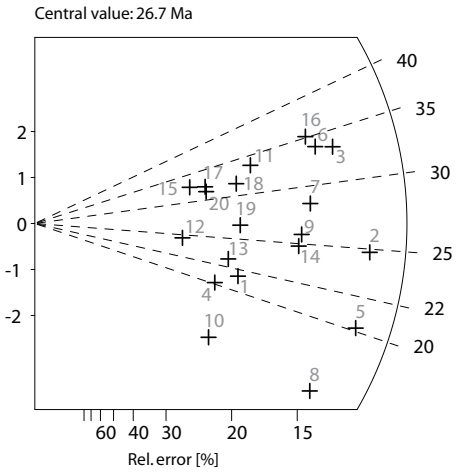

Crystal	Ns	Ni	Area	RhoS (e5)	RhoI (e5)	Age (Ma)	+- 1s	U (ppm)
1	43	70	18	61.097	99.46	21.38	4.18	601.85
2	124	174	60	52.856	74.169	24.79	2.98	448.81
3	112	117	20	143.223	149.616	33.28	4.48	905.35
4	33	57	10	84.399	145.78	20.15	4.44	882.14
5	105	181	60	44.757	77.153	20.19	2.53	466.86
6	100	103	25	102.302	105.371	33.76	4.81	637.62
7	89	109	24	94.842	116.155	28.4	4.12	702.87
8	71	156	40	45.396	99.744	15.85	2.3	603.57
9	80	108	24	85.251	115.09	25.77	3.86	696.42
10	28	64	20	35.806	81.841	15.23	3.47	495.24
11	59	61	15	100.597	104.007	33.63	6.2	629.36
12	24	34	9	68.201	96.618	24.56	6.58	584.65
13	40	61	30	34.101	52.003	22.82	4.68	314.68
14	77	108	20	98.465	138.107	24.81	3.75	835.71
15	30	32	20	38.363	40.921	32.6	8.32	247.62
16	95	94	18	134.982	133.561	35.13	5.19	808.2
17	36	39	20	46.036	49.872	32.1	7.46	301.78
18	50	55	18	71.043	78.147	31.61	6.23	472.88
19	48	63	25	49.105	64.45	26.51	5.12	390
20	36	40	18	51.151	56.834	31.3	7.23	343.91

Sample number:	**RD 36**
Mineral:	Zircon
Irradiation code:	eth-369-2
Ns:	1529
Ni:	1346
Area:	834
RohS:	29.4
RohI:	25.9
Pooled Age:	40.0 ± 3.6
Mean Age:	39.8 ± 3.6
Central Age:	39.2 ± 4.2
Chi-sq.:	25.57
P(%)	14.27
Dispersion:	0.11
RohD:	5.3
Nd:	2947
U standard	CN 1
Zeta ±1σ	133 ± 2.5
counted by	EW

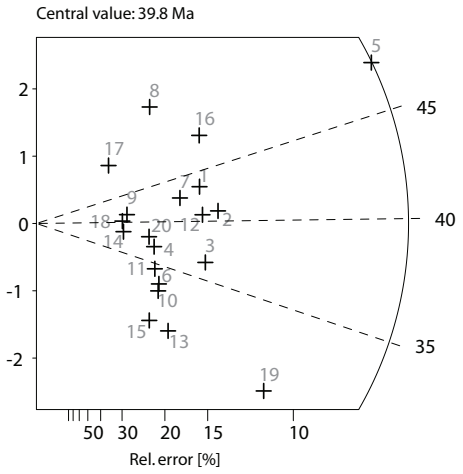

Cryst	Ns	Ni	Area	RhoS (e5)	RhoI (e5)	Age (Ma)	+- 1s	U (ppm)
1	90	73	18	80.08	64.95	43.38	6.93	388.11
2	108	93	42	41.18	35.46	40.87	5.88	211.90
3	88	85	25	56.37	54.45	36.44	5.62	325.37
4	43	41	50	13.77	13.13	36.92	8.12	78.47
5	401	295	90	71.36	52.50	47.81	3.88	313.68
6	44	47	80	8.81	9.41	32.96	6.97	56.22
7	69	57	50	22.10	18.26	42.59	7.71	109.10
8	52	31	28	29.74	17.73	58.95	13.47	105.95
9	27	23	30	14.41	12.28	41.31	11.77	73.37
10	43	47	90	7.65	8.36	32.22	6.85	49.98
11	42	43	12	56.05	57.39	34.39	7.52	342.92
12	90	78	28	51.48	44.61	40.60	6.37	266.59
13	48	58	20	38.44	46.45	29.15	5.74	277.52
14	24	22	40	9.61	8.81	38.40	11.38	52.63
15	35	43	40	14.01	17.22	28.67	6.57	102.88
16	96	69	80	19.22	13.81	48.93	7.83	82.54
17	20	13	16	20.02	13.01	54.08	19.32	77.75
18	24	21	15	25.63	22.42	40.22	12.06	133.98
19	145	170	50	46.45	54.45	30.04	3.49	325.37
20	40	37	30	21.35	19.75	38.05	8.74	118.03

Sample number:	**RD 37**
Mineral:	Zircon
Irradiation code:	eth-369-6
Ns:	1585
Ni:	1530
Area:	838
RohS:	31.4
RohI:	29.2
Pooled Age:	37.2 ± 3.2
Mean Age:	36.6 ± 4.4
Central Age:	36.4 ± 4.2
Chi-sq.:	34.49
P(%)	1.61
Dispersion:	0.14
RohD:	5.2
Nd:	2947
U standard	CN 1
Zeta $\pm 1\sigma$	133 ± 2.5
counted by	EW

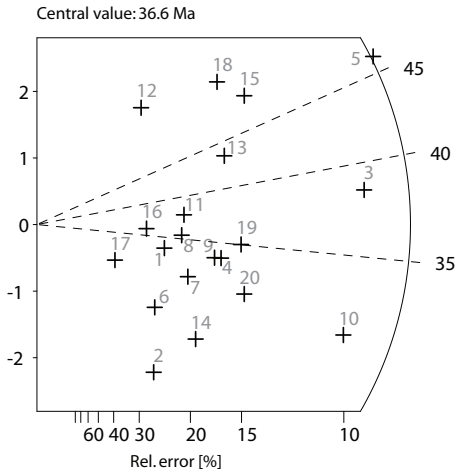

Crystal	Ns	Ni	Area	RhoS (e5)	RhoI (e5)	Age (Ma)	+- 1s	U (ppm)
1	34	35	28	19.45	20.02	33.64	8.15	121.61
2	23	39	40	9.21	15.62	20.45	5.40	94.86
3	240	216	70	54.91	49.42	38.47	3.75	300.20
4	71	73	28	40.61	41.75	33.69	5.68	253.64
5	280	210	70	64.06	48.05	46.13	4.38	291.86
6	26	34	14	29.74	38.89	26.50	6.94	236.27
7	46	51	50	14.73	16.34	31.24	6.41	99.23
8	45	44	9	80.08	78.30	35.42	7.57	475.63
9	66	68	20	52.85	54.45	33.62	5.88	330.78
10	189	211	80	37.84	42.24	31.03	3.21	256.60
11	48	44	35	21.96	20.13	37.77	7.95	122.30
12	32	18	35	14.64	8.24	61.44	18.17	50.03
13	84	67	30	44.84	35.77	43.39	7.20	217.28
14	47	62	30	25.09	33.10	26.27	5.13	201.06
15	110	78	25	70.47	49.97	48.79	7.33	303.54
16	26	25	70	5.95	5.72	36.01	10.13	34.75
17	12	14	32	6.01	7.01	29.70	11.71	42.56
18	87	57	42	33.18	21.74	52.78	9.10	132.03
19	89	88	30	47.51	46.98	35.02	5.35	285.38
20	87	96	100	13.93	15.38	31.39	4.72	93.40

Sample number:	**RD 39**
Mineral:	Zircon
Irradiation code:	eth-369-12
Ns:	1647
Ni:	1521
Area:	793
RohS:	33.3
RohI:	30.7
Pooled Age:	36.6 ± 3.2
Mean Age:	36.5 ± 4.0
Central Age:	36.5 ± 3.8
Chi-sq.:	29.17
P(%)	6.33
Dispersion:	0.10
RohD:	5.09
Nd:	2947
U standard	CN 1
Zeta ±1σ	133 ± 2.5
counted by	EW

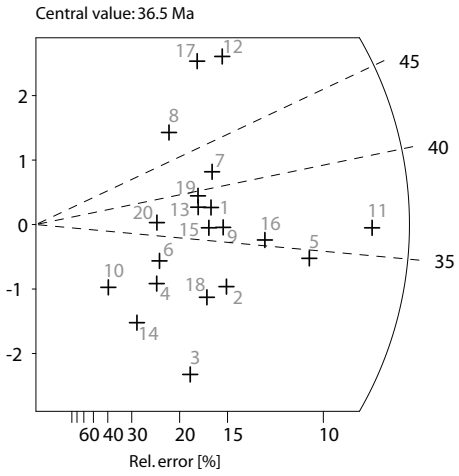

Crystal	Ns	Ni	Area	RhoS (e5)	RhoI (e5)	Age (Ma)	+- 1s	U (ppm)
1	79	70	50	25.304	22.422	38.1	6.33	139.68
2	85	91	40	34.033	36.435	31.55	4.83	226.99
3	49	70	40	19.619	28.027	23.66	4.45	174.61
4	33	38	60	8.808	10.143	29.34	7.02	63.19
5	183	179	100	29.308	28.668	34.52	3.74	178.6
6	36	38	18	32.031	33.81	32	7.49	210.64
7	84	68	50	26.906	21.781	41.69	6.89	135.69
8	53	36	20	42.441	28.828	49.66	10.8	179.59
9	88	82	40	35.234	32.832	36.23	5.64	204.54
10	11	15	24	7.34	10.01	24.78	9.86	62.36
11	284	264	70	64.977	60.401	36.32	3.25	376.29
12	110	68	28	62.918	38.894	54.54	8.54	242.31
13	68	60	16	68.065	60.058	38.26	6.85	374.16
14	21	30	28	12.012	17.159	23.66	6.76	106.9
15	75	70	30	40.038	37.369	36.18	6.09	232.81
16	130	124	50	41.64	39.718	35.4	4.54	247.44
17	85	50	16	85.082	50.048	57.31	10.32	311.8
18	67	75	36	29.806	33.365	30.18	5.13	207.86
19	69	59	49	22.552	19.284	39.48	7.08	120.14
20	37	34	28	21.163	19.447	36.74	8.78	121.16

Sample number:	**RD 40**
Mineral:	Zircon
Irradiation code:	eth-369-14
Ns:	641
Ni:	585
Area:	268
RohS:	38.3
RohI:	35.0
Pooled Age:	34.2 ± 4.6
Mean Age:	35.1 ± 4.2
Central Age:	34.3 ± 5.2
Chi-sq.:	18.14
P(%)	31.60
Dispersion:	0.13
RohD:	5.05
Nd:	2947
U standard	CN 1
Zeta ±1σ	133 ± 2.5
counted by	EW

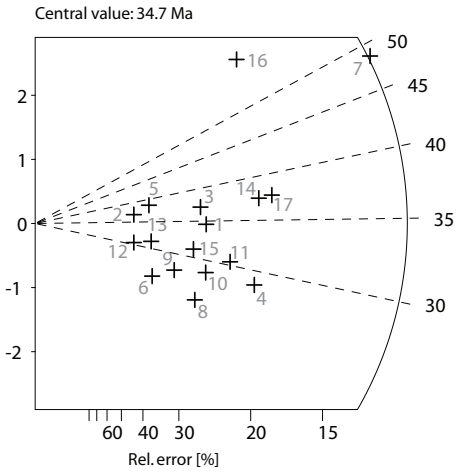

Crystal	Ns	Ni	Area	RhoS (e5)	RhoI (e5)	Age (Ma)	+- 1s	U (ppm)
1	32	31	24	21.35	20.69	34.56	8.76	129.98
2	11	10	20	8.81	8.01	36.82	16.12	50.32
3	31	28	24	20.69	18.69	37.06	9.71	117.40
4	48	56	30	25.63	29.90	28.71	5.70	187.85
5	15	13	5	48.05	41.64	38.62	14.67	261.64
6	13	17	9	23.13	30.25	25.62	9.46	190.08
7	148	102	25	94.81	65.34	48.53	6.37	410.58
8	24	32	8	48.05	64.06	25.13	6.82	402.53
9	19	23	16	19.02	23.02	27.67	8.61	144.66
10	29	34	9	51.61	60.50	28.57	7.26	380.17
11	39	43	6	104.10	114.78	30.38	6.76	721.20
12	10	11	10	16.02	17.62	30.45	13.33	110.70
13	14	15	9	24.91	26.69	31.26	11.64	167.72
14	57	51	18	50.72	45.38	37.41	7.28	285.13
15	26	28	15	27.76	29.90	31.10	8.51	187.85
16	61	34	15	65.13	36.30	59.95	12.93	228.10
17	64	57	25	41.00	36.52	37.58	6.92	229.44

Sample number:	**RD 41**
Mineral:	Zircon
Irradiation code:	eth-369-18
Ns:	621
Ni:	562
Area:	280
RohS:	35.5
RohI:	32.1
Pooled Age:	36.4 ± 4.6
Mean Age:	36.8 ± 4.0
Central Age:	36.4 ± 4.6
Chi-sq.:	13.29
P(%)	82.32
Dispersion:	0.00
RohD:	4.96
Nd:	2947
U standard	CN 1
Zeta $\pm 1\sigma$	133 ± 2.5
counted by	EW

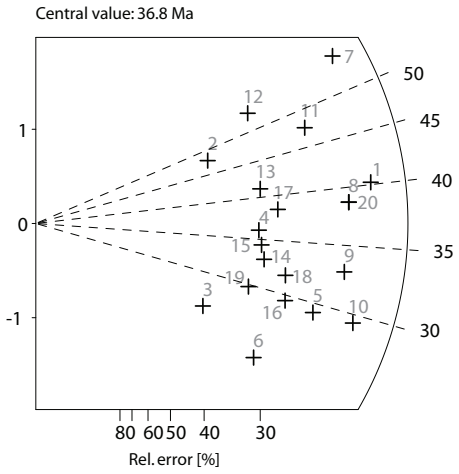

Crystal	Ns	Ni	Area	RhoS (e5)	RhoI (e5)	Age (Ma)	+- 1s	U (ppm)
1	55	45	20	44.04	36.04	40.20	8.15	230.38
2	16	11	4	64.06	44.04	47.81	18.77	281.58
3	11	14	9	19.57	24.91	25.87	10.45	159.28
4	23	21	15	24.56	22.42	36.04	10.92	143.35
5	32	36	15	34.17	38.44	29.26	7.15	245.74
6	18	25	9	32.03	44.49	23.71	7.36	284.42
7	52	31	20	41.64	24.82	55.11	12.59	158.71
8	47	40	24	31.36	26.69	38.65	8.38	170.65
9	42	42	28	24.02	24.02	32.91	7.23	153.59
10	42	47	15	44.84	50.18	29.42	6.29	320.83
11	39	27	15	41.64	28.83	47.48	11.95	184.31
12	26	16	9	46.27	28.47	53.39	17.02	182.03
13	25	20	12	33.37	26.69	41.11	12.38	170.65
14	23	23	6	61.39	61.39	32.91	9.74	392.50
15	23	22	15	24.56	23.49	34.40	10.30	150.18
16	26	29	8	52.05	58.06	29.51	8.01	371.17
17	28	24	15	29.90	25.63	38.38	10.72	163.83
18	27	28	14	30.89	32.03	31.74	8.60	204.78
19	19	21	9	33.81	37.37	29.78	9.46	238.92
20	47	40	18	41.82	35.59	38.65	8.38	227.54

Sample number:	**RD 43**
Mineral:	Zircon
Irradiation code:	eth-369-21/22
Ns:	900
Ni:	775
Area:	343
RohS:	42.0
RohI:	36.2
Pooled Age:	37.7 ± 4.2
Mean Age:	37.9 ± 4.2
Central Age:	37.5 ± 4.6
Chi-sq.:	23.21
P(%)	22.83
Dispersion:	0.10
RohD:	4.89
Nd:	2947
U standard	CN 1
Zeta $\pm 1\sigma$	133 ± 2.5
counted by	EW

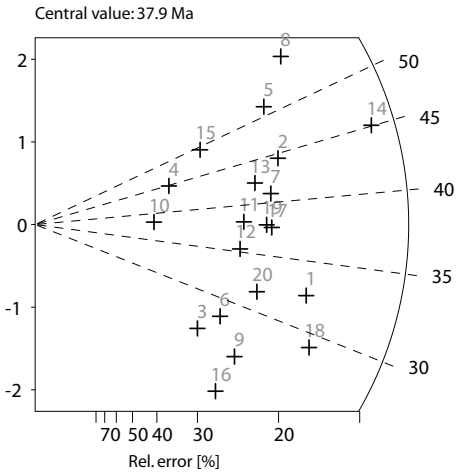

Cryst	Ns	Ni	Area	RhoS (e5)	RhoI (e5)	Age (Ma)	+- 1s	U (ppm)
1	62	62	20	49.648	49.648	32.45	5.89	321.92
2	59	43	15	62.994	45.911	44.48	9	297.69
3	20	25	20	16.015	20.019	25.97	7.82	129.81
4	18	13	9	32.031	23.133	44.89	16.38	150
5	57	36	12	76.073	48.046	51.3	11.01	311.54
6	27	31	10	43.242	49.648	28.27	7.48	321.92
7	53	42	15	56.588	44.843	40.92	8.52	290.77
8	70	40	20	56.054	32.031	56.68	11.33	207.69
9	30	38	10	48.046	60.858	25.63	6.3	394.61
10	13	11	8	26.025	22.021	38.33	15.74	142.79
11	40	34	21	30.505	25.93	38.16	8.96	168.13
12	37	34	15	39.505	36.302	35.31	8.44	235.38
13	47	36	9	83.636	64.061	42.33	9.44	415.38
14	114	82	33	55.326	39.796	45.07	6.63	258.04
15	29	19	10	46.445	30.429	49.46	14.66	197.31
16	23	34	24	15.348	22.688	21.97	5.96	147.11
17	51	44	32	25.525	22.021	37.6	7.8	142.79
18	60	67	16	60.058	67.064	29.07	5.22	434.85
19	49	42	20	39.238	33.632	37.84	8.02	218.08
20	41	42	24	27.36	28.027	31.68	7	181.73

Sample number:	**RD 57**
Mineral:	Zircon
Irradiation code:	eth-369-25
Ns:	1386
Ni:	1383
Area:	715
RohS:	32.0
RohI:	31.0
Pooled Age:	32.0 ± 3.0
Mean Age:	33.2 ± 2.8
Central Age:	31.9 ± 3.2
Chi-sq.:	29.52
P(%)	20.11
Dispersion:	0.09
RohD:	4.81
Nd:	2947
U standard	CN 1
Zeta $\pm 1\sigma$	133 ± 2.5
counted by	EW

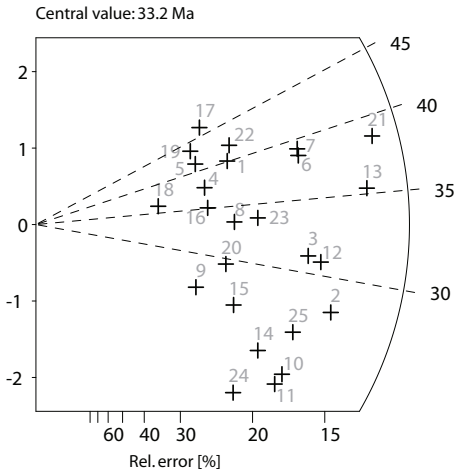

Table with grain data see next page.

Continuation of RD57–data set.

Crystal	Ns	Ni	Area	RhoS (e5)	RhoI (e5)	Age (Ma)	+- 1s	U (ppm)
1	44	35	30	23.49	18.69	40.08	9.14	123.23
2	87	99	24	58.06	66.06	28.05	4.19	435.70
3	78	80	42	29.74	30.51	31.11	5.02	201.19
4	33	28	12	44.04	37.37	37.59	9.71	246.46
5	31	24	9	55.16	42.71	41.18	11.25	281.67
6	81	67	32	40.54	33.53	38.55	6.45	221.15
7	81	66	28	46.33	37.75	39.13	6.57	248.97
8	43	41	30	22.96	21.89	33.46	7.36	144.35
9	25	30	10	40.04	48.05	26.60	7.24	316.88
10	56	76	21	42.71	57.96	23.52	4.19	382.26
11	52	73	50	16.66	23.38	22.74	4.17	154.21
12	85	88	25	54.45	56.37	30.82	4.76	371.80
13	123	111	60	32.83	29.63	35.34	4.72	195.41
14	46	61	56	13.16	17.45	24.07	4.74	115.06
15	38	46	40	15.22	18.42	26.37	5.82	121.47
16	33	30	25	21.14	19.22	35.09	8.90	126.75
17	35	24	24	23.36	16.02	46.48	12.38	105.63
18	17	15	27	10.08	8.90	36.15	12.84	58.68
19	30	22	6	80.08	58.72	43.47	12.25	387.29
20	37	40	40	14.81	16.02	29.52	6.78	105.63
21	133	110	40	53.25	44.04	38.56	5.07	290.47
22	46	35	12	61.39	46.71	41.90	9.46	308.07
23	54	51	24	36.04	34.03	33.78	6.65	224.45
24	34	53	20	27.23	42.44	20.49	4.53	279.91
25	64	78	28	36.61	44.61	26.19	4.47	294.24

	Sample number:	**RD 58**
	Mineral:	Zircon
	Irradiation code:	eth-369-29
	Ns:	1734
	Ni:	1553
	Area:	477
	RohS:	58.2
	RohI:	52.1
	Pooled Age:	34.2 ± 3.0
v	Mean Age:	35.1 ± 2.8
	Central Age:	34.3 ± 3.0
	Chi-sq.:	20.14
	P(%)	38.60
	Dispersion:	0.03
	RohD:	4.72
	Nd:	2947
	U standard	CN 1
	Zeta ±1σ	133 ± 2.5
	counted by	EW

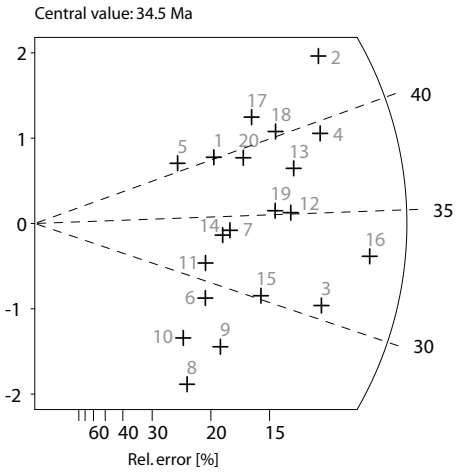

Crystal	Ns	Ni	Area	RhoS (e5)	RhoI (e5)	Age (Ma)	+- 1s	U (ppm)
1	59	46	16	59.057	46.044	40.16	7.97	309.25
2	156	111	30	83.28	59.257	43.99	5.58	397.99
3	131	134	28	74.929	76.645	30.63	3.85	514.78
4	148	118	30	79.009	62.994	39.27	4.96	423.09
5	38	29	9	67.62	51.605	41.02	10.17	346.6
6	45	49	21	34.319	37.369	28.78	5.99	250.99
7	64	59	12	85.415	78.742	33.98	6.2	528.86
8	32	45	9	56.944	80.077	22.3	5.19	537.83
9	51	61	12	68.065	81.411	26.2	5.02	546.79
10	32	40	9	56.944	71.179	25.08	5.98	478.07
11	47	47	9	83.636	83.636	31.33	6.52	561.73
12	112	100	21	85.415	76.264	35.08	4.91	512.22
13	119	99	25	76.233	63.421	37.64	5.22	425.96
14	59	55	25	37.796	35.234	33.6	6.36	236.64
15	81	84	24	54.052	56.054	30.21	4.77	376.48
16	186	176	100	29.789	28.187	33.11	3.59	189.32
17	89	66	16	89.086	66.063	42.21	6.95	443.71
18	107	83	25	68.546	53.171	40.36	6	357.12
19	99	88	36	44.042	39.149	35.24	5.25	262.94
20	79	63	20	63.261	50.448	39.26	6.71	338.83

Sample number:	**RD 61**
Mineral:	Zircon
Irradiation code:	eth-369-34/36
Ns:	940
Ni:	397
Area:	248
RohS:	60.7
RohI:	25.6
Pooled Age:	34.2 ± 9.4
Mean Age:	35.1 ± 7.8
Central Age:	34.3 ± 9.4
Chi-sq.:	13.56
P(%)	80.85
Dispersion:	0.00
RohD:	4.59
Nd:	2947
U standard	CN 1
Zeta ±1σ	133 ± 2.5
counted by	EW

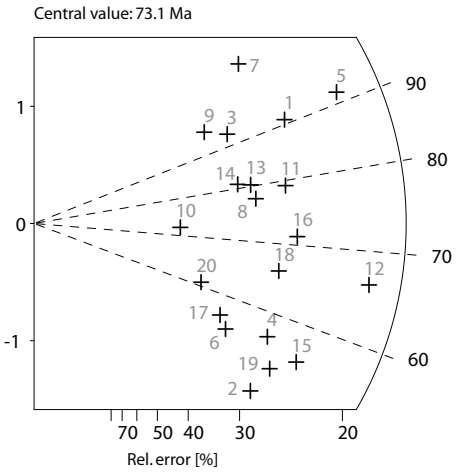

Crystal	Ns	Ni	Area	RhoS (e5)	RhoI (e5)	Age (Ma)	+- 1s	U (ppm)
1	66	22	8	132.13	44.04	90.94	22.51	304.33
2	32	20	15	34.17	21.35	48.66	13.93	147.55
3	40	13	8	80.08	26.03	93.25	29.87	179.83
4	41	22	15	43.78	23.49	56.64	15.04	162.31
5	97	32	10	155.35	51.25	91.88	18.89	354.13
6	27	15	9	48.05	26.69	54.72	17.68	184.44
7	51	14	10	81.68	22.42	110.26	33.39	154.93
8	46	18	12	61.39	24.02	77.55	21.66	166.00
9	32	10	16	32.03	10.01	96.95	35.22	69.17
10	19	8	9	33.81	14.24	72.10	30.45	98.37
11	60	23	9	106.77	40.93	79.15	19.52	282.81
12	94	43	20	75.27	34.43	66.39	12.35	237.93
13	45	17	9	80.08	30.25	80.30	22.96	209.04
14	40	15	10	64.06	24.02	80.90	24.58	166.00
15	51	28	16	51.05	28.03	55.36	13.10	193.67
16	61	26	18	54.27	23.13	71.23	16.79	159.85
17	26	14	9	46.27	24.91	56.45	18.77	172.15
18	50	23	15	53.39	24.56	66.02	16.73	169.69
19	40	23	10	64.06	36.84	52.87	13.91	254.53
20	22	11	20	17.62	8.81	60.77	22.50	60.87

Sample number:	**RD 63**
Mineral:	Zircon
Irradiation code:	eth-369-37
Ns:	612
Ni:	1206
Area:	554
RohS:	17.7
RohI:	34.9
Pooled Age:	15.3 ± 1.8
Mean Age:	16.0 ± 1.0
Central Age:	15.5 ± 2.0
Chi-sq.:	26.81
P(%)	10.91
Dispersion:	0.14
RohD:	4.55
Nd:	2947
U standard	CN 1
Zeta ±1σ	133 ± 2.5
counted by	EW

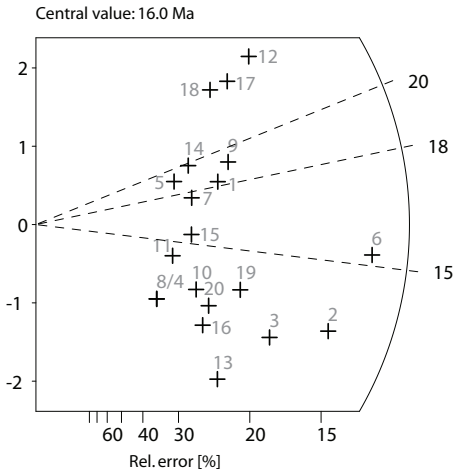

Crystal	Ns	Ni	Area	RhoS (e5)	RhoI (e5)	Age (Ma)	+- 1s	U (ppm)
1	29	48	12	38.70	64.06	18.25	4.32	446.68
2	67	154	42	25.55	58.72	13.15	1.96	409.45
3	42	103	40	16.82	41.24	12.32	2.28	287.55
4	11	29	9	19.57	51.61	11.47	4.07	359.82
5	17	27	16	17.02	27.03	19.02	5.91	188.44
6	93	184	50	29.79	58.94	15.27	1.98	410.94
7	21	36	15	22.42	38.44	17.62	4.86	268.01
8	11	29	15	11.75	30.96	11.47	4.07	215.89
9	33	52	20	26.43	41.64	19.17	4.30	290.34
10	20	47	12	26.69	62.73	12.86	3.45	437.37
11	15	32	14	17.16	36.61	14.17	4.45	255.24
12	45	55	25	28.83	35.23	24.71	5.01	245.67
13	24	72	30	12.81	38.44	10.08	2.39	268.01
14	21	32	16	21.02	32.03	19.82	5.59	223.34
15	20	39	20	16.02	31.23	15.50	4.28	217.75
16	21	55	28	12.01	31.46	11.54	2.98	219.35
17	36	45	40	14.41	18.02	24.16	5.44	125.63
18	30	37	25	19.22	23.70	24.48	6.05	165.27
19	33	74	25	21.14	47.41	13.48	2.84	330.54
20	23	56	100	3.68	8.97	12.41	3.09	62.53

Sample number:	**RD 64**
Mineral:	Zircon
Irradiation code:	eth-355-42
Ns:	1675
Ni:	1443
Area:	568
RohS:	75.4
RohI:	65.0
Pooled Age:	34.2 ± 3.0
Mean Age:	35.1 ± 3.2
Central Age:	34.3 ± 3.6
Chi-sq.:	31.01
P(%)	4.03
Dispersion:	0.13
RohD:	4.45
Nd:	3627
U standard	CN 1
Zeta ±1σ	133 ± 2.5
counted by	EW

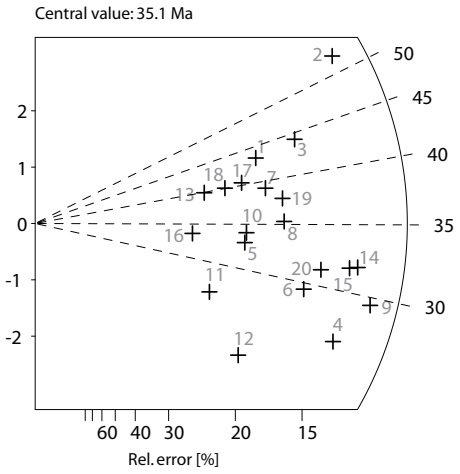

Crystal	Ns	Ni	Area	RhoS (e5)	RhoI (e5)	Age (Ma)	+- 1s	U (ppm)
1	75	51	30	63.94	43.48	43.33	7.94	310.23
2	153	86	40	97.83	54.99	52.38	7.18	392.34
3	105	70	30	89.51	59.68	44.19	6.91	425.80
4	105	117	30	89.51	99.74	26.48	3.62	711.70
5	58	52	18	82.41	73.89	32.89	6.34	527.18
6	90	90	40	57.55	57.55	29.50	4.46	410.59
7	77	58	24	82.06	61.81	39.13	6.87	441.01
8	85	71	30	72.46	60.53	35.30	5.74	431.88
9	140	140	50	71.61	71.61	29.50	3.60	510.96
10	60	52	20	76.73	66.50	34.02	6.50	474.46
11	36	40	16	57.55	63.94	26.55	6.14	456.21
12	45	60	16	71.93	95.91	22.13	4.40	684.32
13	42	31	12	89.51	66.07	39.93	9.51	471.42
14	135	125	50	69.05	63.94	31.85	4.03	456.21
15	128	119	40	81.84	76.09	31.72	4.12	542.90
16	33	29	12	70.33	61.81	33.55	8.58	441.01
17	63	46	28	57.55	42.02	40.36	7.89	299.80
18	53	39	16	84.72	62.34	40.05	8.51	444.81
19	87	68	30	74.17	57.97	37.71	6.18	413.63
20	105	99	36	74.60	70.33	31.28	4.45	501.84

Sample number:	**RD 68**
Mineral:	Zircon
Irradiation code:	eth-355-9
Ns:	1528
Ni:	1523
Area:	553
RohS:	70.7
RohI:	70.4
Pooled Age:	34.4 ± 3.0
Mean Age:	35.4 ± 3.0
Central Age:	34.5 ± 3.2
Chi-sq.:	23.65
P(%)	21.00
Dispersion:	0.07
RohD:	5.18
Nd:	3627
U standard	CN 1
Zeta ±1σ	133 ± 2.5
counted by	EW

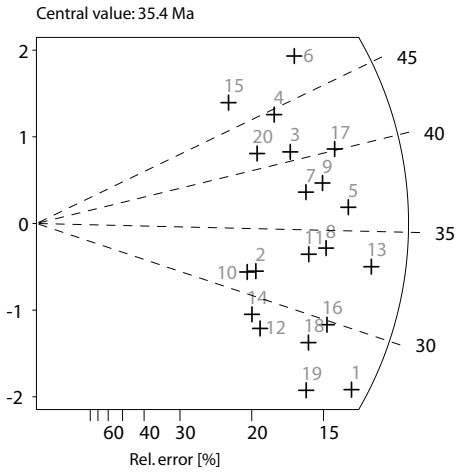

Crystal	Ns	Ni	Area	RhoS (e5)	RhoI (e5)	Age (Ma)	+- 1s	U (ppm)
1	96	121	30	81.84	103.15	27.25	3.79	632.21
2	50	54	36	35.52	38.36	31.79	6.29	235.12
3	76	64	24	80.99	68.20	40.74	6.99	417.99
4	70	54	25	71.61	55.24	44.46	8.13	338.57
5	108	102	25	110.49	104.35	36.34	5.10	639.52
6	87	61	36	61.81	43.34	48.90	8.26	265.60
7	82	75	25	83.89	76.73	37.52	6.07	470.24
8	90	91	21	109.61	110.83	33.95	5.12	679.23
9	93	84	25	95.14	85.93	37.99	5.80	526.67
10	46	50	16	73.53	79.92	31.59	6.50	489.83
11	79	81	18	112.25	115.09	33.48	5.36	705.36
12	49	60	32	39.16	47.95	28.05	5.45	293.90
13	119	123	40	76.09	78.65	33.21	4.35	481.99
14	46	55	18	65.36	78.15	28.72	5.78	478.95
15	48	34	30	40.92	28.99	48.41	10.92	177.65
16	85	98	36	60.39	69.62	29.78	4.48	426.70
17	104	89	30	88.66	75.87	40.09	5.88	465.01
18	73	88	32	58.34	70.33	28.49	4.57	431.05
19	69	91	30	58.82	77.58	26.04	4.21	475.46
20	58	48	24	61.81	51.15	41.46	8.16	313.49

Sample number:	**RD 75**
Mineral:	Zircon
Irradiation code:	eth-355-38
Ns:	1388
Ni:	1488
Area:	650
RohS:	54.6
RohI:	58.5
Pooled Age:	28.1 ± 2.6
Mean Age:	28.7 ± 2.8
Central Age:	27.9 ± 2.8
Chi-sq.:	24.50
P(%)	17.78
Dispersion:	0.09
RohD:	4.53414
Nd:	3627
U standard	CN 1
Zeta ±1σ:	133 ± 2.5
counted by	EW

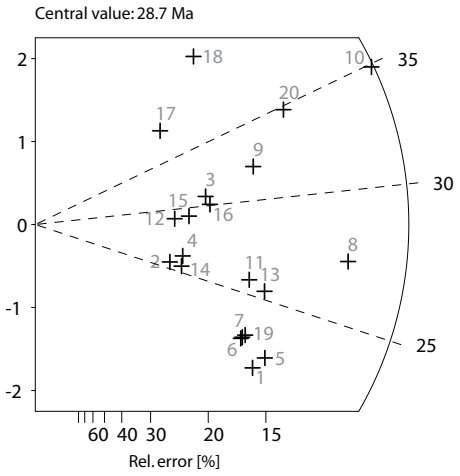

Crystal	Ns	Ni	Area	RhoS (e5)	RhoI (e5)	Age (Ma)	+- 1s	U (ppm)
1	68	94	24	72.464	100.171	21.78	3.51	700.79
2	28	33	12	59.676	70.332	25.53	6.59	492.04
3	49	48	30	41.773	40.921	30.71	6.28	286.28
4	34	39	16	54.348	62.34	26.23	6.19	436.13
5	77	103	36	54.703	73.174	22.5	3.44	511.92
6	65	85	21	79.162	103.52	23.02	3.84	724.22
7	63	83	36	44.757	58.966	22.85	3.86	412.52
8	156	172	100	39.898	43.99	27.29	3.09	307.75
9	82	77	30	69.906	65.644	32.03	5.15	459.24
10	204	176	80	65.217	56.266	34.85	3.69	393.63
11	71	83	30	60.529	70.759	25.74	4.21	495.02
12	32	33	9	90.935	93.777	29.17	7.27	656.06
13	81	96	40	51.79	61.381	25.39	3.88	429.42
14	33	39	20	42.199	49.872	25.46	6.06	348.9
15	39	40	18	55.413	56.834	29.33	6.64	397.61
16	51	51	24	54.348	54.348	30.08	6	380.21
17	30	23	20	38.363	29.412	39.21	10.91	205.76
18	52	35	24	55.413	37.298	44.64	9.82	260.93
19	62	82	30	52.856	69.906	22.76	3.87	489.06
20	111	96	50	56.777	49.105	34.77	4.92	343.53

Sample number:	**RD 78**
Mineral:	Zircon
Irradiation code:	eth-355-16
Ns:	1043
Ni:	1081
Area:	824
RohS:	20.3
RohI:	21.0
Pooled Age:	32.1 ± 3.2
Mean Age:	32.6 ± 2.6
Central Age:	32.1 ± 3.2
Chi-sq.:	13.41
P(%)	81.69
Dispersion:	0.00
RohD:	5.02
Nd:	3627
U standard	CN 1
Zeta ±1σ	133 ± 2.5
counted by	EW

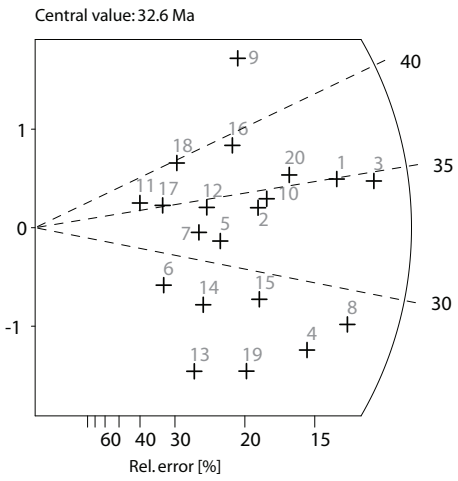

Crystal	Ns	Ni	Area	RhoS (e5)	RhoI (e5)	Age (Ma)	+- 1s	U (ppm)
1	106	101	40	42.441	40.439	34.95	4.94	255.48
2	57	56	60	15.215	14.948	33.9	6.43	94.44
3	133	128	60	35.501	34.166	34.6	4.37	215.85
4	76	94	100	12.172	15.054	26.94	4.21	95.11
5	38	40	100	6.086	6.406	31.64	7.21	40.47
6	17	21	18	15.126	18.685	26.97	8.83	118.05
7	30	31	12	40.038	41.373	32.23	8.29	261.39
8	103	120	56	29.457	34.319	28.6	3.91	216.82
9	56	40	20	44.843	32.031	46.58	9.71	202.36
10	62	60	70	14.185	13.727	34.41	6.29	86.73
11	13	12	16	13.012	12.012	36.07	14.47	75.89
12	34	33	16	34.033	33.032	34.31	8.43	208.69
13	24	36	24	16.015	24.023	22.22	5.88	151.77
14	29	36	18	25.803	32.031	26.84	6.73	202.36
15	53	62	50	16.976	19.859	28.48	5.38	125.47
16	48	41	30	25.625	21.888	38.97	8.34	138.28
17	19	18	24	12.679	12.012	35.15	11.59	75.89
18	25	21	15	26.692	22.422	39.63	11.77	141.65
19	44	60	70	10.067	13.727	24.44	4.89	86.73
20	76	71	25	48.687	45.484	35.64	5.95	287.36

Sample number:	**RD 81**
Mineral:	Zircon
Irradiation code:	eth-355-20
Ns:	932
Ni:	845
Area:	633
RohS:	23.6
RohI:	21.4
Pooled Age:	36.1 ± 3.8
Mean Age:	35.8 ± 3.2
Central Age:	35.9 ± 4.0
Chi-sq.:	16.63
P(%)	61.52
Dispersion:	0.05
RohD:	4.93
Nd:	3627
U standard	CN 1
Zeta ±1σ	133 ± 2.5
counted by	EW

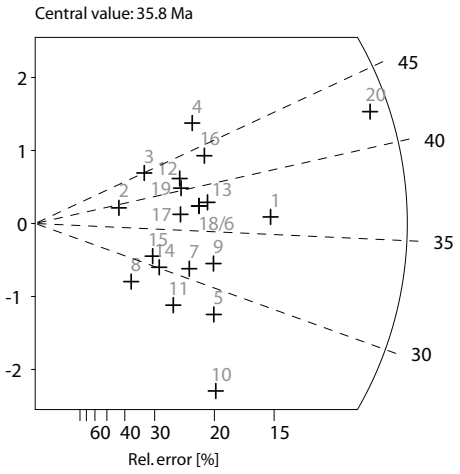

Crystal	Ns	Ni	Area	RhoS (e5)	RhoI (e5)	Age (Ma)	+- 1s	U (ppm)
1	91	82	40	36.435	32.832	36.3	5.6	211.14
2	12	10	18	10.677	8.897	39.24	16.83	57.22
3	22	16	21	16.778	12.202	44.94	14.81	78.47
4	48	32	30	25.625	17.083	49.01	11.25	109.86
5	46	54	32	23.022	27.026	27.88	5.64	173.81
6	45	39	49	14.708	12.747	37.74	8.31	81.98
7	36	38	16	36.035	38.037	31	7.25	244.62
8	13	16	15	13.88	17.083	26.6	9.95	109.86
9	49	50	42	18.685	19.066	32.06	6.5	122.62
10	43	62	32	21.521	31.03	22.71	4.54	199.56
11	27	33	20	21.621	26.425	26.78	6.98	169.95
12	37	29	25	23.703	18.578	41.71	10.4	119.48
13	50	43	30	26.692	22.955	38.03	7.97	147.63
14	23	25	18	20.464	22.244	30.11	8.73	143.05
15	21	22	49	6.864	7.191	31.23	9.56	46.24
16	52	39	27	30.844	23.133	43.59	9.3	148.77
17	35	31	40	14.013	12.412	36.93	9.15	79.82
18	45	39	24	30.029	26.025	37.74	8.31	167.37
19	37	30	25	23.703	19.218	40.33	9.96	123.6
20	200	155	80	40.038	31.03	42.18	4.64	199.56

Sample number:	**RD 82**
Mineral:	Zircon
Irradiation code:	eth-355-23
Ns:	851
Ni:	636
Area:	235
RohS:	58.0
RohI:	43.3
Pooled Age:	43.2 ± 5.0
Mean Age:	42.9 ± 4.0
Central Age:	43.2 ± 5.0
Chi-sq.:	4.72
P(%)	78.71
Dispersion:	0.00
RohD:	4.87
Nd:	3627
U standard	CN 1
Zeta $\pm 1\sigma$	133 ± 2.5
counted by	EW

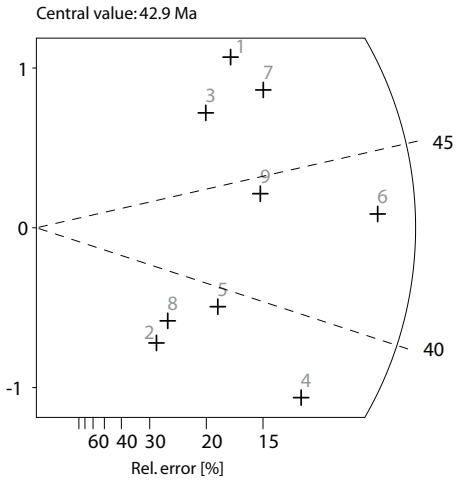

Crystal	Ns	Ni	Area	RhoS (e5)	RhoI (e5)	Age (Ma)	+- 1s	U (ppm)
1	85	53	30	45.377	28.294	51.69	9.14	184.44
2	26	24	8	52.05	48.046	34.96	9.93	313.21
3	63	41	18	56.054	36.479	49.53	10.02	237.8
4	131	113	30	69.934	60.325	37.4	4.89	393.25
5	63	52	36	28.027	23.133	39.09	7.39	150.8
6	236	176	40	94.491	70.468	43.24	4.44	459.37
7	112	74	30	59.791	39.505	48.79	7.41	257.52
8	32	28	18	28.472	24.913	36.88	9.59	162.4
9	103	75	25	65.983	48.046	44.29	6.81	313.21

Sample number:	**RD 88**
Mineral:	Zircon
Irradiation code:	eth-369-51
Ns:	550
Ni:	1061
Area:	772
RohS:	11.4
RohI:	22.0
Pooled Age:	34.2 ± 1.8
Mean Age:	35.1 ± 1.6
Central Age:	34.3 ± 1.8
Chi-sq.:	20.95
P(%)	33.95
Dispersion:	0.10
RohD:	4.25
Nd:	2947
U standard	CN 1
Zeta $\pm 1\sigma$	133 ± 2.5
counted by	EW

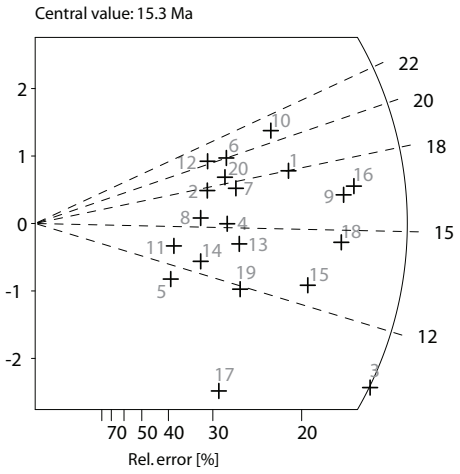

Crystal	Ns	Ni	Area	RhoS (e5)	RhoI (e5)	Age (Ma)	+- 1s	U (ppm)
1	37	58	40	14.81	23.22	17.99	3.81	173.50
2	17	27	30	9.08	14.41	17.75	5.52	107.69
3	54	147	100	8.65	23.54	10.36	1.67	175.90
4	20	37	15	21.35	39.51	15.24	4.25	295.15
5	9	23	15	9.61	24.56	11.04	4.35	183.47
6	22	31	14	25.17	35.46	20.01	5.60	264.95
7	23	37	12	30.70	49.38	17.53	4.68	368.94
8	15	27	9	26.69	48.05	15.67	5.06	358.97
9	53	91	42	20.21	34.70	16.42	2.87	259.26
10	34	46	24	22.69	30.70	20.83	4.74	229.34
11	10	21	32	5.01	10.51	13.43	5.17	78.52
12	18	25	28	10.30	14.30	20.30	6.30	106.84
13	22	44	24	14.68	29.36	14.10	3.70	219.37
14	14	31	30	7.47	16.55	12.74	4.12	123.65
15	38	84	90	6.76	14.95	12.76	2.52	111.68
16	57	96	100	9.13	15.38	16.74	2.83	114.87
17	15	57	24	10.01	38.04	7.43	2.16	284.18
18	50	97	100	8.01	15.54	14.54	2.56	116.07
19	21	50	18	18.69	44.49	11.85	3.10	332.38
20	21	32	25	13.45	20.50	18.50	5.22	153.16

Sample number:	**RD 91**
Mineral:	Zircon
Irradiation code:	eth-355-26/28
Ns:	1858
Ni:	1651
Area:	792
RohS:	37.57
RohI:	33.39
Pooled Age:	35.7 ± 3.0
Mean Age:	37.6 ± 4.2
Central Age:	35.9 ± 4.0
Chi-sq.:	40.74
P(%)	0.40
Dispersion:	0.15
RohD:	4.79
Nd:	3627
U standard	CN 1
Zeta ±1σ	133 ± 2.5
counted by	EW

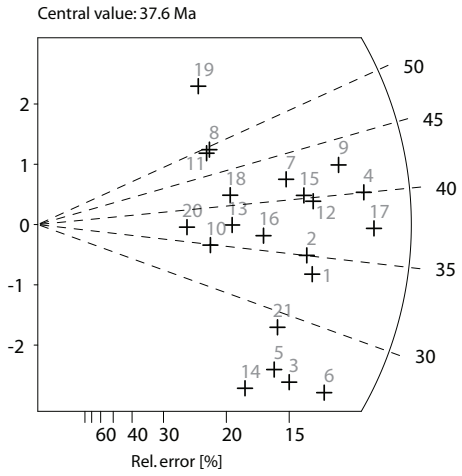

Crystal	Ns	Ni	Area	RhoS (e5)	RhoI (e5)	Age (Ma)	+- 1s	U (ppm)
1	109	103	30	58.19	54.99	33.60	4.69	364.36
2	107	97	56	30.60	27.74	35.02	4.99	183.82
3	80	100	60	21.35	26.69	25.42	3.87	176.87
4	169	134	50	54.13	42.92	40.02	4.74	284.41
5	71	88	20	56.86	70.47	25.63	4.14	466.95
6	105	128	40	42.04	51.25	26.06	3.49	339.60
7	101	76	25	64.70	48.69	42.17	6.49	322.62
8	53	34	12	70.74	45.38	49.43	10.93	300.69
9	149	111	30	79.54	59.26	42.59	5.45	392.66
10	44	40	24	29.36	26.69	34.92	7.68	176.87
11	51	33	24	34.03	22.02	49.01	11.02	145.92
12	120	96	30	64.06	51.25	39.67	5.52	339.60
13	58	49	36	25.80	21.80	37.57	7.35	144.45
14	52	72	21	39.66	54.91	22.95	4.22	363.86
15	113	89	40	45.24	35.63	40.29	5.80	236.13
16	77	67	50	24.66	21.46	36.48	6.16	142.21
17	173	147	100	27.71	23.54	37.36	4.29	156.00
18	60	46	30	32.03	24.56	41.39	8.18	162.72
19	55	27	24	36.70	18.02	64.52	15.25	119.39
20	34	29	20	27.23	23.22	37.21	9.45	153.88
21	77	85	70	17.62	19.45	28.77	4.58	128.87

Sample number:	**RD 92**
Mineral:	Zircon
Irradiation code:	eth-355-30
Ns:	1895
Ni:	2048
Area:	761
RohS:	39.9
RohI:	43.1
Pooled Age:	28.9 ± 2.4
Mean Age:	29.4 ± 3
Central Age:	28.9 ± 3.2
Chi-sq.:	42.88
P(%)	0.13
Dispersion:	0.15
RohD:	4.71
Nd:	3627
U standard	CN 1
Zeta $\pm 1\sigma$	133 ± 2.5
counted by	EW

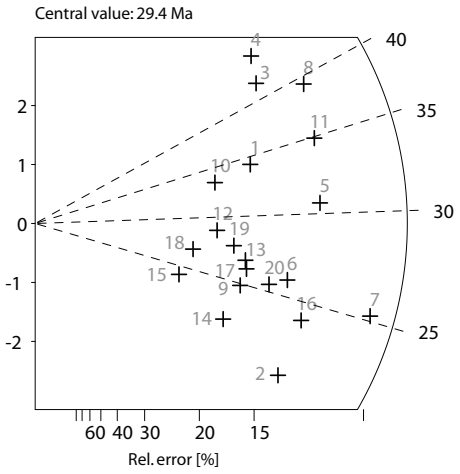

Crystal	Ns	Ni	Area	RhoS (e5)	RhoI (e5)	Age (Ma)	+- 1s	U (ppm)
1	90	82	21	68.637	62.536	34.29	5.31	421.06
2	91	137	40	36.435	54.853	20.78	2.86	369.33
3	106	79	35	48.504	36.149	41.9	6.32	243.4
4	106	73	21	80.84	55.672	45.33	6.99	374.85
5	149	152	50	47.726	48.687	30.64	3.61	327.81
6	108	130	49	35.299	42.49	25.97	3.44	286.09
7	188	233	100	30.109	37.316	25.23	2.55	251.25
8	151	120	50	48.366	38.437	39.3	4.91	258.8
9	70	88	50	22.422	28.187	24.87	4.03	189.79
10	62	58	30	33.098	30.963	33.4	6.16	208.48
11	153	137	50	49.007	43.882	34.89	4.2	295.46
12	59	64	24	39.371	42.708	28.82	5.25	287.56
13	76	89	60	20.286	23.756	26.7	4.22	159.95
14	56	79	15	59.791	84.348	22.17	3.91	567.92
15	34	44	20	27.226	35.234	24.16	5.55	237.23
16	116	151	40	46.445	60.458	24.02	3.03	407.07
17	76	91	28	43.47	52.05	26.11	4.11	350.46
18	43	50	18	38.259	44.487	26.89	5.63	299.54
19	69	78	40	27.627	31.23	27.65	4.62	210.28
20	92	113	20	73.671	90.487	25.46	3.63	609.26

Sample number:	**RD 93**
Mineral:	Zircon
Irradiation code:	eth-355-33
Ns:	166
Ni:	418
Area:	231
RohS:	11.5
RohI:	29.0
Pooled Age:	12.3 ± 2.4
Mean Age:	12.9 ± 2
Central Age:	12.3 ± 2.4
Chi-sq.:	6.52
P(%)	68.67
Dispersion:	0.01
RohD:	4.64
Nd:	3627
U standard	CN 1
Zeta $\pm 1\sigma$	133 ± 2.5
counted by	EW

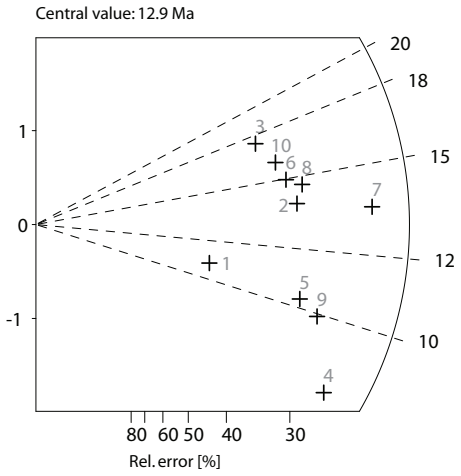

Crystal	Ns	Ni	Area	RhoS (e5)	RhoI (e5)	Age (Ma)	+- 1s	U (ppm)
1	7	20	15	7.47	21.35	10.80	4.75	145.83
2	17	38	20	13.61	30.43	13.80	4.04	207.81
3	13	23	12	17.35	30.70	17.43	6.07	209.63
4	18	69	50	5.77	22.10	8.05	2.14	150.94
5	16	48	18	14.24	42.71	10.29	2.98	291.67
6	16	33	16	16.02	33.03	14.96	4.57	225.58
7	28	64	30	14.95	34.17	13.50	3.08	233.33
8	18	38	16	18.02	38.04	14.61	4.20	259.76
9	18	56	30	9.61	29.90	9.92	2.70	204.17
10	15	29	24	10.01	19.35	15.96	5.09	132.16

Sample number:	**RD 94**
Mineral:	Zircon
Irradiation code:	eth-355-35
Ns:	1266
Ni:	1014
Area:	368
RohS:	55.10
RohI:	44.13
Pooled Age:	38.1 ± 3.8
Mean Age:	39.6 ± 4.0
Central Age:	38.1 ± 3.8
Chi-sq.:	16.45
P(%)	62.70
Dispersion:	0.00
RohD:	4.60
Nd:	3627
U standard	CN 1
Zeta $\pm 1\sigma$	133 ± 2.5
counted by	EW

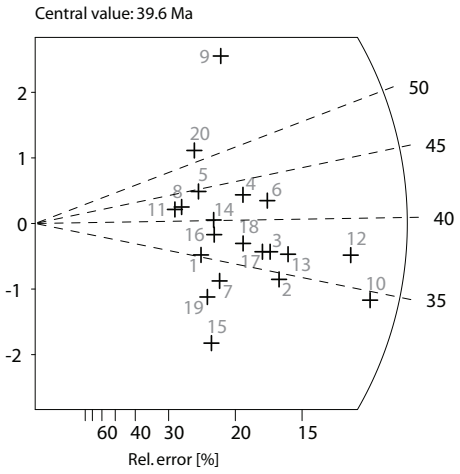

Crystal	Ns	Ni	Area	RhoS (e5)	RhoI (e5)	Age (Ma)	+- 1s	U (ppm)
1	37	32	10	59.26	51.25	35.28	8.56	353.36
2	79	70	24	52.72	46.71	34.43	5.72	322.08
3	76	63	30	40.57	33.63	36.80	6.34	231.90
4	65	46	15	69.40	49.11	43.09	8.37	338.64
5	41	28	10	65.66	44.84	44.64	11.00	309.19
6	80	58	18	71.18	51.61	42.06	7.33	355.82
7	44	41	18	39.15	36.48	32.75	7.16	251.53
8	32	23	10	51.25	36.84	42.42	11.65	253.98
9	70	31	30	37.37	16.55	68.71	14.92	114.11
10	149	132	40	59.66	52.85	34.44	4.21	364.41
11	29	21	9	51.61	37.37	42.11	12.11	257.66
12	138	113	30	73.67	60.33	37.25	4.82	415.94
13	88	73	28	50.33	41.75	36.77	5.89	287.90
14	46	35	12	61.39	46.71	40.08	9.05	322.08
15	36	42	9	64.06	74.74	26.17	5.98	515.32
16	45	36	16	45.04	36.04	38.13	8.58	248.46
17	71	59	18	63.17	52.50	36.71	6.53	361.95
18	60	49	15	64.06	52.32	37.35	7.25	360.73
19	37	37	14	42.33	42.33	30.52	7.14	291.84
20	43	25	12	57.39	33.37	52.41	13.25	230.05

Apatite fission track grain-age data

Sample number:	**RD 2**
Mineral:	Apatite
Irradiation code:	eth-328-5
Ns:	289
Ni:	2279
Area:	930
RohS:	4.98
RohI:	39.25
Pooled Age:	34.7 ± 5.0
Mean Age:	36.0 ± 6.4
Central Age:	34.7 ± 5.0
Chi-sq.:	16.36
P(%)	63.29
Dispersion:	0.03
RohD:	13.18
Nd:	4611
U standard	CN 5
Zeta $\pm 1\sigma$	416 ± 13
counted by	EW

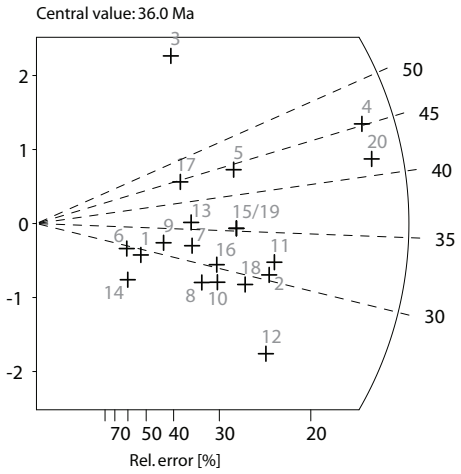

Crystal	Ns	Ni	Area	RhoS (e5)	RhoI (e5)	Age (Ma)	+- 1s	U (ppm)
1	4	38	25	2.56	24.34	28.80	15.17	21.24
2	20	179	63	5.08	45.50	30.56	7.28	39.70
3	8	24	16	8.01	24.02	90.76	37.18	20.96
4	41	248	100	6.57	39.72	45.17	7.77	34.65
5	15	93	40	6.01	37.24	44.07	12.36	32.49
6	3	28	30	1.60	14.95	29.31	17.84	13.04
7	9	76	40	3.60	30.43	32.39	11.47	26.55
8	10	99	36	4.45	44.04	27.64	9.22	38.42
9	6	51	24	4.00	34.03	32.18	13.93	29.69
10	12	116	35	5.49	53.08	28.30	8.64	46.31
11	21	180	63	5.34	45.76	31.91	7.44	39.92
12	19	220	80	3.80	44.04	23.64	5.71	38.42
13	9	68	24	6.01	45.38	36.19	12.90	39.59
14	3	36	20	2.40	28.83	22.81	13.73	25.15
15	15	116	48	5.01	38.70	35.36	9.78	33.77
16	12	108	63	3.05	27.46	30.39	9.31	23.95
17	8	49	21	6.10	37.37	44.61	17.08	32.60
18	16	151	54	4.75	44.78	28.99	7.69	39.07
19	15	116	48	5.01	38.70	35.36	9.78	33.77
20	43	283	100	6.89	45.32	41.53	6.95	39.54

Sample number:	**RD 6**
Mineral:	Apatite
Irradiation code:	eth-328-13
Ns:	138
Ni:	1005
Area:	1175
RohS:	1.88
RohI:	13.70
Pooled Age:	31.0 ± 6.0
Mean Age:	34.1 ± 6.0
Central Age:	31.0 ± 6.0
Chi-sq.:	15.62
P(%)	68.26
Dispersion:	0.02
RohD:	10.87
Nd:	4611
U standard	CN 5
Zeta $\pm 1\sigma$	416 ± 13
counted by	EW

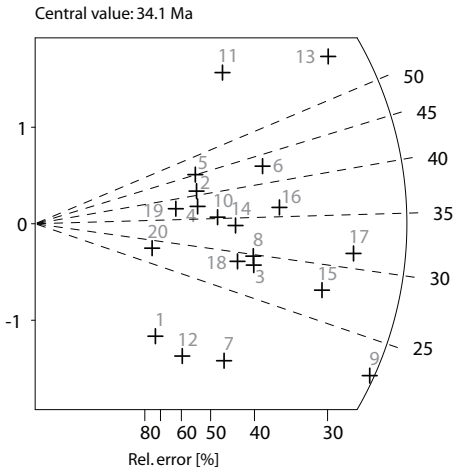

Crystal	Ns	Ni	Area	RhoS (e5)	RhoI (e5)	Age (Ma)	+- 1s	U (ppm)
1	2	31	36	0.89	13.79	14.57	10.64	14.59
2	4	22	60	1.07	5.87	40.98	22.32	6.21
3	7	55	80	1.40	11.01	28.72	11.57	11.65
4	4	24	70	0.92	5.49	37.58	20.34	5.81
5	4	20	20	3.20	16.02	45.07	24.73	16.94
6	8	42	60	2.14	11.21	42.93	16.63	11.86
7	5	64	49	1.63	20.92	17.64	8.21	22.13
8	7	53	100	1.12	8.49	29.80	12.03	8.98
9	16	160	60	4.27	42.71	22.57	5.97	45.18
10	5	32	50	1.60	10.25	35.24	16.99	10.84
11	6	19	24	4.00	12.68	71.02	33.35	13.41
12	3	45	100	0.48	7.21	15.06	8.99	7.62
13	14	55	100	2.24	8.81	57.31	17.27	9.32
14	6	40	40	2.40	16.02	33.83	14.86	16.94
15	12	98	90	2.14	17.44	27.63	8.50	18.45
16	9	56	60	2.40	14.95	36.24	13.07	15.81
17	15	108	40	6.01	43.24	31.33	8.70	45.74
18	6	47	36	2.67	20.91	28.80	12.53	22.12
19	3	18	50	0.96	5.77	37.58	23.47	6.10
20	2	16	50	0.64	5.13	28.20	21.18	5.42

Sample number:	**RD 7**
Mineral:	Apatite
Irradiation code:	eth-329-2
Ns:	280
Ni:	2230
Area:	988
RohS:	4.54
RohI:	36.15
Pooled Age:	32.5 ± 4.8
Mean Age:	36.0 ± 5.6
Central Age:	32.6 ± 4.8
Chi-sq.:	20.39
P(%)	37.17
Dispersion:	0.03
RohD:	12.49
Nd:	4450
U standard	CN 5
Zeta $\pm 1\sigma$	416 ± 13
counted by	EW

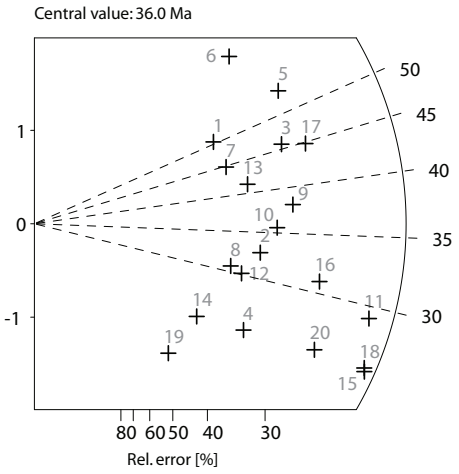

Crystal	Ns	Ni	Area	RhoS (e5)	RhoI (e5)	Age (Ma)	+- 1s	U (ppm)
1	8	41	18	7.12	36.48	50.50	19.60	33.58
2	12	95	35	5.49	43.47	32.74	10.09	40.02
3	15	85	48	5.01	28.36	45.69	12.89	26.11
4	10	105	32	5.01	52.55	24.70	8.22	48.38
5	15	72	40	6.01	28.83	53.91	15.41	26.54
6	10	38	21	7.63	28.98	68.02	24.29	26.68
7	9	52	20	7.21	41.64	44.82	16.25	38.34
8	9	76	36	4.00	33.81	30.70	10.87	31.13
9	16	109	50	5.13	34.91	38.03	10.27	32.14
10	14	102	40	5.61	40.84	35.57	10.21	37.60
11	26	231	100	4.16	37.00	29.18	6.12	34.06
12	10	86	36	4.45	38.26	30.14	10.13	35.22
13	11	69	40	4.40	27.63	41.29	13.48	25.43
14	6	66	35	2.75	30.20	23.58	10.09	27.80
15	25	251	100	4.00	40.20	25.83	5.49	37.01
16	19	159	63	4.83	40.42	30.98	7.60	37.21
17	18	104	50	5.77	33.31	44.82	11.55	30.67
18	25	249	100	4.00	39.88	26.04	5.54	36.71
19	4	59	24	2.67	39.37	17.59	9.11	36.25
20	18	181	100	2.88	28.99	25.79	6.44	26.69

Sample number:	**RD 11**
Mineral:	Apatite
Irradiation code:	eth-329-12
Ns:	80
Ni:	558
Area:	877
RohS:	1.46
RohI:	10.19
Pooled Age:	30.4 ± 7.6
Mean Age:	37.9 ± 8.4
Central Age:	30.4 ± 7.6
Chi-sq.:	8.90
P(%)	97.51
Dispersion:	0.00
RohD:	10.21
Nd:	4450
U standard	CN 5
Zeta ±1σ	416 ± 13
counted by	EW

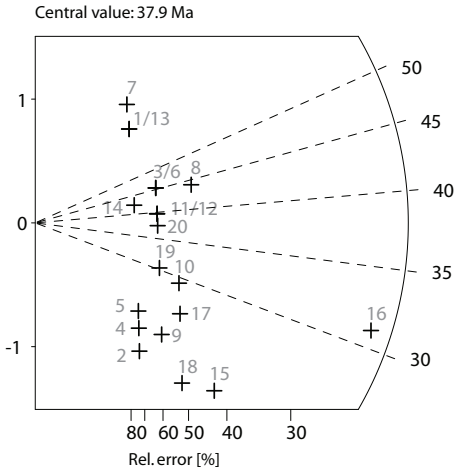

Crystal	Ns	Ni	Area	RhoS (e5)	RhoI (e5)	Age (Ma)	+- 1s	U (ppm)
1	2	6	12	2.67	8.01	70.43	57.56	9.02
2	2	24	42	0.76	9.15	17.68	13.03	10.30
3	3	14	49	0.98	4.58	45.36	28.90	5.15
4	2	21	40	0.80	8.41	20.20	14.97	9.47
5	2	19	40	0.80	7.61	22.32	16.61	8.57
6	3	14	50	0.96	4.48	45.36	28.90	5.05
7	2	5	14	2.29	5.72	84.42	70.69	6.44
8	5	24	48	1.67	8.01	44.11	21.74	9.02
9	3	29	48	1.00	9.68	21.94	13.33	10.90
10	4	29	70	0.92	6.64	29.24	15.63	7.47
11	3	16	42	1.14	6.10	39.71	25.02	6.87
12	3	16	60	0.80	4.27	39.71	25.02	4.81
13	2	6	15	2.14	6.41	70.43	57.56	7.21
14	2	10	24	1.34	6.67	42.35	32.84	7.51
15	6	60	70	1.37	13.73	21.21	9.11	15.46
16	22	150	21	16.78	114.40	31.08	7.18	128.81
17	4	33	60	1.07	8.81	25.70	13.64	9.92
18	4	44	100	0.64	7.05	19.28	10.09	7.93
19	3	21	36	1.34	9.34	30.28	18.72	10.52
20	3	17	36	1.34	7.56	37.38	23.44	8.52

Sample number:	**RD 12**
Mineral:	Apatite
Irradiation code:	eth-330-2
Ns:	415
Ni:	4279
Area:	1301
RohS:	5.11
RohI:	52.68
Pooled Age:	28.6 ± 3.6
Mean Age:	29.8 ± 3.8
Central Age:	28.6 ± 3.6
Chi-sq.:	20.17
P(%)	38.43
Dispersion:	0.02
RohD:	14.21
Nd:	3733
U standard	CN 5
Zeta ±1σ	416 ± 13
counted by	EW

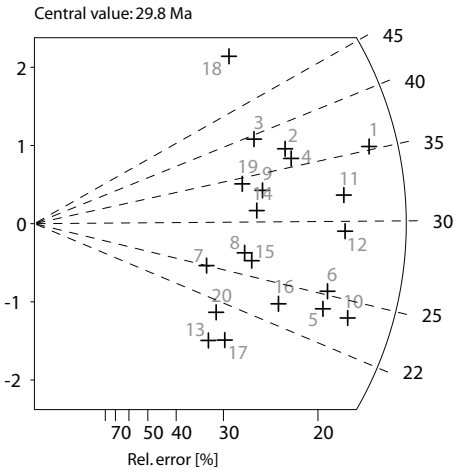

Crystal	Ns	Ni	Area	RhoS (e5)	RhoI (e5)	Age (Ma)	+- 1s	U (ppm)
1	39	326	100	6.25	52.21	35.27	6.10	42.25
2	22	175	100	3.52	28.03	37.06	8.48	22.68
3	17	127	50	5.45	40.68	39.45	10.28	32.92
4	23	189	80	4.60	37.84	35.87	8.02	30.62
5	28	343	100	4.48	54.93	24.09	4.81	44.45
6	29	339	70	6.64	77.56	25.24	4.96	62.76
7	10	118	70	2.29	27.00	25.00	8.28	21.85
8	15	164	56	4.29	46.90	26.98	7.34	37.95
9	18	160	50	5.77	51.25	33.17	8.33	41.47
10	33	406	80	6.61	81.28	23.98	4.42	65.77
11	33	305	100	5.29	48.85	31.91	5.95	39.53
12	33	332	100	5.29	53.17	29.32	5.45	43.03
13	10	161	40	4.00	64.46	18.33	6.01	52.16
14	17	161	60	4.54	42.98	31.14	8.02	34.78
15	16	179	30	8.54	95.56	26.37	6.94	77.33
16	20	251	40	8.01	100.50	23.51	5.53	81.32
17	12	185	50	3.84	59.26	19.15	5.74	47.95
18	14	74	25	8.97	47.41	55.69	16.35	38.36
19	15	129	30	8.01	68.87	34.28	9.43	55.73
20	11	155	70	2.52	35.46	20.94	6.58	28.70

Sample number:	**RD 19**
Mineral:	Apatite
Irradiation code:	eth-331-3
Ns:	358
Ni:	3651
Area:	1338
RohS:	4.29
RohI:	43.70
Pooled Age:	28.0 ± 3.6
Mean Age:	28.7 ± 3.0
Central Age:	28.0 ± 3.6
Chi-sq.:	17.87
P(%)	53.10
Dispersion:	0.05
RohD:	13.74
Nd:	6179
U standard	CN 5
Zeta $\pm 1\sigma$	416 ± 13
counted by	EW

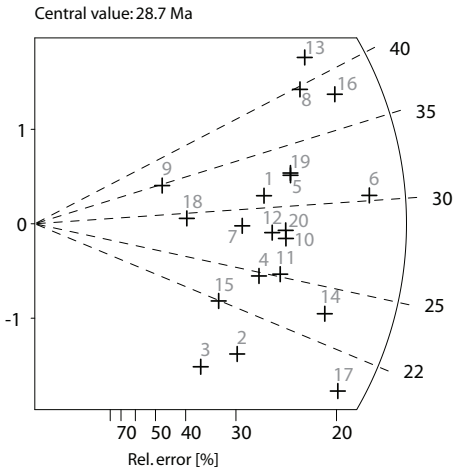

Crystal	Ns	Ni	Area	RhoS (e5)	RhoI (e5)	Age (Ma)	+- 1s	U (ppm)
1	16	147	50	5.13	47.09	31.04	8.24	39.40
2	12	180	50	3.84	57.66	19.03	5.71	48.24
3	8	138	50	2.56	44.20	16.55	6.05	36.99
4	15	173	60	4.00	46.18	24.74	6.71	38.64
5	20	176	80	4.00	35.23	32.41	7.72	29.48
6	34	320	100	5.45	51.25	30.30	5.56	42.88
7	13	130	48	4.34	43.38	28.53	8.35	36.29
8	22	158	50	7.05	50.61	39.68	9.13	42.35
9	5	41	50	1.60	13.13	34.77	16.51	10.99
10	19	196	50	6.09	62.78	27.65	6.71	52.53
11	18	204	60	4.81	54.45	25.18	6.25	45.56
12	17	173	60	4.54	46.18	28.03	7.19	38.64
13	23	154	60	6.14	41.11	42.56	9.62	34.40
14	25	303	100	4.00	48.53	23.55	4.96	40.60
15	10	130	50	3.20	41.64	21.95	7.24	34.84
16	28	211	60	7.47	56.32	37.83	7.71	47.13
17	27	382	100	4.32	61.18	20.18	4.07	51.19
18	7	68	100	1.12	10.89	29.36	11.70	9.11
19	20	175	100	3.20	28.03	32.59	7.77	23.45
20	19	192	60	5.07	51.25	28.23	6.86	42.88

Sample number:	**RD 22**
Mineral:	Apatite
Irradiation code:	eth-331-4
Ns:	85
Ni:	698
Area:	1286
RohS:	1.06
RohI:	8.69
Pooled Age:	34.0 ± 8.2
Mean Age:	42.3 ± 11.2
Central Age:	34.0 ± 8.2
Chi-sq.:	11.14
P(%)	91.91
Dispersion:	0.00
RohD:	13.47
Nd:	6179
U standard	CN 5
Zeta ±1σ	416 ± 13
counted by	EW

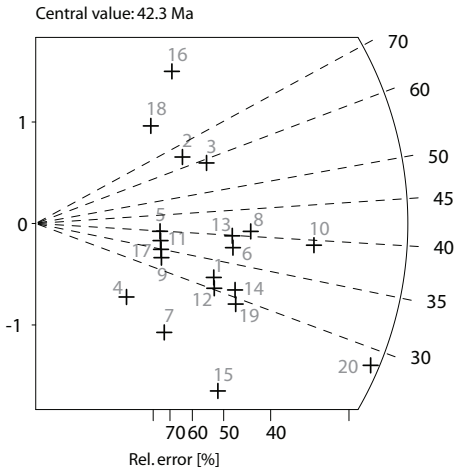

Crystal	Ns	Ni	Area	RhoS (e5)	RhoI (e5)	Age (Ma)	+- 1s	U (ppm)
1	4	35	70	0.92	8.01	31.94	16.89	6.84
2	3	13	25	1.92	8.33	64.34	41.27	7.11
3	4	19	70	0.92	4.35	58.72	32.36	3.71
4	1	14	25	0.64	8.97	19.98	20.70	7.66
5	2	14	30	1.07	7.47	39.91	30.20	6.38
6	5	37	100	0.80	5.93	37.75	18.03	5.06
7	2	29	100	0.32	4.64	19.30	14.12	3.97
8	6	41	100	0.96	6.57	40.88	17.92	5.61
9	2	17	15	2.14	18.15	32.88	24.61	15.50
10	10	71	40	4.00	28.43	39.34	13.36	24.27
11	2	15	56	0.57	4.29	37.25	28.07	3.66
12	4	37	100	0.64	5.93	30.22	15.94	5.06
13	5	35	63	1.27	8.90	39.91	19.13	7.60
14	5	45	100	0.80	7.21	31.06	14.68	6.15
15	4	62	32	2.00	31.03	18.05	9.33	26.49
16	3	7	100	0.48	1.12	118.98	82.20	0.96
17	2	16	60	0.53	4.27	34.93	26.22	3.65
18	2	6	60	0.53	1.60	92.73	75.78	1.37
19	5	48	50	1.60	15.38	29.12	13.72	13.13
20	14	137	90	2.49	24.38	28.57	8.07	20.81

Sample number:	**RD 24**
Mineral:	Apatite
Irradiation code:	eth-331-9
Ns:	102
Ni:	1092
Area:	1151
RohS:	1.42
RohI:	15.19
Pooled Age:	23.5 ± 5.2
Mean Age:	26.1 ± 5.6
Central Age:	23.5 ± 5.6
Chi-sq.:	13.89
P(%)	79.03
Dispersion:	0.01
RohD:	12.10
Nd:	6179
U standard	CN 5
Zeta $\pm 1\sigma$	416 ± 13
counted by	EW

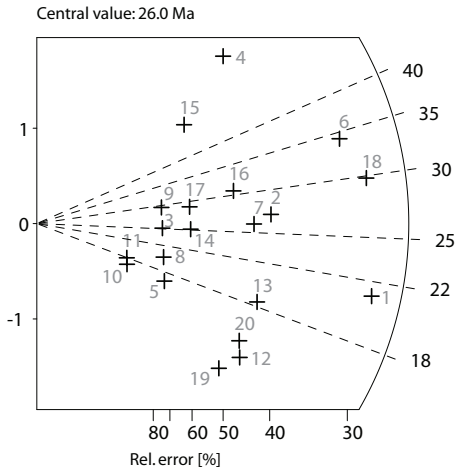

Crystal	Ns	Ni	Area	RhoS (e5)	RhoI (e5)	Age (Ma)	+- 1s	U (ppm)
1	14	167	100	2.24	26.75	21.07	5.91	25.41
2	7	65	40	2.80	26.03	27.06	10.80	24.73
3	2	20	35	0.92	9.15	25.13	18.66	8.69
4	5	20	42	1.91	7.63	62.64	31.39	7.25
5	2	30	40	0.80	12.01	16.76	12.26	11.41
6	12	88	50	3.84	28.19	34.24	10.60	26.78
7	6	58	100	0.96	9.29	25.99	11.18	8.83
8	2	25	24	1.34	16.68	20.11	14.79	15.85
9	2	17	30	1.07	9.08	29.55	22.11	8.62
10	1	15	36	0.45	6.67	16.76	17.32	6.34
11	1	14	80	0.20	2.80	17.96	18.60	2.66
12	5	92	80	1.00	18.42	13.67	6.29	17.50
13	6	82	50	1.92	26.27	18.40	7.81	24.95
14	3	30	56	0.86	8.58	25.13	15.24	8.15
15	3	15	28	1.72	8.58	50.16	31.77	8.15
16	5	41	100	0.80	6.57	30.63	14.55	6.24
17	3	26	50	0.96	8.33	28.99	17.70	7.91
18	14	118	50	4.48	37.80	29.80	8.48	35.91
19	4	84	100	0.64	13.45	11.98	6.14	12.78
20	5	85	60	1.34	22.69	14.79	6.83	21.56

Sample number:	**RD 26**
Mineral:	Apatite
Irradiation code:	eth-331-13
Ns:	286
Ni:	3055
Area:	1709
RohS:	2.68
RohI:	28.63
Pooled Age:	21.4 ± 3.0
Mean Age:	21.2 ± 3.0
Central Age:	21.4 ± 3.0
Chi-sq.:	21.41
P(%)	31.47
Dispersion:	0.07
RohD:	11.01
Nd:	6179
U standard	CN 5
Zeta ±1σ	416 ± 13
counted by	EW

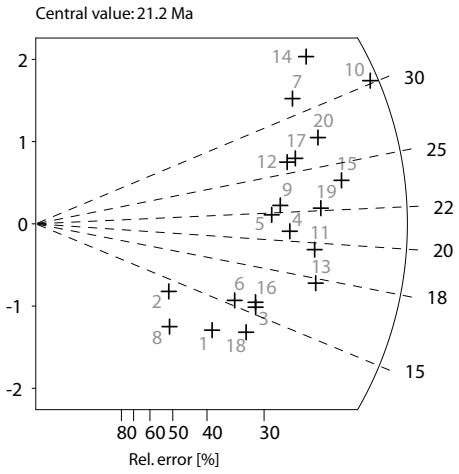

Crystal	Ns	Ni	Area	RhoS (e5)	RhoI (e5)	Age (Ma)	+- 1s	U (ppm)
1	7	125	49	2.29	40.86	12.81	5.00	42.67
2	4	66	60	1.07	17.62	13.87	7.16	18.40
3	11	163	100	1.76	26.11	15.44	4.84	27.26
4	15	166	100	2.40	26.59	20.66	5.61	27.77
5	13	136	100	2.08	21.78	21.86	6.39	22.75
6	9	134	70	2.06	30.66	15.37	5.32	32.02
7	16	115	50	5.13	36.84	31.79	8.55	38.47
8	4	82	50	1.28	26.27	11.16	5.73	27.43
9	14	142	70	3.20	32.49	22.54	6.36	33.93
10	27	204	100	4.32	32.67	30.24	6.28	34.12
11	18	210	100	2.88	33.63	19.60	4.86	35.13
12	15	132	100	2.40	21.14	25.97	7.13	22.08
13	18	232	100	2.88	37.16	17.75	4.38	38.81
14	18	116	100	2.88	18.58	35.44	9.06	19.40
15	22	211	100	3.52	33.79	23.84	5.40	35.29
16	11	160	100	1.76	25.63	15.73	4.93	26.76
17	16	140	60	4.27	37.37	26.12	6.95	39.03
18	10	166	100	1.60	26.59	13.78	4.51	27.77
19	19	196	100	3.04	31.39	22.16	5.38	32.78
20	19	159	100	3.04	25.46	27.31	6.69	26.60

Sample number:	**RD 29**
Mineral:	Apatite
Irradiation code:	eth-363-7
Ns:	78
Ni:	1006
Area:	563
RohS:	2.22
RohI:	28.62
Pooled Age:	21.9 ± 5.4
Mean Age:	22.6 ± 4.0
Central Age:	21.9 ± 5.4
Chi-sq.:	12.10
P(%)	88.13
Dispersion:	0.02
RohD:	13.49
Nd:	4917
U standard	CN 5
Zeta ±1σ	416 ± 13
counted by	EW

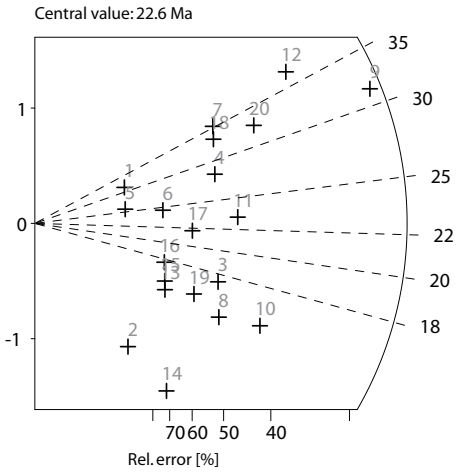

Crystal	Ns	Ni	Area	RhoS (e5)	RhoI (e5)	Age (Ma)	+- 1s	U (ppm)
1	1	9	8	2.00	18.02	31.34	33.05	15.36
2	1	37	20	0.80	29.63	7.64	7.74	25.25
3	4	65	30	2.14	34.70	17.37	8.97	29.57
4	4	40	24	2.67	26.69	28.21	14.82	22.75
5	1	11	10	1.60	17.62	25.65	26.80	15.01
6	2	23	15	2.14	24.56	24.54	18.11	20.93
7	4	32	20	3.20	25.63	35.24	18.73	21.84
8	4	76	40	1.60	30.43	14.86	7.64	25.93
9	14	126	56	4.00	36.04	31.34	8.89	30.71
10	6	109	56	1.72	31.17	15.54	6.54	26.57
11	5	61	50	1.60	19.54	23.13	10.79	16.65
12	8	61	28	4.58	34.89	36.97	13.96	29.74
13	2	38	16	2.00	38.04	14.86	10.79	32.42
14	2	71	40	0.80	28.43	7.96	5.71	24.23
15	2	36	18	1.78	32.03	15.69	11.41	27.30
16	2	32	20	1.60	25.63	17.65	12.88	21.84
17	3	39	24	2.00	26.03	21.71	13.03	22.18
18	4	34	24	2.67	22.69	33.17	17.57	19.34
19	3	54	36	1.34	24.02	15.69	9.32	20.47
20	6	52	28	3.43	29.74	32.54	14.07	25.35

Sample number:	**RD 30**
Mineral:	Apatite
Irradiation code:	eth-332-6
Ns:	53
Ni:	660
Area:	1158
RohS:	0.73
RohI:	9.13
Pooled Age:	20.0 ± 5.8
Mean Age:	23.6 ± 5.8
Central Age:	20.0 ± 6.0
Chi-sq.:	16.38
P(%)	63.17
Dispersion:	0.06
RohD:	11.97
Nd:	2946
U standard	CN 5
Zeta ±1σ	416 ± 13
counted by	EW

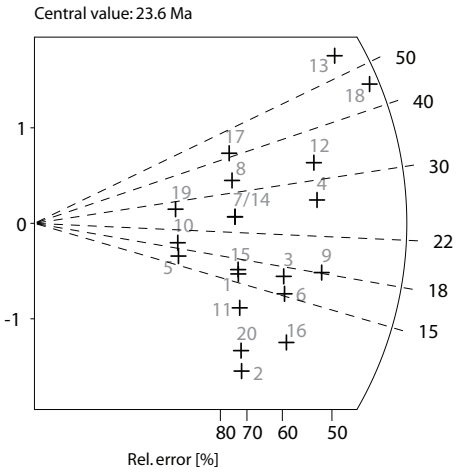

Crystal	Ns	Ni	Area	RhoS (e5)	RhoI (e5)	Age (Ma)	+- 1s	U (ppm)
1	2	31	40	0.80	12.41	16.04	11.72	11.92
2	2	64	100	0.32	10.25	7.78	5.59	9.85
3	3	44	70	0.69	10.07	16.96	10.14	9.67
4	4	37	70	0.92	8.47	26.86	14.17	8.13
5	1	15	24	0.67	10.01	16.58	17.13	9.62
6	3	49	100	0.48	7.85	15.23	9.07	7.54
7	2	20	100	0.32	3.20	24.85	18.45	3.08
8	2	15	21	1.53	11.44	33.12	24.96	10.99
9	4	55	100	0.64	8.81	18.08	9.39	8.46
10	1	13	40	0.40	5.21	19.13	19.86	5.00
11	2	40	50	0.64	12.81	12.44	9.02	12.31
12	4	30	100	0.64	4.81	33.12	17.67	4.62
13	5	22	20	4.00	17.62	56.35	27.99	16.92
14	2	20	50	0.64	6.41	24.85	18.45	6.15
15	2	30	60	0.53	8.01	16.58	12.12	7.69
16	3	66	60	0.80	17.62	11.31	6.69	16.92
17	2	12	25	1.28	7.69	41.37	31.63	7.39
18	6	33	30	3.20	17.62	45.12	20.09	16.92
19	1	9	28	0.57	5.15	27.61	29.12	4.95
20	2	55	70	0.46	12.58	9.05	6.52	12.09

Sample number:	**RD 32**
Mineral:	Apatite
Irradiation code:	eth-332-8
Ns:	144
Ni:	1560
Area:	1488
RohS:	1.55
RohI:	16.79
Pooled Age:	22.1 ± 4.2
Mean Age:	23.9 ± 3.8
Central Age:	22.1 ± 4.2
Chi-sq.:	12.15
P(%)	87.92
Dispersion:	0.00
RohD:	11.55
Nd:	2946
U standard	CN 5
Zeta ±1σ	416 ± 13
counted by	EW

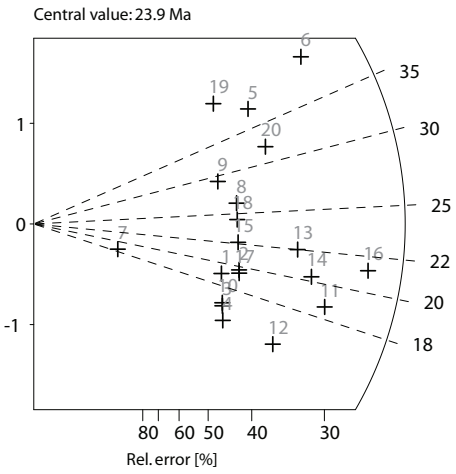

Crystal	Ns	Ni	Area	RhoS (e5)	RhoI (e5)	Age (Ma)	+- 1s	U (ppm)
1	5	63	100	0.80	10.09	19.04	8.87	10.05
2	6	73	100	0.96	11.69	19.72	8.40	11.64
3	5	73	100	0.80	11.69	16.43	7.62	11.64
4	5	78	100	0.80	12.49	15.38	7.12	12.44
5	7	44	42	2.67	16.78	38.11	15.57	16.71
6	11	64	90	1.96	11.39	41.16	13.52	11.34
7	1	13	24	0.67	8.68	18.45	19.16	8.64
8	6	55	70	1.37	12.58	26.16	11.29	12.53
9	5	41	70	1.14	9.38	29.23	13.89	9.34
10	5	72	70	1.14	16.47	16.66	7.73	16.40
11	12	154	42	4.58	58.72	18.69	5.64	58.47
12	8	124	100	1.28	19.86	15.48	5.68	19.77
13	10	109	100	1.60	17.46	22.00	7.31	17.38
14	11	130	70	2.52	29.74	20.30	6.42	29.61
15	6	65	50	1.92	20.82	22.14	9.48	20.73
16	16	181	70	3.66	41.41	21.20	5.58	41.23
17	6	74	60	1.60	19.75	19.45	8.29	19.67
18	6	59	100	0.96	9.45	24.39	10.49	9.41
19	5	28	30	2.67	14.95	42.76	20.82	14.88
20	8	60	100	1.28	9.61	31.95	12.08	9.57

Sample number:	**RD 34**
Mineral:	Apatite
Irradiation code:	eth-356-4
Ns:	532
Ni:	4153
Area:	1285
RohS:	6.63
RohI:	51.76
Pooled Age:	33.2 ± 3.8
Mean Age:	33.5 ± 2.6
Central Age:	33.2 ± 3.8
Chi-sq.:	14.85
P(%)	78.50
Dispersion:	0.01
RohD:	12.48
Nd:	7878
U standard	CN 5
Zeta ±1σ	416 ± 13
counted by	EW

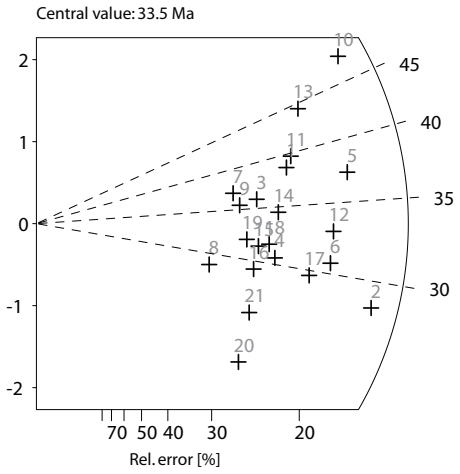

Crystal	Ns	Ni	Area	RhoS (e5)	RhoI (e5)	Age (Ma)	+- 1s	U (ppm)
1	26	174	70	5.95	39.81	38.66	8.23	36.70
2	45	409	100	7.21	65.50	28.49	4.57	60.38
3	20	144	35	9.15	65.89	35.94	8.66	60.74
4	23	195	50	7.37	62.46	30.54	6.81	57.58
5	40	278	60	10.68	74.21	37.23	6.42	68.40
6	35	295	70	8.01	67.49	30.72	5.59	62.22
7	16	112	50	5.13	35.87	36.97	9.96	33.07
8	12	108	40	4.81	43.24	28.77	8.81	39.86
9	17	124	60	4.54	33.10	35.48	9.25	30.51
10	39	211	50	12.49	67.59	47.79	8.48	62.30
11	27	176	60	7.21	46.98	39.69	8.31	43.30
12	36	283	60	9.61	75.54	32.93	5.93	69.63
13	29	169	70	6.64	38.67	44.38	9.04	35.64
14	24	180	30	12.81	96.09	34.51	7.59	88.58
15	20	165	40	8.01	66.06	31.38	7.50	60.90
16	19	168	80	3.80	33.63	29.28	7.15	31.00
17	30	262	100	4.81	41.96	29.65	5.80	38.68
18	22	180	80	4.40	36.04	31.64	7.22	33.22
19	18	146	40	7.21	58.46	31.91	8.04	53.89
20	16	192	60	4.27	51.25	21.59	5.66	47.24
21	18	182	80	3.60	36.44	25.61	6.39	33.59

Sample number:	**RD 35**
Mineral:	Apatite
Irradiation code:	eth-356-7
Ns:	335
Ni:	2659
Area:	986
RohS:	5.44
RohI:	43.19
Pooled Age:	33.0 ± 4.4
Mean Age:	33.7 ± 4.8
Central Age:	33.0 ± 4.4
Chi-sq.:	19.88
P(%)	40.16
Dispersion:	0.04
RohD:	12.63
Nd:	7878
U standard	CN 5
Zeta ±1σ	416 ± 13
counted by	EW

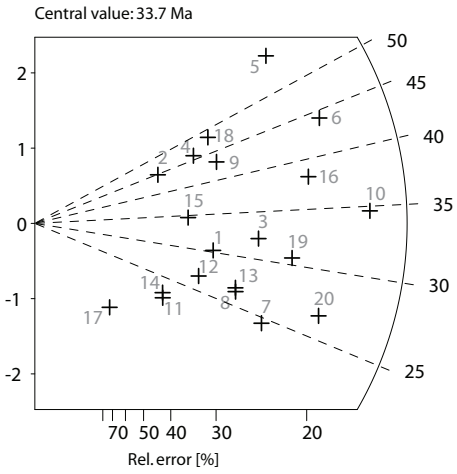

Crystal	Ns	Ni	Area	RhoS (e5)	RhoI (e5)	Age (Ma)	+- 1s	U (ppm)
1	12	104	50	3.84	33.31	30.23	9.27	30.34
2	6	35	24	4.00	23.36	44.86	19.88	21.28
3	19	155	60	5.07	41.37	32.11	7.88	37.69
4	10	57	40	4.00	22.82	45.91	15.81	20.79
5	22	101	60	5.87	26.96	56.95	13.53	24.56
6	32	190	60	8.54	50.72	44.08	8.55	46.20
7	19	203	54	5.64	60.21	24.53	5.94	54.84
8	15	149	35	6.86	68.18	26.38	7.20	62.11
9	13	79	40	5.21	31.63	43.07	12.97	28.81
10	43	325	100	6.89	52.05	34.65	5.74	47.41
11	6	71	24	4.00	47.38	22.15	9.45	43.16
12	10	98	45	3.56	34.88	26.74	8.92	31.77
13	15	147	40	6.01	58.86	26.74	7.30	53.61
14	6	69	36	2.67	30.70	22.79	9.73	27.96
15	9	68	24	6.01	45.38	34.66	12.35	41.33
16	29	199	70	6.64	45.53	38.16	7.69	41.47
17	2	35	21	1.53	26.69	14.99	10.91	24.31
18	12	65	40	4.81	26.03	48.30	15.26	23.71
19	25	214	63	6.36	54.40	30.61	6.55	49.56
20	30	295	100	4.81	47.25	26.65	5.18	43.04

Sample number:	**RD 36**
Mineral:	Apatite
Irradiation code:	eth-368-2
Ns:	128
Ni:	1594
Area:	669
RohS:	3.06
RohI:	38.16
Pooled Age:	27.0 ± 5.2
Mean Age:	33.3 ± 8.2
Central Age:	28.1 ± 6.2
Chi-sq.:	23.00
P(%)	23.74
Dispersion:	0.19
RohD:	16.22
Nd:	5595
U standard	CN 5
Zeta ±1σ	416 ± 13
counted by	EW

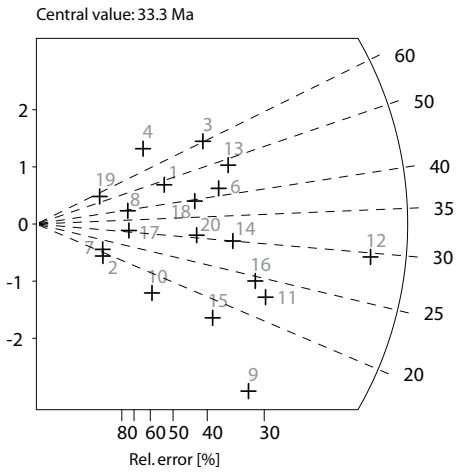

Crystal	Ns	Ni	Area	RhoS (e5)	RhoI (e5)	Age (Ma)	+- 1s	U (ppm)
1	4	28	36	1.779	12.456	48.03	25.72	8.83
2	1	18	36	0.445	8.008	18.72	19.24	5.68
3	7	39	22	5.096	28.391	60.28	24.83	20.13
4	3	13	24	2.002	8.675	77.4	49.65	6.15
5	0	8	50	0	2.562	0	0.01	1.82
6	8	64	40	3.203	25.625	42.04	15.83	18.17
7	1	16	21	0.763	12.202	21.06	21.71	8.65
8	2	17	10	3.203	27.226	39.58	29.62	19.3
9	10	260	60	2.669	69.4	12.97	4.2	49.2
10	3	62	50	0.961	19.859	16.31	9.66	14.08
11	12	178	50	3.844	57.015	22.71	6.82	40.42
12	26	296	32	13.012	148.142	29.57	6.13	105.02
13	9	63	10	14.414	100.897	48.03	17.19	71.53
14	9	101	18	8.008	89.864	30	10.49	63.71
15	7	134	60	1.868	35.768	17.6	6.85	25.36
16	11	152	50	3.523	48.687	24.37	7.66	34.52
17	2	22	25	1.281	14.094	30.6	22.63	9.99
18	6	51	24	4.004	34.033	39.58	17.13	24.13
19	1	6	21	0.763	4.576	55.99	60.51	3.24
20	6	66	30	3.203	35.234	30.6	13.09	24.98

Sample number:	**RD 37**
Mineral:	Apatite
Irradiation code:	eth-368-4
Ns:	92
Ni:	911
Area:	660
RohS:	2.23
RohI:	22.11
Pooled Age:	33.4 ± 7.6
Mean Age:	35.2 ± 6.2
Central Age:	33.4 ± 7.6
Chi-sq.:	5.74
P(%)	99.85
Dispersion:	0.00
RohD:	15.95
Nd:	5595
U standard	CN 5
Zeta $\pm 1\sigma$	416 ± 13
counted by	EW

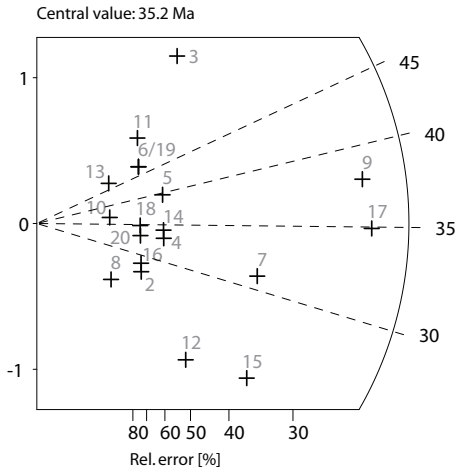

Crystal	Ns	Ni	Area	RhoS (e5)	RhoI (e5)	Age (Ma)	+- 1s	U (ppm)
1	0	9	49	0.00	2.94	0.00	0.01	2.12
2	2	24	24	1.34	16.02	27.59	20.33	11.55
3	4	20	16	4.00	20.02	66.03	36.23	14.43
4	3	30	28	1.72	17.16	33.10	20.07	12.37
5	3	25	35	1.37	11.44	39.70	24.29	8.25
6	2	14	27	1.19	8.30	47.23	35.74	5.99
7	9	96	30	4.81	51.25	31.03	10.87	36.94
8	1	14	60	0.27	3.74	23.66	24.50	2.69
9	20	175	16	20.02	175.17	37.81	9.02	126.28
10	1	9	28	0.57	5.15	36.77	38.77	3.71
11	2	12	24	1.34	8.01	55.07	42.10	5.77
12	4	61	37	1.73	26.40	21.72	11.24	19.03
13	1	7	21	0.76	5.34	47.23	50.52	3.85
14	3	29	100	0.48	4.64	34.24	20.80	3.35
15	8	111	35	3.66	50.79	23.87	8.78	36.61
16	2	23	20	1.60	18.42	28.79	21.25	13.28
17	21	199	50	6.73	63.74	34.92	8.10	45.95
18	2	19	12	2.67	25.36	34.84	25.92	18.28
19	2	14	18	1.78	12.46	47.23	35.74	8.98
20	2	20	30	1.07	10.68	33.10	24.57	7.70

Sample number:	**RD 38**
Mineral:	Apatite
Irradiation code:	eth-368-7
Ns:	60
Ni:	587
Area:	569
RohS:	1.69
RohI:	16.52
Pooled Age:	33.0 ± 9.2
Mean Age:	42.8 ± 8.8
Central Age:	35.3 ± 10.8
Chi-sq.:	18.20
P(%)	44.26
Dispersion:	0.26
RohD:	15.55
Nd:	5595
U standard	CN 5
Zeta ±1σ	416 ± 13
counted by	EW

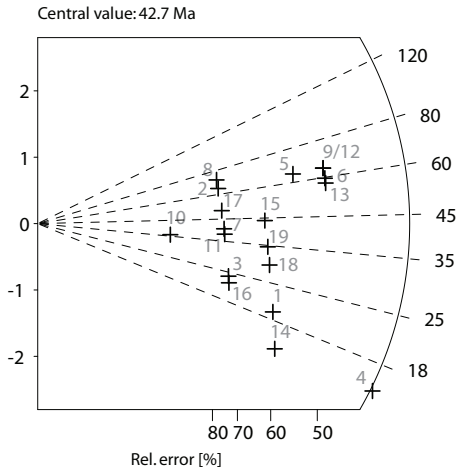

Crystal	Ns	Ni	Area	RhoS (e5)	RhoI (e5)	Age (Ma)	+- 1s	U (ppm)
1	3	50	30	1.60	26.69	19.38	11.54	19.74
2	2	10	21	1.53	7.63	64.36	49.90	5.64
3	2	27	17	1.88	25.44	23.91	17.54	18.81
4	6	130	18	5.34	115.67	14.91	6.25	85.55
5	4	20	18	3.56	17.80	64.36	35.32	13.16
6	5	27	21	3.81	20.59	59.62	29.10	15.23
7	2	16	24	1.34	10.68	40.30	30.26	7.90
8	2	9	15	2.14	9.61	71.48	55.93	7.11
9	5	25	36	2.22	11.12	64.36	31.61	8.23
10	1	9	28	0.57	5.15	35.84	37.80	3.81
11	2	17	24	1.34	11.34	37.94	28.39	8.39
12	5	25	22	3.64	18.20	64.36	31.61	13.46
13	5	28	46	1.74	9.75	57.50	27.98	7.21
14	3	69	80	0.60	13.81	14.05	8.30	10.22
15	3	22	60	0.80	5.87	43.95	27.09	4.34
16	2	29	25	1.28	18.58	22.27	16.30	13.74
17	2	13	24	1.34	8.68	49.57	37.69	6.42
18	3	33	20	2.40	26.43	29.34	17.72	19.54
19	3	28	40	1.20	11.21	34.56	21.03	8.29

Sample number:	**RD 39**
Mineral:	Apatite
Irradiation code:	eth-368-8
Ns:	65
Ni:	678
Area:	653
RohS:	1.59
RohI:	16.63
Pooled Age:	30.7 ± 8.2
Mean Age:	36.2 ± 5.8
Central Age:	30.7 ± 8.2
Chi-sq.:	9.23
P(%)	96.95
Dispersion:	0.01
RohD:	15.42
Nd:	5595
U standard	CN 5
Zeta ±1σ	416 ± 13
counted by	EW

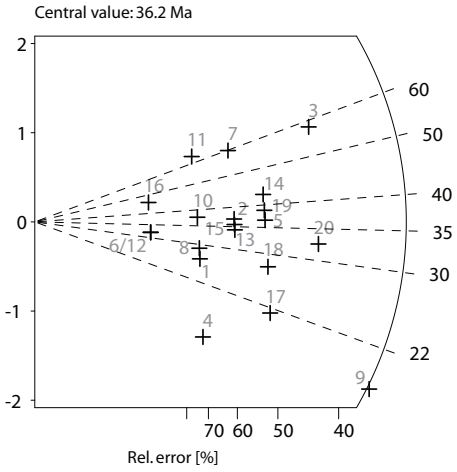

Crystal	Ns	Ni	Area	RhoS (e5)	RhoI (e5)	Age (Ma)	+- 1s	U (ppm)
1	2	24	18	1.78	21.35	26.66	19.65	15.93
2	3	26	20	2.40	20.82	36.89	22.53	15.53
3	6	33	18	5.34	29.36	58.04	25.83	21.91
4	2	45	24	1.34	30.03	14.23	10.30	22.40
5	4	35	56	1.14	10.01	36.54	19.33	7.47
6	1	10	24	0.67	6.67	31.98	33.56	4.98
7	3	16	24	2.00	10.68	59.84	37.70	7.97
8	2	22	40	0.80	8.81	29.08	21.50	6.57
9	8	140	50	2.56	44.84	18.30	6.68	33.46
10	2	17	32	1.00	8.51	37.61	28.15	6.35
11	2	10	24	1.34	6.67	63.81	49.47	4.98
12	1	10	21	0.76	7.63	31.98	33.56	5.69
13	3	28	24	2.00	18.69	34.26	20.85	13.94
14	4	30	10	6.41	48.05	42.61	22.73	35.85
15	3	27	50	0.96	8.65	35.53	21.66	6.45
16	1	7	18	0.89	6.23	45.64	48.82	4.65
17	4	60	36	1.78	26.69	21.34	11.04	19.91
18	4	46	24	2.67	30.70	27.82	14.53	22.90
19	4	33	40	1.60	13.21	38.75	20.56	9.86
20	6	59	100	0.96	9.45	32.52	13.98	7.05

Sample number:	**RD 40**
Mineral:	Apatite
Irradiation code:	eth-368-11
Ns:	171
Ni:	1641
Area:	924
RohS:	2.96
RohI:	28.44
Pooled Age:	32.5 ± 5.6
Mean Age:	34.9 ± 3.6
Central Age:	32.5 ± 5.6
Chi-sq.:	6.02
P(%)	99.79
Dispersion:	0.00
RohD:	15.01
Nd:	5595
U standard	CN 5
Zeta ±1σ	416 ± 13
counted by	EW

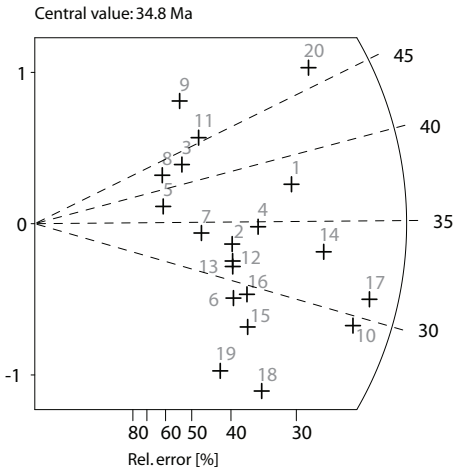

Crystal	Ns	Ni	Area	RhoS (e5)	RhoI (e5)	Age (Ma)	+- 1s	U (ppm)
1	12	99	100	1.922	15.855	37.74	11.61	12.15
2	7	66	30	3.737	35.234	33.03	13.18	26.99
3	4	29	15	4.271	30.963	42.92	22.94	23.72
4	9	81	48	3.003	27.026	34.6	12.21	20.71
5	3	25	30	1.602	13.346	37.36	22.86	10.22
6	7	76	25	4.484	48.687	28.69	11.38	37.3
7	5	46	40	2.002	18.418	33.85	15.98	14.11
8	3	22	27	1.779	13.05	42.44	26.16	10
9	4	23	16	4.004	23.022	54.08	29.35	17.64
10	18	190	80	3.603	38.037	29.51	7.35	29.14
11	5	34	30	2.669	18.151	45.75	21.97	13.91
12	7	69	35	3.203	31.573	31.6	12.58	24.19
13	7	70	45	2.491	24.913	31.15	12.39	19.09
14	15	141	50	4.805	45.163	33.13	9.07	34.6
15	8	92	50	2.562	29.468	27.09	10.03	22.58
16	8	85	45	2.847	30.251	29.32	10.89	23.18
17	20	201	100	3.203	32.191	30.99	7.34	24.66
18	9	118	48	3.003	39.371	23.77	8.26	30.16
19	6	81	50	1.922	25.945	23.09	9.8	19.88
20	14	93	60	3.737	24.824	46.83	13.52	19.02

Sample number:	**RD 41**
Mineral:	Apatite
Irradiation code:	eth-368-13
Ns:	234
Ni:	2267
Area:	692
RohS:	5.42
RohI:	52.47
Pooled Age:	31.6 ± 4.8
Mean Age:	31.9 ± 3.6
Central Age:	31.6 ± 4.8
Chi-sq.:	12.28
P(%)	87.34
Dispersion:	0.00
RohD:	14.74
Nd:	5595
U standard	CN 5
Zeta $\pm 1\sigma$	416 ± 13
counted by	EW

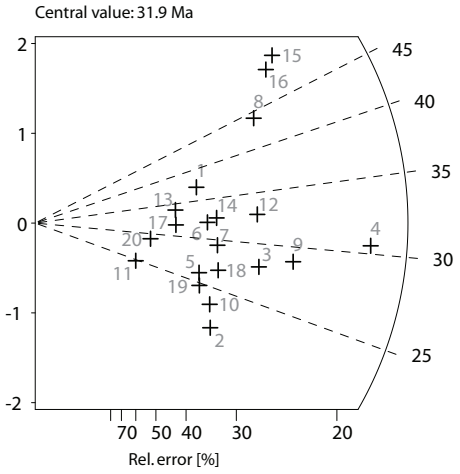

Crystal	Ns	Ni	Area	RhoS (e5)	RhoI (e5)	Age (Ma)	+- 1s	U (ppm)
1	8	66	40	3.20	26.43	37.06	13.93	20.61
2	9	129	40	3.60	51.65	21.36	7.40	40.29
3	15	164	40	6.01	65.66	27.99	7.61	51.22
4	34	341	70	7.78	78.02	30.50	5.58	60.86
5	8	94	40	3.20	37.64	26.04	9.63	29.36
6	9	86	30	4.81	45.91	32.01	11.27	35.82
7	10	104	30	5.34	55.52	29.42	9.79	43.31
8	15	104	30	8.01	55.52	44.08	12.27	43.31
9	20	212	70	4.58	48.50	28.86	6.82	37.84
10	9	118	24	6.01	78.74	23.35	8.11	61.43
11	3	37	12	4.00	49.38	24.82	14.92	38.52
12	15	140	50	4.81	44.84	32.77	8.97	34.98
13	6	54	16	6.01	54.05	33.98	14.67	42.17
14	10	94	35	4.58	43.01	32.54	10.88	33.55
15	18	107	24	12.01	71.40	51.38	13.21	55.70
16	17	104	25	10.89	66.62	49.93	13.17	51.97
17	6	58	12	8.01	77.41	31.64	13.61	60.39
18	10	114	40	4.00	45.64	26.84	8.90	35.61
19	8	99	40	3.20	39.64	24.73	9.13	30.92
20	4	42	24	2.67	28.03	29.14	15.28	21.86

Sample number:	**RD 43**
Mineral:	Apatite
Irradiation code:	eth-368-15
Ns:	85
Ni:	713
Area:	720
RohS:	1.89
RohI:	15.86
Pooled Age:	35.8 ± 8.6
Mean Age:	38.3 ± 6.4
Central Age:	35.8 ± 8.6
Chi-sq.:	10.54
P(%)	93.85
Dispersion:	0.00
RohD:	14.47
Nd:	5595
U standard	CN 5
Zeta $\pm 1\sigma$	416 ± 13
counted by	EW

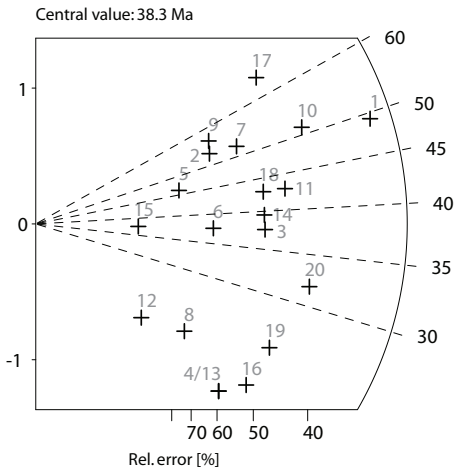

Cryst	Ns	Ni	Area	RhoS (e5)	RhoI (e5)	Age (Ma)	+- 1s	U (ppm)
1	11	67	40	4.40	26.83	49.24	16.10	21.32
2	3	17	40	1.20	6.81	52.91	33.18	5.41
3	5	40	100	0.80	6.41	37.52	17.84	5.09
4	3	49	80	0.60	9.81	18.40	10.96	7.79
5	2	13	40	0.80	5.21	46.15	35.09	4.14
6	3	24	18	2.67	21.35	37.52	23.01	16.97
7	4	23	24	2.67	15.35	52.14	28.30	12.20
8	2	28	32	1.00	14.01	21.47	15.73	11.14
9	3	16	30	1.60	8.54	56.20	35.41	6.79
10	7	41	42	2.67	15.63	51.19	21.01	12.42
11	6	42	30	3.20	22.42	42.86	18.76	17.82
12	1	16	18	0.89	14.24	18.79	19.38	11.31
13	3	49	30	1.60	26.16	18.40	10.96	20.79
14	5	38	30	2.67	20.29	39.49	18.83	16.12
15	1	8	20	0.80	6.41	37.52	39.82	5.09
16	4	58	32	2.00	29.03	20.73	10.74	23.07
17	5	23	20	4.00	18.42	65.11	32.21	14.63
18	5	35	40	2.00	14.01	42.86	20.54	11.14
19	5	60	30	2.67	32.03	25.04	11.69	25.45
20	7	66	24	4.67	44.04	31.85	12.71	35.00

Sample number:	**RD 57**
Mineral:	Apatite
Irradiation code:	eth-368-17
Ns:	135
Ni:	1420
Area:	1404
RohS:	1.54
RohI:	16.20
Pooled Age:	28.0 ± 5.4
Mean Age:	31.2 ± 6.0
Central Age:	28.0 ± 5.4
Chi-sq.:	11.69
P(%)	89.84
Dispersion:	0.00
RohD:	14.20
Nd:	5595
U standard	CN 5
Zeta ±1σ	416 ± 13
counted by	EW

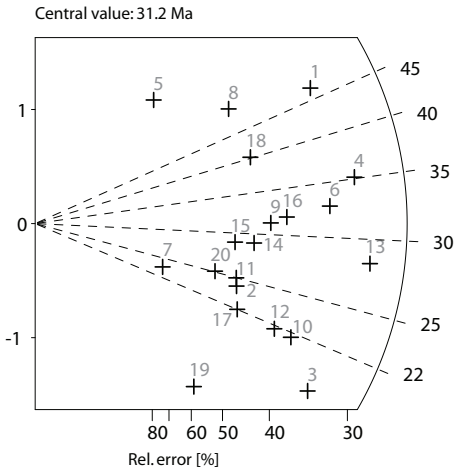

Crystal	Ns	Ni	Area	RhoS (e5)	RhoI (e5)	Age (Ma)	+- 1s	U (ppm)	Dpar
1	10	63	70	2.29	14.41	46.73	15.98	11.67	1.88
2	5	61	50	1.60	19.54	24.17	11.27	15.82	2.02
3	9	141	100	1.44	22.58	18.83	6.51	18.28	2.16
4	13	109	60	3.47	29.10	35.14	10.38	23.56	2.19
5	2	8	28	1.14	4.58	73.44	58.11	3.70	1.94
6	11	99	100	1.76	15.86	32.74	10.47	12.84	1.90
7	2	25	50	0.64	8.01	23.59	17.36	6.48	2.15
8	5	29	100	0.80	4.64	50.74	24.63	3.76	1.97
9	7	66	100	1.12	10.57	31.26	12.47	8.56	1.80
10	8	109	100	1.28	17.46	21.65	7.96	14.13	1.89
11	5	59	48	1.67	19.69	24.99	11.67	15.94	2.02
12	7	95	100	1.12	15.22	21.73	8.54	12.32	1.97
13	14	146	100	2.24	23.38	28.27	7.97	18.93	1.96
14	6	61	70	1.37	13.96	28.99	12.44	11.30	1.72
15	5	51	48	1.67	17.02	28.90	13.58	13.78	2.13
16	8	74	56	2.29	21.16	31.86	11.91	17.14	2.09
17	5	67	50	1.60	21.46	22.01	10.23	17.38	1.93
18	6	44	60	1.60	11.75	40.16	17.53	9.51	1.97
19	3	66	54	0.89	19.57	13.42	7.93	15.85	2.14
20	4	47	60	1.07	12.55	25.10	13.10	10.16	1.99

Sample number:	**RD 58**
Mineral:	Apatite
Irradiation code:	eth-368-20
Ns:	64
Ni:	594
Area:	1396
RohS:	0.73
RohI:	6.82
Pooled Age:	30.9 ± 8.4
Mean Age:	34.6 ± 7.6
Central Age:	30.9 ± 8.4
Chi-sq.:	9.72
P(%)	95.96
Dispersion:	0.00
RohD:	13.80
Nd:	5595
U standard	CN 5
Zeta ±1σ	416 ± 13
counted by	EW

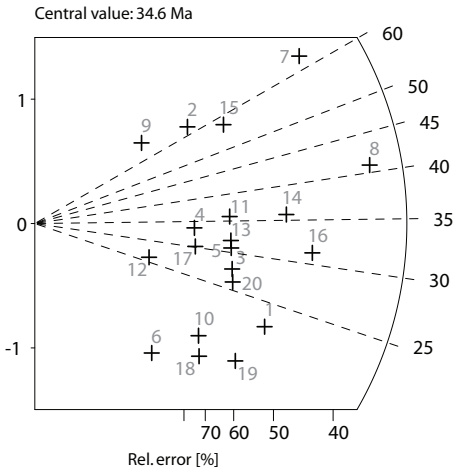

Crystal	Ns	Ni	Area	RhoS (e5)	RhoI (e5)	Age (Ma)	+- 1s	U (ppm)	Dpar
1	4	51	56	1.14	14.59	22.47	11.69	12.15	1.46
2	2	9	42	0.76	3.43	63.48	49.67	2.86	1.49
3	3	31	80	0.60	6.21	27.72	16.79	5.17	1.51
4	2	17	60	0.53	4.54	33.68	25.21	3.78	1.50
5	3	28	60	0.80	7.47	30.68	18.67	6.23	1.49
6	1	24	42	0.38	9.15	11.95	12.20	7.63	1.39
7	6	27	200	0.48	2.16	63.48	28.73	1.80	1.37
8	9	63	100	1.44	10.09	40.88	14.63	8.41	1.45
9	1	4	40	0.40	1.60	71.37	79.83	1.33	1.37
10	2	32	50	0.64	10.25	17.92	13.07	8.54	1.60
11	3	24	18	2.67	21.35	35.78	21.95	17.80	1.51
12	1	11	56	0.29	3.15	26.04	27.22	2.62	1.44
13	3	27	100	0.48	4.32	31.82	19.39	3.60	1.41
14	5	40	50	1.60	12.81	35.78	17.02	10.68	1.45
15	3	15	50	0.96	4.81	57.16	36.20	4.00	1.57
16	6	55	100	0.96	8.81	31.24	13.47	7.34	1.35
17	2	19	42	0.76	7.25	30.15	22.43	6.04	1.49
18	2	36	100	0.32	5.77	15.93	11.58	4.80	1.52
19	3	48	80	0.60	9.61	17.92	10.68	8.01	1.58
20	3	33	70	0.69	7.55	26.04	15.73	6.29	1.54

Sample number:	**RD 61**
Mineral:	Apatite
Irradiation code:	eth-368-26
Ns:	233
Ni:	1470
Area:	870
RohS:	4.3
RohI:	27.1
Pooled Age:	43.0 ± 6.8
Mean Age:	46.8 ± 9.6
Central Age:	43.0 ± 6.8
Chi-sq.:	23.11
P(%)	23.24
Dispersion:	0.05
RohD:	13.09
Nd:	4631
U standard	CN 5
Zeta $\pm 1\sigma$	416 ± 13
counted by	EW

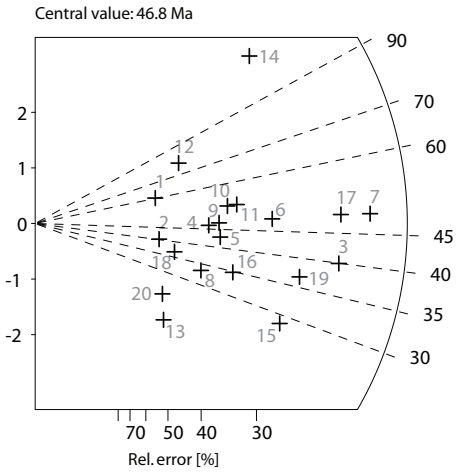

Crystal	Ns	Ni	Area	RhoS (e5)	RhoI (e5)	Age (Ma)	+- 1s	U (ppm)
1	4	18	30	2.14	9.61	60.22	33.35	8.44
2	4	27	9	7.12	48.05	40.21	21.59	42.22
3	24	163	54	7.12	48.34	39.96	8.85	42.48
4	8	47	30	4.27	25.09	46.17	17.73	22.05
5	9	57	24	6.01	38.04	42.84	15.44	33.42
6	15	85	35	6.86	38.89	47.86	13.51	34.18
7	30	168	48	10.01	56.05	48.43	9.74	49.25
8	7	57	56	2.00	16.30	33.35	13.41	14.32
9	9	52	50	2.88	16.66	46.95	17.03	14.64
10	10	52	50	3.20	16.66	52.14	18.09	14.64
11	11	57	40	4.40	22.82	52.33	17.33	20.05
12	6	21	24	4.00	14.01	77.32	35.89	12.31
13	4	57	40	1.60	22.82	19.08	9.89	20.05
14	15	34	36	6.67	15.13	119.00	37.11	13.29
15	15	142	100	2.40	22.74	28.69	7.85	19.98
16	10	78	40	4.00	31.23	34.81	11.75	27.44
17	25	140	50	8.01	44.84	48.43	10.65	39.40
18	5	37	24	3.34	24.69	36.69	17.53	21.69
19	18	133	50	5.77	42.60	36.74	9.31	37.43
20	4	45	80	0.80	9.01	24.15	12.63	7.92

Sample number:	**RD 63**
Mineral:	Apatite
Irradiation code:	eth-368-28
Ns:	111
Ni:	3114
Area:	1115
RohS:	1.6
RohI:	44.7
Pooled Age:	9.5 ± 2.0
Mean Age:	10.7 ± 2.0
Central Age:	9.5 ± 2.0
Chi-sq.:	13.70
P(%)	84.56
Dispersion:	0.00
RohD:	12.87
Nd:	4631
U standard	CN 5
Zeta ±1σ	416 ± 13
counted by	EW

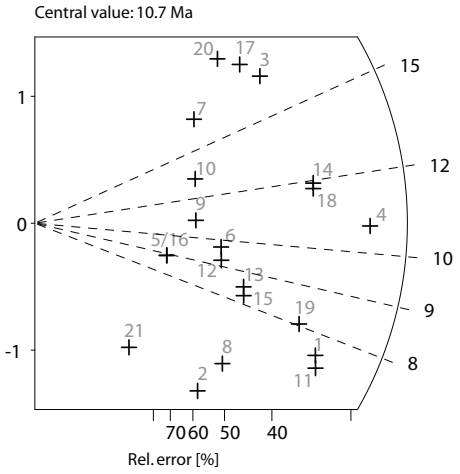

Crystal	Ns	Ni	Area	RhoS (e5)	RhoI (e5)	Age (Ma)	+- 1s	U (ppm)
1	9	320	100	1.44	51.25	7.52	2.56	45.81
2	3	162	80	0.60	32.43	4.95	2.89	28.99
3	6	92	48	2.00	30.70	17.43	7.37	27.44
4	13	327	70	2.97	74.82	10.63	3.03	66.87
5	2	60	25	1.28	38.44	8.92	6.42	34.35
6	4	110	50	1.28	35.23	9.73	4.96	31.49
7	3	46	15	3.20	49.11	17.43	10.40	43.90
8	4	175	18	3.56	155.71	6.11	3.10	139.17
9	3	74	56	0.86	21.16	10.84	6.40	18.92
10	3	61	36	1.34	27.14	13.15	7.79	24.25
11	9	331	70	2.06	75.73	7.27	2.47	67.69
12	4	116	42	1.53	44.23	9.22	4.70	39.53
13	5	157	100	0.80	25.14	8.52	3.88	22.47
14	9	202	30	4.81	107.84	11.91	4.08	96.38
15	5	162	35	2.29	74.13	8.26	3.76	66.25
16	2	60	50	0.64	19.22	8.92	6.42	17.18
17	5	70	50	1.60	22.42	19.09	8.86	20.04
18	9	205	70	2.06	46.90	11.74	4.02	41.92
19	8	266	50	2.56	85.20	8.04	2.90	76.15
20	4	51	70	0.92	11.67	20.96	10.91	10.43
21	1	67	50	0.32	21.46	3.99	4.03	19.18

Sample number:	**RD 64**
Mineral:	Apatite
Irradiation code:	eth-357-15
Ns:	79
Ni:	770
Area:	572
RohS:	2.2
RohI:	21.6
Pooled Age:	29.1 ± 7.2
Mean Age:	32.1 ± 7.0
Central Age:	29.1 ± 7.2
Chi-sq.:	13.16
P(%)	83.04
Dispersion:	0.00
RohD:	13.66
Nd:	5073
U standard	CN 5
Zeta ±1σ	416 ± 13
counted by	EW

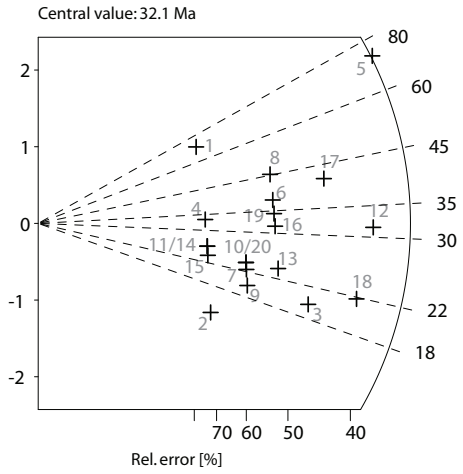

Crystal	Ns	Ni	Area	RhoS (e5)	RhoI (e5)	Age (Ma)	+- 1s	U (ppm)
1	2	8	18	1.78	7.12	70.62	55.88	5.99
2	2	41	35	0.92	18.76	13.84	10.03	15.80
3	5	72	21	3.81	54.91	19.69	9.13	46.25
4	2	17	20	1.60	13.61	33.33	24.94	11.47
5	9	35	40	3.60	14.01	72.63	27.26	11.80
6	4	30	24	2.67	20.02	37.76	20.14	16.86
7	3	38	30	1.60	20.29	22.38	13.45	17.09
8	4	25	24	2.67	16.68	45.29	24.44	14.05
9	3	43	25	1.92	27.55	19.79	11.83	23.20
10	3	36	30	1.60	19.22	23.63	14.22	16.19
11	2	22	16	2.00	22.02	25.77	19.05	18.55
12	8	72	40	3.20	28.83	31.48	11.78	24.28
13	4	48	42	1.53	18.30	23.63	12.32	15.42
14	2	22	19	1.69	18.54	25.77	19.05	15.62
15	2	24	36	0.89	10.68	23.63	17.41	8.99
16	4	36	32	2.00	18.02	31.48	16.63	15.17
17	6	41	32	3.00	20.52	41.43	18.17	17.28
18	7	91	40	2.80	36.44	21.81	8.59	30.69
19	4	33	18	3.56	29.36	34.34	18.22	24.73
20	3	36	30	1.60	19.22	23.63	14.22	16.19

Sample number:	**RD 68**
Mineral:	Apatite
Irradiation code:	eth-356-10
Ns:	206
Ni:	2306
Area:	946
RohS:	3.5
RohI:	39.0
Pooled Age:	23.7 ± 3.8
Mean Age:	26.1 ± 5.2
Central Age:	24.6 ± 5.0
Chi-sq.:	36.50
P(%)	0.92
Dispersion:	0.28
RohD:	12.77
Nd:	7878
U standard	CN 5
Zeta ±1σ	416 ± 13
counted by	EW

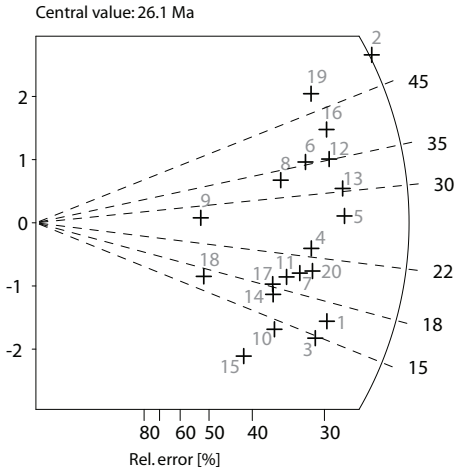

Crystal	Ns	Ni	Area	RhoS (e5)	RhoI (e5)	Age (Ma)	+- 1s	U (ppm)
1	12	194	100	1.92	31.07	16.41	4.91	27.97
2	18	92	42	6.86	35.08	51.78	13.46	31.58
3	11	197	80	2.20	39.44	14.82	4.62	35.51
4	11	127	40	4.40	50.85	22.97	7.26	45.78
5	14	138	50	4.48	44.20	26.90	7.60	39.80
6	11	82	30	5.87	43.78	35.55	11.47	39.41
7	10	132	50	3.20	42.28	20.10	6.63	38.06
8	9	72	30	4.81	38.44	33.13	11.76	34.60
9	4	39	36	1.78	17.35	27.19	14.31	15.62
10	8	150	42	3.05	57.20	14.16	5.16	51.49
11	9	123	70	2.06	28.14	19.41	6.73	25.34
12	13	98	24	8.68	65.40	35.15	10.44	58.88
13	14	122	52	4.31	37.58	30.42	8.64	33.83
14	8	123	32	4.00	61.56	17.26	6.32	55.42
15	6	147	50	1.92	47.09	10.84	4.53	42.39
16	13	85	42	4.96	32.41	40.51	12.14	29.18
17	8	116	50	2.56	37.16	18.30	6.72	33.45
18	4	63	42	1.53	24.02	16.85	8.71	21.63
19	12	64	24	8.01	42.71	49.63	15.70	38.45
20	11	142	60	2.94	37.90	20.55	6.47	34.12

Sample number:	**RD 70**
Mineral:	Apatite
Irradiation code:	eth-356-11
Ns:	154
Ni:	1448
Area:	1039
RohS:	2.4
RohI:	22.3
Pooled Age:	28.3 ± 5.2
Mean Age:	30.7 ± 4.4
Central Age:	28.3 ± 5.2
Chi-sq.:	12.75
P(%)	85.12
Dispersion:	0.01
RohD:	12.82
Nd:	7878
U standard	CN 5
Zeta $\pm 1\sigma$	416 ± 13
counted by	EW

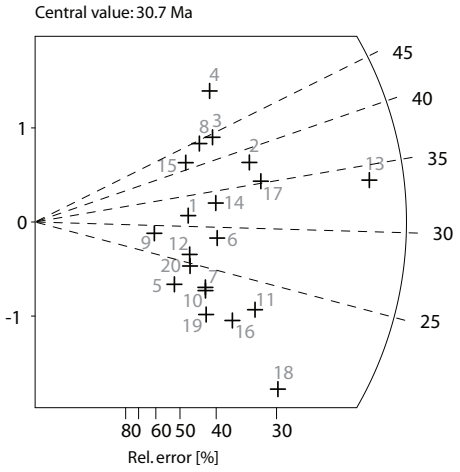

Crystal	Ns	Ni	Area	RhoS (e5)	RhoI (e5)	Age (Ma)	+- 1s	U (ppm)
1	5	42	50	1.602	13.453	31.68	15.02	12.06
2	10	70	64	2.502	17.517	37.99	12.91	15.71
3	7	42	32	3.503	21.02	44.3	18.15	18.85
4	7	34	30	3.737	18.151	54.68	22.77	16.28
5	4	49	50	1.281	15.695	21.74	11.33	14.08
6	7	65	40	2.803	26.025	28.66	11.44	23.34
7	6	70	48	2.002	23.356	22.82	9.74	20.95
8	6	36	30	3.203	19.218	44.3	19.59	17.24
9	3	28	20	2.402	22.422	28.52	17.35	20.11
10	6	71	36	2.669	31.586	22.5	9.6	28.33
11	10	118	50	3.203	37.796	22.57	7.47	33.9
12	5	51	49	1.634	16.669	26.1	12.26	14.95
13	24	189	100	3.844	30.269	33.78	7.41	27.15
14	7	56	50	2.242	17.937	33.26	13.38	16.09
15	5	32	40	2.002	12.812	41.54	20.03	11.49
16	8	102	70	1.83	23.337	20.89	7.7	20.93
17	11	83	60	2.936	22.155	35.25	11.37	19.87
18	12	177	100	1.922	28.347	18.06	5.42	25.42
19	6	79	60	1.602	21.087	20.23	8.59	18.91
20	5	54	60	1.335	14.414	24.65	11.55	12.93

Sample number:	**RD 72**
Mineral:	Apatite
Irradiation code:	eth-356-15
Ns:	88
Ni:	856
Area:	871
RohS:	1.6
RohI:	15.7
Pooled Age:	22.2 ± 5.2
Mean Age:	27.3 ± 6.8
Central Age:	22.2 ± 5.2
Chi-sq.:	19.52
P(%)	42.39
Dispersion:	0.02
RohD:	10.39
Nd:	4019
U standard	CN 5
Zeta $\pm 1\sigma$	416 ± 13
counted by	EW

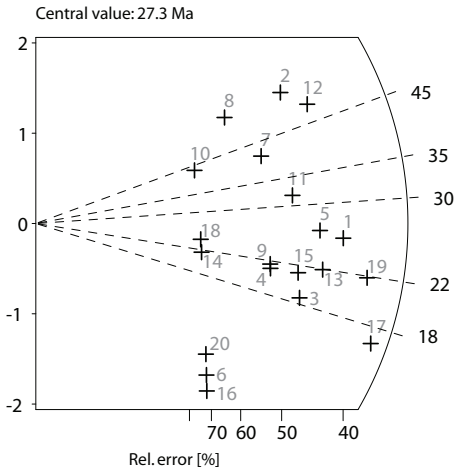

Crystal	Ns	Ni	Area	RhoS (e5)	RhoI (e5)	Age (Ma)	+- 1s	U (ppm)
1	7	59	50	2.24	18.90	25.60	10.27	20.91
2	5	19	36	2.22	8.45	56.64	28.54	9.35
3	5	58	60	1.34	15.48	18.61	8.70	17.13
4	4	41	13	4.93	50.51	21.06	11.05	55.89
5	6	49	40	2.40	19.62	26.42	11.46	21.71
6	2	53	100	0.32	8.49	8.15	5.88	9.39
7	4	21	28	2.29	12.01	41.05	22.44	13.29
8	3	11	24	2.00	7.34	58.69	38.28	8.12
9	4	40	30	2.14	21.35	21.58	11.34	23.63
10	2	10	30	1.07	5.34	43.09	33.41	5.91
11	5	34	30	2.67	18.15	31.71	15.23	20.08
12	6	26	40	2.40	10.41	49.70	22.58	11.52
13	6	59	60	1.60	15.75	21.95	9.44	17.43
14	2	20	20	1.60	16.02	21.58	16.02	17.72
15	5	51	28	2.86	29.17	21.16	9.94	32.28
16	2	60	50	0.64	19.22	7.20	5.18	21.27
17	8	103	100	1.28	16.50	16.77	6.18	18.25
18	2	18	24	1.34	12.01	23.98	17.89	13.29
19	8	79	60	2.14	21.09	21.86	8.14	23.33
20	2	45	48	0.67	15.01	9.60	6.95	16.61

Sample number:	**RD 75**
Mineral:	Apatite
Irradiation code:	eth-368-31
Ns:	58
Ni:	829
Area:	990
RohS:	0.9
RohI:	13.4
Pooled Age:	18.2 ± 5.2
Mean Age:	24.9 ± 6.4
Central Age:	18.4 ± 5.2
Chi-sq.:	17.59
P(%)	48.31
Dispersion:	0.11
RohD:	12.54
Nd:	4631
U standard	CN 5
Zeta ±1σ	416 ± 13
counted by	EW

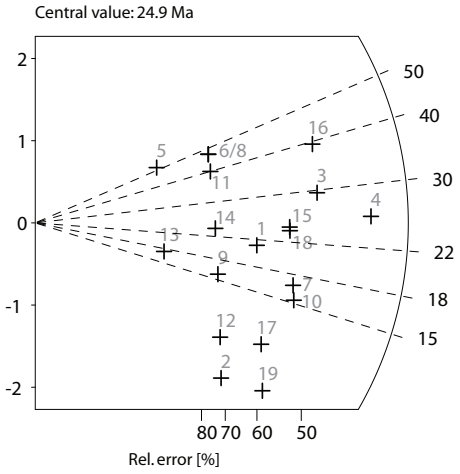

Crystal	Ns	Ni	Area	RhoS (e5)	RhoI (e5)	Age (Ma)	+- 1s	U (ppm)
1	3	37	24	2.00	24.69	21.11	12.69	22.65
2	2	81	80	0.40	16.22	6.43	4.61	14.88
3	5	44	45	1.78	15.66	29.56	13.99	14.37
4	7	71	100	1.12	11.37	25.66	10.20	10.43
5	1	5	18	0.89	4.45	51.94	56.92	4.08
6	2	11	45	0.71	3.92	47.23	36.34	3.59
7	4	62	60	1.07	16.55	16.80	8.69	15.18
8	2	11	40	0.80	4.40	47.23	36.34	4.04
9	2	33	40	0.80	13.21	15.78	11.51	12.12
10	4	68	60	1.07	18.15	15.32	7.90	16.65
11	2	13	15	2.14	13.88	39.99	30.41	12.73
12	2	57	40	0.80	22.82	9.14	6.58	20.94
13	1	15	24	0.67	10.01	17.36	17.94	9.18
14	2	22	40	0.80	8.81	23.66	17.49	8.08
15	4	43	100	0.64	6.89	24.21	12.68	6.32
16	5	33	35	2.29	15.10	39.38	18.95	13.85
17	3	75	100	0.48	12.01	10.42	6.15	11.02
18	4	44	54	1.19	13.05	23.66	12.38	11.97
19	3	104	70	0.69	23.79	7.52	4.41	21.83

Sample number:	**RD 78**
Mineral:	Apatite
Irradiation code:	eth-356-17
Ns:	94
Ni:	642
Area:	729
RohS:	2.1
RohI:	14.1
Pooled Age:	32.0 ± 7.4
Mean Age:	34.2 ± 9.4
Central Age:	32.0 ± 7.6
Chi-sq.:	20.32
P(%)	37.55
Dispersion:	0.08
RohD:	10.52
Nd:	4019
U standard	CN 5
Zeta ±1σ	416 ± 13
counted by	EW

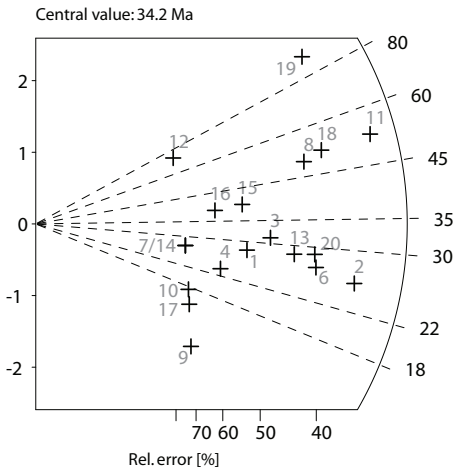

Crystal	Ns	Ni	Area	RhoS (e5)	RhoI (e5)	Age (Ma)	+- 1s	U (ppm)
1	4	31	20	3.20	24.82	28.17	15.00	27.14
2	9	77	54	2.67	22.84	25.52	9.03	24.97
3	5	35	60	1.34	9.34	31.18	14.95	10.22
4	3	28	35	1.37	12.81	23.40	14.24	14.01
5	0	10	35	0.00	4.58	0.00	0.01	5.00
6	7	57	40	2.80	22.82	26.81	10.78	24.96
7	2	16	16	2.00	16.02	27.29	20.49	17.51
8	7	31	36	3.11	13.79	49.21	20.66	15.08
9	2	44	42	0.76	16.78	9.94	7.19	18.35
10	2	25	54	0.59	7.42	17.48	12.86	8.11
11	11	46	27	6.53	27.29	52.10	17.58	29.84
12	2	6	15	2.14	6.41	72.51	59.26	7.00
13	6	46	42	2.29	17.54	28.47	12.40	19.18
14	2	16	30	1.07	8.54	27.29	20.49	9.34
15	4	22	60	1.07	5.87	39.65	21.60	6.42
16	3	17	25	1.92	10.89	38.49	24.14	11.91
17	2	29	28	1.14	16.59	15.07	11.03	18.14
18	8	34	40	3.20	13.61	51.27	20.23	14.89
19	8	19	30	4.27	10.14	91.46	38.68	11.09
20	7	53	40	2.80	21.22	28.83	11.64	23.20

Sample number:	**RD 80**
Mineral:	Apatite
Irradiation code:	eth-356-19
Ns:	23
Ni:	154
Area:	796
RohS:	0.5
RohI:	3.1
Pooled Age:	33.0 ± 15.0
Mean Age:	53.8 ± 25.4
Central Age:	33.1 ± 15.2
Chi-sq.:	19.21
P(%)	44.35
Dispersion:	0.12
RohD:	10.64
Nd:	4019
U standard	CN 5
Zeta $\pm 1\sigma$	416 ± 13
counted by	EW

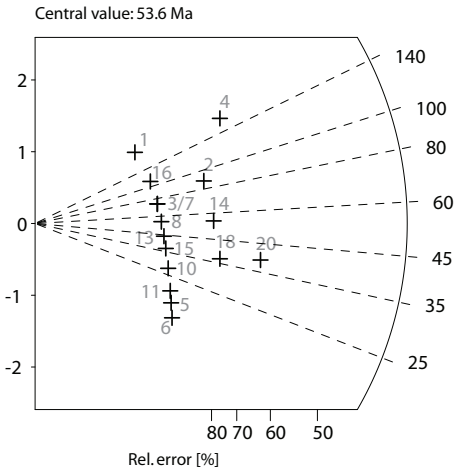

Crystal	Ns	Ni	Area	RhoS (e5)	RhoI (e5)	Age (Ma)	+- 1s	U (ppm)
1	1	1	20	0.80	0.80	217.63	307.87	0.87
2	2	5	55	0.58	1.46	87.94	73.64	1.57
3	1	3	24	0.67	2.00	73.36	84.75	2.16
4	3	4	21	2.29	3.05	163.91	125.32	3.30
5	1	13	50	0.32	4.16	17.00	17.66	4.50
6	1	16	50	0.32	5.13	13.82	14.25	5.54
7	1	3	28	0.57	1.72	73.36	84.75	1.85
8	1	4	32	0.50	2.00	55.10	61.63	2.16
9	0	20	100	0.00	3.20	0.00	0.00	3.46
10	1	8	27	0.59	4.75	27.61	29.30	5.13
11	1	11	16	1.00	11.01	20.09	21.00	11.90
12	0	3	50	0.00	0.96	0.00	0.02	1.04
13	1	5	30	0.53	2.67	44.12	48.35	2.88
14	2	8	40	0.80	3.20	55.10	43.60	3.46
15	1	6	40	0.40	2.40	36.79	39.75	2.60
16	1	2	30	0.53	1.07	109.73	134.45	1.15
17	0	9	40	0.00	3.60	0.00	0.01	3.89
18	2	12	49	0.65	3.92	36.79	28.13	4.24
19	0	4	30	0.00	2.14	0.00	0.02	2.31
20	3	17	64	0.75	4.25	38.94	24.43	4.60

Sample number:	**RD 81**
Mineral:	Apatite
Irradiation code:	eth-356-23
Ns:	30
Ni:	340
Area:	885
RohS:	0.5
RohI:	6.2
Pooled Age:	19.9 ± 7.8
Mean Age:	20.6 ± 6.4
Central Age:	19.9 ± 7.8
Chi-sq.:	8.49
P(%)	98.10
Dispersion:	0.00
RohD:	10.86
Nd:	4019
U standard	CN 5
Zeta ±1σ	416 ± 13
counted by	EW

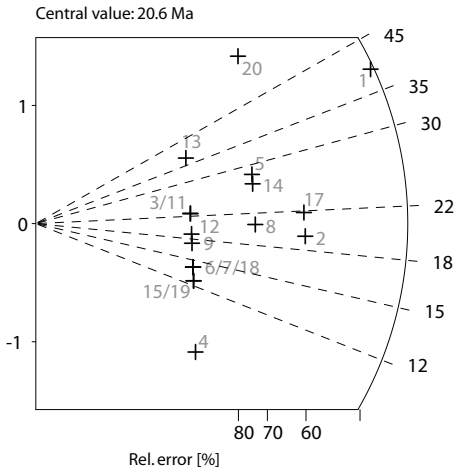

Crystal	Ns	Ni	Area	RhoS (e5)	RhoI (e5)	Age (Ma)	+- 1s	U (ppm)
1	5	29	70	1.14	6.64	38.82	18.85	7.03
2	3	35	80	0.60	7.01	19.33	11.65	7.42
3	1	10	18	0.89	8.90	22.55	23.66	9.42
4	1	33	32	0.50	16.52	6.84	6.95	17.49
5	2	16	30	1.07	8.54	28.17	21.15	9.05
6	1	16	100	0.16	2.56	14.10	14.54	2.71
7	1	16	27	0.59	9.49	14.10	14.54	10.05
8	2	22	52	0.62	6.78	20.50	15.16	7.18
9	1	13	49	0.33	4.25	17.35	18.02	4.50
10	0	12	30	0.00	6.41	0.00	0.01	6.78
11	1	10	28	0.57	5.72	22.55	23.66	6.06
12	1	12	30	0.53	6.41	18.79	19.57	6.78
13	1	6	20	0.80	4.81	37.53	40.56	5.09
14	2	17	25	1.28	10.89	26.52	19.84	11.53
15	1	18	90	0.18	3.20	12.54	12.89	3.39
16	0	3	28	0.00	1.72	0.00	0.02	1.82
17	3	31	40	1.20	12.41	21.82	13.22	13.15
18	1	16	20	0.80	12.81	14.10	14.54	13.57
19	1	18	16	1.00	18.02	12.54	12.89	19.08
20	2	7	100	0.32	1.12	64.21	51.53	1.19

Sample number:	**RD 82**
Mineral:	Apatite
Irradiation code:	eth-356-24
Ns:	58
Ni:	559
Area:	1062
RohS:	0.9
RohI:	8.4
Pooled Age:	23.6 ± 6.8
Mean Age:	28.8 ± 7.8
Central Age:	23.6 ± 6.8
Chi-sq.:	9.10
P(%)	97.19
Dispersion:	0.00
RohD:	10.95
Nd:	4019
U standard	CN 5
Zeta ±1σ	416 ± 13
counted by	EW

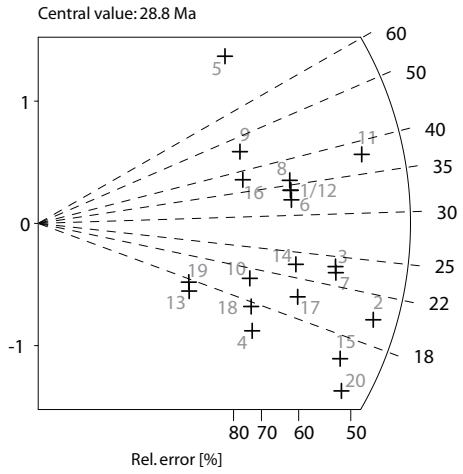

Crystal	Ns	Ni	Area	RhoS (e5)	RhoI (e5)	Age (Ma)	+- 1s	U (ppm)
1	3	20	70	0.69	4.58	34.08	21.13	4.81
2	5	57	100	0.80	9.13	19.95	9.33	9.59
3	4	38	49	1.31	12.42	23.93	12.61	13.04
4	2	30	80	0.40	6.01	15.17	11.09	6.31
5	2	5	24	1.34	3.34	90.48	75.77	3.50
6	3	21	40	1.20	8.41	32.46	20.07	8.83
7	4	39	27	2.37	23.13	23.32	12.27	24.29
8	3	19	36	1.34	8.45	35.87	22.32	8.88
9	2	10	40	0.80	4.00	45.40	35.20	4.20
10	2	22	18	1.78	19.57	20.68	15.29	20.56
11	5	30	50	1.60	9.61	37.86	18.33	10.09
12	3	20	36	1.34	8.90	34.08	21.13	9.34
13	1	14	60	0.27	3.74	16.25	16.83	3.92
14	3	29	60	0.80	7.74	23.52	14.29	8.13
15	4	56	100	0.64	8.97	16.25	8.43	9.42
16	2	12	40	0.80	4.81	37.86	28.94	5.05
17	3	34	30	1.60	18.15	20.07	12.11	19.06
18	2	26	100	0.32	4.16	17.50	12.86	4.37
19	1	13	32	0.50	6.51	17.50	18.17	6.83
20	4	64	70	0.92	14.64	14.22	7.35	15.38

Sample number:	**RD 85**
Mineral:	Apatite
Irradiation code:	eth-368-35
Ns:	48
Ni:	406
Area:	749
RohS:	1.0
RohI:	8.7
Pooled Age:	29.6 ± 9.2
Mean Age:	38.5 ± 12.0
Central Age:	29.6 ± 9.2
Chi-sq.:	14.25
P(%)	76.89
Dispersion:	0.00
RohD:	12.06
Nd:	4631
U standard	CN 5
Zeta $\pm 1\sigma$	416 ± 13
counted by	EW

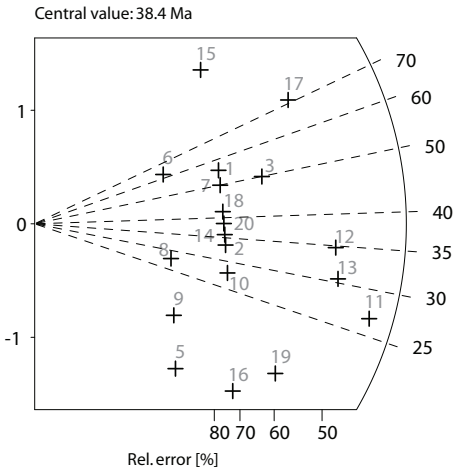

Crystal	Ns	Ni	Area	RhoS (e5)	RhoI (e5)	Age (Ma)	+- 1s	U (ppm)
1	2	9	24	1.34	6.01	55.50	43.43	5.73
2	2	15	15	2.14	16.02	33.36	25.14	15.27
3	3	15	26	1.85	9.24	49.97	31.65	8.81
4	0	16	49	0.00	5.23	0.00	0.00	4.99
5	1	24	30	0.53	12.81	10.44	10.66	12.22
6	1	4	45	0.36	1.42	62.41	69.81	1.36
7	2	10	40	0.80	4.00	49.97	38.75	3.82
8	1	9	20	0.80	7.21	27.81	29.33	6.87
9	1	15	36	0.45	6.67	16.70	17.26	6.36
10	2	18	30	1.07	9.61	27.81	20.75	9.16
11	6	56	49	1.96	18.30	26.82	11.56	17.45
12	5	36	40	2.00	14.41	34.74	16.63	13.75
13	5	41	80	1.00	8.21	30.52	14.49	7.83
14	2	14	40	0.80	5.61	35.73	27.04	5.35
15	2	4	23	1.39	2.79	124.22	107.66	2.66
16	2	38	60	0.53	10.14	13.19	9.58	9.67
17	4	14	48	1.34	4.67	71.27	40.48	4.45
18	2	12	25	1.28	7.69	41.67	31.86	7.33
19	3	43	50	0.96	13.77	17.48	10.45	13.13
20	2	13	19	1.69	10.96	38.48	29.25	10.45

Sample number:	**RD 87**
Mineral:	Apatite
Irradiation code:	eth-368-39
Ns:	96
Ni:	798
Area:	614
RohS:	2.5
RohI:	20.8
Pooled Age:	29.1 ± 6.6
Mean Age:	31.8 ± 5.6
Central Age:	29.1 ± 6.6
Chi-sq.:	8.53
P(%)	98.05
Dispersion:	0.00
RohD:	11.65
Nd:	4631
U standard	CN 5
Zeta $\pm 1\sigma$	416 ± 13
counted by	EW

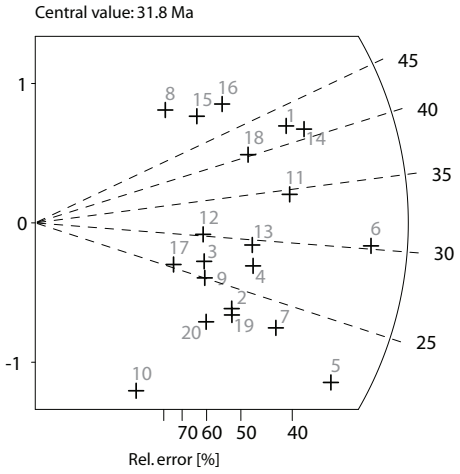

Crystal	Ns	Ni	Area	RhoS (e5)	RhoI (e5)	Age (Ma)	+- 1s	U (ppm)
1	7	40	24	4.671	26.692	42.27	17.38	26.35
2	4	42	28	2.288	24.023	23.04	12.08	23.71
3	3	27	16	3.003	27.026	26.87	16.38	26.68
4	5	44	28	2.86	25.167	27.48	13	24.84
5	9	102	70	2.059	23.337	21.35	7.46	23.04
6	12	96	60	3.203	25.625	30.22	9.31	25.3
7	6	63	45	2.135	22.422	23.04	9.87	22.13
8	2	8	13	2.464	9.856	60.3	47.72	9.73
9	3	29	20	2.402	23.222	25.02	15.2	22.92
10	1	26	18	0.89	23.133	9.31	9.5	22.84
11	7	49	48	2.336	16.349	34.52	14	16.14
12	3	24	18	2.669	21.354	30.22	18.53	21.08
13	5	41	25	3.203	26.265	29.48	14	25.93
14	8	47	40	3.203	18.818	41.12	15.79	18.58
15	3	14	21	2.288	10.677	51.72	32.95	10.54
16	4	19	28	2.288	10.868	50.81	28.01	10.73
17	2	19	28	1.144	10.868	25.46	18.95	10.73
18	5	30	30	2.669	16.015	40.26	19.5	15.81
19	4	43	30	2.135	22.955	22.5	11.79	22.66
20	3	35	24	2.002	23.356	20.74	12.5	23.06

Sample number:	**RD 88**
Mineral:	Apatite
Irradiation code:	eth-368-41
Ns:	150
Ni:	3143
Area:	926
RohS:	2.6
RohI:	54.4
Pooled Age:	11.3 ± 2.0
Mean Age:	13.4 ± 3.0
Central Age:	11.3 ± 2.0
Chi-sq.:	16.77
P(%)	60.57
Dispersion:	0.01
RohD:	11.43
Nd:	4631
U standard	CN 5
Zeta $\pm 1\sigma$	416 ± 13
counted by	EW

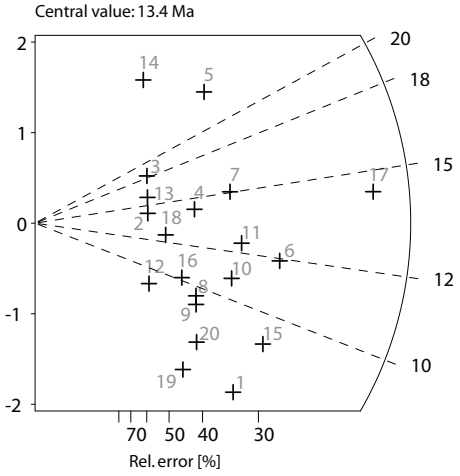

Crystal	Ns	Ni	Area	RhoS (e5)	RhoI (e5)	Age (Ma)	+- 1s	U (ppm)
1	9	301	80	1.80	60.26	7.10	2.42	60.64
2	3	50	40	1.20	20.02	14.25	8.48	20.15
3	3	39	40	1.20	15.62	18.26	10.96	15.71
4	6	100	40	2.40	40.04	14.25	6.01	40.29
5	7	70	20	5.61	56.05	23.73	9.44	56.41
6	14	279	70	3.20	63.83	11.92	3.29	64.23
7	9	142	56	2.57	40.61	15.05	5.20	40.87
8	6	149	40	2.40	59.66	9.57	4.00	60.03
9	6	155	35	2.75	70.93	9.20	3.84	71.37
10	9	197	50	2.88	63.10	10.85	3.72	63.50
11	10	191	50	3.20	61.18	12.43	4.06	61.56
12	3	79	30	1.60	42.17	9.02	5.32	42.44
13	3	45	12	4.00	60.06	15.83	9.45	60.44
14	3	20	50	0.96	6.41	35.56	22.05	6.45
15	12	316	70	2.75	72.30	9.02	2.67	72.75
16	5	117	42	1.91	44.61	10.15	4.65	44.89
17	27	448	100	4.32	71.75	14.31	2.88	72.20
18	4	76	30	2.14	40.57	12.50	6.43	40.83
19	5	185	36	2.22	82.30	6.42	2.92	82.82
20	6	184	35	2.75	84.20	7.75	3.22	84.72

Sample number:	**RD 91**
Mineral:	Apatite
Irradiation code:	eth-356-26
Ns:	38
Ni:	937
Area:	790
RohS:	0.8
RohI:	19.0
Pooled Age:	9.3 ± 3.2
Mean Age:	8.8 ± 3.0
Central Age:	9.3 ± 3.2
Chi-sq.:	11.27
P(%)	91.46
Dispersion:	0.00
RohD:	11.08
Nd:	4019
U standard	CN 5
Zeta $\pm 1\sigma$	416 ± 13
counted by	EW

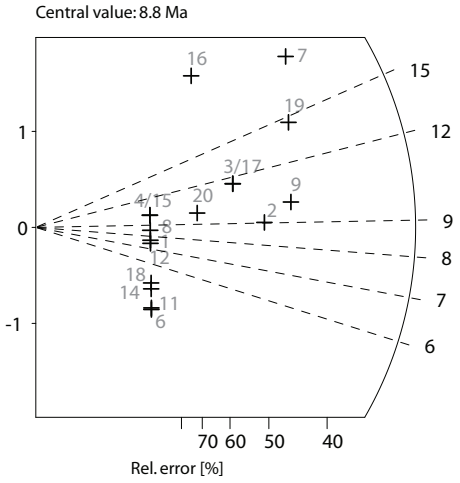

Crystal	Ns	Ni	Area	RhoS (e5)	RhoI (e5)	Age (Ma)	+- 1s	U (ppm)
1	1	30	48	0.33	10.01	7.67	7.81	10.39
2	4	102	49	1.31	33.34	9.03	4.61	34.62
3	3	60	32	1.50	30.03	11.51	6.82	31.18
4	1	23	24	0.67	15.35	10.01	10.23	15.94
5	0	12	21	0.00	9.15	0.00	0.01	9.50
6	1	62	24	0.67	41.37	3.71	3.75	42.96
7	5	57	32	2.50	28.53	20.18	9.44	29.62
8	1	27	45	0.36	9.61	8.53	8.69	9.98
9	5	116	70	1.14	26.54	9.92	4.55	27.56
10	0	31	80	0.00	6.21	0.00	0.00	6.44
11	1	61	27	0.59	36.18	3.78	3.81	37.57
12	1	31	21	0.76	23.64	7.43	7.55	24.55
13	0	3	28	0.00	1.72	0.00	0.02	1.78
14	1	50	47	0.34	17.04	4.61	4.65	17.69
15	1	23	28	0.57	13.16	10.01	10.23	13.66
16	2	16	30	1.07	8.54	28.73	21.57	8.87
17	3	60	48	1.00	20.02	11.51	6.82	20.79
18	1	47	35	0.46	21.51	4.90	4.95	22.33
19	5	79	45	1.78	28.12	14.56	6.74	29.19
20	2	47	56	0.57	13.44	9.80	7.08	13.96

Sample number:	**RD 92**
Mineral:	Apatite
Irradiation code:	eth-357-3
Ns:	62
Ni:	2737
Area:	910
RohS:	1.1
RohI:	48.2
Pooled Age:	6.3 ± 1.6
Mean Age:	6.8 ± 1.8
Central Age:	6.3 ± 1.6
Chi-sq.:	15.23
P(%)	70.79
Dispersion:	0.00
RohD:	13.40
Nd:	5073
U standard	CN 5
Zeta ±1σ	416 ± 13
counted by	EW

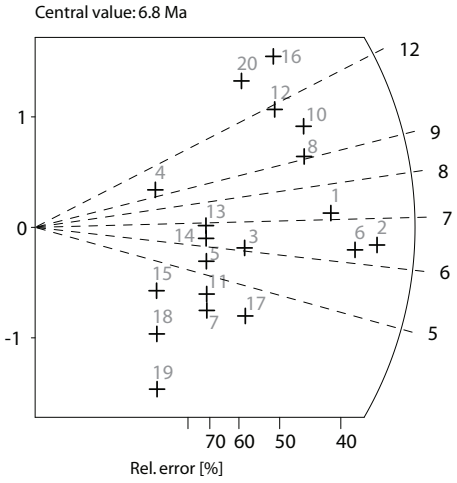

Crystal	Ns	Ni	Area	RhoS (e5)	RhoI (e5)	Age (Ma)	+- 1s	U (ppm)
1	6	233	70	1.37	53.31	7.17	2.98	45.74
2	8	347	70	1.83	79.39	6.42	2.31	68.12
3	3	137	27	1.78	81.26	6.10	3.57	69.73
4	1	29	20	0.80	23.22	9.61	9.78	19.93
5	2	102	48	0.67	34.03	5.46	3.91	29.20
6	7	310	40	2.80	124.12	6.29	2.41	106.51
7	2	140	50	0.64	44.84	3.98	2.84	38.48
8	5	153	27	2.97	90.75	9.10	4.15	77.88
9	0	76	28	0.00	43.47	0.00	0.00	37.30
10	5	135	30	2.67	72.07	10.32	4.71	61.84
11	2	126	50	0.64	40.36	4.42	3.16	34.63
12	4	95	70	0.92	21.74	11.73	6.00	18.65
13	2	81	60	0.53	21.62	6.88	4.93	18.55
14	2	88	30	1.07	46.98	6.33	4.53	40.31
15	1	73	32	0.50	36.54	3.82	3.85	31.35
16	4	74	40	1.60	29.63	15.05	7.74	25.42
17	3	196	60	0.80	52.32	4.27	2.49	44.89
18	1	108	30	0.53	57.66	2.58	2.59	49.47
19	1	178	100	0.16	28.51	1.57	1.57	24.46
20	3	56	28	1.72	32.03	14.92	8.85	27.49

Sample number:	**RD 94**
Mineral:	Apatite
Irradiation code:	eth-357-8
Ns:	149
Ni:	1603
Area:	925
RohS:	2.58
RohI:	27.76
Pooled Age:	26.1 ± 4.8
Mean Age:	27.5 ± 5.2
Central Age:	26.1 ± 4.8
Chi-sq.:	15.12
P(%)	71.52
Dispersion:	0.00
RohD:	13.51
Nd:	5073
U standard	CN 5
Zeta $\pm 1\sigma$	416 ± 13
counted by	EW

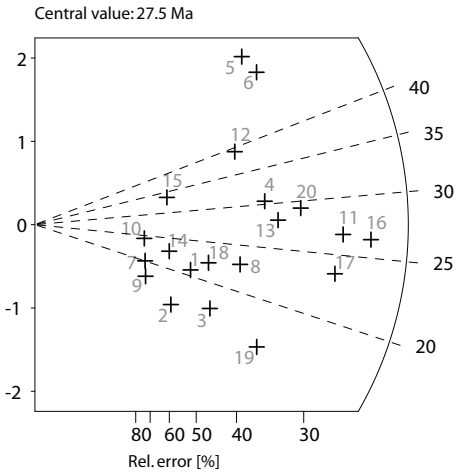

Crystal	Ns	Ni	Area	RhoS (e5)	RhoI (e5)	Age (Ma)	+- 1s	U (ppm)
1	4	54	32	2.00	27.03	20.78	10.79	23.01
2	3	54	24	2.00	36.04	15.59	9.26	30.68
3	5	81	70	1.14	18.53	17.32	8.00	15.78
4	9	83	50	2.88	26.59	30.39	10.72	22.64
5	8	37	28	4.58	21.16	60.46	23.67	18.02
6	9	47	32	4.50	23.52	53.58	19.58	20.03
7	2	28	24	1.34	18.69	20.04	14.68	15.91
8	7	86	42	2.67	32.79	22.83	9.01	27.92
9	2	32	36	0.89	14.24	17.54	12.80	12.12
10	2	23	24	1.34	15.35	24.39	18.00	13.07
11	16	168	100	2.56	26.91	26.70	7.05	22.91
12	7	50	60	1.87	13.35	39.22	15.88	11.36
13	10	100	48	3.34	33.37	28.04	9.35	28.41
14	3	37	25	1.92	23.70	22.74	13.67	20.18
15	3	25	24	2.00	16.68	33.63	20.58	14.20
16	19	202	80	3.80	40.44	26.37	6.39	34.43
17	15	179	60	4.00	47.78	23.50	6.37	40.68
18	5	63	36	2.22	28.03	22.26	10.37	23.86
19	8	139	70	1.83	31.80	16.15	5.90	27.08
20	12	115	60	3.20	30.70	29.25	8.93	26.13

Sample number:	**MR 132**
Mineral:	Apatite
Irradiation code:	eth-319-5
Ns:	81
Ni:	517
Area:	682
RohS:	1.90
RohI:	12.14
Pooled Age:	36.1 ± 9.0
Mean Age:	38.0 ± 10.6
Central Age:	36.0 ± 9.2
Chi-sq.:	16.97
P(%)	59.22
Dispersion:	0.08
RohD:	11.11
Nd:	3794
U standard	CN 5
Zeta ±1σ	416 ± 13
counted by	EW

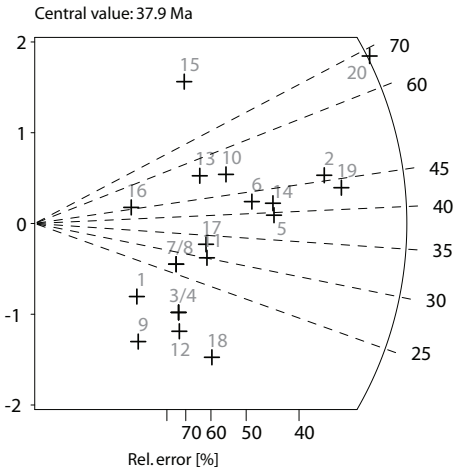

Crystal	Ns	Ni	Area	RhoS (e5)	RhoI (e5)	Age (Ma)	+- 1s	U (ppm)
1	1	14	10	1.60	22.42	16.48	17.07	23.21
2	9	45	28	5.15	25.74	46.05	16.89	26.65
3	2	25	35	0.92	11.44	18.46	13.58	11.84
4	2	25	36	0.89	11.12	18.46	13.58	11.51
5	6	35	24	4.00	23.36	39.49	17.50	24.18
6	5	27	21	3.81	20.59	42.65	20.82	21.32
7	2	17	60	0.53	4.54	27.13	20.30	4.70
8	2	17	25	1.28	10.89	27.13	20.30	11.27
9	1	23	70	0.23	5.26	10.04	10.26	5.45
10	4	18	35	1.83	8.24	51.15	28.33	8.53
11	3	23	60	0.80	6.14	30.07	18.49	6.36
12	2	29	20	1.60	23.22	15.92	11.65	24.04
13	3	13	24	2.00	8.68	53.10	34.07	8.98
14	6	33	30	3.20	17.62	41.88	18.64	18.24
15	3	6	30	1.60	3.20	114.51	81.07	3.32
16	1	5	21	0.76	3.81	46.05	50.47	3.95
17	3	21	35	1.37	9.61	32.93	20.36	9.95
18	3	44	32	1.50	22.02	15.74	9.41	22.80
19	10	53	36	4.45	23.58	43.45	15.06	24.41
20	13	44	50	4.16	14.09	67.91	21.57	14.59

Sample number:	**MR 208**
Mineral:	Apatite
Irradiation code:	eth-317-6
Ns:	138
Ni:	711
Area:	1009
RohS:	2.19
RohI:	11.29
Pooled Age:	46.3 ± 9.2
Mean Age:	50.9 ± 10.0
Central Age:	47.1 ± 10.8
Chi-sq.:	25.64
P(%)	17.79
Dispersion:	0.24
RohD:	11.52
Nd:	4075
U standard	CN 5
Zeta $\pm 1\sigma$	416 ± 13
counted by	EW

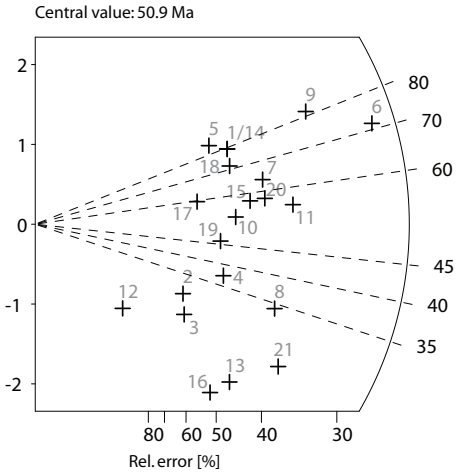

Crystal	Ns	Ni	Area	RhoS (e5)	RhoI (e5)	Age (Ma)	+- 1s	U (ppm)
1	6	18	40	2.40	7.21	79.38	37.53	7.19
2	3	24	60	0.80	6.41	29.88	18.33	6.40
3	3	28	32	1.50	14.01	25.62	15.59	13.99
4	5	32	25	3.20	20.50	37.33	18.00	20.46
5	5	14	28	2.86	8.01	85.02	44.39	7.99
6	18	60	60	4.81	16.02	71.49	19.37	15.99
7	8	30	40	3.20	12.01	63.59	25.40	11.99
8	8	56	64	2.00	14.01	34.14	12.96	13.99
9	12	35	56	3.43	10.01	81.64	27.46	9.99
10	6	27	70	1.37	6.18	53.03	24.01	6.17
11	10	43	50	3.20	13.77	55.49	19.58	13.75
12	1	14	25	0.64	8.97	17.09	17.70	8.95
13	5	59	30	2.67	31.50	20.28	9.47	31.44
14	6	18	24	4.00	12.01	79.38	37.53	11.99
15	7	29	30	3.74	15.48	57.58	24.33	15.45
16	4	56	40	1.60	22.42	17.09	8.87	22.38
17	4	16	25	2.56	10.25	59.63	33.40	10.23
18	6	20	80	1.20	4.00	71.49	33.37	4.00
19	5	26	100	0.80	4.16	45.92	22.48	4.16
20	8	33	80	1.60	6.61	57.83	22.88	6.59
21	8	73	50	2.56	23.38	26.21	9.80	23.34

Sample number:	**MR 220**
Mineral:	Apatite
Irradiation code:	eth-317-13
Ns:	60
Ni:	251
Area:	1039
RohS:	0.93
RohI:	3.87
Pooled Age:	48.2 ± 14.2
Mean Age:	62.1 ± 20.0
Central Age:	48.2 ± 14.2
Chi-sq.:	14.58
P(%)	69.06
Dispersion:	0.04
RohD:	9.73
Nd:	4075
U standard	CN 5
Zeta ±1σ	416 ± 13
counted by	EW

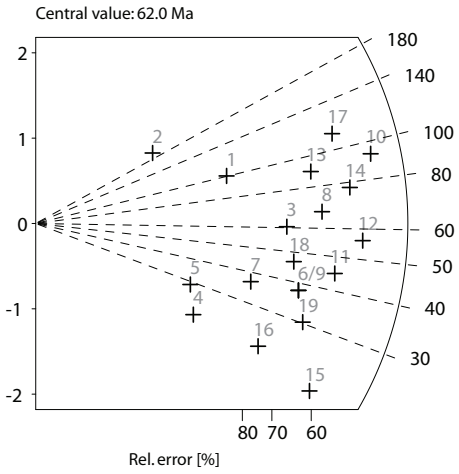

Crystal	Ns	Ni	Area	RhoS (e5)	RhoI (e5)	Age (Ma)	+- 1s	U (ppm)
1	2	4	20	1.602	3.203	100.44	87.06	3.78
2	1	1	20	0.801	0.801	199.34	282	0.95
3	3	10	36	1.335	4.449	60.45	39.85	5.26
4	1	10	42	0.381	3.813	20.21	21.21	4.51
5	1	7	35	0.458	3.203	28.86	30.87	3.78
6	3	16	60	0.801	4.271	37.85	23.85	5.05
7	2	11	50	0.641	3.523	36.71	28.24	4.16
8	4	12	42	1.525	4.576	67.13	38.83	5.41
9	3	16	100	0.48	2.562	37.85	23.85	3.03
10	6	13	50	1.922	4.164	92.77	45.9	4.92
11	4	18	100	0.641	2.883	44.83	24.83	3.41
12	5	18	70	1.144	4.118	55.99	28.37	4.87
13	4	9	42	1.525	3.432	89.36	53.79	4.05
14	5	13	60	1.335	3.47	77.4	40.82	4.1
15	3	32	60	0.801	8.542	18.95	11.46	10.09
16	2	19	100	0.32	3.043	21.28	15.83	3.6
17	5	9	42	1.907	3.432	111.51	62.32	4.05
18	3	13	40	1.201	5.205	46.55	29.86	6.15
19	3	20	70	0.686	4.576	30.3	18.79	5.41

Sample number:	**MR 222**
Mineral:	Apatite
Irradiation code:	eth-317-3
Ns:	441
Ni:	4771
Area:	1316
RohS:	5.37
RohI:	58.06
Pooled Age:	23.6 ± 2.8
Mean Age:	24.4 ± 2.6
Central Age:	23.7 ± 3.0
Chi-sq.:	21.14
P(%)	32.91
Dispersion:	0.09
RohD:	12.29
Nd:	4075
U standard	CN 5
Zeta ±1σ	416 ± 13
counted by	EW

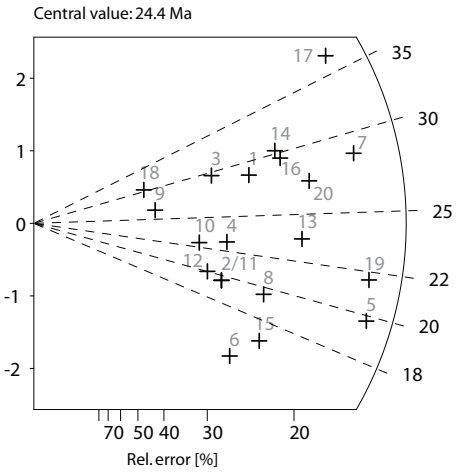

Crystal	Ns	Ni	Area	RhoS (e5)	RhoI (e5)	Age (Ma)	+- 1s	U (ppm)
1	19	169	48	6.34	56.39	28.67	7.01	52.78
2	14	182	90	2.49	32.39	19.63	5.49	30.32
3	13	112	45	4.63	39.86	29.59	8.73	37.31
4	15	168	56	4.29	48.05	22.78	6.19	44.97
5	44	568	100	7.05	90.97	19.77	3.17	85.15
6	15	255	100	2.40	40.84	15.01	4.02	38.23
7	42	375	100	6.73	60.06	28.56	4.75	56.22
8	21	274	70	4.81	62.69	19.56	4.48	58.68
9	6	58	30	3.20	30.96	26.38	11.35	28.98
10	11	125	40	4.40	50.05	22.45	7.10	46.85
11	14	182	60	3.74	48.58	19.63	5.49	45.47
12	12	153	70	2.75	35.01	20.01	6.04	32.77
13	29	316	100	4.64	50.61	23.41	4.62	47.37
14	24	202	70	5.49	46.22	30.29	6.63	43.26
15	20	304	60	5.34	81.15	16.79	3.92	75.96
16	25	216	50	8.01	69.19	29.51	6.32	64.76
17	36	249	50	11.53	79.76	36.84	6.69	74.66
18	5	42	32	2.50	21.02	30.35	14.40	19.68
19	45	531	100	7.21	85.04	21.62	3.44	79.61
20	31	290	45	11.03	103.21	27.26	5.24	96.61

Sample number:	**MR 248**
Mineral:	Apatite
Irradiation code:	eth-317-14
Ns:	321
Ni:	2128
Area:	1271
RohS:	4.05
RohI:	26.81
Pooled Age:	29.7 ± 4.2
Mean Age:	31.3 ± 4.6
Central Age:	30.0 ± 5.2
Chi-sq.:	30.21
P(%)	4.92
Dispersion:	0.21
RohD:	9.48
Nd:	4075
U standard	CN 5
Zeta ±1σ	416 ± 13
counted by	EW

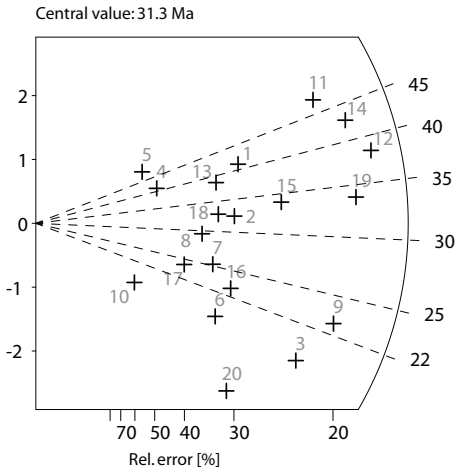

Crystal	Ns	Ni	Area	RhoS (e5)	RhoI (e5)	Age (Ma)	+- 1s	U (ppm)
1	14	67	100	2.24	10.73	41.06	12.15	13.02
2	13	79	50	4.16	25.30	32.36	9.75	30.70
3	21	216	70	4.81	49.42	19.14	4.43	59.97
4	5	24	42	1.91	9.15	40.94	20.18	11.10
5	4	16	24	2.67	10.68	49.10	27.50	12.96
6	10	102	100	1.60	16.34	19.30	6.43	19.82
7	10	78	40	4.00	31.23	25.23	8.52	37.89
8	9	60	70	2.06	13.73	29.50	10.60	16.66
9	28	241	100	4.48	38.60	22.86	4.63	46.83
10	3	33	42	1.14	12.58	17.90	10.81	15.27
11	27	112	35	12.36	51.25	47.35	10.29	62.19
12	38	195	90	6.76	34.70	38.30	6.92	42.11
13	11	56	48	3.67	18.69	38.61	12.80	22.67
14	33	152	70	7.55	34.78	42.66	8.33	42.20
15	20	116	70	4.58	26.54	33.90	8.29	32.20
16	12	103	80	2.40	20.62	22.93	7.04	25.02
17	7	57	35	3.20	26.08	24.17	9.71	31.65
18	11	66	35	5.03	30.20	32.77	10.73	36.65
19	34	198	100	5.45	31.71	33.76	6.38	38.48
20	11	157	70	2.52	35.92	13.80	4.33	43.59

Sample number:	**MR 253**
Mineral:	Apatite
Irradiation code:	eth-317-5
Ns:	200
Ni:	1304
Area:	1149
RohS:	2.79
RohI:	18.18
Pooled Age:	37.5 ± 6.2
Mean Age:	40.2 ± 7.4
Central Age:	37.9 ± 6.8
Chi-sq.:	23.14
P(%)	23.12
Dispersion:	0.15
RohD:	11.78
Nd:	4075
U standard	CN 5
Zeta ±1σ	416 ± 13
counted by	EW

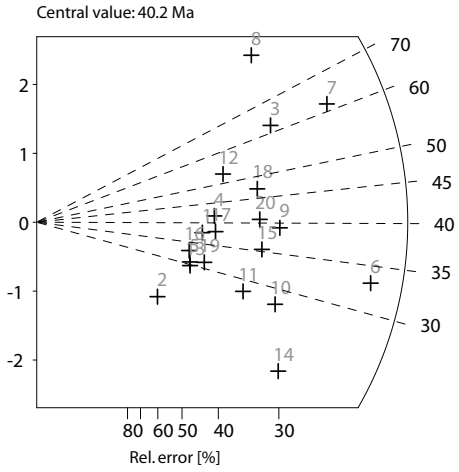

Crystal	Ns	Ni	Area	RhoS (e5)	RhoI (e5)	Age (Ma)	+- 1s	U (ppm)
1	6	39	48	2.00	13.01	37.57	16.53	12.71
2	3	35	24	2.00	23.36	20.96	12.63	22.81
3	13	51	100	2.08	8.17	62.13	19.43	7.98
4	7	41	40	2.80	16.42	41.68	17.11	16.03
5	5	40	50	1.60	12.81	30.54	14.53	12.51
6	24	177	70	5.49	40.50	33.13	7.30	39.55
7	20	79	100	3.20	12.65	61.71	15.60	12.36
8	12	32	60	3.20	8.54	91.20	31.04	8.34
9	13	81	100	2.08	12.97	39.19	11.79	12.67
10	12	105	70	2.75	24.02	27.93	8.57	23.46
11	9	78	28	5.15	44.61	28.20	9.98	43.57
12	8	37	40	3.20	14.81	52.74	20.65	14.47
13	5	41	42	1.91	15.63	29.80	14.16	15.27
14	12	140	60	3.20	37.37	20.96	6.35	36.50
15	11	76	80	2.20	15.22	35.35	11.47	14.86
16	5	37	36	2.22	16.46	33.01	15.77	16.08
17	7	45	35	3.20	20.59	37.99	15.49	20.11
18	11	57	70	2.52	13.04	47.10	15.60	12.74
19	6	47	36	2.67	20.91	31.19	13.57	20.42
20	11	66	60	2.94	17.62	40.69	13.33	17.21

Sample number:	**MR 255**
Mineral:	Apatite
Irradiation code:	eth-319-9
Ns:	301
Ni:	1635
Area:	1493
RohS:	3.23
RohI:	17.54
Pooled Age:	37.5 ± 5.4
Mean Age:	41.3 ± 6.0
Central Age:	37.5 ± 5.4
Chi-sq.:	18.00
P(%)	52.22
Dispersion:	0.01
RohD:	9.81
Nd:	3794
U standard	CN 5
Zeta $\pm 1\sigma$	416 ± 13
counted by	EW

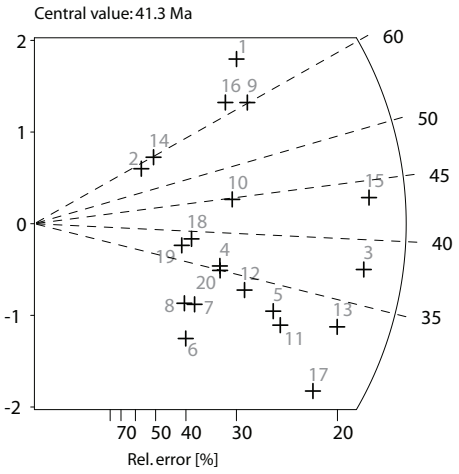

Crystal	Ns	Ni	Area	RhoS (e5)	RhoI (e5)	Age (Ma)	+- 1s	U (ppm)
1	15	43	50	4.81	13.77	70.78	21.37	16.15
2	4	14	28	2.29	8.01	58.03	32.96	9.39
3	35	189	100	5.61	30.27	37.67	7.06	35.49
4	11	63	100	1.76	10.09	35.52	11.68	11.83
5	18	113	49	5.88	36.93	32.42	8.31	43.30
6	7	57	70	1.60	13.04	25.01	10.05	15.29
7	8	55	36	3.56	24.47	29.61	11.25	28.69
8	7	49	40	2.80	19.62	29.08	11.79	23.00
9	16	54	100	2.56	8.65	60.17	17.26	10.14
10	13	59	100	2.08	9.45	44.80	13.82	11.08
11	19	123	60	5.07	32.83	31.44	7.83	38.49
12	14	85	100	2.24	13.61	33.52	9.74	15.96
13	29	179	100	4.64	28.67	32.97	6.70	33.61
14	5	17	40	2.00	6.81	59.73	30.46	7.98
15	37	173	90	6.58	30.79	43.49	8.02	36.10
16	13	42	100	2.08	6.73	62.84	20.07	7.89
17	24	176	100	3.84	28.19	27.76	6.12	33.05
18	8	42	100	1.28	6.73	38.74	15.01	7.89
19	7	38	50	2.24	12.17	37.47	15.47	14.27
20	11	64	80	2.20	12.81	34.97	11.48	15.02

Appendix IV: Confined track length data

Len: Measured track length in μm.

MDpar: Corresponding mean fission-track etch pit diameter parallel to the crystallographic c-axis in μm.

MDprp: Corresponding mean fission-track etch pit diameter perpendicular to the c-axis in μm.

<C: Angle between track and c-axis in °.

Data sets

Sample number: **RD 2**
Mineral: Apatite
Irradiation code: eth-328-5

#	Len	MDpar (5N)	MDprp (5N)	<C	#	Len	MDpar (5N)	MDprp (5N)	<C
1	12.97	1.43	0.25	50.55	47	14.74	1.43	0.30	72.20
2	12.09	1.28	0.36	71.05	48	14.18	1.43	0.28	87.89
3	11.94	1.40	0.30	48.39	49	12.05	1.44	0.31	65.34
4	15.18	1.39	0.38	63.82	50	12.97	1.42	0.34	84.95
5	13.20	1.08	2.32	57.95	51	12.22	1.35	0.38	58.44
6	15.47	1.26	0.39	52.06	52	13.82	1.53	0.33	73.21
7	13.89	1.36	0.34	62.22	53	11.85	1.41	0.30	73.78
8	10.43	1.62	0.35	82.04	54	14.80	1.33	0.35	72.66
9	14.58	1.46	0.34	45.75	55	12.05	1.33	0.35	68.37
10	14.40	1.38	0.31	68.00	56	13.89	1.41	0.37	83.04
11	12.92	1.38	0.31	64.05	57	13.92	1.45	0.34	74.46
12	13.41	1.41	0.34	73.35	58	15.38	1.50	0.33	47.54
13	12.24	1.31	0.32	54.10	59	14.46	1.50	0.33	58.49
14	12.29	1.42	0.36	31.68	60	15.32	1.55	0.44	71.84
15	12.37	1.47	0.29	72.21	61	13.04	1.42	0.37	46.09
16	14.20	1.55	0.33	37.15	62	13.97	1.48	0.38	74.32
17	12.95	1.53	0.45	29.88	63	15.48	1.46	0.34	58.99
18	12.20	1.51	0.31	38.43	64	13.51	1.40	0.40	48.05
19	13.96	1.46	0.28	62.83	65	12.96	1.40	0.40	78.06
20	14.15	1.42	0.64	63.24	66	13.65	1.14	0.31	43.08
21	12.21	1.46	0.34	42.56	67	12.58	1.73	0.30	46.69
22	10.82	1.35	0.35	60.08	68	11.86	1.57	0.29	44.08
23	12.15	1.39	0.31	55.80	69	12.17	1.34	0.36	75.78
24	13.55	1.54	0.38	53.49	70	12.06	1.56	0.32	52.12
25	10.02	1.47	0.34	66.03	71	13.19	1.48	0.37	75.40
26	11.74	1.50	0.33	67.97	72	11.86	1.52	0.34	86.38
27	13.02	1.50	0.33	55.12	73	14.51	1.40	0.35	51.23
28	11.72	1.58	0.38	55.96	74	7.53	1.78	0.18	65.59
29	12.55	1.38	0.30	60.68	75	10.56	1.46	0.36	71.89
30	14.13	1.59	0.30	39.54	76	12.74	1.46	0.35	66.16
31	13.73	1.52	0.34	72.76	77	13.04	1.46	0.35	60.61
32	13.92	1.46	0.31	69.95	78	12.43	1.53	0.27	55.72
33	13.80	1.52	0.33	55.37	79	12.81	1.44	0.30	80.98
34	11.97	1.53	0.48	49.87	80	13.83	1.47	0.33	68.03
35	13.22	1.53	0.48	53.24	81	12.38	1.50	0.32	53.95
36	14.88	1.34	0.33	89.07	82	13.06	1.57	0.35	74.59
37	13.99	1.27	0.31	51.87	83	12.26	1.40	0.35	60.61
38	9.42	1.46	0.37	64.62	84	13.40	1.35	0.32	47.90
39	12.68	1.54	0.35	73.57	85	12.32	1.46	0.32	48.29
40	13.41	1.44	0.37	62.99	86	11.44	1.47	0.32	65.54
41	11.30	1.37	0.36	41.52	87	12.53	1.34	0.30	40.32
42	12.22	1.36	0.37	48.77	88	13.42	1.57	0.43	57.39
43	11.10	1.35	0.34	74.66	89	13.02	1.37	0.36	69.40
44	11.11	1.38	0.41	69.88	90	14.56	1.44	0.32	57.94
45	13.86	1.45	0.44	29.02	91	12.24	1.39	0.41	76.88
46	13.91	1.42	0.35	40.07					

Sample number: **RD 26**
Mineral: Apatite
Irradiation code: eth-331-13

#	Len	MDpar (5N)	MDprp (5N)	<C	#	Len	MDpar (5N)	MDprp (5N)	<C
1	14.54	1.70	0.49	70.55	47	14.02	1.22	0.40	55.75
2	12.73	1.44	0.45	80.83	48	13.28	1.32	0.35	59.37
3	9.91	1.75	0.47	48.51	49	13.55	1.30	0.39	79.66
4	15.30	1.20	0.49	58.08	50	14.81	1.40	0.37	73.23
5	10.48	1.66	0.58	17.22	51	13.80	1.52	0.45	60.57
6	14.06	1.56	0.48	59.79	52	6.16	1.52	0.45	37.97
7	11.01	1.19	0.36	45.05	53	14.32	1.42	0.43	85.72
8	12.75	1.49	0.33	55.98	54	13.26	1.33	0.32	44.58
9	14.18	1.65	0.51	64.33	55	15.55	1.41	0.31	75.38
10	9.32	1.56	0.44	37.59	56	14.96	1.46	0.42	43.66
11	9.33	1.58	0.42	86.91	57	15.87	1.35	0.38	54.48
12	13.68	1.56	0.57	80.34	58	8.30	1.32	0.38	45.74
13	15.28	1.73	0.60	49.56	59	14.46	1.36	0.41	50.54
14	14.92	1.52	0.36	51.40	60	13.37	1.40	0.41	74.88
15	15.21	1.52	0.36	57.42	61	14.45	1.40	0.41	59.27
16	9.57	1.34	0.48	41.30	62	12.98	1.36	0.38	71.20
17	15.57	1.43	0.38	65.98	63	9.88	1.31	0.29	58.43
18	12.34	1.02	0.41	84.69	64	14.73	1.36	0.29	39.43
19	15.02	1.19	0.36	51.52	65	9.50	1.48	0.45	53.72
20	14.00	1.36	0.45	81.03	66	12.35	1.39	0.40	84.03
21	13.47	1.24	0.34	48.58	67	11.47	1.43	0.34	75.08
22	14.24	1.21	0.42	72.09	68	13.65	1.47	0.34	63.55
23	13.86	1.39	0.40	53.23	69	13.94	1.47	0.34	74.83
24	14.11	1.13	0.40	78.14	70	14.24	1.30	0.38	60.15
25	13.17	1.22	0.43	48.47	71	14.83	1.30	0.38	64.01
26	12.00	1.32	0.42	89.04	72	14.01	1.30	0.38	60.29
27	10.69	1.33	0.44	62.91	73	15.05	1.36	0.38	27.97
28	9.33	1.34	0.34	65.57	74	7.74	1.32	0.38	82.66
29	12.45	1.42	0.39	67.17	75	12.61	1.22	0.31	67.51
30	14.09	1.31	0.44	77.31	76	12.60	1.36	0.38	75.53
31	14.08	1.30	0.47	73.16	77	12.85	1.37	0.40	55.94
32	9.17	1.47	0.41	75.80	78	14.33	1.36	0.39	74.53
33	13.80	1.47	0.40	47.98	79	6.95	1.27	0.41	51.48
34	10.29	1.27	0.31	52.75	80	13.56	1.28	0.37	44.84
35	13.74	1.47	0.47	80.61	81	9.89	1.29	0.35	71.40
36	14.54	1.42	0.35	66.57	82	14.97	1.38	0.42	59.04
37	11.43	1.40	0.47	42.73	83	13.53	1.36	0.48	56.61
38	15.21	1.45	0.31	84.45	84	13.68	1.22	0.40	55.82
39	13.43	1.45	0.39	58.77	85	8.56	1.39	0.38	70.38
40	13.36	1.16	0.35	68.21	86	14.95	1.37	0.32	57.76
41	15.34	1.32	0.41	65.09	87	14.09	1.29	0.40	72.26
42	14.33	1.18	0.33	74.33	88	11.36	1.30	0.32	83.24
43	12.72	1.18	0.33	62.39	89	15.69	1.43	0.54	44.02
44	14.79	1.38	0.38	67.69	90	14.44	1.33	0.54	66.98
45	14.83	1.17	0.33	63.64	91	14.02	1.22	0.32	81.41
46	14.98	1.17	0.33	66.56					

Sample number: **RD 34**
Mineral: Apatite
Irradiation code: eth-356-4

#	Len	MDpar (5N)	MDprp (5N)	<C	#	Len	MDpar (5N)	MDprp (5N)	<C
1	13.70	1.96	0.58	60.35	53	14.58	1.66	0.40	60.13
2	14.57	1.96	0.58	20.11	54	14.27	1.66	0.40	86.39
3	13.91	1.71	0.63	76.88	55	15.42	1.80	0.58	0.23
4	13.33	1.89	0.57	53.76	56	14.56	1.63	0.43	69.50
5	14.02	1.79	0.65	47.87	57	14.77	1.44	0.51	75.77
6	15.47	1.77	0.59	61.02	58	13.56	1.38	0.45	73.57
7	14.56	1.83	0.59	51.31	59	13.69	1.38	0.45	69.36
8	14.08	1.83	0.59	61.43	60	14.54	1.74	0.50	76.10
9	14.18	1.72	0.53	74.64	61	14.43	1.74	0.50	48.22
10	13.76	1.72	0.53	82.85	62	14.71	1.81	0.46	52.05
11	15.15	1.64	0.43	85.16	63	14.33	1.81	0.46	53.82
12	13.57	1.93	0.61	57.98	64	15.17	1.75	0.44	59.58
13	15.18	1.98	0.38	73.93	65	15.15	1.75	0.44	43.54
14	14.85	1.75	0.43	52.14	66	14.94	1.90	0.41	59.37
15	14.42	1.64	0.44	63.39	67	12.67	1.70	0.42	59.14
16	13.03	1.64	0.44	72.85	68	14.13	1.85	0.43	51.27
17	15.04	1.69	0.45	64.02	69	14.03	1.73	0.53	70.14
18	14.45	1.69	0.45	72.81	70	12.90	1.73	0.53	77.32
19	14.01	1.77	0.48	80.00	71	15.69	1.75	0.60	36.73
20	14.16	1.91	0.57	49.27	72	12.36	1.68	0.49	65.61
21	15.33	1.91	0.57	57.13	73	14.14	1.70	0.57	74.90
22	14.51	1.91	0.57	36.34	74	14.77	1.67	0.46	34.37
23	14.39	1.75	0.49	57.50	75	13.99	1.56	0.64	57.28
24	14.92	1.94	0.52	66.57	76	13.89	1.56	0.64	57.12
25	13.95	1.94	0.52	48.58	77	12.40	1.78	0.52	75.49
26	14.78	1.72	0.65	71.58	78	12.99	1.76	0.43	63.76
27	13.56	1.72	0.65	64.83	79	14.02	1.82	0.58	54.32
28	14.23	1.57	0.50	82.77	80	14.17	1.75	0.44	89.49
29	14.05	1.96	0.47	75.65	81	13.58	1.49	0.39	58.78
30	14.95	1.86	0.40	81.33	82	15.19	1.64	0.42	70.08
31	14.08	1.86	0.40	82.36	83	14.60	1.40	0.37	56.45
32	14.08	1.67	0.51	72.63	84	13.06	1.63	0.36	56.47
33	15.21	1.72	0.49	56.25	85	13.35	1.72	0.53	89.22
34	15.26	1.76	0.59	72.62	86	13.70	1.57	0.47	58.13
35	13.06	1.73	0.34	64.80	87	14.84	1.64	0.40	31.95
36	13.63	1.95	0.55	79.15	88	14.18	1.85	0.49	81.43
37	13.59	1.95	0.55	49.05	89	14.30	1.85	0.49	53.62
38	13.40	1.95	0.55	72.53	90	13.65	1.59	0.44	69.86
39	12.33	1.99	0.62	73.17	91	14.98	1.61	0.54	71.69
40	14.73	1.78	0.40	73.93	92	15.99	1.61	0.54	76.88
41	13.19	1.78	0.40	62.18	93	13.90	1.79	0.76	65.01
42	12.92	1.71	0.43	73.08	94	14.17	1.73	0.55	63.62
43	12.92	1.78	0.71	85.58	95	14.66	1.59	0.48	71.88
44	13.57	1.78	0.71	64.37	96	13.14	1.73	0.54	47.39
45	14.29	1.42	0.34	75.91	97	12.15	1.78	0.52	69.12
46	13.07	1.78	0.55	83.37	98	14.01	1.66	0.49	69.42
47	14.46	1.74	0.54	28.58	99	14.99	1.66	0.49	44.22
48	12.71	1.74	0.54	74.60	100	15.35	1.68	0.42	72.19
49	14.06	1.62	0.56	56.60	101	14.22	1.68	0.42	82.18
50	15.04	1.82	0.46	75.38	102	13.48	1.76	0.72	55.22
51	17.07	1.82	0.53	72.90	103	13.12	1.76	0.72	44.71
52	13.86	1.82	0.53	55.81	104	14.46	1.76	0.72	50.60

Sample number: **RD 64**
Mineral: Apatite
Irradiation code: eth-357-15

#	Len	MDpar (7%)	MDpar (5N)	MDprp (7%)	MDprp (5N)	<C
1	15.80	1.92	1.53	0.96	0.77	53.43
2	13.89	1.92	1.53	0.96	0.77	64.46
3	15.51	1.79	1.43	0.74	0.60	51.54
4	8.39	1.77	1.42	0.99	0.79	83.16
5	11.33	1.86	1.48	0.70	0.56	72.08
6	12.80	1.50	1.20	0.72	0.58	68.45
7	12.50	1.76	1.41	0.78	0.62	44.11
8	11.64	2.05	1.64	0.89	0.71	85.34
9	13.05	1.74	1.39	0.73	0.58	69.41
10	15.21	2.11	1.69	0.84	0.67	27.57
11	13.02	1.72	1.37	0.78	0.62	77.88
12	14.45	1.82	1.45	0.87	0.69	58.68
13	10.62	1.28	1.02	0.57	0.45	2.30
14	7.57	1.59	1.27	0.66	0.53	82.78
15	16.85	1.81	1.45	0.81	0.65	11.55
16	14.96	1.52	1.22	0.62	0.49	71.48
17	17.27	1.56	1.25	0.71	0.57	52.88
18	13.60	1.52	1.22	0.72	0.58	53.82
19	14.88	1.83	1.47	0.64	0.51	77.47
20	13.66	1.52	1.21	0.64	0.51	55.26
21	12.38	1.71	1.37	0.79	0.63	54.17
22	12.40	1.61	1.29	0.88	0.70	52.42
23	13.33	1.43	1.14	0.63	0.51	88.60
24	13.88	1.81	1.44	0.87	0.69	17.43
25	15.02	1.70	1.36	0.77	0.61	28.42
26	12.95	1.81	1.45	0.96	0.77	65.07
27	15.57	1.55	1.24	0.54	0.43	57.20
28	10.12	1.67	1.33	0.84	0.67	50.58
29	14.92	2.25	1.80	0.84	0.67	88.77
30	14.68	1.97	1.58	0.59	0.47	54.51
31	15.71	1.87	1.49	0.90	0.72	70.43
32	15.13	1.87	1.49	0.90	0.72	42.21
33	12.55	1.89	1.51	1.20	0.96	51.04
34	14.00	1.99	1.59	1.04	0.83	67.97
35	12.96	1.87	1.49	0.78	0.63	83.18
36	12.21	1.79	1.43	0.83	0.67	61.74
37	11.86	1.77	1.41	0.88	0.71	84.01
38	15.96	2.01	1.61	0.73	0.58	78.91
39	15.47	1.91	1.52	0.86	0.69	80.92
40	15.76	1.74	1.39	0.84	0.67	30.77
41	14.26	1.75	1.40	0.85	0.68	63.77
42	13.37	1.75	1.40	0.66	0.53	66.91
43	14.30	1.96	1.57	0.67	0.54	61.52
44	14.95	1.64	1.31	0.74	0.59	48.10
45	13.35	1.64	1.31	0.74	0.59	28.66
46	13.21	1.69	1.35	0.82	0.66	87.04
47	13.85	1.82	1.45	0.88	0.70	71.99
48	12.40	1.91	1.53	0.58	0.46	40.62
49	15.30	1.45	1.16	0.72	0.58	30.52
50	13.33	1.90	1.52	0.87	0.70	85.80
51	13.25	1.51	1.21	0.81	0.65	41.47
52	13.90	1.65	1.32	0.80	0.64	65.56
53	13.39	1.79	1.43	0.95	0.76	72.29
54	12.23	2.10	1.68	0.94	0.75	18.49
55	14.86	1.61	1.29	0.68	0.54	70.88
56	12.13	1.66	1.33	0.78	0.62	63.04
57	14.42	1.37	1.09	0.64	0.51	70.32
58	13.84	1.43	1.14	0.86	0.69	5.18
59	11.99	1.73	1.39	0.78	0.62	32.72
60	9.49	1.60	1.28	0.79	0.63	60.07
61	14.46	1.86	1.49	1.02	0.82	55.94
62	14.65	1.80	1.44	0.95	0.76	33.86
63	14.30	1.83	1.46	0.68	0.54	27.54
64	14.77	1.85	1.48	0.67	0.53	29.61
65	11.71	1.80	1.44	1.01	0.81	88.84

continued on next page

continuation from previous page

66	13.24	1.89	1.51	0.89	0.71	16.00
67	15.23	1.76	1.41	0.74	0.59	75.68
68	13.74	2.00	1.60	0.98	0.78	71.78
69	15.43	1.79	1.43	0.79	0.63	55.32
70	14.76	1.75	1.40	0.72	0.58	72.44
71	15.75	1.75	1.40	0.75	0.60	70.66
72	14.87	1.57	1.26	0.73	0.59	62.98

Bibliography to Appendices

Bähr, R., Lippolt, H. J., and Wernicke, R. S. (1994). Temperature-induced ^{4}He degassing of specularite and botryoidal hematite – a ^{4}He retentivity study. *Journal of Geophysical Research–Solid Earth*, 99(B9):17695–17707.

Barbarand, J., Carter, A., Wood, I., and Hurford, T. (2003). Compositional and structural control of fission-track annealing in apatite. *Chemical Geology*, 198(1–2):107–137.

Bonfiglioli, G., Ferro, A., and Mojoni, A. (1961). Electron Microscope Investigation on Nature of Tracks of Fission Products in Mica. *Journal of Applied Physics*, 32(12):2499–2503.

Brandon, M. T., Roden-Tice, M. K., and Garver, J. I. (1998). Late Cenozoic exhumation of the Cascadia accretionary wedge in the Olympic Mountains, northwest Washington State. *Geological Society of America Bulletin*, 110(8):985–1009.

Braun, J., van der Beek, P., and Batt, G. (2006). *Quantitative Thermochronology: Numerical Methods for the Interpretation of Thermochronological Data*. Cambridge University Press.

Burtner, R. L. and Nigrini, A. (1994). Thermochronology of the Idaho–Wyoming thrust belt during the sevier orogeny – A new, calibrated, multiprocess thermal-model. *Aapg Bulletin – American Association of Petroleum Geologists*, 78(10):1586–1612.

Carlson, W. D., Donelick, R. A., and Ketcham, R. A. (1999). Variability of apatite fission-track annealing kinetics: I. Experimental results. *American Mineralogist*, 84(9):1213–1223.

Carter, A. (1990). The Thermal History and Annealing Effects in Zircons from the Ordovician of North Wales. *Nuclear Tracks and Radiation Measurements*, 17(3):309–313.

Chadderton, L. T. (2003). Nuclear tracks in solids: registration physics and the compound spike. *Radiation Measurements*, 36(1–6):13–34.

Chadderton, L. T. and Montagupollock, H. M. (1963). Fission fragment damage to crystal lattices – heat-sensitive crystals. *Proceedings of the Royal Society of London Series A – Mathematical and Physical Sciences*, 274:239–252.

Corrigan, J. D. (1991). Thermal anomalies in the central Indian–Ocean – Evidence for dewatering of the Bengal fan. *Journal of Geophysical Research–Solid Earth and Planets*, 96(B9):14263–14275.

Corrigan, J. D. (1993). Apatite fission-track analysis of Oligocene strata in South Texas, USA – Testing annealing models. *Chemical Geology*, 104(1–4):227–249.

Cowan, G. A. and Adler, H. H. (1976). Variability of Natural Abundance of ^{235}U . *Geochimica Et Cosmochimica Acta*, 40(12):1487–1490.

Coyle, D. A. and Wagner, G. A. (1998). Positioning the titanite fission-track partial annealing zone. *Chemical Geology*, 149(1–2):117–125.

Crowley, K. D., Cameron, M., and Schaefer, R. L. (1991). Experimental studies of annealing of etched fission tracks in fluorapatite. *Geochimica Et Cosmochimica Acta*, 55(5):1449–1465.

Damon, P. E. and Kulp, J. L. (1957). Determination of radiogenic helium in zircon by stable isotope dilution technique. *Transactions – American Geophysical Union*, 38(6):945–953.

Dodson, M. H. (1973). Closure temperature in cooling geochronological and petrological systems. *Contributions to Mineralogy and Petrology*, 40(3):259–274.

Donelick, R. A. (1991). Crystallographic orientation dependence of mean etchable fission-track length in apatite: An empirical model and experimental observations. *American Mineralogist*, 76(1–2):83–91.

Donelick, R. A., Ketcham, R. A., and Carlson, W. D. (1999). Variability of apatite fission-track annealing kinetics: II. Crystallographic orientation effects. *American Mineralogist*, 84(9):1224–1234.

Dunai, T. J. and Roselieb, K. (1996). Sorption and diffusion of helium in garnet: Implications for volatile tracing and dating. *Earth and Planetary Science Letters*, 139(3–4):411–421.

Dunkl, I. (2002). Trackkey: a windows program for calculation and graphical presentation of fission track data. *Computers & Geosciences*, 28(1):3–12.

Durrani, S. and Bull, R. (1987). *Solid state nuclear track detection: Principles, methods and applications*. Pergamon Press, Oxford, United States.

Fanale, F. P. and Kulp, J. L. (1962). The helium method and the age of the Cornwall, Pennsylvania magnetite ore. *Economic Geology and the Bulletin of the Society of Economic Geologists*, 57(5):735–746.

Farley, K. A. (2000). Helium diffusion from apatite: General behavior as illustrated by Durango fluorapatite. *Journal of Geophysical Research–Solid Earth*, 105(B2):2903–2914.

Farley, K. A., Wolf, R. A., and Silver, L. T. (1996). The effects of long alpha-stopping distances on (U-Th)/He ages. *Geochimica Et Cosmochimica Acta*, 60(21):4223–4229.

Fleischer, R. L. and Price (1964). Decay constant for spontaneous fission of ^{238}U . *Physical Review B*, 133(1B):1363–1364.

Fleischer, R. L., Price, P. B., and Walker, R. M. (1964). Fission-track ages of zircons. *Journal of Geophysical Research*, 69(22):4885–4888.

Fleischer, R. L., Price, P. B., and Walker, R. M. (1975). *Nuclear tracks in solids. Principles and applications*. University of California Press, Berkeley.

Galbraith, R. F. (1990). The radial plot – Graphical assessment of spread in ages. *Nuclear Tracks and Radiation Measurements*, 17(3):207–214.

Galbraith, R. F. and Laslett, G. M. (1993). Statistical models for mixed fission-track ages. *Nuclear Tracks and Radiation Measurements*, 21(4):459–470.

Gallagher, K. (1995). Evolving temperature histories from apatite fission-track data. *Earth and Planetary Science Letters*, 136(3–4):421–435.

Gleadow, A. J. W. (1981). Fission-track dating methods – What are the real alternatives. *Nuclear Tracks and Radiation Measurements*, 5(1–2):3–14.

Gleadow, A. J. W. and Duddy, I. R. (1981). A natural long-term Track annealing experiment for apatite. *Nuclear Tracks and Radiation Measurements*, 5(1–2):169–174.

Gleadow, A. J. W., Duddy, I. R., Green, P. F., and Hegarty, K. A. (1986a). Fission-Track Lengths in the Apatite Annealing Zone and the Interpretation of Mixed Ages. *Earth and Planetary Science Letters*, 78(2–3):245–254.

Gleadow, A. J. W., Duddy, I. R., Green, P. F., and Lovering, J. F. (1986b). Confined fission-track lengths in apatite – A diagnostic tool for thermal history analysis. *Contributions to Mineralogy and Petrology*, 94(4):405–415.

Gleadow, A. J. W., Hurford, A. J., and Quaife, R. D. (1976). Fission-Track Dating of Zircon – Improved Etching Techniques. *Earth and Planetary Science Letters*, 33(2):273–276.

Gleadow, A. J. W. and Lovering, J. F. (1977). Geometry Factor for External Detectors in Fission-Track Dating. *Nuclear Track Detection*, 1(2):99–106.

Graham, D. W., Jenkins, W. J., Kurz, M. D., and Batiza, R. (1987). Helium Isotope Disequilibrium and Geochronology of Glassy Submarine Basalts. *Nature*, 326(6111):384–386.

Green, P. F. (1981). A New Look at Statistics in Fission-Track Dating. *Nuclear Tracks and Radiation Measurements*, 5(1–2):77–86.

Green, P. F. and Duddy, I. R. (1989). Some Comments on Paleotemperature Estimation from Apatite Fission-Track Analysis. *Journal of Petroleum Geology*, 12(1):111–114.

Green, P. F., Duddy, I. R., Gleadow, A. J. W., Tingate, P. R., and Laslett, G. M. (1986). Thermal Annealing of Fission Tracks in Apatite. 1. A Qualitative Description. *Chemical Geology*, 59(4):237–253.

Green, P. F., Duddy, I. R., Laslett, G. M., Hegarty, K. A., Gleadow, A. J. W., and Lovering, J. F. (1989). Thermal Annealing of Fission Tracks in Apatite. 4. Quantitative Modeling Techniques and Extension to Geological Timescales. *Chemical Geology*, 79(2):155–182.

Green, P. F. and Durrani, S. A. (1979). Quantitative Assessment of Geometry Factors for Use in Fission-Track Studies. *Nuclear Track Detection*, 2(4):207–213.

Hejl, E. (1995). Evidence for Unetchable Gaps in Apatite Fission Tracks. *Chemical Geology*, 122(1–4):259–269.

Hurford, A. J. and Green, P. F. (1983). The zeta age calibration of fission-track dating. *Chemical Geology*, 41(4):285–317.

Hurley, P. M. (1952). Alpha ionization damage as a cause of low He ratios. *EOS Transactions of the American Geophysical Union*, 33:174–183.

Jaffey, A. H., Flynn, K. F., Glendeni, L., Bentley, W. C., and Essling, A. M. (1971). Precision measurement of half-lives and specific activities of ^{235}U and ^{238}U . *Physical Review C*, 4(5):1889–1906.

Kasuya, M. and Naeser, C. W. (1988). The effect of alpha-damage on fission-track annealing in zircon. *Nuclear Tracks and Radiation Measurements*, 14(4):477–480.

Ketcham, R. A. (2005). Forward and inverse modeling of low-temperature thermochronometry data. In *Low-Temperature Thermochronology: Techniques, Interpretations, and Applications*, volume 58 of *Reviews in Mineralogy and Geochemistry*, pages 275–314. Mineralogical Soc America, Chantilly.

Kohn, B., Gleadow, A., Belton, D., Osadetz, K., and Brown, R. (2006). Low temperature thermochronology on cratons: rechecking the rules of the game. In *European Conference of Thermochronology*.

Lippolt, H. J. and Weigel, E. (1988). ^{4}He diffusion in ^{40}Ar-retentive minerals. *Geochimica Et Cosmochimica Acta*, 52(6):1449–1458.

Naeser, C. W. and Dodge, F. (1969). Fission-track ages of accessory minerals from granitic rocks of the central Sierra Nevada Batholith, California. *Geological Society of America Bulletin*, 80:2201–2212.

Naeser, C. W. and Forbes, R. B. (1976). Variation of Fission-Track Ages with Depth in 2 Deep Drill Holes. *Transactions – American Geophysical Union*, 57(4):353–353.

Naeser, C. W. and McKee, E. H. (1970). Fission-track and K-Ar Ages of Tertiary ash-flow tuffs, north-central Nevada. *Geological Society of America Bulletin*, 81(11):3375–3384.

Paul, T. A. and Fitzgerald, P. G. (1992). Transmission Electron Microscopic Investigation of Fission Tracks in Fluorapatite. *American Mineralogist*, 77(3–4):336–344.

Price, P. B. and Walker, R. M. (1963). Fossil Tracks of Charged Particles in Mica and Age of Minerals. *Journal of Geophysical Research*, 68(16):4847–4862.

Rahn, M. K., Brandon, M. T., Batt, G. E., and Garver, J. I. (2004). A zero-damage model for fission-track annealing in zircon. *American Mineralogist*, 89(4):473–484.

Reiners, P. W. and Farley, K. A. (1999). Helium diffusion and (U-Th)/He thermochronometry of titanite. *Geochimica Et Cosmochimica Acta*, 63(22):3845–3859.

Reiners, P. W., Farley, K. A., and Hickes, H. J. (2002). He diffusion and (U-Th)/He thermochronometry of zircon: initial results from Fish Canyon Tuff and Gold Butte. In *9th International Conference on Fission Track Dating and Thermochronology*, volume 349, pages 297–308, Lome, Australia. Elsevier Science Bv.

Roberts, J. H., Gold, R., and Armani, R. J. (1968). Spontaneous-Fission Decay Constant of ^{238}U . *Physical Review*, 174(4):1482–1484.

Rutherford, E. (1907). The velocity and energy of the alpha particles from radioactive substances. *Philosophical Magazine*, 13(73–78):110–117.

Seitz, F. (1949). On the Disordering of Solids by Action of Fast Massive Particles. *Discussions of the Faraday Society*, (5):271–282.

Strutt, R. J. (1905). On the radio-active minerals. *Proceedings of the Royal Society of London Series A – Containing Papers of a Mathematical and Physical Character*, 76(508):88–101.

Tagami, T. and Shimada, C. (1996). Natural long-term annealing of the zircon fission track system around a granitic pluton. *Journal of Geophysical Research – Solid Earth*, 101(B4):8245–8255.

Trull, T. W., Kurz, M. D., and Jenkins, W. J. (1991). Diffusion of Cosmogenic ^{3}He in Olivine and Quartz – Implications for Surface Exposure Dating. *Earth and Planetary Science Letters*, 103(1–4):241–256.

Wagner, G. A., Hejl, E., and Vandenhaute, P. (1994). The KTB fission-track project – methodical aspects and geological implications. *Radiation Measurements*, 23(1):95–101.

Wagner, G. A. and Van den Haute, P. (1992). *Fission-Track Dating*. Enke, Stuttgart.

Wernicke, R. S. and Lippolt, H. J. (1994a). ^{4}He age discordance and release behavior of a double shell botryoidal hematite from the Schwarzwald, Germany. *Geochimica Et Cosmochimica Acta*, 58(1):421–429.

Wernicke, R. S. and Lippolt, H. J. (1994b). Dating of Vein Specularite Using Internal (U+Th)/^{4}He Isochrons. *Geophysical Research Letters*, 21(5):345–347.

Wolf, R. A. (1997). *Development of the (U-Th)/He Thermochronometer*. PhD thesis, California Institute of Technology.

Wolf, R. A., Farley, K. A., and Kass, D. M. (1998). Modeling of the temperature sensitivity of the apatite (U-Th)/He thermochronometer. *Chemical Geology*, 148(1–2):105–114.

Yamada, R., Tagami, T., and Nishimura, S. (1995a). Confined Fission-Track Length Measurement of Zircon – Assessment of Factors Affecting the Paleotemperature Estimate. *Chemical Geology*, 119(1–4):293–306.

Yamada, R., Tagami, T., Nishimura, S., and Ito, H. (1995b). Annealing Kinetics of Fission Tracks in Zircon – an Experimental-Study. *Chemical Geology*, 122(1–4):249–258.

Yamada, R., Yoshioka, T., Watanabe, K., Tagami, T., Nakamura, H., Hashimoto, T., and Nishimura, S. (1998). Comparison of experimental techniques to increase the number of measurable confined fission tracks in zircon. *Chemical Geology*, 149(1–2):99–107.

Zeitler, P. K., Herczeg, A. L., McDougall, I., and Honda, M. (1987). U-Th-He Dating of Apatite – a Potential Thermochronometer. *Geochimica Et Cosmochimica Acta*, 51(10):2865–2868.

Acknowledgments

I would like to thank Diane Seward for initiating this project and giving me the opportunity to complete a PhD at ETH Zurich. It was always nice to work with her and I will especially keep the chats we had in the counting lab in good memory.

I would like to thank Jean-Pierre Burg for initiating this project, for his effective support in writing up the thesis and the large amount of freedom he gave me after Diane had left.

I appreciated the long discussions I had with Alex Kounov, when my thoughts were turning in circles. This was crucial for getting me started on writing. Alex was a critical reviewer throughout the writing process.

I would like to thank Dimo Dimov and Dimitrios Sokoutis for joining us in the field, providing valuable information on sampling locations and introducing me to Bulgarian and Greek dishes, liquids and traditions.

I thank Danny Stockli from the University of Kansas for measuring (U-Th-Sm)/He on my apatites and Pieter Vermeesch for providing insights into the procedures of (U-Th)/He analysis. I would like to thank Giuditta Fellin for being a nice lab companion, which always had an open ear when I had questions and problems. Frédéric Herman is thanked for introducing me to geodynamic modeling. Kalin Naidenov, Jan Pleuger and Neven Georgiev kindly provided the new geological maps of Bulgaria.

I thank our secretaries Ingrid Okanta and Regula Schälchli for providing save passage through the administrative jungle of ETH. Frowin Pirovino, Andreas Jallas and Margrith Bischof are thanked for the lab assistance and for their brilliant advices concerning the art of polishing. Robert Hofmann and Reto Seifert were always very helpful when things broke in the lab and had to be repaired quickly.

Last but not least I would like to thank all the friends and colleagues from ETH and other places that made life during, after and between working so enjoyable:

Marion Campani, Pierre Bouilhol, Weronika Gorczyk, Claudio Delle Piane, Asghar Dolati and Maria, Marina Armann, Marcel Frehner, Yoli Deubelbeiss, Brian Steiner, Béatriz Quintal, Marc Lambert, Liza Tumarkina, Bettina Baitsch-Ghirardello, Stefan Schmalholz, Jeroen Smit, Santanu Misra, Negar Haghipour, Daniela Hunziker, Sarah Lechman, Filippo Schenker, Claudio Madonna, Rolf Bruijn. Tamara Baumberger, Esther Schwarzenbach, Dave Miller, Sibylle Sautier, Gabi Gassner. Diego Villagomez, Jörg Giese. Jessica Langlade, Marion Louvel, Pinar Ozfirat, Janne Koornneef, Christof Burkhardt and Anne, Ulrik Hans, Greg de Souza, Corinne Bachmann, Sarah Aciego and Tequilla, Colin Maden, Olivier Reubi, Ruth Hindshaw, Giuditta Fellin. Paula Ardia, Mark Caddick, Maarten Aerts, Alister Hack, Sabine Méhay, Luca Caricchi, Pauline Rais, Adélie Delacour, Chris Krugh, Nic Richardson, Martin Wipf, Alex Teague, Lena Melekhova, Andrew Stewart and Frauke, Marcus Gutjahr, Morten Andersen, Basti Georg, Ansgar Grimberg, Caroline Har-

ris, Miri Dühnforth, Isabel Coutand and Djordje. Irene, Patrizia, Marina, Nati, Flu and the Cafe Noar team. Manual Stahlberger for providing a slogan for the hard moments during the last 9 month: *Jede Scheiss isch e Chance...(= everything is a challenge).* Everybody I forgot. My family and Jöggu.